Efficient numerical implementations for the Maxey-Riley-Gatignol Equation

Vom Promotionsausschuss der
Technischen Universität Hamburg
zur Erlangung des akademischen Grades
Doktor der Naturwissenschaften (Dr. rer. nat.)

genehmigte Dissertation (Monographie)

von
Julio Urizarna Carasa

aus
Logroño, Spanien

2025

1. Gutachter: Prof. Dr. Daniel Ruprecht
2. Gutachter: Prof. Dr. Kathrin Padberg-Gehle
3. Gutachter: Prof. Dr. Sabine Le Borne

Tag der mündlichen Prüfung: 24.07.2025

doi: https://doi.org/10.15480/882.16156
ORCiD: https://orcid.org/0000-0002-8856-5211

Acknowledgement

To my advisor, Prof. Dr. Daniel Ruprecht, who trusted my skills when I did not believe in them myself. His guidance, good character and continuous support, specially in bad moments, were indispensable for the completion of this research and thesis.

To my colleagues, specially to Josha Fregin, Judith Angel, Dr. Ikrom Akramov and Dr. Sebastian Götschel, who were helpful and encouraging as well as ready for discussions during my time at the Institut für Mathematik.

To my ex-partner, Ira Tyschko, who encouraged me to start this research and was supportive during our relationship.

To my current partner, Sara Ramirez Sáez, who pushed me during the very last two months of the Ph.D. so I would not diminish the effort.

To the Technische Universität Hamburg and the German government for providing the resources and funding that made this research possible.

Finally, to my family and specially to my mother for their unwavering support and encouragement during this journey, specially during my worst moments. Their belief in me has been my greatest motivation to finish this work.

Summary

The Maxey-Riley-Gatignol Equation (MRGE) models the motion of a finite-sized, spherical, fully-submerged, inertial particle moving in a fluid. Applications using the MRGE are, for example, the study of the spread of Coronavirus particles in a room, the formation of clouds and the so-called marine snow.

The MRGE is a second-order integro-differential equation with a singular kernel. For over 35 years, the academic community was only able to obtain analytical solutions for few specific fields, while a general formula remains unknown. Researchers have used approximations and numerical schemes with high storage requirements or ignored the integral term, although its impact has recently been discovered to be relevant. A major breakthrough was reached in 2019, when Prasath et al. mapped the MRGE to a time-dependent Robin-type boundary condition of the one-dimensional heat equation on a semi-infinite domain, thus removing the requirement to store the full history. They also provided an implicit integral form of the solution by using Fokas method that could be later solved with a numerical scheme and a nonlinear solver.

While Prasath et al.'s numerical scheme can deliver numerical solutions accurately, the need to evaluate nested integrals makes it computationally costly and it becomes impractical for computing trajectories of a large number of particles. On the other hand, the reformulation as a boundary condition of the heat equation opens up new opportunities to solve the MRGE.

This thesis presents a new set of finite differences schemes and compare their accuracy and performance with Prasath et al.'s method as well as other preexisting schemes in six different flow velocity fields. These methods are then applied to study the influence of the often-neglected integral term in single particle trajectories, particle clusters as well as large scale fluid structures. This information provides guidelines to identify in which cases, approximations on the MRGE have a considerable influence on particle trajectories and large scale flow structures and the use of the full MRGE models is relevant.

Contents

1 Introduction **1**

2 The Maxey-Riley-Gatignol equation **5**
- 2.1 Historical background 5
- 2.2 The equation 6
- 2.3 Transformation into a diffusive problem 8

3 A solution of the diffusive problem: Prasath et al.'s approach **11**
- 3.1 The continuous formula: Fokas method 11
- 3.2 Solution formulas for specific fields 23
- 3.3 A formula for the particle's position 24
- 3.4 Discrete formula and code implementation 25
- 3.5 Prasath et al.'s algorithm 36

4 Direct numerical integration of the MRGE: Daitche's schemes **39**
- 4.1 The theory behind Daitche's methods 39
- 4.2 The discretised formula 40
- 4.3 Code implementation 41

5 Finite Difference based solution on the diffusive problem **45**
- 5.1 Discretisation in space: Finite Difference schemes 45
- 5.2 Time integrators 53

6 Convergence and efficiency **61**
- 6.1 Numerical efficiency on flow fields with existing analytical solutions 62
- 6.2 Numerical efficiency for spatially inhomogeneous and unsteady flow fields . 76

7 The effect of the Basset history term **91**
- 7.1 Influence of the BHT on individual particle trajectories 91
- 7.2 Influence of the BHT on the clustering behaviour of the particles 106
- 7.3 Lagrangian Coherent Structures 117

8 Conclusions **127**

A Coefficients for Daitche (2013)'s method **131**

B Matrices for the fourth order formulation **133**

Acknowledgements **135**

1

Introduction

The search for an equation that enables the computation of the trajectory of a small inertial particle from first principles starts back with Stokes [65] in 1851 and finishes with the MRGE presented in Maxey and Riley's paper [42], over a century later. The importance of the MRGE lies in providing an easier framework than Navier-Stokes equations in order to solve a particle's trajectory [39].

A generic solution of the MRGE was kept unresolved for a few decades due to the complex nature of the equation. The MRGE is a second order integro-differential equation with a singular kernel that requires techniques used in the resolution of fractional derivatives [69] as well as implicit problems. Difficulties in the resolution of the MRGE appear due to a history term, called the Basset-Boussinesq History Term or simply Basset History Term (BHT). Without the BHT, the MRGE turns into an ODE that is easily-solvable. However, the BHT is an implicit integral term with a singular kernel that integrates from initial time until final time. This introduces obvious difficulties when an analytical expression is searched upon and numerical methods are implemented.

The work carried out by Van Hinsberg [76] first, providing a second order method based on the approximation of the tail of the Basset force kernel and by Daitche [20] later, introducing a new way to implement schemes of arbitrary order based on quadrature schemes, showed a good progress in the numerical resolution of the MRGE. Despite this evolution, these numerical techniques require to store and use all the particle's historical data in each computation, making it specially hard in situations with large time grids.

A huge step was achieved in 2019, when a group of scientist at the International Centre for Theoretical Sciences in Bengaluru (India) published a way to transform the MRGE as a time-dependent modified Robin type boundary condition of the one-dimensional diffusion equation over a semi-infinite domain [53]. The history term was then kept encoded within the initial condition of the PDE. This transformation opened the door to solve the MRGE using previously available techniques for solving the heat equation. The authors of Prasath et al. (2019) use Fokas method (also known as Unified Transform Method) [29] to provide an integral form of the solution of the MRGE that they later solved with a numerical technique that involves a nonlinear solver.

In this thesis I provide several novel Finite Differences (FD) approaches for solving one-dimensional differential problems over a semi-infinite domain and apply them on the MRGE. These novel schemes are easily programmable, since they only require to code several matrices, compared with some existing techniques, like the one in Prasath et al. (2019) [53] that requires the computation of two terms with double integrals together with a projection into Chebyshev polynomials and the use of nonlinear solvers. These methods are stable for all set of parameters and do not require the use of additional precision, in comparison with Daitche's 3^{rd} order scheme [20] that is unstable for small values of R and S and require *quad* precision in the calculation and storage of the coefficients. These FD techniques are coupled with two types of time integrators: Fully implicit as well as Implicit-Explicit (IMEX) time integrators. The FD coupled with the implicit time integrators provide a good comparison with Prasath et al.'s method, since both require the use of nonlinear solvers. The implementation of the IMEX methods are part of the novelty of this thesis, since they avoid the use of nonlinear solvers and one can therefore expect a considerable improvement in runtimes. The implementation of the FD schemes as well as the Trapezoidal Rule was undertaken by the author of this dissertation, whereas the DIRK and IMEX time stepping methods were implemented by L. Schlegel in a preliminary study carried out for his bachelor thesis [58].

This dissertation starts with an overview of the MRGE, introducing the MRGE's chronology, the formulation of the nondimensiontal version of the MRGE presented by Maxey and Riley and the form used in this thesis, obtained after neglecting some of the terms. This overview will help the reader to recognise each one of the terms of the MRGE and understand the obstacles that exist to obtain a solution. At the end of the first chapter, the reader will follow the steps undertaken by Prasath et al. [53] for the transformation of the MRGE.

Chapters 3 and 4 present two of the already-existing numerical techniques implemented and used to validate our results: Prasath et al.'s scheme [53] and the Linear Multistep Methods developed by Daitche [20] for the MRGE. Along with the method's steps and description, the major algorithms used are presented with pseudocode to help with the understanding to the accompanying Python ToolBox [72].

Chapter 5 presents the Finite Difference schemes that the author of this thesis and a bachelor student, Leon Schlegel, implemented published in Urizarna et al. (2025) [73] together with our supervisor, Prof. Dr. Daniel Ruprecht. These methods are based on Prasath et al.'s reformulation of the MRGE as well as Koleva's [37] FD scheme for the heat equation in a semi-infite domain. The schemes presented here open up a new set of opportunities not only in the resolution of the MRGE but also in the development of newer schemes of arbitrary accuracy in differential problems defined over a semi-infinite domain.

Old and new schemes are compared in chapter 6 in order to identify trends. Trends are identified using convergence tables and plots as well as work-precision plots that are obtained for particles moving in six different velocity flow fields. With these trends, a collection of guidelines is provided for an efficient calculation of particle trajectories in these fields that could be extrapolated to other examples.

Finally, the accompanying schemes implementations in the Python ToolBox [72] are used to observe the effect of the history term on single particles as well as particle clusters with different characteristics on very varied flow fields, from simple steady and spatially homogeneous flows to fully turbulent flows. Observations show that omitting the BHT plays a nonneglectible role in single particle trajectories as well as larger scale Lagrangian features at medium and high Stokes numbers in all fields and also at low Stokes numbers in turbulent flows. In those cases, neglecting the BHT results in an overestimation of the ejection of the particle trajectories around vortices, a big difference in amplitude in oscillatory backgrounds and a general overvaluation of the large scale features.

2

The Maxey-Riley-Gatignol equation

2.1 Historical background

The MRGE is the result of applying second Newton's law on a fully-submerged small spherical rigid particle that moves in a fluid. This model was first attempted by Stokes [65] in 1851, studying the oscillatory motion of a pendulum in a fluid. Basset [8], Boussinesq [11] and Oseen [50] investigated the motion of a sphere settling in a fluid at rest under the effect of gravity. Their work resulted in what is known as the Basset-Boussinesq-Ossen (BBO) Equation. Boussinesq and Basset were the first ones to propose the BHT, which is an integral force term that accounts for the influence of the lagging boundary layer.

Tchen [70] used the BBO equation as a baseline and extended it to the case of a particle settling under the effect of gravity in (1) an unsteady uniform flow and (2) an unsteady nonuniform flow. Tchen accomplished this task by writing the BBO equation "in a frame of reference moving with the fluid, accounting for various inertial forces that arise in this frame" [39].

Authors like Corrsin and Lumley [17] identified additional "effects introduced by the field inhomogeneity in space-time" and corrected Tchen's work by modifying some of the terms. These efforts culminated in 1983 with Maxey and Riley's [42] as well as Gatignol's [31] work in what is now called the Maxey-Riley-Gatignol Equation that considered zero initial relative velocity of the particle with respect to the fluid and whose final form was obtained after Auton et al. [5] included the added mass term. A few years later, Maxey [43] modified the original equation for the more realistic and general case of a particle with nonzero initial relative velocity.

The integrodifferential nature of the MRGE together with the singular kernel, present in the BHT, make it a difficult problem to solve both analytically and numerically. For this reason, many researchers used the MRGE neglecting the problematic term under the assumption that it was relatively small for sufficiently small Stokes numbers [19, 66, 59].

An important discovery was made in 1988 by Tatom [69], who found the equivalence between the Basset-Boussinesq history term and the half-derivative of the Riemann-Liouville type and funded the basis for the progress carried out over 20 years later.

Many successful numerical schemes approximations were applied on the MRGE in the decade of the 2010s: First in 2011, Van Hinsberg et al. [76] used exponential functions to approximate the tail of the BHT, obtaining a second order method that decreased CPU times and memory requirements considerably. In 2013, Daitche [20] applied quadrature schemes to approximate the half-derivative formulation of the BHT that he later integrated using linear multistep methods. On the other hand, other authors decided to approximate the history kernel instead. In 2014, Klinkenberg et al. [35] approximated the BHT using exponential filters. Two years later, Elghannay & Tafti [25] used Mei and Adrian's approximation [44] of the history kernel that combined the short and long time limits of the history kernel. In 2018 Parmar et al. [52] provided a method based in exponential sums to approximate the history kernel up to arbitrary accuracy.

During the same decade progress was done regarding existence and uniqueness of mild solutions. Mild solutions correspond to the solutions that solve the integrated problem. In 2014 Farazmand and Haller [26] proved local existence and uniqueness of mild solutions as well as strong solutions for the case of zero initial relative velocity. One year later Langlois et al. [39] demonstrated global existence and uniqueness of mild solutions.

A major step was achieved in 2019 by Prasath et al. [53], who were able to set the MRGE as a time-dependent modified Robin type boundary condition of the one-dimensional heat equation. For this, the equivalence between the half-derivative and the Dirichlet-to-Neumann map [29] for the heat equation was used.

Based on Prasath et al.'s transformation, Prof. Dr. Daniel Ruprecht and I developed in 2023 an open Python Toolbox [74] that uses Prasath et al.'s formulas, based on Fokas method, on the examples provided by Prasath et al. as well as a generic field discretely-given. Early in 2024, we also implemented with the help of Leon Schlegel, a bachelor student, several numerical schemes in the transformed diffusive problem [73], comparing the efficiency and performance of these methods with the schemes in Daitche (2013) [20] and Prasath et al. (2019) [53]. Later in the same year Prof. Dr. Daniel Ruprecht and I, together with two external researchers, Kathrin Padberg-Gehle and Alexandra Von Kameke, sent for publication a paper that studied the influence of the BHT on three different velocity fields [75].

2.2 The equation

A widely-accepted version of the MRGE given by Langlois et al. [39] is

$$\begin{aligned}
\dot{\boldsymbol{y}}(t) &= \boldsymbol{v}(t), && (2.1)\\
\rho_p \dot{\boldsymbol{v}}(t) &= \rho_f \frac{D\boldsymbol{u}}{Dt} + && \text{(Force exerted by undisturbed fluid)}\\
&+ (\rho_p - \rho_f)\, \boldsymbol{g} + && \text{(Bouyancy force)}\\
&- \frac{9\nu\rho_f}{2a^2}\, \boldsymbol{w}(t) + && \text{(Stokes drag)}\\
&- \frac{\rho_f}{2}\left[\dot{\boldsymbol{v}} - \frac{D}{Dt}\left(\boldsymbol{u} + \frac{a^2}{10}\Delta\boldsymbol{u}\right)\right] + && \text{(Added mass term)}\\
&- \frac{9\rho_f}{2a}\sqrt{\frac{\nu}{\pi}}\left[\int_{t_0}^{t} \frac{\dot{\boldsymbol{\omega}}(s)}{\sqrt{t-s}} ds + \frac{\boldsymbol{\omega}(t_0)}{\sqrt{t-t_0}}\right] && \text{(Basset-Boussinesq memory Term)}
\end{aligned}$$

where

$$\boldsymbol{\omega}(t) := \boldsymbol{v}(t) - \boldsymbol{u}(\boldsymbol{y}(t), t) - \frac{a^2}{6}\Delta\boldsymbol{u}(\boldsymbol{y}(t), t), \tag{2.2}$$

$\boldsymbol{v}(t)$ is the particle's velocity at time t, ρ_p and ρ_f are the densities of the particle and the fluid, $\boldsymbol{u} := \boldsymbol{u}(\boldsymbol{y}(t), t)$ is the fluid's velocity at the particle's position at time t, i.e. $\boldsymbol{y}(t)$, $\boldsymbol{g}$ is the gravity's acceleration, ν is the kinematic viscosity and a is the particle's radius. The terms that include the Laplace operator Δ, are referred to as the Faxèn Corrections, that evaluate the drag force, torque and stresslet on a particle under low Reynolds numbers [13].

Each term on the right hand side of the MRGE accounts for a forcing term. The first term, consisting of the material derivative, considers the force that a massless and dimensionless particle, also called ideal particle or ideal tracer, experiments in a fluid flow. The second term accounts for the buoyancy force due to differences in densities. The third term, called Stokes drag, estimates the friction force exerted by the fluid due to the difference in their velocities. This term thus tends to relax the particle velocity towards the fluid velocity. The fourth element considers the inertia of the fluid's volume that is dragged along with the particle as it moves in the fluid. The Basset-Boussinesq memory term, also called Basset memory term or Basset history term (BHT), is perhaps the most relevant term in this paper. This is the most problematic term since it is made up of two terms with singularities at initial and final time. Additionally, the integral in the memory term for the whole time interval, accounting for the particle's history, as a part of a differential equation hinders both the analytical and numerical resolution of the MRGE.

The MRGE can be simplified by first scaling the space, time and velocity variables by using the characteristic length scale L, velocity scale U and time scale $T := {}^{L}\!/_{U}$. Using the dimensionless variables $\boldsymbol{y} \mapsto {}^{\boldsymbol{y}}\!/_{L}$ $\boldsymbol{v} \mapsto {}^{\boldsymbol{v}}\!/_{U}$ $\boldsymbol{u} \mapsto {}^{\boldsymbol{u}}\!/_{U}$ and $\boldsymbol{t} \mapsto {}^{\boldsymbol{t}}\!/_{T}$ as well as rearranging some of the terms, the MRGE given by Langlois et al [39] can be simplified as follows

$$\dot{\boldsymbol{y}}(t) = \boldsymbol{v}(t), \tag{2.3a}$$

$$R\dot{\boldsymbol{v}}(t) = \frac{D\boldsymbol{u}}{Dt} + \frac{2T}{3U}(\beta - 1)\,\boldsymbol{g} - \frac{1}{S}\,\boldsymbol{\omega}(t) + \frac{a^2}{30L^2}\frac{D}{Dt}(\Delta\boldsymbol{u}) + \tag{2.3b}$$

$$-\sqrt{\frac{3}{\pi S}}\left(\frac{\boldsymbol{\omega}(t_0)}{\sqrt{t-t_0}} + \int_{t_0}^{t}\frac{\dot{\boldsymbol{\omega}}(s)}{\sqrt{t-s}}ds\right), \tag{2.3c}$$

where

$$\boldsymbol{\omega}(t) := \boldsymbol{v}(t) - \boldsymbol{u}(\boldsymbol{y}(t), t) - \frac{a^2}{6L^2}\Delta\boldsymbol{u}(\boldsymbol{y}(t), t) \tag{2.4}$$

and

$$\beta = \frac{\rho_p}{\rho_f}, \quad R = \frac{1+2\beta}{3}, \quad S = \frac{a^2}{3T\nu}, \tag{2.5}$$

are the density ratio β, effective density ratio R and the Stokes number S.

The MRGE can be simplified by (1) assuming that the particle radius is very small compared to the length scales of the flow, i.e. $a << L$, so that the Faxèn corrections can be neglected and (2) omitting the buoyancy force, which is a purely vertical force and therefore does not apply to particles moving in a horizontal plane, as it is the case in all the flows used in this paper. The MRGE then simplifies to

$$\dot{\boldsymbol{y}}(t) = \boldsymbol{v}(t), \tag{2.6a}$$

$$R\dot{\boldsymbol{v}}(t) = \frac{D\boldsymbol{u}}{Dt} - \underbrace{\frac{1}{S}(\boldsymbol{v}-\boldsymbol{u})}_{\text{Stokes drag}} - \underbrace{\sqrt{\frac{3}{S}}\left\{\frac{\boldsymbol{v}(t_0)-\boldsymbol{u}(t_0)}{\sqrt{\pi(t-t_0)}} + \int_0^t \frac{\dot{\boldsymbol{v}}(s)-\dot{\boldsymbol{u}}(s)}{\sqrt{\pi(t-s)}}ds\right\}}_{\text{Basset History Term}}. \tag{2.6b}$$

Equation (2.6) corresponds with the version of the equation provided in Prasath et al. (2019) [53] which is the one used in this paper. From now on, every time the MRGE and their terms will be mentioned in this paper will correspond to equation (2.6).

2.3 Transformation into a diffusive problem

The singularities and the integral term in equation (2.6) make both its analytical and numerical resolution difficult to obtain. The MRGE without the BHT becomes an easily-solvable ODE. An analytical solution can in that case be found for certain simple and analytically given flow fields using standard methods, such as the method of separation of variables or variation of constants. However, the integro-differential nature of the full MRGE introduced by the BHT and its singularities make these standard methods impossible to apply. One could use the equivalence between the BHT and the half-derivative of the relative velocity shown by Tatom [69] and apply methods for the resolution of Differential Equations with rational derivatives. Quadrature schemes have been successfully applied on the full MRGE in Van Hinsberg et al. (2011) [76] and Daitche (2013) [20]. Although these numerical schemes hold rapidly increasing storage requirements and running times to account for the history term in large time grids.

In 2019, Prasath et al. [53] published a way to transform the MRGE into a forced time-dependent modified Robin boundary condition of the one-dimensional diffusion equation. The one-dimensional diffusion equation is a widely-studied problem for which different analytical resolution methods (such as Fokas method) and numerical approximations (such as finite differences methods) are known. Prasath et al.'s transformation [53, 74] starts by using the equivalence between the BHT and the half-derivative of the Riemann-Liouville type provided by Tatom [69]:

$$R\dot{\boldsymbol{v}}(t) = \frac{D\boldsymbol{u}}{Dt} - \frac{1}{S}(\boldsymbol{v}-\boldsymbol{u}) - \sqrt{\frac{3}{S}}\left(\frac{\partial}{\partial t}\right)^{1/2}(\boldsymbol{v}-\boldsymbol{u}). \tag{2.7}$$

This half derivative is equivalent to what is known as the Dirichlet-to-Neumann map, which is the relation between two different boundary conditions of the diffusion equation so that the solution to the problem is the same. This means that given the following two diffusive problems applied on $\boldsymbol{q} : [0,\infty) \times [t_0, T] \mapsto \mathbb{R}^{2,3}$, one with a Dirichlet boundary condition and another one with a Neumann boundary condition:

Dirichlet boundary condition

$$\boldsymbol{q}_t(x,t) = \boldsymbol{q}_{xx}(x,t), \tag{2.8a}$$
$$\boldsymbol{q}(x,t_0) = \boldsymbol{0}, \tag{2.8b}$$
$$\boldsymbol{q}(0,t) = \boldsymbol{h}(t). \tag{2.8c}$$

Neumann boundary condition

$$\boldsymbol{q}_t(x,t) = \boldsymbol{q}_{xx}(x,t), \tag{2.9a}$$
$$\boldsymbol{q}(x,t_0) = \boldsymbol{0}, \tag{2.9b}$$
$$\boldsymbol{q}_x(0,t) = \boldsymbol{g}(t). \tag{2.9c}$$

The solution will be the same if the following relation holds

$$\left(\frac{\partial}{\partial t}\right)^{1/2} \boldsymbol{q}(0,t) = \left(\frac{\partial}{\partial t}\right)^{1/2} \boldsymbol{h}(t) = \frac{\boldsymbol{q}(0,t_0)}{\sqrt{\pi(t-t_0)}} + \int_{t_0}^{t} \frac{\dot{\boldsymbol{q}}(0,s)}{\sqrt{\pi(t-t_0)}} ds = \boldsymbol{g}(t) = \boldsymbol{q}_x(0,t). \tag{2.10}$$

Using $\boldsymbol{q}(0,t) := \boldsymbol{v}(t) - \boldsymbol{u}(\boldsymbol{y}(t),t)$, equation (2.7) transforms into

$$\begin{aligned} \boldsymbol{q}_t(0,t) &= \left(\frac{1}{R}-1\right)\frac{D\boldsymbol{u}}{Dt} - \boldsymbol{q}(0,t)\cdot\nabla_y \boldsymbol{u} - \frac{1}{RS}\,\boldsymbol{q}(0,t) - \frac{1}{R}\sqrt{\frac{3}{S}}\left(\frac{\partial}{\partial t}\right)^{1/2} \boldsymbol{q}(0,t) && \text{(2.11a)} \\ &= \left(\frac{1}{R}-1\right)\frac{D\boldsymbol{u}}{Dt} - \boldsymbol{q}(0,t)\cdot\nabla_y \boldsymbol{u} - \frac{1}{RS}\,\boldsymbol{q}(0,t) - \frac{1}{R}\sqrt{\frac{3}{S}}\,\boldsymbol{q}_x(0,t) && \text{(2.11b)} \end{aligned}$$

which can be placed as a boundary condition of a one-dimensional diffusive problem.

Solving the following diffusive problem at the boundary will therefore be equivalent to solving the MRGE,

$$\begin{aligned} \boldsymbol{q}_t(x,t) &= \boldsymbol{q}_{xx}(x,t), && x>0, t\in(t_0,T], && \text{(2.12a)} \\ \boldsymbol{q}(x,t_0) &= \boldsymbol{0}, && x>0, && \text{(2.12b)} \\ \boldsymbol{q}_t(0,t) + \alpha\boldsymbol{q}(0,t) - \gamma\boldsymbol{q}_x(0,t) &= \boldsymbol{f}(\boldsymbol{q}(0,t),\boldsymbol{y}(t),t), && t\in[t_0,T], && \text{(2.12c)} \\ \dot{\boldsymbol{y}}(t) &= \boldsymbol{q}(0,t) + \boldsymbol{u}(\boldsymbol{y}(t)), && t\in[t_0,T], && \text{(2.12d)} \\ \lim_{t\to t_0} \boldsymbol{q}(0,t) &= \boldsymbol{q}_0, && && \text{(2.12e)} \\ \boldsymbol{y}(0) &= \boldsymbol{y}_0, && && \text{(2.12f)} \end{aligned}$$

where

$$\alpha = \frac{1}{RS}, \quad \gamma = \frac{1}{R}\sqrt{\frac{3}{S}}, \quad \boldsymbol{f}\left(\boldsymbol{q}(0,t),\boldsymbol{y}(t),t\right) = \left(\frac{1}{R}-1\right)\frac{D\boldsymbol{u}}{Dt} - \boldsymbol{q}(0,t)\cdot\nabla_y \boldsymbol{u}(\boldsymbol{y}(t),t).$$

The absolute velocity $\boldsymbol{v}(t)$ has two or three components, depending on the dimensions of the flow considered. Thus, $\boldsymbol{q}$ is a vector-valued variable and solving problem (2.12) consists in solving two or three independent diffusive problems, one for every component of the relative velocity. Note that considering the vertical buoyancy force will be critical in flow fields that consider the vertical component.

3

A solution of the diffusive problem: Prasath et al.'s approach

3.1 The continuous formula: Fokas method

Prasath et al. [53] solves the reformulated diffusive system (2.12) with the so-called Fokas Method or Unified Transform Method [29]. This method provides an integral in the Fourier plane as a representation of the solution of initial-boundary value problems for linear evolution PDEs containing x-derivatives of arbitrary order and constant coefficients formulated on the half-line [28, 29, 22].

Fokas's method is a natural choice to solve the reformulated problem, since the heat equation is a linear evolution PDE with constant coefficients defined on the half-line, with a non-standard boundary condition. The complex boundary condition and the unbounded spatial domain, i.e. $x \in [0, \infty)$, make classical methods for the heat equation, like separation of variables, less suited. This solution integral expression is not easily solvable in most cases by using classical methods for integrals, however it can be evaluated using numerical techniques.

In the following parts I show all the steps followed by Prasath et al. [53] in order to obtain the integral solution expression and provide some additional details and explanations that the author of this thesis found relevant for understanding at the time of reading.

3.1.1 The local relation

The first step in Fokas's method is to rewrite equation (2.12a) in divergence form, also referred to as the local relation [22] of equation (2.12a).

Definition 3.1 (A function in divergence form)**.** A partial differential equation is said to be in divergence form if it is written as the divergence of another function, i.e.

$$\nabla \cdot \boldsymbol{F} = \frac{\partial F^{(1)}}{\partial x^{(1)}} + \frac{\partial F^{(2)}}{\partial x^{(2)}} + \cdots + \frac{\partial F^{(m)}}{\partial x^{(m)}} = 0, \tag{3.1}$$

where $\boldsymbol{F} : A \longrightarrow \mathbb{R}^n$ is a continuously-differentiable function, $A \subseteq \mathbb{R}^m$ is an open subset and $n, m \in \mathbb{N}$.

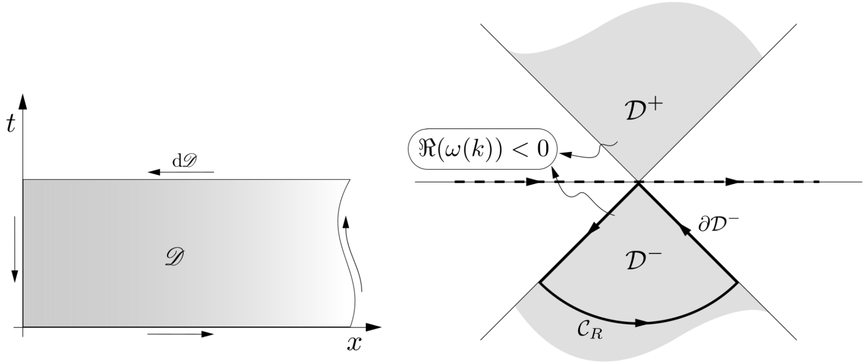

Figure 3.1: (Left) Definition domain of equation (2.12) in the time-pseudospace plane. (Right) Domain in $\mathbb{C}$ where the factor e^{k^2t} decays. Figure obtained from Prasath et al. [53].

Proposition 3.2 (Divergence form of equation (2.12a)). *Let* $\mathscr{D} := [0,\infty) \times [t_0, T]$ *be the subset of* $\mathbb{R}^2$ *shown in Figure 3.1. Given a function* $\boldsymbol{q} : \mathcal{D} \longrightarrow \mathbb{R}^n$*, with* $n \in \{2,3\}$*, that satisfies the heat equation*

$$\boldsymbol{q}_t(x,t) = \boldsymbol{q}_{xx}(x,t), \tag{3.2}$$

equation (3.2) *can be rewritten in* <u>*divergence form*</u> *as follows*

$$\left(e^{-ikx+k^2t}\boldsymbol{q}(x,t)\right)_t - \left(e^{-ikx+k^2t}\left(ik\boldsymbol{q}(x,t) + \boldsymbol{q}_x(x,t)\right)\right)_x = 0, \tag{LR}$$

where $k \in \mathbb{C}^-$.

Proof. Start by multiplying equation (2.12a) by e^{-ikx+k^2t} for $k \in \mathbb{C}^-$,

$$e^{-ikx+k^2t}\boldsymbol{q}_t(x,t) - e^{-ikx+k^2t}\boldsymbol{q}_{xx}(x,t) = 0. \tag{3.3}$$

Obtain the time derivative by adding a zero made up of the addition and subtraction of the term $k^2e^{-ikx+k^2t}\boldsymbol{q}(x,t)$,

$$\left(e^{-ikx+k^2t}\boldsymbol{q}(x,t)\right)_t - k^2e^{-ikx+k^2t}\boldsymbol{q}(x,t) - e^{-ikx+k^2t}\boldsymbol{q}_{xx}(x,t) = 0. \tag{3.4}$$

Change the coefficient $-k^2 = (ik)^2$,

$$\left(e^{-ikx+k^2t}\boldsymbol{q}(x,t)\right)_t + (ik)^2e^{-ikx+k^2t}\boldsymbol{q}(x,t) - e^{-ikx+k^2t}\boldsymbol{q}_{xx}(x,t) = 0, \tag{3.5}$$

and add another zero composed of the addition and subtraction of $ike^{-ikx+k^2t}\boldsymbol{q}_x(x,t)$, so that the x-derivative can be evaluated and the PDE presented in divergence form,

$$\left(e^{-ikx+k^2t}\boldsymbol{q}(x,t)\right)_t - \left(e^{-ikx+k^2t}\left(ik\boldsymbol{q}(x,t) + \boldsymbol{q}_x(x,t)\right)\right)_x = 0. \tag{LR}$$

This is what is called the *local relation.* ☐

3.1.2 The global relation

Fokas [29] applies *Green's theorem* [54] on the local relation (LR) in order to obtain an equation that relates the values at the boundaries of the domains. He refers to it as the global relation.

Theorem 3.3 (Green's theorem [54, 64])**.** *Let $E \subset \mathbb{R}^2$ be a closed set bounded by a simple closed curve C. Given M and N two continuously-differentiable functions of $(x^{(1)}, x^{(2)})$ defined over E, then*

$$\oint_C M dx^{(1)} + N dx^{(2)} = \iint_E \left(\frac{\partial N}{\partial x^{(1)}} - \frac{\partial M}{\partial x^{(2)}} \right) dx\, dy.$$

where the positive path of integration along C is counterclockwise.

Proof. Proof in [81]. ☐

Proposition 3.4 (The global relation of equation (2.12a))**.** *The local relation*

$$\left(e^{-ikx+k^2t}\boldsymbol{q}(x,t)\right)_t - \left(e^{-ikx+k^2t}\left(ik\boldsymbol{q}(x,t) + \boldsymbol{q}_x(x,t)\right)\right)_x = 0, \tag{LR}$$

can be written as

$$\int_0^\infty e^{-ikx+k^2t_0}\boldsymbol{q}(x,t_0)dx - \int_0^\infty e^{-ikx+k^2T}\boldsymbol{q}(x,T)dx - \int_{t_0}^T e^{k^2t}\left(ik\boldsymbol{q}(0,t) + \boldsymbol{q}_x(0,t)\right)dt = 0, \tag{GR}$$

which is an equation relating the values of $\boldsymbol{q}$ at the boundaries, called the global relation.

Proof. Integrate the local relation (LR) over the Domain, $\mathscr{D}$,

$$\int\int_{\mathscr{D}} \left(e^{-ikx+k^2t}\boldsymbol{q}(x,t)\right)_t - \left(e^{-ikx+k^2t}\left(ik\boldsymbol{q}(x,t) + \boldsymbol{q}_x(x,t)\right)\right)_x dtdx = 0. \tag{3.6}$$

Use *Green's theorem* [54, 64] to change it to a integral over the boundaries,

$$\int_{d\mathscr{D}} \left[e^{-ikx+k^2t}\boldsymbol{q}(x,t)dx + e^{-ikx+k^2t}\left(ik\boldsymbol{q}(x,t) + \boldsymbol{q}_x(x,t)\right)dt\right] = 0 \tag{3.7}$$

and splitting the domain at the boundaries, the *global relation*,

$$\int_0^\infty e^{-ikx+k^2t_0}\boldsymbol{q}(x,t_0)dx - \int_0^\infty e^{-ikx+k^2T}\boldsymbol{q}(x,T)dx - \int_{t_0}^T e^{k^2t}\left(ik\boldsymbol{q}(0,t) + \boldsymbol{q}_x(0,t)\right)dt = 0 \tag{GR}$$

is obtained. ☐

Prasath et al. [53] identify in the global relation (GR) two types of transforms: The (half-line) Fourier transforms in the positive pseudospace, $x \geq 0$, which they write with a hat and the time transforms, with a tilde.

Definition 3.5 (Half-line Fourier transform)**.** Let E be a subset of $[0,\infty)\times\mathbb{R}$, $F : E \longrightarrow \mathbb{R}^n$ with $n \in \{2,3\}$ a function of (x,t) and $k \in \mathbb{C}^-$, then

$$\hat{F}(k,t) := \int_0^\infty e^{-ikx}F(x,t)dx \tag{3.8}$$

is called the half-line Fourier transform of F.

In this work, I refer to the *half-line Fourier transform* as simply the *Fourier transform*, since most of the Fourier transforms are of that kind. The opposite will always be stated. As stated in [22], these *half-line Fourier transforms* are interpreted as "whole-line transforms of functions that are zero for $x < 0$".

Definition 3.6 (Time transform)**.** Let E be a subset of $\mathbb{R}^2$, $F : E \longrightarrow \mathbb{R}^n$ with $n \in \{2,3\}$ a function of (x,t) and $k \in \mathbb{C}^-$, then

$$\tilde{F}(k^2,t_0,t_f) := \int_{t_0}^{t_f} e^{k^2 s}F(0,s)ds \tag{3.9}$$

is called the time transform of F.

The notation used for the transforms is borrowed from Prasath et al. [53], so with

$$\hat{\boldsymbol{q}}_0(k) := \int_0^\infty e^{-ikx}\boldsymbol{q}(x,t_0)dx, \tag{3.10}$$

$$\hat{\boldsymbol{q}}(k,T) := \int_0^\infty e^{-ikx}\boldsymbol{q}(x,T)dx, \tag{3.11}$$

$$\tilde{\boldsymbol{g}}_0(k^2,t_0,T) := \int_{t_0}^{T} e^{k^2 t}\boldsymbol{q}(0,t)dt, \tag{3.12}$$

$$\tilde{\boldsymbol{g}}_1(k^2,t_0,T) := \int_{t_0}^{T} e^{k^2 t}\boldsymbol{q}_x(0,t)dt \tag{3.13}$$

the global equation can be written as follows

$$e^{k^2 t_0}\hat{\boldsymbol{q}}_0(k) - e^{k^2 T}\hat{\boldsymbol{q}}(k,T) - \tilde{\boldsymbol{g}}_1(k^2,t_0,T) - ik\tilde{\boldsymbol{g}}_0(k^2,t_0,T) = 0, \quad k \in \mathbb{C}^-. \tag{GR*}$$

3.1.3 The integral form of the solution of the Maxey-Riley-Gatignol equation

Obtaining the integral form of the solution of the MRGE is not an easy task that requires the use of many steps and several theorems from complex analysis. In order to easy the reading process, these steps are split into propositions.

First, one must obtain the time transform of the boundary condition (2.12c).

Proposition 3.7 (Time transform of equation (2.12c))**.** *Given the reformulated problem* (2.12)*, the time transform of the boundary condition* (2.12c) *is given by*

$$e^{k^2 T}\boldsymbol{q}(0,T) - e^{k^2 t_0}\boldsymbol{q}_0(k) + (\alpha - k^2)\tilde{\boldsymbol{g}}_0(k^2,t_0,T) - \gamma\tilde{\boldsymbol{g}}_1(k^2,t_0,T) = \tilde{\boldsymbol{f}}(k^2,t_0,T). \tag{3.14}$$

Proof. Multiply equation (2.12c) by e^{k^2t} for $t_0 < t < T$, $k \in \mathbb{C}^-$ and integrate over time, obtaining

$$\int_{t_0}^{T} e^{k^2t}\boldsymbol{q}_t(0,t)dt + \alpha \int_{t_0}^{T} e^{k^2t}\boldsymbol{q}(0,t)dt - \gamma \int_{t_0}^{T} e^{k^2t}\boldsymbol{q}_x(0,t)dt = \int_{t_0}^{T} e^{k^2t}\boldsymbol{f}(\boldsymbol{q}(0,t),\boldsymbol{y}(t),t)dt. \tag{3.15}$$

Then apply integration by parts on the first term,

$$\int_{t_0}^{T} e^{k^2t}\boldsymbol{q}_t(0,t)dt = e^{k^2T}\boldsymbol{q}(0,T) - e^{k^2t_0}\boldsymbol{q}(0,t_0) - k^2\int_{t_0}^{T} e^{k^2t}\boldsymbol{q}(0,t)dt, \tag{3.16}$$

so that

$$\begin{aligned} e^{k^2T}\boldsymbol{q}(0,T) - e^{k^2t_0}\boldsymbol{q}(0,t_0) + (\alpha - k^2)\int_{t_0}^{T} e^{k^2t}\boldsymbol{q}(0,t)dt - \gamma\int_{t_0}^{T} e^{k^2t}\boldsymbol{q}_x(0,t)dt = \\ = \int_{t_0}^{T} e^{k^2t}\boldsymbol{f}(\boldsymbol{q}(0,t),\boldsymbol{y}(t),t)dt, \end{aligned} \tag{3.17}$$

abbreviated as

$$e^{k^2T}\boldsymbol{q}(0,T) - e^{k^2t_0}\boldsymbol{q}_0(k) + (\alpha - k^2)\tilde{\boldsymbol{g}}_0(k^2,t_0,T) - \gamma\tilde{\boldsymbol{g}}_1(k^2,t_0,T) = \tilde{\boldsymbol{f}}(k^2,t_0,T).$$

□

With the time transform of the boundary condition, one of the boundary terms in the global relation (GR*) can be eliminated and the expression simplified. An expression for the relative velocity can be derived from this simpler expression thanks to some theorems from complex analysis borrowed from the literature. These theorems are presented hereafter.

Theorem 3.8 (Theorem 4.3.2 in Ablowitz and Fokas (1997) [1])**.** *If on a circular arc C_R of radius R and center $z = 0, zf(z) \to 0$ uniformly as $R \to \infty$, then*

$$\lim_{R\to\infty}\int_{C_R} f(z)\, dz = 0. \tag{3.18}$$

Proof. Available in Ablowitz and Fokas (1997) [1, p. 245]. □

Theorem 3.9 (Cauchy's theorem [36])**.** *Let $V \subset \mathbb{C}$ be an open subset, $\overline{V}$ its closure and $f(z)$ be complex differentiable (also called holomorphic) on $\overline{V}$, then*

$$\int_{\partial\overline{V}} f(z)dz = 0. \tag{3.19}$$

Proof. Available in Kodaira (1984) [36, p.101]. □

Proposition 3.10 (A general integral formula for $\boldsymbol{q}(0,t)$)**.** *Given problem* (2.12)*, a solution formula for $\boldsymbol{q}(0,t)$ is given by the following equation*

$$\begin{aligned} -\pi\boldsymbol{q}(0,t) = &\int_{\delta\mathcal{D}^-}\int_{t_0}^{t} \frac{ike^{-k^2(t-s)}}{(\alpha - k^2 + ik\gamma)}\boldsymbol{f}(\boldsymbol{q},\boldsymbol{y},s)\, ds\, dk + \\ &+ \int_{\delta\mathcal{D}^-} \frac{ike^{-k^2(t-t_0)}\,(\boldsymbol{q}_0 + \gamma\hat{\boldsymbol{q}}_0(k))}{(\alpha - k^2 + ik\gamma)}\, dk \end{aligned} \tag{3.20}$$

with $\delta\mathcal{D}^- := \{k \in \mathbb{C} : \Re(k^2) = 0 \wedge \Im(k) < 0\}$ (see Figure 3.1).

Proof. Using equation (3.14), the term $\boldsymbol{g}_1(k^2\tilde{,} t_0, T)$ can be eliminated in (GR*) to obtain

$$\begin{aligned}(\alpha - k^2 + ik\gamma)\tilde{\boldsymbol{g}}_0(k^2, t_0, T) = \tilde{\boldsymbol{f}}(k^2, t_0, T) + {} & e^{k^2 t_0}\left(\boldsymbol{q}_0 + \gamma\hat{\boldsymbol{q}}_0(k)\right) + \\ - {} & e^{k^2 T}\left(\boldsymbol{q}(0,T) + \gamma\hat{\boldsymbol{q}}(k,T)\right).\end{aligned} \tag{3.21}$$

Multiply equation (3.21) by $ike^{-k^2 t}$ for $t_0 < t < T$ and integrate in k over $\delta\mathcal{D}^-$, yielding

$$\begin{aligned}\int_{\delta\mathcal{D}^-} ike^{-k^2 t}\tilde{\boldsymbol{g}}_0(k^2, T)dk = & \int_{\delta\mathcal{D}^-} \frac{ike^{-k^2 t}\tilde{\boldsymbol{f}}(k^2, T)}{(\alpha - k^2 + ik\gamma)}dk + \\ & + \int_{\delta\mathcal{D}^-} \frac{ike^{k^2(t_0 - t)}\left(\boldsymbol{q}_0 + \gamma\hat{\boldsymbol{q}}_0(k)\right)}{(\alpha - k^2 + ik\gamma)}dk + \\ & - \int_{\delta\mathcal{D}^-} \frac{ike^{k^2(T - t)}\left(\boldsymbol{q}(0,T) + \gamma\hat{\boldsymbol{q}}(k,T)\right)}{(\alpha - k^2 + ik\gamma)}.\end{aligned} \tag{3.22}$$

Use the definition of $\tilde{\boldsymbol{g}}_0$,

$$\begin{aligned}\int_{\delta\mathcal{D}^-}\int_0^T ike^{-k^2(t-s)}\boldsymbol{q}(0,s)dsdk = & \int_{\delta\mathcal{D}^-} \frac{ike^{-k^2 t}\tilde{\boldsymbol{f}}(k^2, T)}{(\alpha - k^2 + ik\gamma)}dk + \\ & + \int_{\delta\mathcal{D}^-} \frac{ike^{k^2(t_0 - t)}\left(\boldsymbol{q}_0 + \gamma\hat{\boldsymbol{q}}_0(k)\right)}{(\alpha - k^2 + ik\gamma)}dk + \\ & - \int_{\delta\mathcal{D}^-} \frac{ike^{k^2(T - t)}\left(\boldsymbol{q}(0,T) + \gamma\hat{\boldsymbol{q}}(k,T)\right)}{(\alpha - k^2 + ik\gamma)}\end{aligned} \tag{3.23}$$

and the change of variables $k^2 = -2\pi il$ on the left integral,

$$\begin{aligned}-\pi\int_{-\infty}^{\infty}\int_0^T e^{2\pi i(t-s)l}\boldsymbol{q}(0,s)dsdl = & \int_{\delta\mathcal{D}^-} \frac{ike^{-k^2 t}\tilde{\boldsymbol{f}}(k^2, T)}{(\alpha - k^2 + ik\gamma)}dk + \\ & + \int_{\delta\mathcal{D}^-} \frac{ike^{k^2(t_0 - t)}\left(\boldsymbol{q}_0 + \gamma\hat{\boldsymbol{q}}_0(k)\right)}{(\alpha - k^2 + ik\gamma)}dk + \\ & - \int_{\delta\mathcal{D}^-} \frac{ike^{k^2(T - t)}\left(\boldsymbol{q}(0,T) + \gamma\hat{\boldsymbol{q}}(k,T)\right)}{(\alpha - k^2 + ik\gamma)},\end{aligned} \tag{3.24}$$

so that the standard Fourier inversion formula [80] can be applied,

$$\begin{aligned}-\pi\boldsymbol{q}(0,t) = & \int_{\delta\mathcal{D}^-} \frac{ike^{-k^2 t}\tilde{\boldsymbol{f}}(k^2, T)}{(\alpha - k^2 + ik\gamma)}dk + \int_{\delta\mathcal{D}^-} \frac{ike^{k^2(t_0 - t)}\left(\boldsymbol{q}_0 + \gamma\hat{\boldsymbol{q}}_0(k)\right)}{(\alpha - k^2 + ik\gamma)}dk + \\ & - \int_{\delta\mathcal{D}^-} \frac{ike^{k^2(T - t)}\left(\boldsymbol{q}(0,T) + \gamma\hat{\boldsymbol{q}}(k,T)\right)}{(\alpha - k^2 + ik\gamma)}dk.\end{aligned} \tag{3.25}$$

Use now the definition of $\tilde{\boldsymbol{f}}$,

$$\begin{aligned}-\pi\boldsymbol{q}(0,t) = & \int_{\delta\mathcal{D}^-} \frac{ike^{-k^2 t}}{(\alpha - k^2 + ik\gamma)}\int_{t_0}^T e^{k^2 s}\boldsymbol{f}(\boldsymbol{q}, \boldsymbol{y}, s)dsdk + \\ & + \int_{\delta\mathcal{D}^-} \frac{ike^{k^2(t_0 - t)}\left(\boldsymbol{q}_0 + \gamma\hat{\boldsymbol{q}}_0(k)\right)}{(\alpha - k^2 + ik\gamma)}dk + \\ & - \int_{\delta\mathcal{D}^-} \frac{ike^{k^2(T - t)}\left(\boldsymbol{q}(0,T) + \gamma\hat{\boldsymbol{q}}(k,T)\right)}{(\alpha - k^2 + ik\gamma)}dk,\end{aligned} \tag{3.26}$$

with the following abbreviation $\boldsymbol{f}(\boldsymbol{q},\boldsymbol{y},s) := \boldsymbol{f}(\boldsymbol{q}(0,s),\boldsymbol{y}(s),s)$ and split the time integral in the first term into two with different domains: One for $s \in [t_0, t]$ and another one for $s \in [t, T]$,

$$\begin{aligned} -\pi\boldsymbol{q}(0,t) = &\int_{\delta\mathcal{D}^-} \frac{ike^{-k^2t}}{(\alpha - k^2 + ik\gamma)} \left(\int_{t_0}^{t} e^{k^2s}\boldsymbol{f}(\boldsymbol{q},\boldsymbol{y},s)ds + \int_{t}^{T} e^{k^2s}\boldsymbol{f}(\boldsymbol{q},\boldsymbol{y},s)ds \right) dk + \\ &+ \int_{\delta\mathcal{D}^-} \frac{ike^{k^2(t_0-t)}\left(\boldsymbol{q}_0 + \gamma\hat{\boldsymbol{q}}_0(k)\right)}{(\alpha - k^2 + ik\gamma)} dk + \\ &- \int_{\delta\mathcal{D}^-} \frac{ike^{k^2(T-t)}\left(\boldsymbol{q}(0,T) + \gamma\hat{\boldsymbol{q}}(k,T)\right)}{(\alpha - k^2 + ik\gamma)} dk. \end{aligned} \tag{3.27}$$

By linearity, the first term can be separated into two integrals with different domains,

$$-\pi\boldsymbol{q}(0,t) = \int_{\delta\mathcal{D}^-} \int_{t_0}^{t} \frac{ike^{-k^2(t-s)}}{(\alpha - k^2 + ik\gamma)} \boldsymbol{f}(\boldsymbol{q},\boldsymbol{y},s)\, ds\, dk + \tag{3.28a}$$

$$+ \int_{\delta\mathcal{D}^-} \int_{t}^{T} \frac{ike^{k^2(s-t)}}{(\alpha - k^2 + ik\gamma)} \boldsymbol{f}(\boldsymbol{q},\boldsymbol{y},s)\, ds\, dk + \tag{3.28b}$$

$$+ \int_{\delta\mathcal{D}^-} \frac{ike^{k^2(t_0-t)}\left(\boldsymbol{q}_0 + \gamma\hat{\boldsymbol{q}}_0(k)\right)}{(\alpha - k^2 + ik\gamma)}\, dk + \tag{3.28c}$$

$$- \int_{\delta\mathcal{D}^-} \frac{ike^{k^2(T-t)}\left(\boldsymbol{q}(0,T) + \gamma\hat{\boldsymbol{q}}(k,T)\right)}{(\alpha - k^2 + ik\gamma)}\, dk. \tag{3.28d}$$

The second and fourth integrals, namely terms (3.28b) and (3.28d), consist of decaying exponentials as $k \to \pm\infty$, since $\Re\left\{k^2\right\} \leq 0\ \forall k \in \mathcal{D}^- := \{k \in \mathbb{C} : \Re(k^2) \leq 0 \wedge \Im(k) < 0\}$, as well as $(s-t) > 0\ \forall s \in [t,T]$ and $(T-t) > 0$. Theorem 3.8 shows that these integrals over the circular arc $\mathcal{C}_R := \{Re^{i\theta} : \theta \in [5\pi/4, 7\pi/4]\}$ will vanish as $R \to \infty$, which means that the curve can be closed and these two integrals treated as contour integrals over the closed curve $\delta\mathcal{D}^- \cup \mathcal{C}_R$.

$$-\pi\boldsymbol{q}(0,t) = \int_{\delta\mathcal{D}^-} \int_{t_0}^{t} \frac{ike^{-k^2(t-s)}}{(\alpha - k^2 + ik\gamma)} \boldsymbol{f}(\boldsymbol{q},\boldsymbol{y},s)dsdk + \tag{3.29a}$$

$$+ \int_{\delta\mathcal{D}^- \cup\, \mathcal{C}_R} \int_{t}^{T} \frac{ike^{k^2(s-t)}}{(\alpha - k^2 + ik\gamma)} \boldsymbol{f}(\boldsymbol{q},\boldsymbol{y},s)dsdk + \tag{3.29b}$$

$$+ \int_{\delta\mathcal{D}^-} \frac{ike^{k^2(t_0-t)}\left(\boldsymbol{q}_0 + \gamma\hat{\boldsymbol{q}}_0(k)\right)}{(\alpha - k^2 + ik\gamma)} dk + \tag{3.29c}$$

$$- \int_{\delta\mathcal{D}^- \cup\, \mathcal{C}_R} \frac{ike^{k^2(T-t)}\left(\boldsymbol{q}(0,T) + \gamma\hat{\boldsymbol{q}}(k,T)\right)}{(\alpha - k^2 + ik\gamma)} dk. \tag{3.29d}$$

The integrands above have two poles, located at

$$k_{1,2} = \frac{1}{2}\left(i\gamma \pm \sqrt{4\alpha - \gamma^2}\right). \tag{3.30}$$

Since the parameters α and γ are positive, the poles lie on the upper complex plane, outside the contour $\delta\mathcal{D}^- \cup \mathcal{C}_R$. Integrands (3.29b) and (3.29d) are therefore holomorphic over the set closed by $\delta\mathcal{D}^- \cup \mathcal{C}_R$ and by Cauchy's theorem (Theorem 3.9) they have no contribution. The resulting equation is as follows

$$
\begin{aligned}
-\pi \boldsymbol{q}(0,t) = & \int_{\delta\mathcal{D}^-}\int_{t_0}^{t} \frac{ike^{-k^2(t-s)}}{(\alpha-k^2+ik\gamma)}\boldsymbol{f}(\boldsymbol{q},\boldsymbol{y},s)dsdk + \\
& + \int_{\delta\mathcal{D}^-} \frac{ike^{-k^2(t-t_0)}\left(\boldsymbol{q}_0+\gamma\hat{\boldsymbol{q}}_0(k)\right)}{(\alpha-k^2+ik\gamma)}dk.
\end{aligned}
$$

□

Proposition 3.11. *The integration domain in equation* (3.20) *can be deformed into the real axis, i.e.*

$$
\begin{aligned}
\pi \boldsymbol{q}(0,t) = & \int_{-\infty}^{\infty}\int_{t_0}^{t} \frac{ike^{-k^2(t-s)}}{(\alpha-k^2+ik\gamma)}\boldsymbol{f}(\boldsymbol{q},\boldsymbol{y},s)\, ds\, dk + \\
& + \int_{-\infty}^{\infty} \frac{ike^{-k^2(t-t_0)}\left(\boldsymbol{q}_0+\gamma\hat{\boldsymbol{q}}_0(k)\right)}{(\alpha-k^2+ik\gamma)}\, dk.
\end{aligned}
\tag{3.31}
$$

Proof. Note that on sets $E^\pm := \mathbb{C}^\pm \setminus \mathcal{D}^\pm$, $\Re\left\{k^2\right\} \geq 0$ and hence $-k^2(t-s) \leq 0$ and $-k^2(t-t_0) \leq 0$. Like before, an appeal to theorem 3.8 shows that the integral of these functions over the contour $\tilde{\mathcal{C}}_R := \{\lim_{R\to\infty} Re^{i\theta} : \theta \in [\pi, {}^{5\pi}/_4] \cup [{}^{7\pi}/_4, 2\pi]\}$ is zero, permitting the following change in the integrals

$$
\int_{\delta D^-} \ldots\, dk = \left(-\int_{\delta E^-} - \int_{-\infty}^{\infty}\right) \ldots\, dk = \left(-\int_{\delta E^- \cup\, \delta\tilde{\mathcal{C}}_R} - \int_{-\infty}^{\infty}\right) \ldots\, dk. \tag{3.32}
$$

Integrals in equation (3.20) can then be modified as follows

$$
\begin{aligned}
-\pi \boldsymbol{q}(0,t) = & \left(-\int_{\delta E^- \cup\, \delta\tilde{\mathcal{C}}_R} - \int_{-\infty}^{\infty}\right)\left(\int_{t_0}^{t} \frac{ike^{-k^2(t-s)}}{(\alpha-k^2+ik\gamma)}\boldsymbol{f}(\boldsymbol{q},\boldsymbol{y},s)ds\right)dk + \\
& + \left(-\int_{\delta E^- \cup\, \delta\tilde{\mathcal{C}}_R} - \int_{-\infty}^{\infty}\right)\left(\frac{ike^{-k^2(t-t_0)}\left(\boldsymbol{q}_0+\gamma\hat{\boldsymbol{q}}_0(k)\right)}{(\alpha-k^2+ik\gamma)}\right)dk.
\end{aligned}
\tag{3.33}
$$

Again, the poles of the integrands lie on the upper complex plane (see equation (3.30)), so that the integrands are holomorphic over the whole simply connected set E^-. By theorem 3.9 (Cauchy's theorem), integrals over $\delta E^- \cup \delta\tilde{\mathcal{C}}_R$ hold no contribution, leaving the equation as follows

$$
\begin{aligned}
\pi \boldsymbol{q}(0,t) = & \int_{-\infty}^{\infty}\int_{t_0}^{t} \frac{ike^{-k^2(t-s)}}{(\alpha-k^2+ik\gamma)}\boldsymbol{f}(\boldsymbol{q},\boldsymbol{y},s)\, ds\, dk + \\
& + \int_{-\infty}^{\infty} \frac{ike^{-k^2(t-t_0)}\left(\boldsymbol{q}_0+\gamma\hat{\boldsymbol{q}}_0(k)\right)}{(\alpha-k^2+ik\gamma)}\, dk.
\end{aligned}
$$

□

Proposition 3.12. *Equation* (3.31) *can be simplified to obtain the following expression with purely real part,*

$$\begin{aligned}\frac{\pi}{2}\boldsymbol{q}(0,t) = &\int_0^\infty \int_{t_0}^t \frac{k^2\gamma e^{-k^2(t-s)}}{(\alpha-k^2)^2+k^2\gamma^2}\boldsymbol{f}(\boldsymbol{q},\boldsymbol{y},s)dsdk + \\ &-\int_0^\infty ke^{-k^2(t-t_0)}\Im\left\{\frac{(\boldsymbol{q}_0+\gamma\hat{\boldsymbol{q}}_0(k))}{(\alpha-k^2+ik\gamma)}\right\}dk,\end{aligned}\tag{3.34}$$

Proof. Start off by separating the real and imaginary parts of this equation (3.31). The separation in the first term is done by multiplying and dividing by the complex conjugate of the denominator

$$\begin{aligned}\pi\boldsymbol{q}(0,t) = &\int_{-\infty}^\infty \int_{t_0}^t \frac{ike^{-k^2(t-s)}}{(\alpha-k^2+ik\gamma)}\frac{(\alpha-k^2-ik\gamma)}{(\alpha-k^2-ik\gamma)}\boldsymbol{f}(\boldsymbol{q},\boldsymbol{y},s)dsdk + \\ &+\int_{-\infty}^\infty ike^{-k^2(t-t_0)}\Re\left\{\frac{(\boldsymbol{q}_0+\gamma\hat{\boldsymbol{q}}_0(k))}{(\alpha-k^2+ik\gamma)}\right\}dk + \\ &+\int_{-\infty}^\infty i^2ke^{-k^2(t-t_0)}\Im\left\{\frac{(\boldsymbol{q}_0+\gamma\hat{\boldsymbol{q}}_0(k))}{(\alpha-k^2+ik\gamma)}\right\}dk,\end{aligned}\tag{3.35}$$

so that the denominator has no imaginary part

$$\begin{aligned}\pi\boldsymbol{q}(0,t) = &\int_{-\infty}^\infty \int_{t_0}^t \frac{ike^{-k^2(t-s)}(\alpha-k^2-ik\gamma)}{((\alpha-k^2)^2+k^2\gamma^2)}\boldsymbol{f}(\boldsymbol{q},\boldsymbol{y},s)dsdk + \\ &+\int_{-\infty}^\infty ike^{-k^2(t-t_0)}\Re\left\{\frac{(\boldsymbol{q}_0+\gamma\hat{\boldsymbol{q}}_0(k))}{(\alpha-k^2+ik\gamma)}\right\}dk + \\ &+\int_{-\infty}^\infty i^2ke^{-k^2(t-t_0)}\Im\left\{\frac{(\boldsymbol{q}_0+\gamma\hat{\boldsymbol{q}}_0(k))}{(\alpha-k^2+ik\gamma)}\right\}dk\end{aligned}\tag{3.36}$$

and the imaginary and real parts of the first term can be clearly differentiated

$$\pi\boldsymbol{q}(0,t) = \int_{-\infty}^\infty \int_{t_0}^t \frac{k^2\gamma e^{-k^2(t-s)}}{(\alpha-k^2)^2+k^2\gamma^2}\boldsymbol{f}(\boldsymbol{q},\boldsymbol{y},s)dsdk + \tag{3.37a}$$

$$+\int_{-\infty}^\infty \int_{t_0}^t \frac{ik(\alpha-k^2)e^{-k^2(t-s)}}{(\alpha-k^2)^2+k^2\gamma^2}\boldsymbol{f}(\boldsymbol{q},\boldsymbol{y},s)dsdk + \tag{3.37b}$$

$$+\int_{-\infty}^\infty ike^{-k^2(t-t_0)}\Re\left\{\frac{(\boldsymbol{q}_0+\gamma\hat{\boldsymbol{q}}_0(k))}{(\alpha-k^2+ik\gamma)}\right\}dk + \tag{3.37c}$$

$$+\int_{-\infty}^\infty i^2ke^{-k^2(t-t_0)}\Im\left\{\frac{(\boldsymbol{q}_0+\gamma\hat{\boldsymbol{q}}_0(k))}{(\alpha-k^2+ik\gamma)}\right\}dk. \tag{3.37d}$$

Integrands (3.37b) and (3.37d) are odd with respect the variable k and therefore its integral over $\mathbb{R}$ is zero. On the other hand, integrands (3.37a) and (3.37c) are even with respect the variable k and hence their integrals over $\mathbb{R}$ are equivalent to double the integral over the interval $[0,+\infty)$. Symmetric properties in equations (3.37c) and (3.37d) are easier to see by following the same procedure done before (multiplying and dividing by the conjugate of the denominator) and using the definition of $\hat{\boldsymbol{q}}_0(k)$ as follows

$$\frac{(\boldsymbol{q}_0+\gamma\hat{\boldsymbol{q}}_0(k))}{(\alpha-k^2+ik\gamma)} = \frac{\boldsymbol{q}_0\left(\alpha-k^2-ik\gamma\right)+\gamma\hat{\boldsymbol{q}}_0(k)\left(\alpha-k^2-ik\gamma\right)}{(\alpha-k^2)^2+k^2\gamma^2}\tag{3.38}$$

where

$$\hat{\boldsymbol{q}}_0(k) = \int_0^\infty e^{ikx}\boldsymbol{q}(x,t_0)dx = \int_0^\infty \left(\cos(kx) + i\sin(kx)\right)\boldsymbol{q}(x,t_0)dx = \tag{3.39a}$$

$$= \underbrace{\int_0^\infty \cos(kx)\boldsymbol{q}(x,t_0)dx}_{=:(\hat{\boldsymbol{q}}_0(k))_{even}} + i\underbrace{\int_0^\infty \sin(kx)\boldsymbol{q}(x,t_0)dx}_{=:(\hat{\boldsymbol{q}}_0(k))_{odd}} = \tag{3.39b}$$

$$= (\hat{\boldsymbol{q}}_0(k))_{even} + i\,(\hat{\boldsymbol{q}}_0(k))_{odd}\,, \tag{3.39c}$$

so (3.38) simplifies into

$$\frac{(\boldsymbol{q}_0 + \gamma\hat{\boldsymbol{q}}_0(k))}{(\alpha - k^2 + ik\gamma)} = \frac{(\alpha - k^2)\,\boldsymbol{q}_0}{(\alpha-k^2)^2 + k^2\gamma^2} - \frac{ik\gamma\,\boldsymbol{q}_0}{(\alpha-k^2)^2+k^2\gamma^2} + \tag{3.40a}$$

$$+\frac{\gamma(\alpha-k^2)\,(\hat{\boldsymbol{q}}_0(k))_{even}}{(\alpha-k^2)^2+k^2\gamma^2} + \frac{(-ik\gamma^2)\,(\hat{\boldsymbol{q}}_0(k))_{even}}{(\alpha-k^2)^2+k^2\gamma^2} \tag{3.40b}$$

$$+\frac{i\gamma(\alpha-k^2)\,(\hat{\boldsymbol{q}}_0(k))_{odd}}{(\alpha-k^2)^2+k^2\gamma^2} + \frac{k\gamma^2\,(\hat{\boldsymbol{q}}_0(k))_{odd}}{(\alpha-k^2)^2+k^2\gamma^2}, \tag{3.40c}$$

thus

$$\Re\left\{\frac{(\boldsymbol{q}_0 + \gamma\hat{\boldsymbol{q}}_0(k))}{(\alpha - k^2 + ik\gamma)}\right\} = \frac{(\alpha-k^2)\boldsymbol{q}_0 + \gamma(\alpha-k^2)\,(\hat{\boldsymbol{q}}_0(k))_{even} + k\gamma^2\,(\hat{\boldsymbol{q}}_0(k))_{odd}}{(\alpha-k^2)^2+k^2\gamma^2} \tag{3.41}$$

as well as

$$\Im\left\{\frac{(\boldsymbol{q}_0 + \gamma\hat{\boldsymbol{q}}_0(k))}{(\alpha - k^2 + ik\gamma)}\right\} = \frac{-k\gamma\boldsymbol{q}_0 - k\gamma^2\,(\hat{\boldsymbol{q}}_0(k))_{even} + \gamma(\alpha-k^2)\,(\hat{\boldsymbol{q}}_0(k))_{odd}}{(\alpha-k^2)^2+k^2\gamma^2}. \tag{3.42}$$

The real part (3.41) is even with respect to k and multiplied by an odd term, such as the term $ike^{-k^2(t-t_0)}$ in (3.37c), the result is an odd term. Similarly, the Imaginary part (3.42) is odd with respect to k and multiplied by the same odd term, the result is an even term.

Employing the integration properties of even and odd functions stated before in (3.37), the resulting expression for $\boldsymbol{q}(0,t)$ is:

$$\begin{aligned}\frac{\pi}{2}\boldsymbol{q}(0,t) = &\int_0^\infty\int_{t_0}^t \frac{k^2\gamma e^{-k^2(t-s)}}{(\alpha-k^2)^2+k^2\gamma^2}\boldsymbol{f}(\boldsymbol{q},\boldsymbol{y},s)dsdk + \\ &-\int_0^\infty ke^{-k^2(t-t_0)}\Im\left\{\frac{(\boldsymbol{q}_0+\gamma\hat{\boldsymbol{q}}_0(k))}{(\alpha-k^2+ik\gamma)}\right\}dk,\end{aligned}$$

□

Expression (3.34) of the solution of the system (2.12) can already be used to obtain an analytic integral formula for the dynamics of particles in some specific velocity flow fields. These flow fields usually have easy expressions of $\boldsymbol{f}$. In fact, Prasath et al. [53] use it for certain scenarios of particles in time-dependent spatially homogeneous fields (cases in which $\boldsymbol{f}(\boldsymbol{q}(0,t),\boldsymbol{y}(t),t) = \boldsymbol{f}(t)$), such as a quiescent flow, a sedimenting particle and a oscillatory background; as well as a steady but spatially inhomogeneous linear field (with $\boldsymbol{f}(\boldsymbol{q}(0,t),\boldsymbol{y}(t),t) = \boldsymbol{f}(\boldsymbol{y}(t),t)$), the Couette Flow.

However, velocity fields are in general time-dependent and spatially inhomogeneous, which means that an analytic expression cannot be obtained in most cases. For this reason, Prasath et al. [53] describe a numerical scheme that includes the use of a nonlinear solver on (3.34) and that can be used in all type of flows for which the velocity field is known. In order to implement this method efficiently on equation (3.34) requires modifications in the order of integration on the first term so some terms can be precalculated before each iteration. The reason for doing this will become more evident for the reader in the following sections.

Given the term

$$\int_0^\infty \int_{t_0}^{t_j} \boldsymbol{f}(\boldsymbol{q},\boldsymbol{y},s)\frac{k^2\gamma e^{-k^2(t_j-s)}}{(\alpha-k^2)^2+k^2\gamma^2}dsdk, \tag{3.43}$$

the order of integration can be switched by using *Fubini's theorem.* $\boldsymbol{f}$ is then assumed to be a continuous and bounded function. This assumption is coherent with the physical properties of the fluids normally considered: continuous isotropic fluids at points where its velocity is finite.

Theorem 3.13 (Fubini's theorem [23]). *Let* $(\chi_1,\mathcal{A}_1,\mu)$ *and* $(\chi_2,\mathcal{A}_2,\nu)$ *be two complete measure spaces and let*

$$(\chi_1\times\chi_2)\ni(x,y)\longrightarrow f(x,y)\text{ be integrable in }(\chi_1\times\chi_2). \tag{3.44}$$

Then

$$\int_{(\chi_1\times\chi_2)} f(x,y)\,d(\mu\times\nu)=\int_{\chi_1}\left(\int_{\chi_2} f(x,y)\,d\nu\right)d\mu \tag{3.45a}$$

$$=\int_{\chi_2}\left(\int_{\chi_1} f(x,y)\,d\mu\right)d\nu. \tag{3.45b}$$

Proof. Available in DiBenedetto (2002) [23]. □

Proposition 3.14 (Switching the order of integration in (3.43)). *Let* $\chi_1:=[0,\infty)$, $\chi_2:=[t_0,t_f]$ *with* $t_0,t_f\in\mathbb{R}$ *and* $t_f>t_0$, *and* $\boldsymbol{f}:\mathbb{R}^n\times\mathbb{R}^n\times\mathbb{R}\to\mathbb{R}^n$, *with* $n\in\mathbb{N}$, *be a continuous bounded function, bounded by a positive scalar* $C>0$, *i.e.*

$$\max\Big(|f^{(1)}(\boldsymbol{q},\boldsymbol{y},s)|,|f^{(2)}(\boldsymbol{q},\boldsymbol{y},s)|,\dots,|f^{(n)}(\boldsymbol{q},\boldsymbol{y},s)|\Big)\le C, \tag{3.46}$$

then

$$\int_{\chi_1}\int_{\chi_2} \boldsymbol{f}(\boldsymbol{q},\boldsymbol{y},s)\frac{k^2\gamma e^{-k^2(t_j-s)}}{(\alpha-k^2)^2+k^2\gamma^2}dsdk=\int_{\chi_2}\int_{\chi_1} \boldsymbol{f}(\boldsymbol{q},\boldsymbol{y},s)\frac{k^2\gamma e^{-k^2(t_j-s)}}{(\alpha-k^2)^2+k^2\gamma^2}dsdk, \tag{3.47}$$

for all $\alpha,\gamma>0$.

Proof. Integrability of (3.43) is shown by finding an upper bound for the absolute value of the integral. For simplicity, consider only one component of $\boldsymbol{f}$: the maximum component of $\boldsymbol{f}\,(\boldsymbol{q},\boldsymbol{y},s)$. Without loss of generality, assume that the maximum is hold at the first component, i.e. $\max\big(f^{(1)}(\boldsymbol{q},\boldsymbol{y},s),f^{(2)}(\boldsymbol{q},\boldsymbol{y},s),\dots,f^{(n)}(\boldsymbol{q},\boldsymbol{y},s)\big)=f^{(1)}$ with $f^{(1)}:=f^{(1)}(\boldsymbol{q},\boldsymbol{y},s)$.

Start off by using the properties of the absolute value and the fact that $\boldsymbol{f}$ is bounded:

$$\left|\int_0^\infty\int_{t_0}^{t_j} f^{(1)}\frac{k^2\gamma e^{-k^2(t_j-s)}}{(\alpha-k^2)^2+k^2\gamma^2}dsdk\right| \leq \int_0^\infty\int_{t_0}^{t_j}\left|f^{(1)}\frac{k^2\gamma e^{-k^2(t_j-s)}}{(\alpha-k^2)^2+k^2\gamma^2}\right|dsdk \tag{3.48a}$$

$$= \int_0^\infty\int_{t_0}^{t_j}\left|f^{(1)}\right|\left|\frac{k^2\gamma e^{-k^2(t_j-s)}}{(\alpha-k^2)^2+k^2\gamma^2}\right|dsdk \tag{3.48b}$$

$$\leq \int_0^\infty\int_{t_0}^{t_j} C\cdot\left|\frac{k^2\gamma e^{-k^2(t_j-s)}}{(\alpha-k^2)^2+k^2\gamma^2}\right|dsdk. \tag{3.48c}$$

Drop the absolute value, since the integrand is positive for all values $s \in [t_0, t_j]$ and $k \in [0, \infty)$, integrate the terms that depend on time and rearrange as follows:

$$\int_0^\infty\int_{t_0}^{t_j} C\cdot\left|\frac{k^2\gamma e^{-k^2(t_j-s)}}{(\alpha-k^2)^2+k^2\gamma^2}\right| ds\, dk = C\int_0^\infty \frac{k^2\gamma\int_{t_0}^{t_j} e^{-k^2(t_j-s)}ds}{(\alpha-k^2)^2+k^2\gamma^2}\, dk \tag{3.49a}$$

$$= C\int_0^\infty \frac{\cancel{k^2}\gamma}{(\alpha-k^2)^2+k^2\gamma^2}\frac{1-e^{-k^2(t_j-t_0)}}{\cancel{k^2}}\, dk \tag{3.49b}$$

$$= C\gamma\int_0^\infty \frac{1-e^{-k^2(t_j-t_0)}}{(\alpha-k^2)^2+k^2\gamma^2}\, dk. \tag{3.49c}$$

The exponential term is always positive, thus

$$C\gamma\int_0^\infty \frac{1-e^{-k^2(t_j-t_0)}}{(\alpha-k^2)^2+k^2\gamma^2}\, dk \leq C\gamma\int_0^\infty \frac{1}{(\alpha-k^2)^2+k^2\gamma^2}\, dk. \tag{3.50}$$

Split the integral into two, one for $k \in \left[0, \frac{\sqrt{\alpha}}{2}\right]$ and another one for $k \in \left(\frac{\sqrt{\alpha}}{2}, +\infty\right]$ and apply two different bounds for each integral, using the inequalities $(\alpha-k^2)^2+k^2\gamma^2 \geq (\alpha-k^2)^2$ and $(\alpha-k^2)^2+k^2\gamma^2 \geq k^2\gamma^2$:

$$C\gamma\int_0^\infty \frac{1}{(\alpha-k^2)^2+k^2\gamma^2}dk = C\gamma\int_0^{\sqrt{\alpha}/2} \frac{1}{(\alpha-k^2)^2+k^2\gamma^2}\, dk + \tag{3.51a}$$

$$+\, C\gamma\int_{\sqrt{\alpha}/2}^\infty \frac{1}{(\alpha-k^2)^2+k^2\gamma^2}\, dk \leq \tag{3.51b}$$

$$\leq C\gamma\left(\int_0^{\sqrt{\alpha}/2}\frac{1}{(\alpha-k^2)^2}dk + \frac{1}{\gamma^2}\int_{\sqrt{\alpha}/2}^\infty \frac{1}{k^2}dk\right). \tag{3.51c}$$

The first integral is bounded, since its integrand is continuous over the compact domain $\left[0, \frac{\sqrt{\alpha}}{2}\right]$. The second integral belongs to the set of converging improper integrals of the type $\int_a^\infty \frac{1}{k^p}dk$ with $a > 0$ and $p > 1$, thus it is bounded. The sum of these two integrals is therefore bounded and the function integrable so theorem 3.13 (Fubini's theorem) can be applied and the order of integration switched. □

Switching the integration order, one obtains:

$$\int_{t_0}^t\int_0^\infty \boldsymbol{f}(\boldsymbol{q},\boldsymbol{y},s)\frac{k^2\gamma e^{-k^2(t-s)}}{(\alpha-k^2)^2+k^2\gamma^2}\, dk\, ds = \int_{t_0}^t \boldsymbol{f}(\boldsymbol{q},\boldsymbol{y},s)\int_0^\infty \frac{k^2\gamma e^{-k^2(t-s)}}{(\alpha-k^2)^2+k^2\gamma^2}\, dk\, ds \tag{3.52}$$

so the integral formula of the MRGE translates into

$$\frac{\pi}{2}\boldsymbol{q}(0,t) = \underbrace{\int_{t_0}^{t} \boldsymbol{f}(\boldsymbol{q},\boldsymbol{y},s)\mathcal{L}(t-s)\, ds}_{=:\boldsymbol{\mathcal{F}}(t)} - \underbrace{\int_{0}^{\infty} ke^{-k^2(t-t_0)}\Im\left\{\frac{(\boldsymbol{q}_0+\gamma\hat{\boldsymbol{q}}_0(k))}{(\alpha-k^2+ik\gamma)}\right\} dk}_{=:\boldsymbol{\mathcal{H}}(t)}, \tag{3.53}$$

where

$$\mathcal{L}(t-s) := \int_0^\infty \frac{k^2\gamma e^{-k^2(t-s)}}{(\alpha-k^2)^2+k^2\gamma^2}dk. \tag{3.54}$$

3.2 Solution formulas for specific fields

Prasath et al. [53] provide a few examples of velocity fields in which either formulae (3.34) or (3.53) can be used to obtain an explicit solution expression. In all these examples, the initial time is set to be zero, i.e. $t_0 = 0$, for simplicity and it is assumed that the particle has no preexisting history at the point of starting its motion, i.e. zero initial condition almost everywhere, namely

$$\boldsymbol{q}(x,0) = \begin{cases} \boldsymbol{q}_0, & \textit{if} \quad x = 0, \\ \boldsymbol{0}, & \textit{if} \quad x \neq 0. \end{cases} \tag{3.55}$$

and therefore $\hat{\boldsymbol{q}}_0(k) = \boldsymbol{0}$, leaving the solution formula as

$$\frac{\pi}{2}\boldsymbol{q}(0,t) = \int_0^t \boldsymbol{f}(\boldsymbol{q},\boldsymbol{y},s)\mathcal{L}(t-s)ds + \boldsymbol{q}_0\int_0^\infty \frac{k^2\gamma e^{-k^2t}}{(\alpha-k^2)^2+k^2\gamma^2}\, dk. \tag{3.56}$$

These examples are:

1. A relaxing particle in a quiescent flow [53, Example 1, p. 10], i.e. absence of background flow or $\boldsymbol{f}(\boldsymbol{q}(0,t),\boldsymbol{y}(t),t) = \boldsymbol{0}\ \forall\ t \geq 0$,

$$\boldsymbol{q}(0,t) = \frac{2}{\pi}\ \boldsymbol{q}_0\int_0^\infty \frac{k^2\gamma e^{-k^2t}}{(\alpha-k^2)^2+k^2\gamma^2}dk. \tag{3.57}$$

2. A sedimenting particle [53, Example 2, p. 12], i.e. a particle settling under the effect of gravity. Since gravity is considered as a constant force acting in the vertical direction, one may just consider a scalar forcing term with constant value or $f(q(0,t),y(t),t) = \sigma \in \mathbb{R}\ \forall t \geq 0$. In this case, it is more convenient to use equation (3.53), since the time integral can be solved analytically,

$$\frac{\pi}{2}q(0,t) = \int_0^\infty \frac{k^2\gamma\sigma}{(\alpha-k^2)^2+k^2\gamma^2}\int_0^t e^{-k^2(t-s)}dsdk\ + q_0\int_0^\infty \frac{k^2\gamma e^{-k^2t}}{(\alpha-k^2)^2+k^2\gamma^2}dk, \tag{3.58}$$

resulting in

$$\begin{aligned}\frac{\pi}{2}q(0,t) = &\int_0^\infty \frac{k^2\gamma\sigma}{(\alpha-k^2)^2+k^2\gamma^2}\frac{1-e^{-k^2t}}{k^2}dk + \\ &+ q_0\int_0^\infty \frac{k^2\gamma e^{-k^2t}}{(\alpha-k^2)^2+k^2\gamma^2}dk.\end{aligned} \tag{3.59}$$

By rearranging the terms one obtains

$$q(0,t) = \frac{2}{\pi}\sigma \int_0^\infty \frac{\gamma(1-e^{-k^2 t})}{(\alpha-k^2)^2+k^2\gamma^2} dk + \frac{2}{\pi} q_0 \int_0^\infty \frac{\gamma k^2 e^{-k^2 t}}{(\alpha-k^2)^2+k^2\gamma^2} dk. \tag{3.60}$$

3. A particle in an oscillatory background with single frequency [53, Example 3, p. 14], or mathematically $f(q(0,t), y(t), t) = \sin(\lambda t)$ with $\lambda \in \mathbb{R}$. In this case I also consider the scalar case for simplicity:

$$\begin{aligned} \frac{\pi}{2} q(0,t) = &\int_0^\infty \frac{k^2\gamma}{(\alpha-k^2)^2+k^2\gamma^2} \int_0^t e^{-k^2(t-s)} \sin(\lambda s) ds dk + \\ &+ q_0 \int_0^\infty \frac{k^2\gamma e^{-k^2 t}}{(\alpha-k^2)^2+k^2\gamma^2} dk, \end{aligned} \tag{3.61}$$

resulting in

$$\begin{aligned} q(0,t) = &\frac{2}{\pi}\gamma \int_0^\infty \frac{k^2}{(\alpha-k^2)^2+k^2\gamma^2} \left\{ \frac{\lambda e^{-k^2 t} - \lambda \cos(\lambda t) + k^2 \sin(\lambda t)}{\lambda^2 + k^4} \right\} dk + \\ &+ \frac{2}{\pi}\gamma q_0 \int_0^\infty \frac{k^2 e^{-k^2 t}}{(\alpha-k^2)^2+k^2\gamma^2} dk. \end{aligned} \tag{3.62}$$

4. A particle in the Couette flow [53, Example 4, p. 16], which is the only spatially inhomogeneous case considered by Prasath et al. for which one can use equation (3.34) to obtain an analytical solution. The Couette flow has the advantage that it is a two-dimensional time-independent linear flow, i.e.

$$\boldsymbol{u}(\boldsymbol{y}(t), t) = \begin{bmatrix} \lambda y^{(2)}(t) \\ 0 \end{bmatrix}. \tag{3.63}$$

Being consistent with Prasath et al.'s notation, from now on I will use the superscripts $(\cdot)^{(1)}$ and $(\cdot)^{(2)}$ to refer to the horizontal and vertical components of a vector, respectively. The solution for a particle moving in this field has the following form:

$$\boldsymbol{q}(0,t) = \frac{2}{\pi} \int_0^\infty e^{-k^2 t} \begin{bmatrix} \frac{k^2\gamma}{(\alpha-k^2)^2+k^2\gamma^2} & \lambda \frac{2k^2\gamma(k^2-\alpha)}{((\alpha-k^2)^2+k^2\gamma^2)^2} \\ 0 & \frac{k^2\gamma}{(\alpha-k^2)^2+k^2\gamma^2} \end{bmatrix} \boldsymbol{q}_0 \, dk. \tag{3.64}$$

Note that even though Prasath et al. considers a two-dimensional flow, they do not consider the buoyancy force. This term is to be included if one considers one of the dimensions to be the vertical one.

3.3 A formula for the particle's position

In the previous sections I obtained a formula for the particle's relative velocity using Fokas's method and used it for some specific background flows. However, in most cases one is interested in calculating the particle's position at a certain time. The equation of the definition of the relative velocity, i.e. equation (2.12d), relates both variables $\dot{\boldsymbol{y}}$ and

$\boldsymbol{q}(0,\cdot)$ and it can thus be used to obtain a formula for the particle's position by integrating with respect to the temporal variable in the interval $[t_0, t]$, namely:

$$\int_{t_0}^{t} \dot{\boldsymbol{y}}(s) ds = \int_{t_0}^{t} \left(\boldsymbol{q}(0,s) + \boldsymbol{u}(\boldsymbol{y}(s), s)\right) ds, \tag{3.65}$$

and integrating the term on the left hand side,

$$\boldsymbol{y}(t) = \boldsymbol{y}(t_0) + \int_{t_0}^{t} \left(\boldsymbol{q}(0,s) + \boldsymbol{u}(\boldsymbol{y}(s), s)\right) ds. \tag{3.66}$$

Note that equation (3.66) is an implicit formula and it may require the use of a nonlinear solver.

3.4 Discrete formula and code implementation

Section 3.2 presented examples in which it is possible to obtain an analytical expression for a particle's relative velocity. These fields had simple expressions for $\boldsymbol{f}$ and are quite ideal: they consider flows with special characteristics, for instance time-independent spatially homogeneous background flows or a fully linear background. In most real-life experiments, the flows do not hold any of these characteristics and an analytical expression for the particle dynamics cannot be obtained. For this reason, Prasath et al. (2019) developed in [53, Section 5.3] a numerical technique that can be used in all cases as long as the field is known, by expanding $\boldsymbol{f}$ into a Chebyshev polynomial basis and using a nonlinear solver to overcome the nonlinearity in (3.53).

This section studies how to obtain and implement a numerical solution for one of the spatial dimensions of the problem, particularly for the variables $q_j := q(0, \tau_j)$ and $y_j := y(\tau_j)$, at certain τ_j Chebyshev nodes within a subinterval $[t_r, t_{r+1}]$, where t_r is one of the M equidistant nodes within the time domain $[t_0, t_f]$, with $t_f > t_0$. Each directional dimension is analysed separately to avoid confusions between the vectors with directional components and vectors of discrete solutions, e.g. $\boldsymbol{y}(t) = [y^{(1)}(t), y^{(2)}(t), \dots]$ against $\bar{\boldsymbol{y}}^{(1)}(t) := [y_1^{(1)}(t), y_2^{(1)}(t), \dots]$. The formulas and equations required for the resolution of a particle's trajectory are implemented within our open-access Python Toolbox [72]. For this reason, sketches of the algorithms used in this toolbox are provided after the final formulas. This toolbox is supported by functions available in the SCIPY [77] and NUMPY [33] libraries, versions 1.11.3 and 1.26.1, respectively.

The attached Python toolbox consists of several Python scripts: some that set the parameters of the particle and others that run the numerical method to obtain the solution. This way, every time the user wants to solve the MRGE using the transformation and method described in Prasath et al. [53] using our toolbox, the user may set the particle parameters using the script called *a00_PMTERS_INPUT.py* and create an instance of the class *maxey_riley_Prasath* given in the file *a09_PRTCLE_PRSTH.py*. The user may also choose to use the ready-to-use script that provided in the ToolBox instead, called *a01_SOLVER_PRSTH.py*.

3.4.1 Grid definition

The Chebyshev time nodes τ_j are defined by the formula

$$\tau_j := t_r + \frac{\Delta t}{2}\left(1 - \cos\left(\frac{j\pi}{L-1}\right)\right), \qquad \forall j \in \{0, 1, \ldots, L-1\} \tag{3.67}$$

with $\Delta t := t_{r+1} - t_r$. The implementation of equation (3.67) in the toolbox is carried out within two methods

(1) The one that calculates L Chebyshev nodes,

$$\sigma_j = -\cos\left(\frac{j\pi}{L-1}\right), \quad \forall j \in \{0, 1, \ldots, L-1\}, \tag{3.68}$$

within the $[-1, 1]$ domain

Algorithm 1 Define L Chebyshev nodes, σ_j:

```
function SIGMAV_DEF($L$):
    for $j \leftarrow 0$ to $L-1$ do
        $\boldsymbol{\sigma}[j] \leftarrow -\cos\left(\frac{j\pi}{L-1}\right)$
    end for
    return $\boldsymbol{\sigma}$
end function
```

(2) The one that then maps the σ_j nodes into the time domain $[t_r, t_{r+1}]$ as described in equation (3.67),

Algorithm 2 Define grid nodes in time, τ_j:

```
function TNODES_DEF($L$, $t_r$, $\Delta t$)
    for $j \leftarrow 0$ to $L-1$ do
        $\boldsymbol{\tau}[j] \leftarrow t_r + \frac{\Delta t}{2}(1 + \boldsymbol{\sigma}[j])$
    end for
    return $\boldsymbol{\tau}$
end function
```

This calculation is split into two methods due to efficiency, since the algorithm 1 is only required to be called once – at the beginning of the program –, whereas the τ_j nodes have to be recalculated in each new time interval $[t_r, t_{r+1}]$.

The mapped Chebyshev nodes in the pseudospace, k_l, characterized by

$$k_l = \frac{1 + \tilde{k}_l}{1 - \tilde{k}_l}, \qquad \text{where} \qquad \tilde{k}_l := -\cos\left(\frac{l\pi}{N}\right), \qquad \forall l \in \{0, 1, \ldots, N-1\}, \tag{3.69}$$

are calculated only once, since they remain constant among the whole program. Algorithm 3 provides the method used.

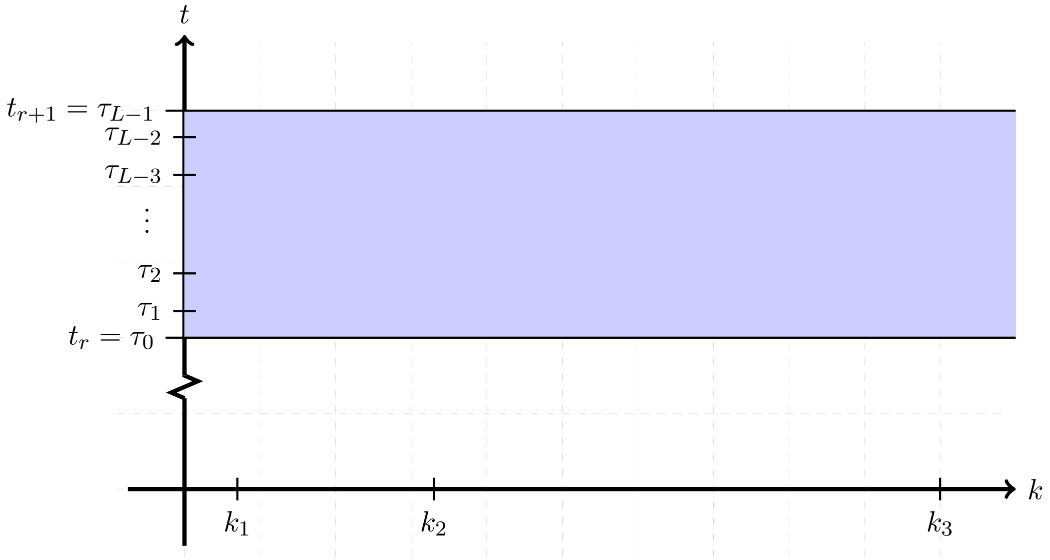

Figure 3.2: Representation of the domain $[t_r, t_{r+1}] \times [0, \infty)$ in light blue as well as some of the Chebyshev nodes in time, τ_j, and Fourier space, $\tilde{k}_l$.

Algorithm 3 Define frequency domain grid nodes, k_l:

```
function KNODES_DEF($N$):
    for $l \leftarrow 0$ to $N-1$ do
        $\tilde{\boldsymbol{k}}[l] \leftarrow -\cos\left(\frac{l\pi}{N}\right)$
        $\boldsymbol{k}[l] \leftarrow \frac{1+\tilde{k}_l}{1-\tilde{k}_l}$
    end for
    return $\tilde{\boldsymbol{k}}$, $\boldsymbol{k}$
end function
```

Note that the nodes τ_j and $\tilde{k}_l$ defined in equation (3.67) and (3.69) respectively, correspond to L and N Chebyshev nodes defined in the intervals $[t_r, t_{r+1}]$ and $[-1, 1)$. Once defined, the $\tilde{k}_l$ nodes are mapped into the semi-infinite domain $[0, \infty)$ by using the rational rule in (3.69), obtaining the k_l nodes at which the quantity $\mathscr{H}$ is defined. A representation of $[t_r, t_{r+1}] \times [0, \infty)$ subdomain and the τ_j and k_l nodes is given in figure 3.2.

3.4.2 Expansion into Chebyshev bases

Consider the continuous formula (3.53) for a generic component and some $t \in [t_r, t_{r+1}]$ and a non-zero initial condition $q(x, t_r) \neq 0 \ \forall x \in [0, \infty)$, i.e.

$$\frac{\pi}{2} q(0,t) = \underbrace{\int_{t_r}^{t} f(\boldsymbol{q}, \boldsymbol{y}, s)\mathcal{L}(t-s)ds}_{=:\, \mathcal{F}(t)} - \underbrace{\int_0^{\infty} k e^{-k^2(t-t_r)} \Im\{\mathscr{H}(k, t_r)\} dk}_{=:\, \mathcal{H}(t)} . \tag{3.70}$$

Then apply the change of variables $m := t - s$ to the time integral of $\mathcal{F}(t)$ as follows

$$\mathcal{F}(t) = \int_0^{\tilde{t}} f(\boldsymbol{q}, \boldsymbol{y}, t-m)\mathcal{L}(m)dm, \tag{3.71}$$

where $\tilde{t} := t - t_r$. The new variable, $\tilde{t}$, is a quantity that describes the distance from t to the initial time in the interval, t_r. This change of variables enables us to generalise the integration for any subinterval independently of the initial time t_r as long as the Chebyshev nodes are distributed equally in all the time interval.

Chebyshev polynomials are defined over the interval $[-1, 1]$. By using the change of variables $l = \frac{2}{\Delta t} m - 1$, the integration can be carried out in this interval (Note that the right integration bound reaches 1 when $\tilde{t} = \Delta t$),

$$\mathcal{F}(t) = \int_{-1}^{\frac{2\tilde{t}-\Delta t}{\Delta t}} f\left(\boldsymbol{q}, \boldsymbol{y}, t - \frac{\Delta t}{2}(l+1)\right) \mathcal{L}\left(\frac{\Delta t}{2}(l+1)\right) \frac{\Delta t}{2} dl. \tag{3.72}$$

Evaluating f at the points τ_j, $\forall j \in \{0, 1, \ldots, L-1\}$ permits to expand it into Chebyshev polynomials, i.e.

$$f\left(\boldsymbol{q}, \boldsymbol{y}, t - \frac{\Delta t}{2}(l+1)\right) \approx \sum_{n=0}^{L-1} c_n(\bar{\boldsymbol{q}}(\boldsymbol{\tau}), \bar{\boldsymbol{y}}(\boldsymbol{\tau}))\, T_n(l), \tag{3.73}$$

where c_n is the n-th Chebyshev coefficient that depends on the discrete values of the relative velocity at the boundary $\bar{\boldsymbol{q}}(\boldsymbol{\tau}) := [\boldsymbol{q}(0, \tau_0), \boldsymbol{q}(0, \tau_1), \ldots, \boldsymbol{q}(0, \tau_{L-1})]^T$ and the discrete trajectories $\bar{\boldsymbol{y}}(\boldsymbol{\tau}) := [\boldsymbol{y}(\tau_0), \boldsymbol{y}(\tau_1), \ldots, \boldsymbol{y}(\tau_{L-1})]^T$; $\boldsymbol{\tau} := [\tau_0, \tau_1, \ldots, \tau_{L-1}]^T$ is the vector of discrete times in the interval $[t_r, t_{r+1}]$ and T_n is the Chebyshev polynomials of the first kind of degree n. The expansion of f into Chebyshev polynomials provides the following approximation of $\mathcal{F}(t)$,

$$\mathcal{F}(t) \approx \underbrace{\sum_{n=0}^{L-1} c_n(\bar{\boldsymbol{q}}(\boldsymbol{\tau}), \bar{\boldsymbol{y}}(\boldsymbol{\tau})) \int_{-1}^{\frac{2\tilde{t}-\Delta t}{\Delta t}} T_n(l) \mathcal{L}\left(\frac{\Delta t}{2}(l+1)\right) \frac{\Delta t}{2} dl,}_{=: \tilde{\mathcal{F}}_n(t)} \tag{3.74}$$

where $\tilde{\mathcal{F}}_n(t)$ is the approximation of $\mathcal{F}(t)$ obtained with Chebyshev polynomials up to degree n.

The integral in $\mathcal{H}(t)$ is discretised by taking the change of variables $k = \frac{1+\tilde{k}}{1-\tilde{k}}$,

$$\mathcal{H}(t) = \int_{-1}^{1} \left(\frac{1+\tilde{k}}{1-\tilde{k}}\right) e^{-\left(\frac{1+\tilde{k}}{1-\tilde{k}}\right)^2 \tilde{t}}\, \Im\left\{\mathscr{H}\left(\frac{1+\tilde{k}}{1-\tilde{k}}, t_r\right)\right\} \frac{2}{(1-\tilde{k})^2}\, d\tilde{k} \tag{3.75}$$

so that the integration domain corresponds to the domain of definition of the Chebyshev polynomials. $\Im\{\mathscr{H}\}$ is expanded into Chebyshev polynomials by evaluating it at the points $k_l = \frac{1-\tilde{k}_l}{1+\tilde{k}_l}$ for all $l \in \{0, 1, \ldots, N-1\}$, i.e.

$$\Im\left\{\mathscr{H}\left(\frac{1+\tilde{k}}{1-\tilde{k}}, t_r\right)\right\} \approx \sum_{p=0}^{N-1} d_p(\hat{\boldsymbol{q}}(\boldsymbol{k}, t_r))\, T_p(\tilde{k}), \tag{3.76}$$

where d_p is the p-th Chebyshev coefficient, $\boldsymbol{k} := [k_0, k_1, \ldots, k_{N-1}]$ is the vector of discrete values of k_l and T_p is the Chebyshev polynomial of the first kind of degree p.

The discretised expression for $\mathcal{H}$ is given by

$$\mathcal{H}(t) \approx \underbrace{\sum_{p=0}^{N-1} d_p(\hat{\boldsymbol{q}}(\boldsymbol{k}, t_r)) \int_{-1}^{1} T_p(\tilde{k}) \mathcal{G}(\tilde{k}, \tilde{t}) d\tilde{k},}_{=: \tilde{\mathcal{H}}_p(t)} \tag{3.77}$$

where

$$\mathcal{G}(\tilde{k}, \tilde{t}) := \left(\frac{1+\tilde{k}}{1-\tilde{k}} \right) e^{-\left(\frac{1+\tilde{k}}{1-\tilde{k}}\right)^2 \tilde{t}} \frac{2}{(1-\tilde{k})^2} \tag{3.78}$$

and $\tilde{\mathcal{H}}_p(t)$ is the approximation of $\mathcal{H}(t)$ obtained with Chebyshev polynomials up to degree n. The full approximation formula for one of the components of $\boldsymbol{q}(0,t)$ then becomes,

$$\begin{aligned} \frac{\pi}{2} q(0,t) \approx & \underbrace{\sum_{n=0}^{L-1} c_n(\bar{\boldsymbol{q}}(\boldsymbol{\tau}), \bar{\boldsymbol{y}}(\boldsymbol{\tau})) \int_{-1}^{\frac{2\tilde{t}-\Delta t}{\Delta t}} T_n(l) \mathcal{L}\left(\frac{\Delta t}{2}(l+1) \right) \frac{\Delta t}{2} dl}_{=: \tilde{\mathcal{F}}_n(t)} + \\ & - \underbrace{\sum_{p=0}^{N-1} d_p(\hat{\boldsymbol{q}}(\boldsymbol{k}, t_r)) \int_{-1}^{1} T_p(\tilde{k}) \mathcal{G}(\tilde{k}, \tilde{t}) d\tilde{k}}_{=: \tilde{\mathcal{H}}_p(t)} . \end{aligned} \tag{3.79}$$

The approximation formula for $\boldsymbol{y}$ is obtained by using the same procedure as before: expanding the integrand of equation (3.66) into a Chebyshev bases of polynomials. Only one of the components of the vector is considered. The change of variables $l = \frac{2}{\Delta t}(s - t_0) - 1$ enables the change in the integration domain into the domain of definition of the Chebyshev polynomials, obtaining

$$y(t) = y(t_0) + \frac{\Delta t}{2} \int_{-1}^{\frac{2\tilde{t}-\Delta t}{\Delta t}} \left(q\left(0, \frac{\Delta t}{2}(l+1) + t_r \right) + u\left(\boldsymbol{y}\left(\frac{\Delta t}{2}(l+1) + t_r \right) \right) \right) dl. \tag{3.80}$$

The Chebyshev expansion of $q + u$ is given by

$$q\left(0, \frac{\Delta t}{2}(l+1) + t_r \right) + u\left(\boldsymbol{y}\left(\frac{\Delta t}{2}(l+1) + t_r \right) \right) \approx \sum_{\kappa=0}^{L-1} b_\kappa(\bar{\boldsymbol{q}}(\boldsymbol{\tau}), \bar{\boldsymbol{y}}(\boldsymbol{\tau})) T_\kappa(l) \tag{3.81}$$

where b_κ is the k-th coefficient of the Chebyshev polynomials and T_κ is the Chebyshev polynomial of the first kind of order κ. Hence, the fully discretised expression becomes

$$y(t) \approx y(t_0) + \frac{\Delta t}{2} \sum_{\kappa=0}^{L-1} b_\kappa(\bar{\boldsymbol{q}}(\boldsymbol{\tau}), \bar{\boldsymbol{y}}(\boldsymbol{\tau})) \int_{-1}^{\frac{2\tilde{t}-\Delta t}{\Delta t}} T_\kappa(l) dl. \tag{3.82}$$

3.4.3 Full discretisation

The interest in section 3.4 consists in obtaining an expression for the discrete solution $q_j := q(0, \tau_j)$ at the Chebyshev time nodes τ_j in the generic interval $[t_r, t_{r+1}]$. Note that

$\tau_0 = t_r$ and $\tau_{L-1} = t_{r+1}$. The distance between the Chebyshev nodes τ_j and the initial interval time t_r, i.e. $\tilde{\tau}_j := \tau_j - t_r$, are kept constant in all time intervals. This results in the following equation

$$\begin{aligned}\frac{\pi}{2} q_j \approx &\underbrace{\sum_{n=0}^{L-1} c_n(\bar{\boldsymbol{q}}(\boldsymbol{\tau}), \bar{\boldsymbol{y}}(\boldsymbol{\tau})) \int_{-1}^{\frac{2\tilde{\tau}_j-\Delta t}{\Delta t}} T_n(l)\mathcal{L}\left(\frac{\Delta t}{2}(l+1)\right)\frac{\Delta t}{2} dl\, +}_{=:\, \tilde{\boldsymbol{\mathcal{F}}}_n(\tau_j)} \\ &\underbrace{- \sum_{p=0}^{N-1} d_p(\hat{\boldsymbol{q}}(\boldsymbol{k},\tau_0)) \int_{-1}^{1} T_p(\tilde{k})\mathcal{G}(\tilde{k},\tilde{\tau}_j)d\tilde{k}\,.}_{=:\tilde{\boldsymbol{\mathcal{H}}}_p(\tau_j)}\end{aligned} \tag{3.83}$$

The sums can be written in compressed form as the dot product of two vectors, i.e.

$$\frac{\pi}{2} q_j \approx \frac{\Delta t}{2} \boldsymbol{c}(\bar{\boldsymbol{q}}(\boldsymbol{\tau}), \bar{\boldsymbol{y}}(\boldsymbol{\tau})) \cdot \mathbb{F}(\tilde{\tau}_j) - \boldsymbol{d}(\hat{\boldsymbol{q}}(\boldsymbol{k},\tau_0)) \cdot \mathbb{H}(\tilde{\tau}_j), \tag{3.84}$$

where

$$\mathbb{F}(\tilde{\tau}_j) := \begin{bmatrix} \int_{-1}^{\frac{2\tilde{\tau}_j-\Delta t}{\Delta t}} T_0(l)\mathcal{L}\left(\frac{\Delta t}{2}(l+1)\right) dl \\ \int_{-1}^{\frac{2\tilde{\tau}_j-\Delta t}{\Delta t}} T_1(l)\mathcal{L}\left(\frac{\Delta t}{2}(l+1)\right) dl \\ \vdots \\ \int_{-1}^{\frac{2\tilde{\tau}_j-\Delta t}{\Delta t}} T_{L-1}(l)\mathcal{L}\left(\frac{\Delta t}{2}(l+1)\right) dl \end{bmatrix}_{L\times 1} \tag{3.85}$$

and

$$\mathbb{H}(\tilde{\tau}_j) := \begin{bmatrix} \int_{-1}^{1} T_0(\tilde{k})\mathcal{G}(\tilde{k},\tilde{\tau}_j)d\tilde{k} \\ \int_{-1}^{1} T_1(\tilde{k})\mathcal{G}(\tilde{k},\tilde{\tau}_j)d\tilde{k} \\ \vdots \\ \int_{-1}^{1} T_{N-1}(\tilde{k})\mathcal{G}(\tilde{k},\tilde{\tau}_j)d\tilde{k} \end{bmatrix}_{N\times 1} . \tag{3.86}$$

Extending equation (3.84) for all τ_j results in

$$\frac{\pi}{2}\bar{\boldsymbol{q}}(\boldsymbol{\tau}) \approx \underbrace{\frac{\Delta t}{2}\, \mathbb{M}_{\mathbb{F}}(\tilde{\boldsymbol{\tau}})\, \boldsymbol{c}(\bar{\boldsymbol{q}}(\boldsymbol{\tau}), \bar{\boldsymbol{y}}(\boldsymbol{\tau}))}_{=:\, \tilde{\boldsymbol{\mathcal{F}}}_n(\tilde{\boldsymbol{\tau}},\bar{\boldsymbol{q}}(\boldsymbol{\tau}),\bar{\boldsymbol{y}}(\boldsymbol{\tau}))} - \underbrace{\mathbb{M}_{\mathbb{H}}(\tilde{\boldsymbol{\tau}})\, \boldsymbol{d}(\hat{\boldsymbol{q}}(\boldsymbol{k},\tau_0))}_{=:\tilde{\boldsymbol{\mathcal{H}}}_p(\tilde{\boldsymbol{\tau}})}, \tag{3.87}$$

where

$$\mathbb{M}_{\mathbb{F}}(\tilde{\boldsymbol{\tau}}) := \begin{bmatrix} \text{—} & \boldsymbol{0}^T & \text{—} \\ \text{—} & \mathbb{F}(\tilde{\tau}_1)^T & \text{—} \\ \text{—} & \mathbb{F}(\tilde{\tau}_2)^T & \text{—} \\ \vdots & \vdots & \vdots \\ \text{—} & \mathbb{F}(\tilde{\tau}_{L-1})^T & \text{—} \end{bmatrix}_{L\times L} , \tag{3.88}$$

$$\mathbb{M}_{\mathbb{H}}(\tilde{\boldsymbol{\tau}}) := \begin{bmatrix} — & \mathbb{H}(\tilde{\tau}_0)^T & — \\ — & \mathbb{H}(\tilde{\tau}_1)^T & — \\ — & \mathbb{H}(\tilde{\tau}_2)^T & — \\ \vdots & \vdots & \vdots \\ — & \mathbb{H}(\tilde{\tau}_{L-1})^T & — \end{bmatrix}_{L\times N} \tag{3.89}$$

and the vectors of coefficients

$$\boldsymbol{c}(\bar{\boldsymbol{q}}(\boldsymbol{\tau}), \bar{\boldsymbol{y}}(\boldsymbol{\tau})) = \begin{bmatrix} c_0(\bar{\boldsymbol{q}}(\boldsymbol{\tau}), \bar{\boldsymbol{y}}(\boldsymbol{\tau})) \\ c_1(\bar{\boldsymbol{q}}(\boldsymbol{\tau}), \bar{\boldsymbol{y}}(\boldsymbol{\tau})) \\ \vdots \\ c_{L-1}(\bar{\boldsymbol{q}}(\boldsymbol{\tau}), \bar{\boldsymbol{y}}(\boldsymbol{\tau})) \end{bmatrix}_L \quad \text{and} \quad \boldsymbol{d}(\hat{\boldsymbol{q}}(\boldsymbol{k}, \tau_0)) = \begin{bmatrix} d_0(\hat{\boldsymbol{q}}(\boldsymbol{k}, \tau_0)) \\ d_1(\hat{\boldsymbol{q}}(\boldsymbol{k}, \tau_0)) \\ \vdots \\ d_{N-1}(\hat{\boldsymbol{q}}(\boldsymbol{k}, \tau_0)) \end{bmatrix}_N . \tag{3.90}$$

Matrices (3.88) and (3.89) can be precomputed at the beginning of the algorithm before the time stepping process, since they only depend on the grid nodes in the time and frequency domains which are constant during the time stepping process.

In the toolbox, $\tilde{\boldsymbol{\mathcal{F}}}_n$ is implemented in the *F_ def* method as follows,

Algorithm 4 Define function $\tilde{\boldsymbol{\mathcal{F}}}_n(\tilde{\boldsymbol{\tau}}, \bar{\boldsymbol{q}}(\boldsymbol{\tau}), \bar{\boldsymbol{y}}(\boldsymbol{\tau}))$ for one spatial dimension

```
function F_DEF($\bar{\boldsymbol{q}}_{guess}$, $\bar{\boldsymbol{y}}_{guess}$, $\tilde{\boldsymbol{\tau}}$, $\mathbb{M}_{\mathbb{F}}$, $\Delta t$):
    $\boldsymbol{c}(\bar{\boldsymbol{q}}_{guess})$ ← Obtain Chebyshev coefficients of $f\,(\bar{\boldsymbol{q}}_{guess}, \bar{\boldsymbol{y}}_{guess}, t_r + \tilde{\boldsymbol{\tau}})$ expanded over $\tilde{\boldsymbol{\tau}}$
    $\tilde{\boldsymbol{\mathcal{F}}}_n(\tilde{\boldsymbol{\tau}}, \bar{\boldsymbol{q}})$ ← $\frac{\Delta t}{2}\,\mathbb{M}_{\mathbb{F}}(\tilde{\boldsymbol{\tau}})\;\boldsymbol{c}(\bar{\boldsymbol{q}}_{guess})$
    return $\tilde{\boldsymbol{\mathcal{F}}}_n(\tilde{\boldsymbol{\tau}}, \bar{\boldsymbol{q}})$, $\boldsymbol{c}(\bar{\boldsymbol{q}}_{guess})$
end function
```

and $\tilde{\boldsymbol{\mathcal{H}}}_p$ in the *H_ def* method,

Algorithm 5 Define function $\tilde{\boldsymbol{\mathcal{H}}}_p(\tilde{\boldsymbol{\tau}})$ for one spatial dimension

```
function H_DEF($\tilde{\boldsymbol{\tau}}$, $\mathbb{M}_{\mathbb{H}}$, $\Delta t$):
    $\Im\{\bar{\mathscr{H}}(\boldsymbol{k}, t_r)\}$ ← Obtain $\Im\{\mathscr{H}(k_l, t_r)\}$ for all $k_l$ in $\boldsymbol{k}$
    $\boldsymbol{d}(\hat{\boldsymbol{q}}(\boldsymbol{k}, \tau_0))$ ← Obtain Chebyshev coefficients of $\Im\{\bar{\mathscr{H}}(\boldsymbol{k}, t_r)\}$ expanded over $\boldsymbol{k}$
    $\tilde{\boldsymbol{\mathcal{H}}}_p(\tilde{\boldsymbol{\tau}})$ ← $\mathbb{M}_{\mathbb{H}}(\tilde{\boldsymbol{\tau}})\;\boldsymbol{d}(\hat{\boldsymbol{q}}(\boldsymbol{k}, \tau_0))$
    return $\tilde{\boldsymbol{\mathcal{H}}}_p(\tilde{\boldsymbol{\tau}})$
end function
```

Due to the dependencies of the function f, the full resolution of (3.87) also requires to solve for y. The discretised version of (3.82) for node $y_j := y(t_j)$ is given by

$$y_j \approx y_0 + \frac{\Delta t}{2} \sum_{\kappa=0}^{L-1} b_\kappa(\bar{\boldsymbol{q}}(\boldsymbol{\tau}), \bar{\boldsymbol{y}}(\boldsymbol{\tau})) \int_{-1}^{\frac{2\tilde{\tau}_j - \Delta t}{\Delta t}} T_\kappa(l)dl. \tag{3.91}$$

Sum in (3.91) can be transformed into a dot-product, leaving the equation as:

$$y_j \approx y_0 + \frac{\Delta t}{2}\, \boldsymbol{b}(\bar{\boldsymbol{q}}(\boldsymbol{\tau}), \bar{\boldsymbol{y}}(\boldsymbol{\tau})) \cdot \mathbb{Y}(\tilde{\tau}_j), \tag{3.92}$$

where

$$\mathbb{Y}(\tilde{\tau}_j) := \begin{bmatrix} \int_{-1}^{\frac{2\tilde{\tau}_j - \Delta t}{\Delta t}} T_0(l)dl \\ \int_{-1}^{\frac{2\tilde{\tau}_j - \Delta t}{\Delta t}} T_1(l)dl \\ \vdots \\ \int_{-1}^{\frac{2\tilde{\tau}_j - \Delta t}{\Delta t}} T_{L-1}(l)dl \end{bmatrix}_L \quad \text{and} \quad \boldsymbol{b}(\bar{\boldsymbol{q}}(\boldsymbol{\tau}), \bar{\boldsymbol{y}}(\boldsymbol{\tau})) = \begin{bmatrix} b_0(\bar{\boldsymbol{q}}(\boldsymbol{\tau}), \bar{\boldsymbol{y}}(\boldsymbol{\tau})) \\ b_1(\bar{\boldsymbol{q}}(\boldsymbol{\tau}), \bar{\boldsymbol{y}}(\boldsymbol{\tau})) \\ \vdots \\ b_{L-1}(\bar{\boldsymbol{q}}(\boldsymbol{\tau}), \bar{\boldsymbol{y}}(\boldsymbol{\tau})) \end{bmatrix}_L . \tag{3.93}$$

Extend equation (3.92) for all Chebyshev nodes, obtaining:

$$\bar{\boldsymbol{y}}(\boldsymbol{\tau}) \approx \bar{\boldsymbol{y}}_0(\boldsymbol{\tau}) + \underbrace{\frac{\Delta t}{2}\, \mathbb{M}_{\mathbb{Y}}(\tilde{\boldsymbol{\tau}})\, \boldsymbol{b}(\bar{\boldsymbol{q}}(\boldsymbol{\tau}), \bar{\boldsymbol{y}}(\boldsymbol{\tau}))}_{=:\tilde{\boldsymbol{\eta}}(\tilde{\boldsymbol{\tau}}, \bar{\boldsymbol{q}}(\boldsymbol{\tau}), \bar{\boldsymbol{y}}(\boldsymbol{\tau}))}, \tag{3.94}$$

where

$$\mathbb{M}_{\mathbb{Y}}(\tilde{\boldsymbol{\tau}}) := \begin{bmatrix} — & \mathbb{Y}(\tilde{\tau}_0)^T & — \\ — & \mathbb{Y}(\tilde{\tau}_1)^T & — \\ \vdots & \vdots & \vdots \\ — & \mathbb{Y}(\tilde{\tau}_{L-1})^T & — \end{bmatrix}_{L \times L} . \tag{3.95}$$

The algorithm for $\tilde{\boldsymbol{\eta}}$ is given by

Algorithm 6 Define function $\tilde{\boldsymbol{\eta}}(\tilde{\boldsymbol{\tau}}, \bar{\boldsymbol{q}}(\boldsymbol{\tau}), \bar{\boldsymbol{y}}(\boldsymbol{\tau}))$

```
function ETA_DEF($\boldsymbol{\tau}$, $\bar{\boldsymbol{q}}_{guess}$, $\bar{\boldsymbol{y}}_{guess}$, $\Delta t$, $\mathbb{M}_{\mathbb{Y}}$)
    $\boldsymbol{u}_{guess} \leftarrow$ Evaluate velocity field at positions $\bar{\boldsymbol{y}}_{guess}$ at times $\boldsymbol{\tau}$
    $\boldsymbol{b}(\bar{\boldsymbol{q}}, \bar{\boldsymbol{y}}) \leftarrow$ Obtain Chebyshev coefficients of $\bar{\boldsymbol{q}}_{guess} + \boldsymbol{u}_{guess}$ expanded over $\tilde{\boldsymbol{\tau}}$
    $\tilde{\boldsymbol{\eta}}(\tilde{\boldsymbol{\tau}}) \leftarrow \frac{\Delta t}{2}\, \mathbb{M}_{\mathbb{Y}}(\tilde{\boldsymbol{\tau}})\, \boldsymbol{b}(\bar{\boldsymbol{q}}, \bar{\boldsymbol{y}})$
    return $\tilde{\boldsymbol{\eta}}(\tilde{\boldsymbol{\tau}})$
end function
```

The values of $\bar{\boldsymbol{y}}_{guess}$ are obtained by using Forward Euler on equation (2.12d). Applying Forward Euler for a single step, the (one-dimensional) discretised expression

$$(y_{guess})_{j+1} = y_j + (\tau_{j+1} - \tau_j)\ (q_j + u_j) \tag{3.96}$$

is obtained, where $q_n := q(0, t_n)$ and $u_n := u(y(t_n))$; which extended for all the values of $\boldsymbol{\tau}$:

$$\underbrace{\begin{bmatrix} (y_{guess})_0 \\ (y_{guess})_1 \\ (y_{guess})_2 \\ \vdots \\ (y_{guess})_{L-1} \end{bmatrix}}_{=:\bar{\boldsymbol{y}}_{guess}} = \begin{bmatrix} y_0 \\ y_0 \\ y_0 \\ \vdots \\ y_0 \end{bmatrix} + \underbrace{\begin{bmatrix} 0 \\ \tau_1 - \tau_0 \\ \tau_2 - \tau_0 \\ \vdots \\ \tau_{L-1} - \tau_0 \end{bmatrix}}_{=:\tilde{\boldsymbol{\tau}}} (q_0 + u_0). \tag{3.97}$$

This algorithm is implemented in the *ForwardEuler* method of our toolbox. Because this algorithm is pretty standard, no pseudocode is provided.

Equations (3.87) and (3.94) produce the following implicit system of equations

$$\begin{cases}\bar{\boldsymbol{q}}(\boldsymbol{\tau}) \approx & \frac{2}{\pi}\tilde{\boldsymbol{\mathcal{F}}}_n(\tilde{\boldsymbol{\tau}}, \bar{\boldsymbol{q}}(\boldsymbol{\tau})) - \frac{2}{\pi}\tilde{\boldsymbol{\mathcal{H}}}_p(\tilde{\boldsymbol{\tau}}) \\ \bar{\boldsymbol{y}}(\boldsymbol{\tau}) \approx & \bar{\boldsymbol{y}}_0(\boldsymbol{\tau}) + \tilde{\boldsymbol{\eta}}(\tilde{\boldsymbol{\tau}}, \bar{\boldsymbol{q}}(\boldsymbol{\tau}), \bar{\boldsymbol{y}}(\boldsymbol{\tau})).\end{cases} \tag{3.98}$$

Passing all terms to the same side, the function $\boldsymbol{\mathcal{J}}$:

$$\boldsymbol{\mathcal{J}}(\bar{\boldsymbol{q}}(\boldsymbol{\tau}), \bar{\boldsymbol{y}}(\boldsymbol{\tau}), \boldsymbol{\tau}) := \begin{bmatrix} \bar{\boldsymbol{q}}(\boldsymbol{\tau}) - \frac{2}{\pi}\tilde{\boldsymbol{\mathcal{F}}}_n(\tilde{\boldsymbol{\tau}}, \bar{\boldsymbol{q}}(\boldsymbol{\tau})) + \frac{2}{\pi}\tilde{\boldsymbol{\mathcal{H}}}_p(\tilde{\boldsymbol{\tau}}) \\ \bar{\boldsymbol{y}}(\boldsymbol{\tau}) - \bar{\boldsymbol{y}}_0(\boldsymbol{\tau}) - \tilde{\boldsymbol{\eta}}(\boldsymbol{\tau}) \end{bmatrix} \approx \boldsymbol{0} \tag{3.99}$$

is obtained, whose zeros are to be found using a nonlinear solver. Prasath et al. (2019) recommend using $\bar{\boldsymbol{q}}_{guess}(\boldsymbol{\tau}) = -\frac{2}{\pi}\tilde{\boldsymbol{\mathcal{H}}}_p(\boldsymbol{\tau})$ as an initial guess. Since $\tilde{\boldsymbol{\mathcal{H}}}_p$ does not depend on $\bar{\boldsymbol{q}}$ and remains constant across the nonlinear solver iterations, it does not need to be recalculated within the nonlinear solver. The algorithms involving equation (3.99) (named *J_ def*) and the nonlinear solver implementation (named *update*) are straight forward and are therefore skipped.

3.4.4 Evolution of the initial condition

As part of Prasath et al. (2019)'s algorithm, quantity $\Im\{\mathscr{H}\}$ has to be calculated at initial time and updated in each time step. This term encodes all the information about the history of the particle from the initial time t_0 til the interval's initial time t_r. For this reason, $\mathscr{H}(k, t_r)$ is called the renormalised initial condition.

At initial time, the discrete expression of the renormalised initial condition $\Im\{\bar{\mathscr{H}}(\boldsymbol{k}, t_0)\} := [\mathscr{H}(k_0, t_0), \mathscr{H}(k_1, t_0), \ldots, \mathscr{H}(k_{N-1}, t_0)]$ is given by

$$\Im\{\bar{\mathscr{H}}(\boldsymbol{k}, t_0)\} = \Im\left\{\frac{q(0, t_0) + \gamma\hat{q}(\boldsymbol{k}, t_0)}{(\alpha - \boldsymbol{k}^2 + i\boldsymbol{k}\gamma)}\right\} = \Im\left\{\frac{q(0, t_0)}{\alpha - \boldsymbol{k}^2 + i\boldsymbol{k}\gamma}\right\} = \tag{3.100}$$

$$= -\frac{\boldsymbol{k}\gamma q(0, t_0)}{(\alpha - \boldsymbol{k}^2)^2 + \boldsymbol{k}^2\gamma^2}, \tag{3.101}$$

where the Fourier transform $\hat{q}(\boldsymbol{k}, t_0)$ has been canceled out because this is equal to zero due to $q(\boldsymbol{x}, t_0)$ being zero almost everywhere. This function is implemented by the *ImCalH_fun* function within our toolbox as follows:

Algorithm 7 Define function $\Im\{\bar{\mathscr{H}}(\boldsymbol{k}, t_0)\}$

```
function ImCalH_fun($\boldsymbol{k}$, $t_0$, $q_0$)
    $\Im\{\bar{\mathscr{H}}(\boldsymbol{k}, t_0) \leftarrow -\frac{\boldsymbol{k}\gamma q_0}{(\alpha-\boldsymbol{k}^2)^2 + \boldsymbol{k}^2\gamma^2}$
    return $\Im\{\bar{\mathscr{H}}(\boldsymbol{k}, t_0)\}$,
end function
```

The update of the renormalised initial condition in the following time steps is obtained by first applying some algebra on equation (3.21), exchanging t_0 with t_r and T with t_{r+1} and discretising the variable k to produce

$$\mathscr{H}(k_l, t_{r+1}) = e^{-k_l^2\Delta t}\mathscr{H}(k_l, t_r) - e^{-k_l^2 t_{r+1}}\tilde{g}_0(k_l^2, t_r, t_{r+1}) + e^{-k_l^2 t_{r+1}}\frac{\tilde{f}(k_l^2, t_r, t_{r+1})}{\alpha - k_l^2 + ik_l\gamma} \tag{3.102}$$

$\forall l \in \{0, 1, \ldots, N-1\}$. Given that only the imaginary part of $\mathscr{H}(k_l, t_{r+1})$ is needed (see equation (3.70)), the real part of expression (3.102) can be omitted, resulting in

$$\begin{aligned}\Im\left\{\mathscr{H}(k_l, t_{r+1})\right\} = e^{-k_l^2 \Delta t}\Im\left\{\mathscr{H}(k_l, t_r)\right\} - \cancelto{0}{\Im\left\{e^{-k_l^2 t_{r+1}}\int_{t_r}^{t_{r+1}} e^{k_l^2 s} q(0,s)ds\right\}} + \\ + \Im\left\{e^{-k_l^2 t_{r+1}}\frac{\tilde{f}(k_l^2, t_r, t_{r+1})}{\alpha - k_l^2 + ik_l\gamma}\right\}\end{aligned} \tag{3.103}$$

or equivalently, using the definition of $\tilde{f}$,

$$\begin{aligned}\Im\left\{\mathscr{H}(k_l, t_{r+1})\right\} = e^{-k_l^2 \Delta t}\Im\left\{\mathscr{H}(k_l, t_r)\right\} + \\ - \frac{k_l\gamma}{(\alpha - k_l^2)^2 + k_l^2\gamma^2}\int_{t_r}^{t_r+1} e^{-k_l^2(t_{r+1}-s)} f(\boldsymbol{q}, \boldsymbol{y}, s)ds.\end{aligned} \tag{3.104}$$

Note that Prasath et al. (2019) does not look for an updating expression for $\Im\{\mathscr{H}\}$ directly but for $\mathscr{H}$ and obtains the imaginary part after that, instead. They do not therefore carry out this last step. The updating expression (3.104) has one term and an integral calculation less in comparison to (3.102) and this translates into a faster computation.

Prasath et al. (2019) tackles the integration within $\tilde{f}$ in the same way as it did with the previous integrals, i.e. using Chebyshev polynomials and storing the values of their integration into a matrix that is later multiplied by the coefficient of the polynomials. Expanding f into Chebyshev polynomials results in

$$\begin{aligned}\Im\left\{\mathscr{H}(k_l, t_{r+1})\right\} \approx e^{-k_l^2 \Delta t}\Im\left\{\mathscr{H}(k_l, t_r)\right\} + \\ - \frac{\Delta t}{2}\sum_{n=0}^{L-1} c_n(\bar{\boldsymbol{q}}(\boldsymbol{\tau}), \bar{\boldsymbol{y}}(\boldsymbol{\tau}))\left(\frac{k_l\gamma}{(\alpha - k_l^2)^2 + k_l^2\gamma^2}\int_{-1}^{1} e^{-k_l^2\frac{\Delta t}{2}(1-\sigma)} T_n(\sigma)d\sigma\right)\end{aligned} \tag{3.105}$$

and in terms of a dot vector product,

$$\Im\left\{\mathscr{H}(k_l, t_{r+1})\right\} \approx e^{-k_l^2 \Delta t}\Im\left\{\mathscr{H}(k_l, t_r)\right\} - \frac{\Delta t}{2}\boldsymbol{c}(\bar{\boldsymbol{q}}(\boldsymbol{\tau}), \bar{\boldsymbol{y}}(\boldsymbol{\tau})) \cdot \mathbb{I}(k_l), \tag{3.106}$$

where

$$\mathbb{I}(k_l) := \begin{bmatrix} \frac{k_l\gamma}{(\alpha-k_l^2)^2+k_l^2\gamma^2}\int_{-1}^{1} e^{-k_l^2\frac{\Delta t}{2}(1-\sigma)} T_0(\sigma)d\sigma \\ \frac{k_l\gamma}{(\alpha-k_l^2)^2+k_l^2\gamma^2}\int_{-1}^{1} e^{-k_l^2\frac{\Delta t}{2}(1-\sigma)} T_1(\sigma)d\sigma \\ \vdots \\ \frac{k_l\gamma}{(\alpha-k_l^2)^2+k_l^2\gamma^2}\int_{-1}^{1} e^{-k_l^2\frac{\Delta t}{2}(1-\sigma)} T_{L-1}(\sigma)d\sigma \end{bmatrix}_L \tag{3.107}$$

and $\boldsymbol{c}(\bar{\boldsymbol{q}}(\boldsymbol{\tau}), \bar{\boldsymbol{y}}(\boldsymbol{\tau}))$ is the same vector of Chebyshev coefficients given in (3.90). Extending this for all the k_l nodes in the vector $\boldsymbol{k}$,

$$\Im\left\{\bar{\mathscr{H}}(\boldsymbol{k}, t_{r+1})\right\} \approx e^{-\boldsymbol{k}^2 \Delta t}\Im\left\{\bar{\mathscr{H}}(\boldsymbol{k}, t_r)\right\} - \underbrace{\frac{\Delta t}{2}\mathbb{M}_{\mathbb{I}}(\boldsymbol{k})\ \boldsymbol{c}(\bar{\boldsymbol{q}}(\boldsymbol{\tau}), \bar{\boldsymbol{y}}(\boldsymbol{\tau})),}_{=:\mathscr{I}} \tag{3.108}$$

where $\bar{\mathscr{H}}(\boldsymbol{k}, t_{r+1}) := [\mathscr{H}(k_0, t_{r+1}), \mathscr{H}(k_1, t_{r+1}), \dots, \mathscr{H}(k_{N-1}, t_{r+1})]^T$ and

$$\mathbb{M}_{\mathbb{I}}(\boldsymbol{k}) := \begin{bmatrix} — & \mathbb{I}(k_0)^T & — \\ — & \mathbb{I}(k_1)^T & — \\ \vdots & \vdots & \vdots \\ — & \mathbb{I}(k_{N-1})^T & — \end{bmatrix}_{N\times L} . \tag{3.109}$$

Equation (3.108) is the expression used within our toolbox [72] for the update of $\Im\{\mathscr{H}\}$ in each time subinterval, given that the matrix $\mathbb{M}_{\mathbb{I}}$ is precomputed at the beginning of the algorithm like the previous matrices.

The expression for the update of $\Im\{\bar{\mathscr{H}}(\boldsymbol{k}, t_r)\}$ $\forall r \in \{1, 2, \dots, M-1\}$ given in (3.108) is implemented by the *ImCalH_update* method

Algorithm 8 Define function $\Im\{\bar{\mathscr{H}}(\boldsymbol{k}, t_r)\}$

```
function ImCalH_update($\boldsymbol{k}$, $\Delta t$, $\Im\{\bar{\mathscr{H}}(\boldsymbol{k}, t_{r-1})\}$, $\boldsymbol{c}(\bar{\boldsymbol{q}})$, $\mathbb{M}_{\mathbb{I}}$)
    $\Im\{\bar{\mathscr{H}}(\boldsymbol{k}, t_r)\} \leftarrow e^{-\boldsymbol{k}^2 \Delta t} \Im\left\{\bar{\mathscr{H}}(\boldsymbol{k}, t_{r-1})\right\} - \frac{\Delta t}{2} \mathbb{M}_{\mathbb{I}}(\boldsymbol{k})\, \boldsymbol{c}(\bar{\boldsymbol{q}}\,)$
    return $\Im\{\bar{\mathscr{H}}(\boldsymbol{k}, t_r)\}$
end function
```

3.4.5 Code of the matrices $\mathbb{M}_{\mathbb{F}}, \mathbb{M}_{\mathbb{H}}, \mathbb{M}_{\mathbb{Y}}$ and $\mathbb{M}_{\mathbb{I}}$

Matrices (3.88), (3.89), (3.109) and (3.95) are programmed by Algorithm 9. This algorithm tries first to import the matrices from a previously saved file. If either of these files does not exist or the matrices do not have the required dimensions, i.e. different values of L and N, or the time step is different to the one used for the calculation of the matrices, then the matrices are calculated.

Matrices values are therefore filled in with a loop over the indexes of the time (j and n) and frequency (l) grids with the required integral results. The integrals are calculated using the functions available in the *polynomial.chebyshev* library within *numpy.* Hence the functions of the integrand must be first projected into the a basis of Chebyshev polynomials (using *chebfit*), then multiplied with the corresponding Chebyshev polynomial (with *chebmul*) and finally integrated (with *chebint*).

Once calculated, the matrices and the value of the time step are saved into one file. Saving the matrices for later use is useful in the cases in which the values of L, N, and Δt coincide, since the values of the matrices depend on these parameters. The definition of the functions $\mathcal{L}$ and $\mathcal{G}$ is omitted for simplicity. These two functions are defined in two separated class methods and they just implement the expression of the functions given in (3.54) and (3.78).

Algorithm 9 Define matrices:

```
function CHEBMAT($L$, $N$, $\tilde{\boldsymbol{\tau}}$, $\Delta t$):
    Try to import $\mathbb{M}_\mathbb{F}$, $\mathbb{M}_\mathbb{H}$, $\mathbb{M}_\mathbb{Y}$, $\mathbb{M}_\mathbb{I}$ and $\Delta t^*$ from file
    if $\mathbb{M}_\mathbb{F}$, $\mathbb{M}_\mathbb{H}$, $\mathbb{M}_\mathbb{Y}$, $\mathbb{M}_\mathbb{I}$ and $\Delta t^*$ do not exist OR dimensions are wrong then
        for $j \leftarrow 0$ to $L-1$ do
            for $n \leftarrow 0$ to $L-1$ do
                $\mathbb{M}_\mathbb{F}[j,n] \leftarrow \int_{-1}^{\frac{2\tilde{\boldsymbol{\tau}}[j]-\Delta t}{\Delta t}} T_n(l)\mathcal{L}\left(\frac{\Delta t}{2}(l+1)\right) dl$
                $\mathbb{M}_\mathbb{Y}[j,n] \leftarrow \int_{-1}^{\frac{2\tilde{\boldsymbol{\tau}}[j]-\Delta t}{\Delta t}} T_n(l)dl$
            end for
            for $l \leftarrow 0$ to $N-1$ do
                $\mathbb{M}_\mathbb{I}[l,j] \leftarrow \frac{\boldsymbol{k}[l]\ \gamma}{(\alpha-\boldsymbol{k}[l]^2)^2+\boldsymbol{k}[l]^2\ \gamma^2} \int_{-1}^{1} e^{-\boldsymbol{k}[l]^2 \frac{\Delta t}{2}(1-\sigma)} T_j(\sigma)d\sigma$
                if $j \neq 0$ then
                    $\mathbb{M}_\mathbb{H}[j,l] \leftarrow \int_{-1}^{1} T_l(\tilde{k})\mathcal{G}(\tilde{k},\tilde{\boldsymbol{\tau}}[j])d\tilde{k}$
                end if
            end for
        end for
    end if
    Save $\mathbb{M}_\mathbb{F}$, $\mathbb{M}_\mathbb{H}$, $\mathbb{M}_\mathbb{Y}$, $\mathbb{M}_\mathbb{I}$ and $\Delta t^*$ in a file.
    return $\mathbb{M}_\mathbb{F}$, $\mathbb{M}_\mathbb{H}$, $\mathbb{M}_\mathbb{Y}$, $\mathbb{M}_\mathbb{I}$
end function
```

3.5 Prasath et al.'s algorithm

Section 3.4 provided an expression to obtain the discrete values $\bar{\boldsymbol{q}}(\boldsymbol{\tau})$ and $\bar{\boldsymbol{y}}(\boldsymbol{\tau})$ at the points $\boldsymbol{\tau}$ in a given time interval $[t_r, t_{r+1}]$. This section describes the algorithm implemented in the toolbox provided in the linked repository [72].

The first step in the algorithm consists in dividing the time domain $[t_0, t_f]$ into M subintervals of size Δt, i.e. $[t_0, t_1], [t_1, t_2], \ldots, [t_{M-1}, t_M]$, where $t_r := t_0 + r\Delta t$, with $r \in \{0, 1, \ldots, M-1\}$. This way, the whole pseudospace-time plane, i.e. the $x - t$ plane, is divided into M subdomains of the type $[0, \infty) \times [t_r, t_{r+1}]$, as shown in the figure 3.1.

The algorithm involves the steps:

(1) Definition of L Chebyshev time nodes, τ_j, and N pseudospatial nodes, k_l, using the rules in (3.67) and (3.69).

(2) Precompute matrices $\mathbb{M}_\mathbb{F}$, $\mathbb{M}_\mathbb{H}$ and $\mathbb{M}_{\mathscr{I}_1}$, as described in (3.88), (3.89), (3.95) and (3.109).

(3) Consider the first subdomain, i.e. $[0, \infty) \times [t_0, t_1]$ whose initial condition, i.e. $\boldsymbol{q}(x, t_0)$, is set to zero everywhere except at $x = 0$, as shown in equation (3.55). The expression for $\Im\{\mathscr{H}\}$ at initial time corresponds to

$$\Im\left\{\mathscr{H}(k_l, t_0)\right\} = \Im\left\{\frac{\boldsymbol{q}(0, t_0)}{\alpha - k_l^2 + ik_l\gamma}\right\}. \tag{3.110}$$

$\Im\left\{\mathscr{H}(k_l, t_0)\right\}$ is expanded into Chebyshev polynomials, calculating coefficients $\bar{\boldsymbol{d}}(\hat{\boldsymbol{q}}(\boldsymbol{k}, \tau_0))$ and $\tilde{\boldsymbol{\mathcal{H}}}_p(\boldsymbol{\tau})$. Setting $\bar{\boldsymbol{q}}_{guess}(\boldsymbol{\tau}) = -\frac{2}{\pi}\tilde{\boldsymbol{\mathcal{H}}}_p(\boldsymbol{\tau})$ as initial guess, expand it into a Chebyshev basis of order $L-1$ and feed the coefficients of it into a nonlinear solver where equation (3.87) is solved at the nodes τ_j. This solution corresponds to the Dirichlet boundary condition on the left boundary for the first time interval $[t_0, t_1]$.

(4) Using equation (3.106), the renormalised initial condition is updated at the top boundary of our subdomain, i.e. $\Im\{\mathscr{H}(k_l, t_1)\}$ for the first interval $[t_0, t_1]$ and $\Im\{\mathscr{H}(k_l, t_{r+1})\}$ for the generic interval $[t_r, t_{r+1}]$.

(5) The new renormalised initial condition is expanded into Chebyshev polynomials, obtaining the new set of Chebyshev coefficients, $\bar{\boldsymbol{d}}(\hat{\boldsymbol{q}}(\boldsymbol{k}, \tau_0))$ so that $\tilde{\boldsymbol{\mathcal{H}}}_p(\boldsymbol{\tau})$ for the τ_j values in the following interval is calculated.

(6) Run again the nonlinear solver, using $\bar{\boldsymbol{q}}_{guess}(\boldsymbol{\tau}) = -\frac{2}{\pi}\tilde{\boldsymbol{\mathcal{H}}}_p(\boldsymbol{\tau})$ as an initial guess on equation (3.87) at the nodes τ_j.

(7) Repeat steps (4) to (6) until the final time node, t_f, is reached.

4

Direct numerical integration of the MRGE: Daitche's schemes

This section presents the numerical integration methods given in Daitche (2013) [20]. Daitche (2013)'s methods consist on a quadrature scheme applied to the singular kernel of the history term embedded into an numerical integration scheme. First the theory behind the three different schemes of first, second and third order provided in Daitche (2013) is provided and then their implementation in our code.

Note that the coefficients are calculated and stored using double precision instead of quadruple precision, as adviced in Daitche (2013) [20]. Daitche and other authors, such as Moreno-Casas and Bombardelli [47], point out that the accuracy of the method may be reduced if the coefficients of the 2^{nd} and 3^{rd} order methods are not calculated using quadruple precision. In chapter 6 this expected loss in convergence order for the 3^{rd} order method is observed. No loss is convergence is observed for the 2^{nd} order one.

4.1 The theory behind Daitche's methods

Daitche (2013) first modifies equation (2.6) by using the identity

$$\int_{t_0}^{t} K(t-s)\frac{d}{ds}f(s)ds + K(t-t_0)f(t_0) = \frac{d}{dt}\int_{t_0}^{t} K(t-s)f(s)ds \tag{4.1}$$

where K is the standard Kernel, defined as $K(t-\tau) := \frac{1}{\sqrt{t-\tau}}$ and $f(s) := \boldsymbol{v}(s) - \boldsymbol{u}(\boldsymbol{y}(s), s)$. Identity (4.1) is obtained by using integration by parts. Using this identity in equation (2.6) gives then the following result

$$\dot{\boldsymbol{y}}(t) = \boldsymbol{v}(t), \tag{4.2a}$$

$$\dot{\boldsymbol{v}}(t) = \frac{1}{R}\frac{D\boldsymbol{u}(\boldsymbol{y}(t),t)}{Dt} - \alpha\left(\boldsymbol{v}(t) - \boldsymbol{u}(\boldsymbol{y}(t),t)\right) - \frac{\gamma}{\sqrt{\pi}}\frac{d}{dt}\int_{t_0}^{t}\frac{\boldsymbol{v}(s) - \boldsymbol{u}(\boldsymbol{y}(s),s)}{\sqrt{t-s}}ds. \tag{4.2b}$$

With the definition of the relative velocity $\boldsymbol{q}_0(t) := \boldsymbol{v}(t) - \boldsymbol{u}(\boldsymbol{y}(t),t)$, equation (4.2) can be reformulated as

$$\dot{\boldsymbol{y}}(t) = \boldsymbol{q}_0(t) + \boldsymbol{u}(\boldsymbol{y}(t),t), \tag{4.3a}$$

$$\dot{\boldsymbol{q}}_0(t) = \underbrace{\left(\frac{1}{R}-1\right)\frac{D\boldsymbol{u}(\boldsymbol{y}(t),t)}{Dt} - \left(\boldsymbol{q}_0(t)\cdot\nabla\right)\boldsymbol{u}(\boldsymbol{y}(t),t) - \alpha\boldsymbol{q}_0(t)}_{=:\boldsymbol{G}(t)} + \\ + \frac{d}{dt}\underbrace{\left(-\frac{\gamma}{\sqrt{\pi}}\int_{t_0}^{t}\frac{\boldsymbol{q}_0(s)}{\sqrt{t-s}}ds\right)}_{=:\boldsymbol{H}(t)}. \tag{4.3b}$$

Integrating (4.3b) between t_0 and t_0+h yields

$$\boldsymbol{q}_0(t_0+h) = \boldsymbol{q}_0(t_0) + \int_{t_0}^{t_0+h}\boldsymbol{G}(s)ds + \boldsymbol{H}(t_0+h) - \boldsymbol{H}(t_0). \tag{4.4}$$

4.2 The discretised formula

The integral in term $\boldsymbol{H}$ in (4.4) is evaluated by using a quadrature scheme:

$$\boldsymbol{H}(t) \approx -\frac{\gamma}{\sqrt{\pi}}\sqrt{h}\sum_{j=0}^{n}\eta_j^n\boldsymbol{q}_0(s_{n-j}) + \mathcal{O}(h^{\nu+1})\sqrt{t-t_0} \tag{4.5}$$

where ν is the convergence order of the method and n is the number of intervals for the approximation of the integral. Coefficients η_j^n are calculated by using the extended formulas given in Daitche (2013) [20] and provided in the appendix A.

The integral of $\boldsymbol{G}$ in equation (4.4) is approximated using Adams-Bashfort multi-step methods as shown below

$$\int_{t_0}^{t_0+h}\boldsymbol{G}(s)ds = h\boldsymbol{G}(t_0) + \mathcal{O}(h^2) \qquad \text{(First order)},$$

$$\int_{t_0}^{t_0+h}\boldsymbol{G}(s)ds = \frac{h}{2}\left(3\boldsymbol{G}(t_0) - \boldsymbol{G}(t_0-h)\right) + \mathcal{O}(h^3) \qquad \text{(Second order)},$$

$$\int_{t_0}^{t_0+h}\boldsymbol{G}(s)ds = \frac{h}{12}\left(23\boldsymbol{G}(t_0) - 16\boldsymbol{G}(t_0-h) + 5\boldsymbol{G}(t_0-2h)\right) + \mathcal{O}(h^4) \qquad \text{(Third order)}.$$

Considering the grid $t_n = t_0 + nh$, and using the following abbreviations $\xi = \gamma\sqrt{\frac{h}{\pi}}$, $q_0^n = q_0(t_n)$, the complete integration schemes of first, second and third order for the Maxey-Riley-Gatignol equation become

$$y^{n+1} = y^n + h(q_0^n + u^n) + \mathcal{O}(h^2), \tag{4.6a}$$

$$(1+\xi\eta_0^{n+1})q_0^{n+1} = q_0^n + h\boldsymbol{G}^n - \xi\sum_{j=0}^{n}\left(\eta_{j+1}^{n+1} - \eta_j^n\right)q_0^{n-j} + \sqrt{t_n - t_0}\,\mathcal{O}(h^2), \tag{4.6b}$$

$$y^{n+1} = y^n + \frac{h}{2}(3(q_0^n + u^n) - (q_0^{n-1} + u^{n-1})) + \mathcal{O}(h^3), \tag{4.6c}$$

$$(1+\xi\eta_0^{n+1})q_0^{n+1} = q_0^n + \frac{h}{2}(3\boldsymbol{G}^n - \boldsymbol{G}^{n-1}) - \xi\sum_{j=0}^{n}\left(\eta_{j+1}^{n+1} - \eta_j^n\right)q_0^{n-j} + \sqrt{t_n - t_0}\,\mathcal{O}(h^3), \tag{4.6d}$$

$$y^{n+1} = y^n + \frac{h}{12}(23(q_0^n + u^n) - 16(q_0^{n-1} + u^{n-1}) + 5(q_0^{n-2} + u^{n-2})) + \mathcal{O}(h^4), \tag{4.6e}$$

$$(1 + \xi\eta_0^{n+1})q_0^{n+1} = q_0^n + \frac{h}{12}(23\boldsymbol{G}^n - 16\boldsymbol{G}^{n-1} + 5\boldsymbol{G}^{n-2}) - \xi\sum_{j=0}^{n}\left(\eta_{j+1}^{n+1} - \eta_j^n\right)q_0^{n-j} + \\ + \sqrt{t_n - t_0}\,\mathcal{O}(h^4). \tag{4.6f}$$

For the second and third order methods, Daitche (2013) recommends the use of the lower order numerical methods with a lower time step in order to obtain the first steps of the highest order method.

4.3 Code implementation

Based on the method given by Daitche [20] and introduced in section 4.1, we programmed our own Python implementation of Daitche's methods.

The particle parameters are set up using the script *a00_PMTERS_INPUT.py*. One can create an instance of the *maxey_riley_Daitche* class from *a09_PRTCLE_DTCHE.py* and use the methods *Euler* (first order method), *AdamBashf2* (second order method) or *AdamBashf3* (third order method) to obtain a numerical solution of a particle's trajectory. The reader may just choose to use the ready-to-use script provided, called *a01_SOLVER_DTCHE.py*, and set the parameter *order_Daitche* to $1, 2$ or 3 to use the appropriate method.

The following section introduces the *methods* that are implemented within the class *maxey_riley_Daitche* class.

4.3.1 The matrix of coefficients

Formulas (4.6b), (4.6d) and (4.6f) use the term $\left(\eta_{j+1}^{n+1} - \eta_j^n\right) \forall j \in \{0, 1, \ldots, n\} \wedge n \in \{0, 1, \ldots, N-1\}$ repeatedly. For this reason, these parameters are calculated at the initialisation of the class and save these values in the matrix

$$\mathbb{M}_\eta := \begin{bmatrix} \eta_1^1 - \eta_0^0 & 0 & 0 & \cdots \\ \eta_1^2 - \eta_0^1 & \eta_2^2 - \eta_1^1 & 0 & \ddots \\ \eta_1^3 - \eta_0^2 & \eta_2^3 - \eta_1^2 & \eta_3^3 - \eta_2^2 & \ddots \\ \vdots & \ddots & \ddots & \ddots \end{bmatrix}, \tag{4.7}$$

and use the dot product between each vector row in $\mathbb{M}_\eta$ and $\boldsymbol{q}_0^{n-j}$ to calculate the sum $\sum_{j=0}^{n}\left(\eta_{j+1}^{n+1} - \eta_j^n\right)\boldsymbol{q}_0^{n-j}$, as follows

$$\sum_{j=0}^{n}\left(\eta_{j+1}^{n+1} - \eta_j^n\right)\boldsymbol{q}_0^{n-j} = \left[(\eta_1^{n+1} - \eta_0^n) \quad (\eta_2^{n+1} - \eta_1^n) \quad \ldots \quad (\eta_{n+1}^{n+1} - \eta_n^n)\right] \begin{bmatrix} \boldsymbol{q}_0^n \\ \boldsymbol{q}_0^{n-1} \\ \vdots \\ \boldsymbol{q}_0^0 \end{bmatrix} \tag{4.8a}$$

$$= \mathbb{M}_\eta[n; 0:n] \cdot \begin{bmatrix} \boldsymbol{q}_0^n \\ \boldsymbol{q}_0^{n-1} \\ \vdots \\ \boldsymbol{q}_0^0 \end{bmatrix} . \tag{4.8b}$$

All the coefficients in the matrix are calculated by using the corresponding equations for the required order. Note that in the code the coefficients η are referenced as α for Euler's method, β for the second order method and η for the third order method. This is the same notation used by A. Daitche in [20].

4.3.2 First order method

The scheme of the method that implements the first order method is shown in Algorithm 10.

Algorithm 10 Algorithm for forward Euler's method:

```
function EULER($\boldsymbol{y}^0$, $\boldsymbol{q}_0^0$, $t_0$, $h$, $\mathbb{M}_\eta$):
    $\xi \leftarrow \gamma\sqrt{\frac{h}{\pi}}$
    $\boldsymbol{y}_v[0]$, $\boldsymbol{q}_{0,v}[0] \leftarrow$ Save $\boldsymbol{y}^0$ and $\boldsymbol{q}_0^0$
    for $n \leftarrow 0$ to $L-1$ do:
        $\boldsymbol{S} = \boldsymbol{0}$
        for $j \leftarrow 0$ to $n$ do:
            $\boldsymbol{S} = \boldsymbol{S} + \mathbb{M}_\eta[n, j] \cdot \boldsymbol{q}_0^{n-j}$
        end for
        $\boldsymbol{u}^n \leftarrow$ Obtain field's velocity at $(\boldsymbol{y}^n, t_0 + nh)$
        $\boldsymbol{y}^{n+1} \leftarrow \boldsymbol{y}^n + h(\boldsymbol{q}_0^n + \boldsymbol{u}^n)$
        $\boldsymbol{G}^n \leftarrow$ Obtain $\boldsymbol{G}$ at $(\boldsymbol{u}^n, \boldsymbol{q}_0^n, t_0 + nh)$
        $\boldsymbol{q}_0^{n+1} \leftarrow \frac{\boldsymbol{q}_0^n + h\boldsymbol{G}^n - \boldsymbol{S}\xi}{1+\eta_0^{n+1}\xi}$
        $\boldsymbol{y}_v[n+1]$, $\boldsymbol{q}_{0,v}[n+1] \leftarrow$ Save $\boldsymbol{y}^{n+1}$ and $\boldsymbol{q}_0^{n+1}$
    end for
    return $\boldsymbol{y}_v, \boldsymbol{q}_{0,v}$
end function
```

4.3.3 Second order method

The scheme of the method that implements the second order Adam Bashforth method is shown in Algorithm 11.

Algorithm 11 Algorithm for Adam Bashforth second order method:

```
function ADAMBASHF2($\boldsymbol{y}^0$, $\boldsymbol{q}_0^0$, $t_0$, $h$, $\mathbb{M}_\eta$):
    $\boldsymbol{y}_v[0]$, $\boldsymbol{q}_{0,v}[0] \leftarrow$ Save $\boldsymbol{y}^0$ and $\boldsymbol{q}_0^0$
    $\boldsymbol{u}^0 \leftarrow$ Obtain field's velocity at $(\boldsymbol{y}^0, t_0)$
    $\boldsymbol{G}^0 \leftarrow$ Obtain $\boldsymbol{G}$ at $(\boldsymbol{u}^0, \boldsymbol{q}_0^0, t_0)$
    $\boldsymbol{t}^* \leftarrow$ Create smaller grid between $t_0$ and $t_1$
    $\boldsymbol{y}_v[1]$, $\boldsymbol{q}_{0,v}[1] \leftarrow$ Calculate first step with EULER method using $\boldsymbol{t}^*$
    $\xi \leftarrow \gamma\sqrt{\frac{h}{\pi}}$
    for $n \leftarrow 1$ to $L-1$ do:
        $\boldsymbol{S} = \boldsymbol{0}$
        for $j \leftarrow 0$ to $n$ do:
            $\boldsymbol{S} = \boldsymbol{S} + \mathbb{M}_\eta[n,j] \cdot \boldsymbol{q}_0^{n-j}$
        end for
        $\boldsymbol{u}^n \leftarrow$ Obtain field's velocity at $(\boldsymbol{y}^n, t_0 + nh)$
        $\boldsymbol{y}^{n+1} \leftarrow \boldsymbol{y}^n + \frac{h}{2}(3(\boldsymbol{q}_0^n + \boldsymbol{u}^n) - (\boldsymbol{q}_0^{n-1} + \boldsymbol{u}^{n-1}))$
        $\boldsymbol{G}^n \leftarrow$ Obtain $\boldsymbol{G}$ at $(\boldsymbol{u}^n, \boldsymbol{q}_0^n, t_0 + nh)$
        $\boldsymbol{q}_0^{n+1} \leftarrow \frac{\boldsymbol{q}_0^n + \frac{h}{2}(3\boldsymbol{G}^n - \boldsymbol{G}^{n-1}) - \boldsymbol{S}\xi}{1 + \eta_0^{n+1}\xi}$
        $\boldsymbol{y}_v[n+1]$, $\boldsymbol{q}_{0,v}[n+1] \leftarrow$ Save $\boldsymbol{y}^{n+1}$ and $\boldsymbol{q}_0^{n+1}$
    end for
    return $\boldsymbol{y}_v, \boldsymbol{q}_{0,v}$
end function
```

4.3.4 Third order method

The scheme of the method that implements the third order Adam Bashforth method is shown in Algorithm 12.

Algorithm 12 Algorithm for Adam Bashforth third order method:

```
function AdamBashf3($\boldsymbol{y}^0$, $\boldsymbol{q}_0^0$, $t_0$, $h$, $\mathbb{M}_\eta$):
    $\boldsymbol{y}_v[0]$, $\boldsymbol{q}_{0,v}[0] \leftarrow$ Save $\boldsymbol{y}^0$ and $\boldsymbol{q}_0^0$
    $\boldsymbol{u}^0 \leftarrow$ Obtain field's velocity at $(\boldsymbol{y}^0, t_0)$
    $\boldsymbol{G}^0 \leftarrow$ Obtain $\boldsymbol{G}$ at $(\boldsymbol{u}^0, \boldsymbol{q}_0^0, t_0)$
    $\boldsymbol{t}^* \leftarrow$ Create smaller grid between $t_0$ and $t_2$
    $\boldsymbol{y}_v[1]$, $\boldsymbol{q}_{0,v}[1]$, $\boldsymbol{y}_v[2]$, $\boldsymbol{q}_{0,v}[2] \leftarrow$ Calculate first two steps with ADAMBASHF2 method using $\boldsymbol{t}^*$
    $\boldsymbol{G}^1 \leftarrow$ Obtain $\boldsymbol{G}$ at $(\boldsymbol{u}^1, \boldsymbol{q}_0^1, t_0 + h)$
    $\xi \leftarrow \gamma\sqrt{\frac{h}{\pi}}$
    for $n \leftarrow 2$ to $L - 1$ do:
        $\boldsymbol{S} = \boldsymbol{0}$
        for $j \leftarrow 0$ to $n$ do:
            $\boldsymbol{S} = \boldsymbol{S} + \mathbb{M}_\eta[n, j] \cdot \boldsymbol{q}_0^{n-j}$
        end for
        $\boldsymbol{u}^n \leftarrow$ Obtain field's velocity at $(\boldsymbol{y}^n, t_0 + nh)$
        $\boldsymbol{y}^{n+1} \leftarrow \boldsymbol{y}^n + \frac{h}{12}(23(\boldsymbol{q}_0^n + \boldsymbol{u}^n) - 16(\boldsymbol{q}_0^{n-1} + \boldsymbol{u}^{n-1}) + 5(\boldsymbol{q}_0^{n-2} + \boldsymbol{u}^{n-2}))$
        $\boldsymbol{G}^n \leftarrow$ Obtain $\boldsymbol{G}$ at $(\boldsymbol{u}^n, \boldsymbol{q}_0^n, t_0 + nh)$
        $\boldsymbol{q}_0^{n+1} \leftarrow \frac{\boldsymbol{q}_0^n + \frac{h}{12}(23\boldsymbol{G}^n - 16\boldsymbol{G}^{n-1} + 5\boldsymbol{G}^{n-2}) - \boldsymbol{S}\xi}{1 + \eta_0^{n+1}\xi}$
        $\boldsymbol{y}_v[n+1]$, $\boldsymbol{q}_{0,v}[n+1] \leftarrow$ Save $\boldsymbol{y}^{n+1}$ and $\boldsymbol{q}_0^{n+1}$
    end for
    return $\boldsymbol{y}_v, \boldsymbol{q}_{0,v}$
end function
```

5

Finite Difference based solution on the diffusive problem

This chapter presents the Finite Differences (FD) approaches derived for the resolution of the MRGE system (2.12) on the unbounded pseudo-spatial domain and their implementation in Python. The schemes consist of spatial discretisations of orders two and four coupled with either a second order fully implicit method (Trapezoidal Rule), a fourth order fully implicit method (a SDIRK method) or a second, third or fourth order IMEX time stepping method.

The FD discretisations used in this paper are a modification of the conventional ones, since the reformulated problem given in equation (2.12) has one boundary condition instead of two. The second order FD scheme was taken from the literature [37, 27, 3], whereas the fourth order method is our own work, obtained from the knowledge acquired from the second order scheme.

The time stepping methods are either well-known numerical integrators, such as the trapezoidal rule [83] or are taken from the scientific literature, like the SDIRK method with name **ESDIRK4(3)6L[2]SA**, taken from Kennedy and Carpenter (2016) [34] or the IMEX methods, from Ascher et al. (1997) [4].

Many of the definitions that provided in this chapter are inspired by the notes of the course in *Numerics for ODEs* hold at the Technische Universität Hamburg [60].

5.1 Discretisation in space: Finite Difference schemes

The numerical approximations of the spatial derivative is carried out with two FD schemes of second and fourth order. FD schemes are a class of numerical techniques used to solve problems with differential equations by approximating derivatives with finite differences [79]. These problems are called boundary value problems (BVP) because some values or relations are known at the spatial boundaries. These are known as boundary conditions. The differential system (2.12) is defined on a semi-infinite spatial domain, i.e. $x \in [0, +\infty)$ and holds one boundary condition at $x = 0$ (2.12c) and the requirement that $\lim_{x\to\infty} \boldsymbol{q}(x, t) = 0$.

There exist techniques in the scientific literature to overcome the fact that the PDE is defined on a semi-infinite domain and include an approximation on a second right boundary condition at a finite point, such as an artificial [67] or transparent boundary conditions [56].

Koleva's scheme [37], based on the results of Alshina et al. [3], demonstrated a very good behaviour to address differential problems on infite domains, without imposing an approximation of the boundary condition at infinity. For this reason it is the discretisation chosen to carry out a second order scheme on diffusive problems defined over the semi-infinite spatial domain, $x \in [0, \infty)$.

Additionally, a novel fourth order FD scheme for differential problems on semi-infinite spatial domains is presented and implemented. This method is based on an extension on Koleva (2005) [37] and Fazio and Janelli (2014) [27]'s methods, with Lele's compact finite differences (CFD) schemes [40]. CFD schemes are chosen over standard FD schemes because they require smaller stencils. The fourth order CFD approximation of the second derivative needs a three-point stencil [40] in comparison to the five-point stencil [78] needed by the standard FD schemes. It is unclear how to eliminate the effect of two ghost cell values in the reformulated MRGE (2.12).

5.1.1 Spatial Grid

The spatial grid is defined using the "quasi-uniform mesh" given in Koleva (2005) [37] and in Fazio and Janelli (2014) [27]. These "quasi-uniform meshes" are obtained by using a strongly monotone and smooth map on a uniform spatial grid defined over $[0, 1)$. A uniform mesh with N grid points is obtained by using the function

$$\xi_n = \frac{n}{N} \quad \forall n \in \{0, 1, \dots, N-1\}. \tag{5.1}$$

Koleva (2005) [37], Fazio and Janelli (2014) [27] and Alshina et al. (2002) [3] provide the following strongly monotone and smooth mappings

$$x_n := x(\xi_n) = -c \ln(1 - \xi_n), \tag{5.2a}$$

$$x_n := x(\xi_n) = \frac{c\xi_n}{(1 - \xi_n)^m}, \quad m > 0, \tag{5.2b}$$

where $c \in (0, \infty)$ is a parameter that governs the distribution of the grids within the half positive real line, approximately distributing half of the grid points within the interval $[0, c]$.

In the FD approximations used for the MRGE, the logarithmic mapping, i.e. equation (5.2a), is used because it ensures a concentration of points around the origin (see figure (5.1)) and therefore "gives slightly better resolution near the boundary $x = 0$ than the algebraic map" (5.2b), according to Fazio and Janelli [27] (2014).

5.1.2 The semidiscrete system

Once the spatial domain has been discretised, the numerical schemes can be applied on the PDE, so that the solution can be approximated at the grid points. The second and fourth order schemes for the spatial discretisation are given in the following subsections. The exact form of the scheme will not influence the overall shape of the system, which will

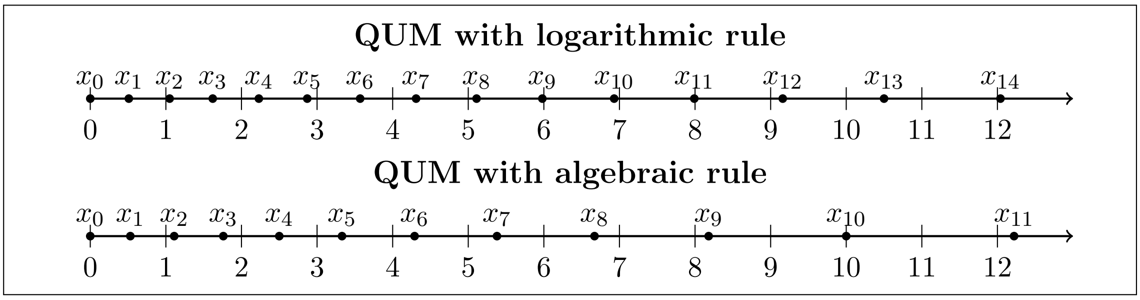

Figure 5.1: Distribution of $N = 20$ nodes in quasi-uniform meshes obtained using (top) the logarithmic rule in equation (5.2a) and (bottom) the algebraic rule in equation (5.2b) with $c = 10$.

be as follows

$$\underbrace{\begin{bmatrix}\dot{\vec{\boldsymbol{q}}}(t)\\ \dot{\boldsymbol{y}}(t)\end{bmatrix}}_{=:\dot{\boldsymbol{\eta}}(t)} = \underbrace{\left[\begin{array}{ccccc|cc} & & & & & 0 & 0\\ & & A_s & & & \vdots & \vdots \\ & & & & & 0 & 0\\ \hline 1&0&0&\dots&0&0&0\\ 0&1&0&\dots&0&0&0\end{array}\right]}_{=:A} \underbrace{\begin{bmatrix}\vec{\boldsymbol{q}}(t)\\ \boldsymbol{y}(t)\end{bmatrix}}_{=:\boldsymbol{\eta}(t)} + \underbrace{\begin{bmatrix}\boldsymbol{v}(\vec{\boldsymbol{q}}_0(t),\boldsymbol{y}(t),t)\\ \boldsymbol{u}(\boldsymbol{y}(t),t)\end{bmatrix}}_{=:\boldsymbol{\omega}(\vec{\boldsymbol{q}}_0(t),\boldsymbol{y}(t),t)} \tag{5.3}$$

where

$$\vec{\boldsymbol{q}}(t) := \begin{bmatrix} q_0^{(1)}(t) & q_0^{(2)}(t) & q_1^{(1)}(t) & q_1^{(2)}(t) & \dots & q_{N-2}^{(1)}(t) & q_{N-2}^{(2)}(t)\end{bmatrix}^T, \tag{5.4}$$

$$\vec{\boldsymbol{q}}_0(t) := \begin{bmatrix} q_0^{(1)}(t) & q_0^{(2)}(t)\end{bmatrix}^T. \tag{5.5}$$

correspond to vectors of time-dependent values of $q_j(t) := q(x_j, t)$, evaluated at the pseudospatial nodes and obtained after discretising (2.12) in space,

$$\boldsymbol{y}(t) := \begin{bmatrix} y^{(1)}(t) & y^{(2)}(t)\end{bmatrix}^T \tag{5.6}$$

corresponds to the trajectory of the particle, $A_s \in \mathbb{R}^{N\times N}$ is a matrix of constant coefficients and $\boldsymbol{v} \in \mathbb{R}^N$ is the term that accounts for the forcing term at the boundary. Matrix A_s and vector $\boldsymbol{v}$ depend on the chosen numerical scheme and the dimensions of the flow field. The following subsection presents two numerical schemes for the spatial discretization and provide the method to construct their respective A_s.

System (5.3) is the result of coupling the semidiscretised PDE, i.e. equation (2.12a), with the equation that relates the relative velocity with the particle trajectory, i.e. equation (2.12d).

Note that vectors (5.4), (5.6), (5.5) correspond to the case of 2D flow fields. In 3D flow fields, a third component, i.e. $q_0^{(3)}(t)$, $q_1^{(3)}(t)$, ..., must be added.

5.1.3 Second order discretisation

This approach is taken from Koleva (2005) [37] that investigated the "numerical solutions of the heat equation on the semi-infinite interval in one dimension" and obtained good convergence results. Koleva (2015)'s scheme provides the following second order finite difference formulas for the derivatives for the discretisation of the the one-dimensional PDE, equation (2.12a),

$$\left.\frac{\partial q(\xi(x),t)}{\partial x}\right|_{x_{n+1/2}} \approx \frac{q_{n+1}(t)-q_n(t)}{2\zeta_n}, \tag{5.7}$$

$$\left.\frac{\partial^2 q(\xi(x),t)}{\partial x^2}\right|_{x_n} \approx \frac{1}{\psi_n}\left[\left.\frac{\partial q(\xi(x),t)}{\partial x}\right|_{x_{n+1/2}} - \left.\frac{\partial q(\xi(x),t)}{\partial x}\right|_{n-1/2}\right] \tag{5.8}$$

where

$$\psi_n := x_{n+1/2} - x_{n-1/2}, \quad \zeta_n := x_{n+3/4} - x_{n+1/4} \tag{5.9}$$

for all $n = 1, 2, ..., N-1$, representing the mesh spacing in the pseudo-space coordinate. For the first derivative at the left boundary, i.e. equation (2.12c), Koleva (2015) provides

$$\left.\frac{\partial q(\xi(x),t)}{\partial x}\right|_{x_0} \approx \frac{1}{2}\left[\left.\frac{\partial q(\xi(x),t)}{\partial x}\right|_{x_{1/2}} + \left.\frac{\partial q(\xi(x),t)}{\partial x}\right|_{x_{-1/2}}\right]. \tag{5.10}$$

The discretised PDE and the boundary condition are coupled by using the ghost mesh point $x_{-1/2}$ in equations (5.10) and (5.8) for $n = 0$. The entries $(a_{i,j})_{1\le i\le 2N,\, 1\le j\le 2N}$ of A_s are

$$a_{11} = a_{22} = -\frac{\gamma + 2\alpha\zeta_0}{\zeta_0(2+\gamma\psi_0)}, \qquad a_{12} = a_{24} = \frac{\gamma}{\zeta_0(2+\gamma\psi_0)} \tag{5.11}$$

for the boundary values and

$$a_{i,i-2} = a_{i+1,i-1} = \frac{1}{2\psi_{\frac{i-1}{2}}\zeta_{\frac{i-3}{2}}}, \tag{5.12}$$

$$a_{i,i} = a_{i+1,i+1} = -\frac{1}{\psi_{\frac{i-1}{2}}}\left(\frac{\zeta_{\frac{i-3}{2}} + \zeta_{\frac{i-1}{2}}}{2\zeta_{\frac{i-3}{2}}\zeta_{\frac{i-1}{2}}}\right), \tag{5.13}$$

$$a_{i,i+2} = a_{i+1,i+3} = \frac{1}{2\psi_{\frac{i-1}{2}}\zeta_{\frac{i-1}{2}}}, \tag{5.14}$$

for $i = 2m+1$ with $m \in \{1, 2, \ldots, N-2\}$. All other matrix entries are zero so that A_s is a sparse pentadiagonal matrix with zero first upper and lower diagonals as shown in Figure 5.2.

The vector $\boldsymbol{v}$, which contains the forcing term that comes from the MRGE as a boundary condition, $\boldsymbol{f}$, is given by

$$\boldsymbol{v}(\boldsymbol{q}_0(t), \boldsymbol{y}(t), t) := \begin{bmatrix} \frac{2}{2+\gamma\psi_0}\boldsymbol{f}^{(1)}(\boldsymbol{q}_0(t), \boldsymbol{y}(t), t) \\ \frac{2}{2+\gamma\psi_0}\boldsymbol{f}^{(2)}(\boldsymbol{q}_0(t), \boldsymbol{y}(t), t) \\ 0 \\ \vdots \\ 0 \end{bmatrix}. \tag{5.15}$$

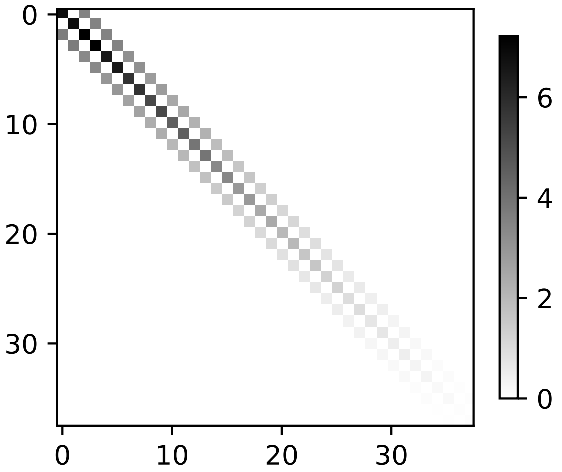

Figure 5.2: Sparsity pattern of matrix A_s for the second order discretisation with $N = 20$ pseudospatial nodes, $c = 10$, $\beta = 2$ and $S = 0.1$. The scale of grey values in the patter correspond to the absolute value of the actual values.

5.1.4 Fourth order discretisation

As in Fazio and Janelli (2014)'s second order approximation given in [27], the discretisation process starts with the chain rule on the derivative of $\boldsymbol{q}(\xi(x), t)$ with respect to x at a generic node x_n, i.e.

$$\left.\frac{\partial \boldsymbol{q}(\xi(x), t)}{\partial x}\right|_{x_n} = \left.\frac{\partial \boldsymbol{q}(\xi(x), t)}{\partial \xi}\right|_{x_n} \cdot \left.\frac{d\xi(x)}{dx}\right|_{x_n}. \tag{5.16}$$

Fazio and Janelli (2014) approximates these derivatives by using centered differences with different stepsize and allowing the cancellation of the terms of the uniform grid ξ_n, so that the resulting expression evaluates the pseudo-space x_n at non-integer points. However, the $\left({}^{d\xi(x)}/{}_{dx}\right)_{x_n}$ can be obtained exactly from equation (5.2a), obtaining a simpler expression for higher order derivative approximations with more complicate stencils.

Since the logarithmic map between grids, i.e. $x : [0, 1) \to [0, \infty)$, is a bijection, its inverse mapping

$$x(\xi) = -c\ln(1 - \xi) \iff \xi(x) = 1 - e^{-x/c} \tag{5.17}$$

can be obtained so that its derivative can be calculated and evaluated at x_n,

$$\left.\frac{\partial \xi(x)}{\partial x}\right|_{x_n} = \frac{1}{c}\, e^{-x_n/c} = \frac{1}{c}\,(1 - \xi_n) = \frac{1}{c}\left(1 - \frac{n}{N}\right), \tag{5.18}$$

and later plugged into (5.16) to obtain the formula that relates the grid derivatives,

$$\left.\frac{\partial \boldsymbol{q}(\xi(x), t)}{\partial x}\right|_{x_n} = \left.\frac{\partial \boldsymbol{q}(\xi(x), t)}{\partial \xi}\right|_{x_n} \cdot \frac{1}{c}\left(1 - \frac{n}{N}\right). \tag{5.19}$$

Formula (5.19) enables to use finite difference approximations for the first derivative in a bounded uniform mesh, i.e. $\forall \xi_n$, and transform them to the Quasi-Uniform Mesh (QUM) in the semi-infinite domain, i.e. $\forall x_n$.

For the approximation of the derivative of $\boldsymbol{q}$ on the equidistant grid at the interior points, i.e. ${}^{\partial \boldsymbol{q}(\xi(x),t)}/_{\partial\xi}|_{x_n}$ $\forall n \in \{1, 2, \dots, N-1\}$, the fourth order Compact Finite Difference (CFD) approximation introduced by Lele [40] in equation (2.1.6) with $\alpha = {}^1/_4$ is used. This CFD approximation is known as Pade's approximation and reads

$$\left.\frac{\partial \boldsymbol{q}(\xi(x),t)}{\partial \xi}\right|_{x_{n-1}} + \left.\frac{4\partial \boldsymbol{q}(\xi(x),t)}{\partial \xi}\right|_{x_n} + \left.\frac{\partial \boldsymbol{q}(\xi(x),t)}{\partial \xi}\right|_{x_{n+1}} \approx \frac{3}{d}\left(\boldsymbol{q}_{n+1}(t) - \boldsymbol{q}_{n-1}(t)\right) \qquad (5.20)$$

with $d := \xi_{n+1} - \xi_n = \frac{1}{N}$ for the interior points with indices $n \in \{1, 2, \dots, N-1\}$.

With equation (5.19), the derivatives with respect to the uniform space variable, ξ, can be replaced by derivatives in the pseudo-space variable, x, so that equation (5.20) becomes

$$\begin{aligned}\frac{3}{d}\left(\boldsymbol{q}_{n+1}(t) - \boldsymbol{q}_{n-1}(t)\right) \approx \left(\frac{Nc}{N-n+1}\right) &\left.\frac{\partial \boldsymbol{q}(\xi(x),t)}{\partial x}\right|_{x_{n-1}} + \\ + \left(\frac{4Nc}{N-n}\right) &\left.\frac{\partial \boldsymbol{q}(\xi(x),t)}{\partial x}\right|_{x_n} + \\ + \left(\frac{Nc}{N-n-1}\right) &\left.\frac{\partial \boldsymbol{q}(\xi(x),t)}{\partial x}\right|_{x_{n+1}}\end{aligned} \qquad (5.21)$$

The second derivative is to be calculated by applying the first derivative twice. The composition of the first derivative twice requires a different treatment of the scheme at the left boundary, $x_n = 0$,

(i) one upwinding approximation including the boundary condition obtained by the same procedure as in Malele et al. (2022) [41] and

(ii) another one without the influence of the boundary condition obtained by using the fourth order upwinding scheme given by Lele (1992) [40].

Malele et al. (2022)'s approach starts by considering a general fourth order expression with the form

$$a_0(\partial_\xi \boldsymbol{q})_0 + a_1(\partial_\xi \boldsymbol{q})_1 = \hat{b}_0\left(\alpha \boldsymbol{q}_0 - \gamma(\partial_x \boldsymbol{q})_0\right) + \frac{1}{d}\left\{b_0\boldsymbol{q}_0 + b_1\boldsymbol{q}_1 + b_2\boldsymbol{q}_2 + b_3\boldsymbol{q}_3\right\}, \qquad (5.22)$$

where $(\partial_\xi \boldsymbol{q})_i := \partial_\xi \boldsymbol{q}(\xi_i, t)$, $(\partial_x \boldsymbol{q})_i := \partial_x \boldsymbol{q}(x(\xi_i), t)$ and $\boldsymbol{q}_i := \boldsymbol{q}(\xi_i, t)$, dropping dependencies for a shorter notation. Change now the derivatives with respect to x to derivatives with respect to ξ, using equation (5.19),

$$a_0(\partial_\xi \boldsymbol{q})_0 + a_1(\partial_\xi \boldsymbol{q})_1 = \hat{b}_0\left(\alpha \boldsymbol{q}_0 - \frac{\gamma}{c}(\partial_\xi \boldsymbol{q})_0\right) + \frac{1}{d}\left\{b_0\boldsymbol{q}_0 + b_1\boldsymbol{q}_1 + b_2\boldsymbol{q}_2 + b_3\boldsymbol{q}_3\right\} \qquad (5.23)$$

whose coefficients can be obtained using Taylor Series around the expansion point ξ_0. These expansions are given below:

$$\begin{array}{rlllll}(\partial_\xi \boldsymbol{q})_0: & 0 & +(\partial_\xi \boldsymbol{q})_0 & & & \\ (\partial_\xi \boldsymbol{q})_1: & 0 & +(\partial_\xi \boldsymbol{q})_0 + d(\partial_\xi^2 \boldsymbol{q})_0 & +\frac{d^2}{2}(\partial_\xi^3 \boldsymbol{q})_0 + \frac{d^3}{6}(\partial_\xi^4 \boldsymbol{q})_0 & +\frac{d^4}{24}(\partial_\xi^5 \boldsymbol{q})_0 + \dots \\ \boldsymbol{q}_0: & \boldsymbol{q}_0 & & & \end{array}$$

$$
\begin{array}{lllllll}
\boldsymbol{q}_1: & \boldsymbol{q}_0 & +d(\partial_\xi \boldsymbol{q})_0 + \frac{d^2}{2}(\partial_\xi^2 \boldsymbol{q})_0 & +\frac{d^3}{6}(\partial_\xi^3 \boldsymbol{q})_0 + \frac{d^4}{24}(\partial_\xi^4 \boldsymbol{q})_0 & +\frac{d^5}{120}(\partial_\xi^5 \boldsymbol{q})_0 + \dots \\
\boldsymbol{q}_2: & \boldsymbol{q}_0 & +2d(\partial_\xi \boldsymbol{q})_0 + \frac{4d^2}{2}(\partial_\xi^2 \boldsymbol{q})_0 & +\frac{8d^3}{6}(\partial_\xi^3 \boldsymbol{q})_0 + \frac{16d^4}{24}(\partial_\xi^4 \boldsymbol{q})_0 & +\frac{32d^5}{120}(\partial_\xi^5 \boldsymbol{q})_0 + \dots \\
\boldsymbol{q}_3: & \boldsymbol{q}_0 & +3d(\partial_\xi \boldsymbol{q})_0 + \frac{9d^2}{2}(\partial_\xi^2 \boldsymbol{q})_0 & +\frac{27d^3}{6}(\partial_\xi^3 \boldsymbol{q})_0 + \frac{81d^4}{24}(\partial_\xi^4 \boldsymbol{q})_0 & +\frac{243d^5}{120}(\partial_\xi^5 \boldsymbol{q})_0 + \dots
\end{array}
$$

Gathering the same terms together results in

$$\boldsymbol{q}_0: \quad 0 \quad +0 \quad +\alpha\hat{b}_0 \quad +\frac{1}{d}b_0 \quad +\frac{1}{d}b_1 \quad +\frac{1}{d}b_2 \quad +\frac{1}{d}b_3 \quad = 0, \tag{5.24a}$$

$$(\partial_\xi \boldsymbol{q})_0: \quad a_0 \quad +a_1 \quad +\frac{\gamma}{c}\hat{b}_0 \quad +0 \quad -b_1 \quad -2b_2 \quad -3b_3 \quad = 0, \tag{5.24b}$$

$$(\partial_\xi^2 \boldsymbol{q})_0: \quad 0 \quad +da_1 \quad +0 \quad +0 \quad -\frac{d}{2}b_1 \quad -\frac{4d}{2}b_2 \quad -\frac{9d}{2}b_3 \quad = 0, \tag{5.24c}$$

$$(\partial_\xi^3 \boldsymbol{q})_0: \quad 0 \quad +\frac{d^2}{2}a_1 \quad +0 \quad +0 \quad -\frac{d^2}{6}b_1 \quad -\frac{8d^2}{6}b_2 \quad -\frac{27d^2}{6}b_3 \quad = 0, \tag{5.24d}$$

$$(\partial_\xi^4 \boldsymbol{q})_0: \quad 0 \quad +\frac{d^3}{6}a_1 \quad +0 \quad +0 \quad -\frac{d^3}{24}b_1 \quad -\frac{16d^3}{24}b_2 \quad -\frac{81d^3}{24}b_3 \quad = 0, \tag{5.24e}$$

$$(\partial_\xi^5 \boldsymbol{q})_0: \quad 0 \quad +\frac{d^4}{24}a_1 \quad +0 \quad +0 \quad -\frac{d^4}{120}b_1 \quad -\frac{32d^4}{120}b_2 \quad -\frac{243d^4}{120}b_3 \quad = 0. \tag{5.24f}$$

For simplicity, set $a_0 = 1$ and $a_1 = 1$. This permits to use the same matrix as in the second step of the numerical CFD approach, i.e. the matrix obtained using Lele (1992)'s approach [40]. Solving the linear system of equations (5.24a) results in the coefficients

$$\hat{b}_0 = -\frac{2c}{3\gamma}, \quad b_0 = \frac{12\alpha dc - 17\gamma}{18\gamma}, \quad b_1 = \frac{1}{2}, \quad b_2 = \frac{1}{2}, \quad b_3 = -\frac{1}{18}. \tag{5.25}$$

Plugging these coefficients in equation (5.22), the fourth order upwinding approximation that includes the boundary term is

$$
\begin{aligned}
(\partial_\xi \boldsymbol{q})_0 + (\partial_\xi \boldsymbol{q})_1 = &- \frac{2c}{3\gamma}\left(\alpha \boldsymbol{q}_0 - \frac{\gamma}{c}(\partial_\xi \boldsymbol{q})_0\right) + \frac{1}{d}\left(\frac{12\alpha dc - 17\gamma}{18\gamma}\right)\boldsymbol{q}_0 + \\
&+ \frac{1}{2d}\boldsymbol{q}_1 + \frac{1}{2d}\boldsymbol{q}_2 - \frac{1}{18d}\boldsymbol{q}_3.
\end{aligned}
\tag{5.26}
$$

Using again expression (5.19) to obtain an expression of the derivatives with respect to x yields

$$
\begin{aligned}
c(\partial_x \boldsymbol{q})_0 + \frac{Nc}{N-1}(\partial_x \boldsymbol{q})_1 = &- \frac{2c}{3\gamma}\left(\alpha \boldsymbol{q}_0 - \gamma(\partial_x \boldsymbol{q})_0\right) + \frac{1}{d}\left(\frac{12\alpha dc - 17\gamma}{18\gamma}\right)\boldsymbol{q}_0 + \\
&+ \frac{1}{2d}\boldsymbol{q}_1 + \frac{1}{2d}\boldsymbol{q}_2 - \frac{1}{18d}\boldsymbol{q}_3.
\end{aligned}
\tag{5.27}
$$

Finally, use boundary condition (2.12c) to exchange $\alpha\boldsymbol{q}_0 - \gamma(\partial_x \boldsymbol{q})_0$ by $\boldsymbol{f}(\boldsymbol{q}_0, \boldsymbol{y}, t)$ and obtain the final expression for Padé's scheme applied to problem

$$
\begin{aligned}
c(\partial_x \boldsymbol{q})_0 + \frac{Nc}{N-1}(\partial_x \boldsymbol{q})_1 = &- \frac{2c}{3\gamma}\left(\boldsymbol{f}(\boldsymbol{q}_0, \boldsymbol{y}_0, t) - (\partial_t \boldsymbol{q})_0\right) + \frac{1}{d}\left(\frac{12\alpha dc - 17\gamma}{18\gamma}\right)\boldsymbol{q}_0 + \\
&+ \frac{1}{2d}\boldsymbol{q}_1 + \frac{1}{2d}\boldsymbol{q}_2 - \frac{1}{18d}\boldsymbol{q}_3.
\end{aligned}
\tag{5.28}
$$

Without abbreviations, the expression for the approximation is

$$c\left.\frac{\partial \boldsymbol{q}(\xi(x),t)}{\partial x}\right|_{x_0} + \frac{Nc}{N-1}\left.\frac{\partial \boldsymbol{q}(\xi(x),t)}{\partial x}\right|_{x_1} \approx \left(\frac{12\alpha dc - 17\gamma}{18\gamma d}\right)\boldsymbol{q}_0(t) + \frac{1}{2d}\boldsymbol{q}_1(t) + \\ + \frac{1}{2d}\boldsymbol{q}_2(t) - \frac{1}{18d}\boldsymbol{q}_3(t) + \\ - \frac{2c}{3\gamma}\left(\boldsymbol{f}(\boldsymbol{q}_0(t),\boldsymbol{y}(t),t) - \left.\frac{\partial \boldsymbol{q}(\xi(x),t)}{\partial t}\right|_{x_0}\right). \tag{5.29}$$

On the other hand, since the second upwinding scheme at $x_n = 0$ does not include a boundary condition, the coefficients of the scheme on the uniform grid are taken directly from Lele (1992) [40, Equation (4.1.4)], so that the scheme reads

$$\left.\frac{\partial \boldsymbol{q}(\xi(x),t)}{\partial \xi}\right|_{x_0} + 3\left.\frac{\partial \boldsymbol{q}(\xi(x),t)}{\partial \xi}\right|_{x_1} \approx \frac{1}{d}\left(-\frac{17}{6}\boldsymbol{q}_0(t) + \frac{3}{2}\boldsymbol{q}_1(t) + \frac{3}{2}\boldsymbol{q}_2(t) - \frac{1}{6}\boldsymbol{q}_3(t)\right). \tag{5.30}$$

Again, the derivatives in the uniform space variable, ξ, are replaced by derivatives in pseudo-space variable x, obtaining

$$c\left.\frac{\partial \boldsymbol{q}(\xi(x),t)}{\partial x}\right|_{x_0} + \left(\frac{3Nc}{N-1}\right)\left.\frac{\partial \boldsymbol{q}(\xi(x),t)}{\partial x}\right|_{x_1} \approx \frac{1}{d}\left(-\frac{17}{6}\boldsymbol{q}_0(t) + \frac{3}{2}\boldsymbol{q}_1(t) + \frac{3}{2}\boldsymbol{q}_2(t) - \frac{1}{6}\boldsymbol{q}_3(t)\right). \tag{5.31}$$

Extending these equations for all the nodes in the mesh, i.e. $x_i\ \forall i \in \mathbb{N}_0$, results in two systems of equations, shown below in compact form,

$$M_1\ D_x\boldsymbol{q}(t) \approx B_1\boldsymbol{q}(t) + K_1(\boldsymbol{q}_0(t),\boldsymbol{y}(t),t) + V_1(\dot{\boldsymbol{q}}_0(t)), \tag{5.32a}$$

$$M_2\ D_x^2\boldsymbol{q}(t) \approx B_2\ D_x\boldsymbol{q}(t), \tag{5.32b}$$

where the matrices and vectors are defined in Appendix B, and $D_x\boldsymbol{q}(t)$ is the vector of spatial derivatives, i.e. $\frac{\partial}{\partial x}\boldsymbol{q}(\xi(x),t)$, evaluated at the grid nodes.

The goal is to gather both systems into a single one and obtain an expression for $D_x^2\boldsymbol{q}(t)$ that depends only on $\boldsymbol{q}(t)$ and $\boldsymbol{y}(t)$. With some algebra and multiplying (5.32a) by M_1^{-1} yields

$$D_x\boldsymbol{q}(t) \approx M_1^{-1}\ B_1\boldsymbol{q}(t) + M_1^{-1}\ K_1(\boldsymbol{q}_0(t),\boldsymbol{y}(t),t) + M_1^{-1}\ V_1(\dot{\boldsymbol{q}}_0(t)), \tag{5.33a}$$

$$M_2\ D_x^2\boldsymbol{q}(t) \approx B_2\ D_x\boldsymbol{q}(t). \tag{5.33b}$$

Substituting the right hand side of (5.33a) into (5.33b) results in

$$M_2 D_x^2\boldsymbol{q}(t) \approx B_2\left(M_1^{-1}\ B_1\boldsymbol{q}(t) + M_1^{-1}\ K_1(\boldsymbol{q}_0(t),\boldsymbol{y}(t),t) + M_1^{-1}\ V_1(\dot{\boldsymbol{q}}_0(t))\right). \tag{5.34}$$

Rearranging the terms provides

$$M_2\ D_x^2\boldsymbol{q}(t) - B_2 M_1^{-1} V_1(\dot{\boldsymbol{q}}_0(t)) \approx B_2 M_1^{-1} B_1\boldsymbol{q}(t) + B_2 M_1^{-1}\ K_1(\boldsymbol{q}_0(t),\boldsymbol{y}(t),t). \tag{5.35}$$

Use now the semidiscretised version of the differential equation (2.12a), viz. $\dot{\boldsymbol{q}}(t) = D_x^2 \boldsymbol{q}(t)$, and transform the matrix $V_1(\dot{\boldsymbol{q}}_0(t))$ as follows,

$$V_1(\dot{\boldsymbol{q}}_0(t)) = \frac{2c}{3\gamma} \begin{bmatrix} \dot{q}_0^{(1)}(t) \\ \dot{q}_0^{(2)}(t) \\ 0 \\ 0 \\ \vdots \\ 0 \end{bmatrix} = \frac{2c}{3\gamma} \underbrace{\begin{bmatrix} 1 & 0 & 0 & \dots \\ 0 & 1 & 0 & \ddots \\ 0 & 0 & 0 & \ddots \\ \vdots & \ddots & \ddots & \ddots \end{bmatrix}}_{=:\mathbb{P}} \dot{\boldsymbol{q}}(t) = \frac{2c}{3\gamma} \mathbb{P} \, \dot{\boldsymbol{q}}(t), \tag{5.36}$$

so that the expressions for A_s and $\boldsymbol{v}$ in the semidiscretised system (5.3) for the fourth order FD scheme is obtained,

$$A_s := \Psi^{-1} B_2 M_1^{-1} B_1, \tag{5.37a}$$

$$\boldsymbol{v}(\boldsymbol{q}_0(t), \boldsymbol{y}(t), t) := \Psi^{-1} B_2 M_1^{-1} K_1(\boldsymbol{q}_0(t), \boldsymbol{y}(t), t), \tag{5.37b}$$

$$\Psi := M_2 - \frac{2c}{3\gamma} B_2 M_1^{-1} \mathbb{P}. \tag{5.37c}$$

5.2 Time integrators

This section introduces the numerical methods used in the time integration of system (5.3). Explicit methods are excluded since the stability limit scales like $\mathcal{O}(\Delta x^2)$ so that even moderate resolution in the pseudo-space would already need a very small time step, making this type of methods inefficient. The time integrators studied here are: two fully implicit methods and four Implicit-Explicit (IMEX) methods.

Implicit Runge-Kutta methods on nonlinear differential equations normally require nonlinear solvers, which have a considerable influence in computational time. IMEX methods combine the use of an implicit method and an explicit method in one differential equation, utilising the strength of both methods. The implicit method is used on the linear stiff part of the equation to avoid the use of the nonlinear solver, ensuring better stability performance. The use of the explicit method on the nonstiff nonlinear part ensures faster computational times compared to a fully implicit method. Omitting the use of the nonlinear solver results in a better performance of the IMEX methods over the implicit methods.

The time grid for the time integration is obtained by dividing the bounded and closed time domain, viz. $[t_0, t_f]$, into $L-1$ equidistant subintervals, i.e.

$$t_0 < t_1 < t_2 < \cdots < t_{L-1} := t_f, \tag{5.38}$$

obtaining L time nodes.

5.2.1 Runge-Kutta methods

Runge-Kutta methods are a family of numerical methods used to approximate the solution of ordinary differential equations of the form

$$y'(t) = f(t, y(t)), \qquad t \in [a, b], \tag{5.39}$$

$$y(a) = y_0. \tag{5.40}$$

These methods were developed at the beginning of the XXth century by Carl Runge [55] and Wilhelm Kutta [38]. They are typically described using tables, called Butcher-tableaus. These tables define the coefficients of the numerical scheme according to a specific pattern.

Definition 5.1 (Butcher tableau)**.** Given one matrix $B \in \mathbb{R}^{s\times s}$ and two vectors $a, c \in \mathbb{R}^s$,

$$\begin{array}{c|c} a & B \\ \hline & c^T \end{array} \tag{5.41}$$

is called the Butcher Tableau of the corresponding Runge-Kutta method

$$y_{n+1} = y_n + h\sum_{i=1}^{s} c_i k_i \tag{5.42a}$$

$$k_i = f\Big(t_n + a_i h,\ y_n + h\sum_{j=1}^{s} b_{ij} k_j\Big), \tag{5.42b}$$

where h is the step and the k_i for $i \in \{1, 2, \ldots, s\}$ are the stages of the method.

The classification of numerical technics in explicit and implicit methods can be done according to the form of the matrix B in the Butcher tableau (5.41).

Definition 5.2 (Explicit Runge-Kutta method)**.** A Runge-Kutta method is called explicit if the coefficients $b_{ij} = 0\ \forall j \geq i$ in equation (5.42b), or equivalently, B is a strictly lower triangular matrix.

Definition 5.3 (Implicit Runge-Kutta method)**.** A Runge-Kutta method is called implicit if $\exists b_{ij} \neq 0$ for some $j \geq i$ in equation (5.42b), or equivalently, B is not a strictly lower triangular matrix.

Implicit methods require the use of a root-finder algorithm, having a considerable influence in computation time in nonlinear problems. On the other hand, explicit methods are often faster but have worse stability properties, i.e. a very small time step may be required in order to ensure a bounded numerical solution (conditional stability).

Definition 5.4 (A-stability)**.** A Runge-Kutta method with formula (5.42) is said to be A-stable if its stability domain, S, contains the left half of the complex plane, i.e. $\{z \in \mathbb{C} \mid \Re\{z\} \leq 0\} \subseteq S$.

Definition 5.5 (L-stability)**.** A Runge-Kutta method with formula (5.42) is said to be L-stable if it is A-stable and $\lim_{|z|\to\infty} |R(z)| = 0$.

A-stability removes the stability constrain from the choice of the step and it is therefore an important property of the numerical schemes. Explicit methods are not A-stable [60]. For this reason no explicit schemes were applied on equation (5.3).

5.2.2 The trapezoidal Rule

The trapezoidal rule (TR) is the first integrator implemented due to its simplicity and the fact that is a widespread scheme in FD. The TR coupled with the second order FD is equivalent to implementing the Crank-Nicolson scheme [18] with constant 1/2. The TR is an implicit, second order Runge-Kutta method with the following Butcher-tableau

$$\begin{array}{c|cc} 0 & 0 & 0 \\ 1 & 1/2 & 1/2 \\ \hline & 1/2 & 1/2 \end{array} \tag{5.43}$$

The TR is an A-stable non-L-stable method [60, Example 32, p. 55], so that the stiff components of the differential equation may not be dumped quickly enough to avoid oscillations to appear on the numerical solution.

The expression of the TR is given by

$$\boldsymbol{\eta}^{n+1} \approx \boldsymbol{\eta}^{n} + \frac{\Delta t}{2}\left(\dot{\boldsymbol{\eta}}^{n} + \dot{\boldsymbol{\eta}}^{n+1}\right), \tag{5.44}$$

where $\boldsymbol{\eta}^n := \boldsymbol{\eta}(t^n)$. By applying it to equation (5.3)

$$\boldsymbol{\eta}^{n+1} \approx \boldsymbol{\eta}^{n} + \frac{\Delta t}{2}\left(\tilde{A}\boldsymbol{\eta}^{n} + \boldsymbol{\omega}^{n} + \tilde{A}\boldsymbol{\eta}^{n+1} + \boldsymbol{\omega}^{n+1}\right), \tag{5.45}$$

is obtained, with $\boldsymbol{W}^n := \boldsymbol{W}(\boldsymbol{\eta}^n, t^n)$. After a little bit of algebra,

$$\left(\mathbb{I} - \frac{\Delta t}{2}\tilde{A}\right)\boldsymbol{\eta}^{n+1} \approx \left(\mathbb{I} + \frac{\Delta t}{2}\tilde{A}\right)\boldsymbol{\eta}^{n} + \frac{\Delta t}{2}\left(\boldsymbol{\omega}^{n} + \boldsymbol{\omega}^{n+1}\right). \tag{5.46}$$

Equation (5.46) represents a nonlinear system of equations (due to the nonlinear dependency of the right hand side on $\boldsymbol{\eta}^{n+1}$ through the term $\boldsymbol{\omega}_{n+1}$), and must be solved using a nonlinear solver, such as the the secant method or the Newton-Raphson method. An approximation of the solution obtained with forward Euler's method on equations (5.3) is used as a guess for the nonlinear solver, i.e.

$$\boldsymbol{\eta}^{n+1}_{guess} := \Delta t\left(\tilde{A}\boldsymbol{\eta}^{n} + \boldsymbol{\omega}^{n}\right). \tag{5.47}$$

5.2.3 The (Simply) Diagonally Implicit Runge-Kutta method

The fourth order simply diagonally implicit Runge-Kutta method ESDIRK4(3)6L[2]SA borrowed from Kennedy and Carpenter (2016) [34] is used as a second implicit time integrator. Simply diagonally implicit Runge-Kutta methods are a type of implicit Runge-Kutta methods whose matrix B is a lower triangular matrix B with $b_{ii} \equiv b \in \mathbb{R} \setminus \{0\}$. The fact that all diagonal entries of matrix B are equal means that some terms can be precalculated and reused, translating into savings in computational work and time.

Definition 5.6 (Diagonally Implicit Runge-Kutta (DIRK) method [34])**.** A Runge-Kutta method is called Diagonally Implicit (DIRK) if the matrix B in their Butcher tableau (5.41) is a lower triangular matrix with at least one nonzero diagonal entry, i.e. $b_{ij} = 0$ for $1 \leq i < j \leq s$ and $b_{ii} \neq 0$ for at least one $i \in \{1, \ldots, s\}$.

The general formula of a DIRK method is therefore given by:

$$y_{n+1} = y_n + h\sum_{i=1}^{s} c_i k_i, \tag{5.48a}$$

$$k_i = f\Big(t_n + a_i h,\ y_n + h\sum_{j=1}^{i} b_{ij}k_j\Big), \tag{5.48b}$$

where the main difference (and advantage) with the general formula (5.42b) is that the final index in the sum in equation (5.48b). This enables solving for each stage, i.e. k_i, individually instead of simultaneously.

Definition 5.7 (Simply Diagonally Implicit Runge-Kutta (SDIRK) method)**.** A DIRK method is called Simply Diagonally Implicit (SDIRK) if $b_{ii} \equiv b \in \mathbb{R}\setminus\{0\}\ \forall i \in \{1, 2, \ldots, s\}$.

The general formula of a SDIRK method is

$$y_{n+1} = y_n + h\sum_{i=1}^{s} c_i k_i, \tag{5.49a}$$

$$k_i = f\Big(t_n + a_i h,\ y_n + h\sum_{j=1}^{i-1} b_{ij}k_j + hbk_i\Big). \tag{5.49b}$$

SDIRK methods are specially useful in linear autonomous problems, since equation (5.49b) then reduces to

$$k_i = f\Big(t_n + a_i h,\ y_n + h\sum_{j=1}^{i-1} b_{ij}k_j + hbk_i\Big) = f\Big(y_n + h\sum_{j=1}^{i-1} b_{ij}k_j + hbk_i\Big) \tag{5.50}$$

$$= f\Big(y_n + h\sum_{j=1}^{i-1} b_{ij}k_j\Big) + hbf(k_i). \tag{5.51}$$

Rearranging the terms,

$$\Big(\mathbb{I} - hbf\Big)k_i = f\Big(y_n + h\sum_{j=1}^{i-1} b_{ij}k_j\Big). \tag{5.52}$$

Since the left term is constant and independent of i, the LU-decomposition of the left matrix can be calculated once and saved in order to be used for all $i \in \{1, 2, \ldots, s\}$. Solving a linear system $Ax = b$, like the one in equation (5.52), for constant A and different b's with a LU-decomposition is cheaper than using Gauss elimination each time [16]. LU-decomposition is also more efficient compared to other methods and decompositions, such as Cramer's rule [2] and QR-decomposition [71].

Regarding uniqueness of solutions of system (5.52), the following theorem 5.8 proves that the system (5.52) will have a solution for $||hbf|| < 1$.

Theorem 5.8 (Sufficient condition for uniqueness of solutions of a linear system)**.** *Let* $\mathbb{I} \in \mathbb{R}^{n\times n}$ *be the identity matrix,* $A \in \mathbb{R}^{n\times n}$ *a matrix of constant coefficients,* $x \in \mathbb{R}^n$ *the* *vector of unknowns,* $b \in \mathbb{R}^n$ *a vector of constant coefficients, for some* $n \in \mathbb{N}$ *and* $||\cdot||$ *a matrix norm. Then the system*

$$(\mathbb{I} - A)x = b \tag{5.53}$$

will have a unique solution if $||A|| < 1$.

Proof. Consider

$$||\mathbb{I} - A|| \geq \underbrace{||\ \mathbb{I}\ ||}_{=1} - ||A|| = 1 - \underbrace{||A||}_{<1} > 0 \tag{5.54}$$

where the triangle inequality for subtractions and the fact that the norm of the identity matrix is 1 were applied. Since

$$\begin{aligned} ||\mathbb{I} - A|| &= \sup_{||x||=1} \{||(\mathbb{I} - A)x||\} = \sup_{||x||=1} \{||\lambda_i x||\} && (5.55)\\ &= \sup_{||x||=1} \{|\lambda|\ ||x||\} = |\lambda_i| \sup_{||x||=1} \{||x||\} && (5.56)\\ &= |\lambda_i| && (5.57) \end{aligned}$$

for any eigenvalue λ_i of $\mathbb{I} - A$ for $i \in \{1, 2, \ldots, n\}$, then $\lambda_i \neq 0$ and therefore system (5.53) has a unique solution. □

The SDIRK method applied on system (5.3) yields

$$\boldsymbol{\eta}^{n+1} \approx \boldsymbol{\eta}^n + h \sum_{i=1}^{s} c_i \boldsymbol{k}_i, \tag{5.58a}$$

$$\boldsymbol{k}_i = \tilde{A}\Big(\boldsymbol{\eta}^n + h \sum_{j=1}^{i-1} b_{ij} \boldsymbol{k}_j + h b_{ii} \boldsymbol{k}_i\Big) + \boldsymbol{\omega}\Big(\boldsymbol{\eta}^n + h \sum_{j=1}^{i} b_{ij} \boldsymbol{k}_j,\ t_n + a_i h\Big), \tag{5.58b}$$

where $b_{ii} = b\ \forall i \in \{1, \ldots, s\}$. Using some algebra and the linearity of $\tilde{A}$ results in

$$\boldsymbol{\eta}^{n+1} \approx \boldsymbol{\eta}^n + h \sum_{i=1}^{s} c_i \boldsymbol{k}_i, \tag{5.59a}$$

$$\Big(\mathbb{I} - hb\tilde{A}\Big)\boldsymbol{k}_i = \tilde{A}\boldsymbol{\eta}^n + h\tilde{A} \sum_{j=1}^{i-1} b_{ij} \boldsymbol{k}_j + \boldsymbol{\omega}\Big(\boldsymbol{\eta}^n + h \sum_{j=1}^{i} b_{ij} \boldsymbol{k}_j,\ t_n + a_i h\Big). \tag{5.59b}$$

Note that the last step removed the implicit term on the linear part of the right hand side. On the other hand, the term $\boldsymbol{\omega}$ on the right hand side still depends on $\boldsymbol{k}_i$, so the system must be solved using a nonlinear solver $\forall i \in \{2, \ldots, s\}$, with the previous stage, i.e. $\boldsymbol{k}_{i-1}$, as the initial guess. The term $\boldsymbol{k}_1$ can be obtained directly without any nonlinear solver, as follows

$$\boldsymbol{k}_1 = \tilde{A}\boldsymbol{\eta}^n + \boldsymbol{\omega}(\boldsymbol{\eta}^n,\ t_n), \tag{5.60}$$

since $b_{11} = a_1 = 0$.

5.2.4 The Implicit-Explicit Methods

The semidiscrete system obtained in equation (5.3) consists of two terms: the linear stiff term, A, that appears from the $1/h^2$ scaling in the discrete Laplacian and a nonlinear term, $\boldsymbol{\omega}$. The problem stiffness inherited from A requires the use of an implicit method. However, the nonlinear term $\boldsymbol{\omega}$ needs to be addressed with an iterative nonlinear solver algorithm, increasing computation times.

IMEX methods have a considerable advantage in problems of this kind, since they treat each different term with a different method: The stiff term is integrated using an implicit method and the nonlinear term using an explicit method [4]. IMEX methods are thus expected to perform much better than fully implicit methods.

Definition 5.9 gives the definition of a general IMEX Runge-Kutta method provided in Ascher et al. (1997) [4] plus some modifications to make it suitable for the schemes provided by Kennedy and Carpenter (2016) [34] in a similar way as done in L. Schlegel (2023) [58].

Definition 5.9 (IMEX Runge-Kutta methods)**.** Consider a general differential equation

$$\boldsymbol{y}'(t) = \boldsymbol{f}(t, \boldsymbol{y}(t)) + \boldsymbol{g}(t, \boldsymbol{y}(t)), \qquad t > t_0 \tag{5.61a}$$

$$\boldsymbol{y}(t_0) = \boldsymbol{y}_0, \tag{5.61b}$$

with $\boldsymbol{y}_0 \in \mathbb{R}^n$, where $\boldsymbol{g}$ is a linear stiff term and $\boldsymbol{f}$ a nonlinear one. Given an implicit method with Butcher Tableau

$$\begin{array}{c|ccccc} 0 & 0 & 0 & 0 & \cdots & 0 \\ a_1 & B_{10} & B_{11} & 0 & \cdots & 0 \\ a_2 & B_{20} & B_{21} & B_{22} & \cdots & 0 \\ \vdots & \vdots & \vdots & \vdots & \ddots & \vdots \\ a_s & B_{s0} & B_{s1} & B_{s2} & \cdots & B_{ss} \\ \hline & c_0 & c_1 & c_2 & \cdots & c_s \end{array} \tag{5.62}$$

and an explicit method

$$\begin{array}{c|ccccc} 0 & 0 & 0 & 0 & \cdots & 0 \\ \hat{a}_1 & \hat{B}_{21} & \ddots & \ddots & \cdots & 0 \\ \hat{a}_2 & \hat{B}_{31} & \hat{B}_{22} & \ddots & \ddots & 0 \\ \vdots & \vdots & \vdots & \ddots & \ddots & \vdots \\ \hat{a}_s & \hat{B}_{s+1,1} & \hat{B}_{s+1,2} & \cdots & \hat{B}_{s+1,s} & 0 \\ \hline & \hat{c}_1 & \hat{c}_2 & \cdots & \cdots & \hat{c}_{s+1} \end{array}\ , \tag{5.63}$$

the corresponding IMEX method has the formula

$$\boldsymbol{y}_{n+1} = \boldsymbol{y}_n + h \sum_{j=0}^{s} c_j \boldsymbol{K}_j + h \sum_{j=1}^{s+1} \hat{c}_j \hat{\boldsymbol{K}}_j, \tag{5.64}$$

where

$$\boldsymbol{K}_i := \boldsymbol{g}(t_n + a_i h, \boldsymbol{y}_i) \qquad \text{as well as} \qquad \hat{\boldsymbol{K}}_i := \boldsymbol{f}(t_n + \hat{a}_i h, \boldsymbol{y}_i), \tag{5.65}$$

and $\boldsymbol{y}_i$ are the internal stages, given by

$$\boldsymbol{y}_i = \boldsymbol{y}_n + h\sum_{j=0}^{i} B_{ij}\boldsymbol{K}_j + h\sum_{j=1}^{i}\hat{B}_{i+1,j}\hat{\boldsymbol{K}}_j. \tag{5.66}$$

IMEX Schemes for the Maxey-Riley-Gatignol Equation

Four IMEX methods are implemented as time integrators of the semidiscrete system 5.3. These schemes are chosen, introduced and implemented by L. Schlegel in his bachelor thesis [58]. As a first order method L. Schlegel chose the IMEX method obtained from merging backward and forward Euler methods, the **Implicit-Explicit Euler** method

$$\begin{array}{c|c} 0 & 0 \\ \hline & 1 \end{array} \qquad \begin{array}{c|c} 1 & 1 \\ \hline & 1 \end{array}. \tag{5.67}$$

All other three methods are taken from the literature, namely, second and third order IMEX are taken from Ascher et al. (1997) [4] and the fourth order method from Kennedy and Carpenter (2016) [34]. The same naming convention corresponds as the one given in their respective sources. Ascher et al. (1997) [4] adopted a naming convention based on triplets (s, σ, p), where s represents the number of stages of the implicit method; σ the number of stages in the explicit method and p the convergence order. Kennedy and Carpenter (2016) [34] use a different nomenclature, similar to the one provided in Dormand and Prince (1986) [24]. The nomenclature of the methods follows the pattern $ESDIRKp(\hat{p}I)sL[q]SA$, which indicates that it is a DIRK method with an specific Butcher Tableau (see [34, Page 7]), where p is the order of the main method, $\hat{p}$ is the order of the embedded method, I indicates if it is an implicit method, s is the number of stages, L is an stability characterization of the method, q is the stage-order of the method and SA is used to indicate some important characteristics of the method.

The **Implicit-Explicit Midpoint (1,2,2)** with tableaus

$$\begin{array}{c|cc} 0 & 0 & 0 \\ \frac{1}{2} & 0 & \frac{1}{2} \\ \hline & 0 & 1 \end{array} \qquad \begin{array}{c|cc} 0 & 0 & 0 \\ \frac{1}{2} & \frac{1}{2} & 0 \\ \hline & 0 & 1 \end{array} \tag{5.68}$$

is the second order scheme. Note that this method is not L-stable and may present problems in the stiffness limit.

The third order combination is given by methods **(2,3,3)** with tableaus

$$\begin{array}{c|ccc} 0 & 0 & 0 & 0 \\ \gamma & 0 & \gamma & 0 \\ 1-\gamma & 0 & 1-2\gamma & \gamma \\ \hline & 0 & \frac{1}{2} & \frac{1}{2} \end{array} \qquad \begin{array}{c|ccc} 0 & 0 & 0 & 0 \\ \gamma & \gamma & 0 & 0 \\ 1-\gamma & \gamma-1 & 2(1-\gamma) & 0 \\ \hline & 0 & \frac{1}{2} & \frac{1}{2} \end{array} \tag{5.69}$$

with $\gamma = \frac{3+\sqrt(3)}{6}$. The DIRK scheme in (5.69) holds the best damping properties for its parameters (stages and convergence) according to Ascher et al. (1997), since $\lim_{|z|\to\infty} R(z) = 1-\sqrt{3}$ (compared to the midpoint) [4].

On the other hand, the fourth order IMEX method consists of the combination of the explicit ESDIRK4(3)6L[2]SA and the implicit ESDIRK4(3I)6L[2]SA schemes provided by

Kennedy and Carpenter (2016) [34]. This method is a A-stable on the second stage and L-stable on stages $3, 4, 5$ and 6 and "it is recommended as a good default method for solving stiff problems at moderate error tolerances" according to Kennedy and Carpenter (2016) [34].

Application of the IMEX scheme to the Maxey-Riley-Gatignol Equation

Applying one of the methods in the previous subsection to the semidiscrete system (5.3) provides the following formula

$$\boldsymbol{\eta}^{n+1} = \boldsymbol{\eta}^n + h\tilde{A}\sum_{i=0}^{s} c_i \boldsymbol{\eta}_i + h\sum_{i=1}^{s+1} \hat{c}_i \boldsymbol{\omega}_i \tag{5.70}$$

where $\boldsymbol{\omega}_i := \boldsymbol{\omega}(\boldsymbol{\eta}_i, t_n + \hat{a}_i h)$ and the stages, $\boldsymbol{\eta}_i$, are calculated as follows

$$\boldsymbol{\eta}_i = \boldsymbol{\eta}^n + h\tilde{A}\sum_{j=0}^{i} B_{ij} \boldsymbol{\eta}_j + h\sum_{j=1}^{i} \hat{B}_{i+1,j} \boldsymbol{\omega}_j. \tag{5.71}$$

This last formula can be simplified by taking the last element i in the linear part out of the sum and send it to the left hand side, obtaining

$$\left(\mathbb{I} - hB_{ii}\tilde{A}\right)\boldsymbol{\eta}_i = \boldsymbol{\eta}^n + h\tilde{A}\sum_{j=0}^{i-1} B_{ij} \boldsymbol{\eta}_j + h\sum_{j=1}^{i} \hat{B}_{i+1,j} \boldsymbol{\omega}_j. \tag{5.72}$$

6

Convergence and efficiency

This chapter presents convergence and efficiency studies of the numerical schemes presented in chapter 5 for six different flow fields. The code needed to reproduce the figures and the tables from this chapter can be found in the code repository in GitHub [72]. These six flow fields have very distinct characteristics and therefore provide a good base to understand how the error may behave for other flow fields.

For three of the flow fields there exists an analytical solution for the Maxey-Riley-Gatignol equation. These fields are (1) the quiescent flow, (2) a rotating vortex and (3) an oscillatory background. For the remaining three, there is no available analytical solution up to our knowledge and an accurate-enough reference solutions is used instead. These methods are (4) the double gyre, (5) the Bickley jet and (6) an experimentally-obtained velocity field referred to as the Faraday flow.

The performance of the schemes is studied by evaluating the experimental convergence rate against a reference solution (an analytical solution when available or a more accurate numerical approximation otherwise) as well as comparing the time it takes for a method to reach a specific error. Some convergence plots are shown for reference, but the main discussion is around the experimentally-computed convergence rates, shown in tables. For simplicity, in all the numerical solutions the number of nodes in time, L, are set to be equal to the number of nodes in the pseudospace, N. The experimentally-computed convergence rates are computed by calculating the slope of the best-fitting line to the points in the convergence plots with the *polyfit* function within the *numpy* [33] library in *Python*.

The efficiency of the methods is presented in work-precision plots, where the achieved error obtained by each method is plotted against their runtimes. The "*real time*" threshold is taken as a reference in work-precision plots to measure how efficient methods are. "*Real time*" is used as an equivalent term of the final time of the scheme, t_f, and it is a critical threshold in experiments because it shows which schemes would be able to calculate the full interval trajectory before final time.

The study of the convergence and the efficiency of the methods is done in the same way as in Urizarna-Carasa et al. (2025) [73], although the results are slightly different for some fields since all inputs are nondimensionalised with scales different from one. Daitche's method also presents here more instabilities due to the change in the inputs. Many of these convergences are mark as "unstable" when the method diverged for one or more meshes. That means that one could still obtain a stable solution with that set of parameters if the right mesh is utilised.

6.1 Numerical efficiency on flow fields with existing analytical solutions

This section introduces three simple velocity fields for which the analytical solution of the full Maxey-Riley-Gatignol Equation is known and analyses the performance of the numerical schemes from chapter 5 for these fields. These fields are normally given by not too complicated analytical expressions. These fields are: (1) the quiescent flow, (2) a steady vortex and (3) an oscillatory background.

The simplicity of these fields is due to some of their properties: They are either steady (time-independent), like the vortex; spatially homogeneous (constant in space), like the oscillatory background; or both steady and spatially homogeneous, like the quiescent flow.

6.1.1 The quiescent flow

The quiescent flow field corresponds to a still fluid with zero velocity everywhere, where particles move until they reach a halt due to friction. The dimensionless velocity profile at each point of the spatial domain, $\boldsymbol{y}(t)$, is

$$\boldsymbol{u}(\boldsymbol{y}(t), t) = \begin{bmatrix} 0 \\ 0 \end{bmatrix}. \tag{6.1}$$

Time and space derivatives are also zero everywhere. This example was provided in Prasath et al. (2019) [53, Example 1]. The analytical solution for the trajectory of a particle moving in a quiescent flow (a so-called relaxing particle) is not explicitly given in Prasath et al. (2019) but can be obtained by using equation (3.56) with $\boldsymbol{f}(t) \equiv \boldsymbol{0}$ to obtain the solution formula (3.57). Using equation (2.12d) with the expression for the field (6.1), the expression for the absolute velocity yields

$$\dot{\boldsymbol{y}}(t) = \frac{2}{\pi} \int_0^\infty \frac{\boldsymbol{q}_0 k^2 \gamma e^{-k^2 t}}{(\alpha - k^2)^2 + k^2 \gamma^2} dk. \tag{6.2}$$

Integrating in time between $[t_0, t_f]$ provides the following expression for the trajectory

$$\boldsymbol{y}(t_f) = \boldsymbol{y}(t_0) + \frac{2}{\pi} \int_{t_0}^{t_f} \int_0^\infty \frac{\boldsymbol{q}_0 k^2 \gamma e^{-k^2 s}}{(\alpha - k^2)^2 + k^2 \gamma^2} dk ds. \tag{6.3}$$

Expression (6.3) can be further simplified by switching the order of integration. The following proposition proves that the order of integration can be switched by using Fubini's theorem (Theorem 3.13).

Proposition 6.1 (Switching the order of integration in equation (6.3)). *Let* $\chi_1 := [0, \infty)$, $\chi_2 := [t_0, t]$ *with* $t_0, t \in \mathbb{R}$ *and* $t_f > t_0$, *then*

$$\int_{\chi_1} \int_{\chi_2} \frac{\boldsymbol{q}_0 k^2 \gamma e^{-k^2 s}}{(\alpha - k^2)^2 + k^2 \gamma^2} dk ds = \int_{\chi_2} \int_{\chi_1} \frac{\boldsymbol{q}_0 k^2 \gamma e^{-k^2 s}}{(\alpha - k^2)^2 + k^2 \gamma^2} dk ds \tag{6.4}$$

for all $\alpha, \gamma > 0$.

Proof. Integrability of (6.4) is shown by finding a finite upper bound. Without loss of generality the maximum component of the initial relative velocity $\boldsymbol{q}_0$ is considered to be the first one i.e. $q_0^{(1)}$. The proof starts off by using the properties of the absolute value and bounding some of the terms of the integrand as follows

$$\left|\int_{t_0}^{t}\int_{0}^{\infty}\frac{q_0^{(1)}k^2\gamma e^{-k^2 s}}{(\alpha-k^2)^2+k^2\gamma^2}dkds\right| \leq \int_{t_0}^{t}\int_{0}^{\infty}\left|\frac{q_0^{(1)}k^2 e^{-k^2 s}}{(\alpha-k^2)^2+k^2\gamma^2}\right|dkds = \tag{6.5a}$$

$$= |q_0^{(1)}|\gamma\int_{t_0}^{t}\int_{0}^{\infty}\frac{k^2}{(\alpha-k^2)^2+k^2\gamma^2}\underbrace{e^{-k^2 s}}_{\leq 1}dkds \leq \tag{6.5b}$$

$$\leq |q_0^{(1)}|\gamma\int_{t_0}^{t}\int_{0}^{\infty}\frac{k^2}{(\alpha-k^2)^2+k^2\gamma^2}dkds = \tag{6.5c}$$

$$= |q_0^{(1)}|\gamma\Delta t\int_{0}^{\infty}\frac{k^2}{(\alpha-k^2)^2+k^2\gamma^2}dk. \tag{6.5d}$$

The integrand in equation (6.5d) has no singularities in the interval $[0,\infty)$ and the only point that could make the integral diverge is as $k\to+\infty$. In order to treat the point at infinity separately, the integral is split into two: one in the interval $[0,1+\sqrt{2\alpha}]$ and another one in $(1+\sqrt{2\alpha},\infty)$, as follows

$$|q_0^{(1)}|\gamma\Delta t\int_{0}^{\infty}\frac{k^2}{(\alpha-k^2)^2+k^2\gamma^2}dk = \underbrace{|q_0^{(1)}|\gamma\Delta t\int_{0}^{1+\sqrt{2\alpha}}\frac{k^2}{(\alpha-k^2)^2+k^2\gamma^2}dk}_{<+\infty} + \tag{6.6a}$$

$$+ |q_0^{(1)}|\gamma\Delta t\int_{1+\sqrt{2\alpha}}^{\infty}\frac{k^2}{(\alpha-k^2)^2+k^2\gamma^2}dk. \tag{6.6b}$$

The integral in the subdomain $[0,1+\sqrt{2\alpha}]$ converges since there are no singularities in the integration domain. For the integral in the second subdomain, the proof continues with

$$|q_0^{(1)}|\gamma\Delta t\int_{1+\sqrt{2\alpha}}^{\infty}\frac{k^2}{(\alpha-k^2)^2+k^2\gamma^2}dk \leq |q_0^{(1)}|\gamma\Delta t\int_{1+\sqrt{2\alpha}}^{\infty}\frac{k^2}{(\alpha-k^2)^2}dk = \tag{6.7a}$$

$$= |q_0^{(1)}|\gamma\Delta t\int_{1+\sqrt{2\alpha}}^{\infty}\frac{k^2}{\alpha^2+k^4-2\alpha k^2}dk \leq \tag{6.7b}$$

$$\leq |q_0^{(1)}|\gamma\Delta t\int_{1+\sqrt{2\alpha}}^{\infty}\frac{k^2}{k^4-2\alpha k^2}dk = \tag{6.7c}$$

$$= |q_0^{(1)}|\gamma\Delta t\int_{1+\sqrt{2\alpha}}^{\infty}\frac{1}{k^2-2\alpha}dk = \tag{6.7d}$$

$$= |q_0^{(1)}|\gamma\Delta t\int_{1+\sqrt{2\alpha}}^{\infty}\frac{1}{(k+\sqrt{2\alpha})(k-\sqrt{2\alpha})}dk. \tag{6.7e}$$

By applying partial fraction decomposition, the integrand can be split it into simpler fractions.

$$|q_0^{(1)}|\gamma\Delta t\int_{1+\sqrt{2\alpha}}^{\infty}\frac{1}{(k+\sqrt{2\alpha})(k-\sqrt{2\alpha})}dk = \frac{|q_0^{(1)}|\gamma\Delta t}{2\sqrt{2\alpha}}\int_{1+\sqrt{2\alpha}}^{\infty}\frac{-1}{(k+\sqrt{2\alpha})}dk + \tag{6.8a}$$

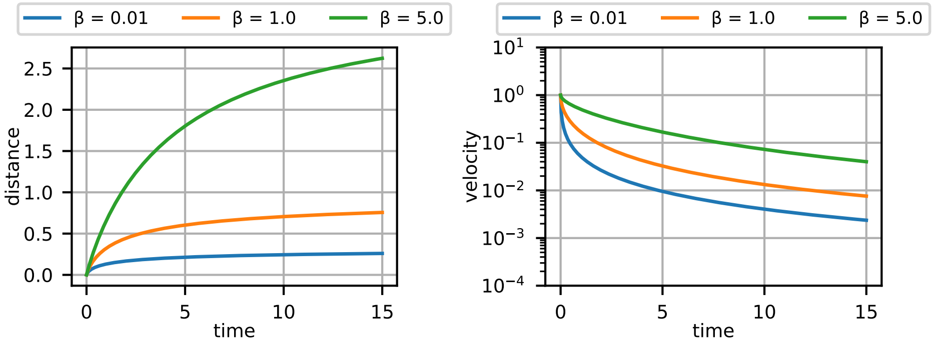

Figure 6.1: Trajectory (left) and relative velocity (right) for three particles moving in the quiescent flow for 15 s with different density ratios ($\beta = 0.01$, $\beta = 1$, $\beta = 5$) and Stokes number $S = 1$. The initial conditions are $\boldsymbol{y}_0 = (0,0)^T$ and $\boldsymbol{q}(0,t_0) = (1,0)^T$.

$$+\frac{|q_0^{(1)}|\gamma\Delta t}{2\sqrt{2\alpha}}\int_{1+\sqrt{2\alpha}}^{\infty}\frac{1}{(k-\sqrt{2\alpha})}dk = \tag{6.8b}$$

$$=\frac{|q_0^{(1)}|\gamma\Delta t}{2\sqrt{2\alpha}}\ln\left.\frac{k-\sqrt{2\alpha}}{k+\sqrt{2\alpha}}\right|_{1+\sqrt{2\alpha}}^{\infty} = \tag{6.8c}$$

$$=\frac{|q_0^{(1)}|\gamma\Delta t}{2\sqrt{2\alpha}}\ln(1+2\sqrt{2\alpha}) \leq \infty. \tag{6.8d}$$

This integral is bounded and thus the sum of both integrals is also bounded. This shows that function is integrable, Fubini's theorem 3.13 can be applied and the order of integration switched. □

Thanks to the change in the integration order, the expression for the trajectory yields

$$\boldsymbol{y}(t) = \boldsymbol{y}(t_0) + \frac{2}{\pi}\int_0^{\infty}\frac{\boldsymbol{q}_0\gamma k^2}{(\alpha-k^2)^2+k^2\gamma^2}\int_{t_0}^{t}e^{-k^2 s}ds dk, \tag{6.9}$$

so that

$$\boldsymbol{y}(t) = \boldsymbol{y}(t_0) + \frac{2}{\pi}\int_0^{\infty}\frac{\boldsymbol{q}_0\gamma}{(\alpha-k^2)^2+k^2\gamma^2}\left(e^{-k^2 t_0} - e^{-k^2 t}\right)dk. \tag{6.10}$$

Figure 6.1 shows the radial distance and absolute velocity against time of three relaxing particles that start at position $\boldsymbol{y}(t_0) = (0,0)^T$ with initial relative and absolute velocity $\boldsymbol{q}_0 = \boldsymbol{v}_0 = (1,0)$. Each particle has a different density ratio β but the same Stokes number $S = 1$. This choice of parameters is the same used in Prasath et al. (2019) for this example [53, Figure 4] and therefore the plots for the velocity coincide.

As expected, particles' velocities reduce with time until they come to a halt due to friction with the fluid. Particle velocities slow down slowlier on particles with higher density ratios, which represents mass. This agrees with Newton's second law: For a given constant force, the larger the mass, the smaller the acceleration (or deceleration).

Table 6.1 provides the experimentally-computed convergence orders for the schemes in chapter 5. The solutions correspond to trajectories of particles in the quiescent flow

Quiescent flow field with non-zero initial relative velocity and $S = 0.1$.					
Method	$R = 1/3$	$R = 7/9$	$R = 1$	$R = 4/3$	$R = 7/3$
Prasath et al. [53]	**1.7**	**2.2**	**2.5**	**2.7**	**3.9**
FD2 + Trap. or IMEX2	1.0	1.0	1.0	1.0	1.0
Daitche 3^{rd} order [20]	unstable	1.8	1.4	1.4	1.4
FD4 + IMEX4 or DIRK4	0.7	0.7	0.7	0.7	0.7

Quiescent flow field with non-zero initial relative velocity and $R = 7/9$						
Method	$S = 0.01$	$S = 0.1$	$S = 0.5$	$S = 1$	$S = 2$	$S = 4$
Prasath et al. [53]	**1.6**	**2.2**	**2.6**	**2.5**	**2.5**	**2.5**
FD2 + Trap. or IMEX2	1.0	1.0	1.0	1.0	1.0	1.0
Daitche 3^{rd} order [20]	unstable	1.8	1.2	1.2	1.2	1.3
FD4 + IMEX4 or DIRK4	0.6	0.7	0.7	0.7	0.7	0.7

Table 6.1: Experimentally-computed convergence orders for a particle moving in the quiescent flow for 1 s for different values of R and S. The initial conditions are $\boldsymbol{y}_0 = (0,0)^T$ and $\boldsymbol{q}(0,t_0) = (0.1,0)^T$ for $t \in [0,1]$.

calculated with for different values of R and S. The data from which these convergence orders were calculated are shown in figures 6.2 and 6.3. Convergence plots show the maximum l_2-norm error against the number of nodes, N.

The table shows that there is a general reduction in convergence orders with respect to their theoretical values, specially noticeable on the FD-based schemes. The second order FD methods lose half of their convergence order, i.e. one order of convergence, whereas the fourth order schemes lose over three fourths of their convergence order, i.e. over three units in the convergence order. This reduction in the convergence rates is expected for the FD-based schemes, since the initial condition of the reformulated problem is discontinuous at t_0, i.e. $\boldsymbol{q}(0,t_0) \neq \boldsymbol{0}$. FD methods are known to perform poorly with discontinuities. Daitche's 3^{rd} order scheme's convergence reduces over one and a half units with respect to their expected value and becomes unstable for the smallest values of R and S. Prasath et al.'s scheme is the best performing method in this example regarding convergence orders and its convergence improves as R and S increase. Figures 6.2 and 6.3 show that the first point is off with respect to the line joining the other ones, which means that the experimentally-computed convergence order is slightly higher than expected if only the last nodes are used for its calculation. The experimentally-computed convergence order for Prasath et al.'s and Daitche's schemes are therefore higher than the actual one. The figures show that the slope of the convergence line is similar between Daitche's and Prasath et al.'s methods and their converge order is expected to be equal to Daitche's one. Nevertheless Prasath et al.'s scheme attains the lowest maximum l_2-norm error among all methods and it is therefore the best performing one in this field, followed by Daitche's 3^{rd} order scheme. Figure 6.3 shows that errors decrease for these two methods as the value of S increases.

Figure 6.4 shows error versus runtimes for a particle in the quiescent flow with $S = 0.1$ and $R = 7/9$, initialized at $\boldsymbol{y} = (0,0)^T$ with $\boldsymbol{q}(0,t_0) = (0.1,0)^T$. Particle's trajectory

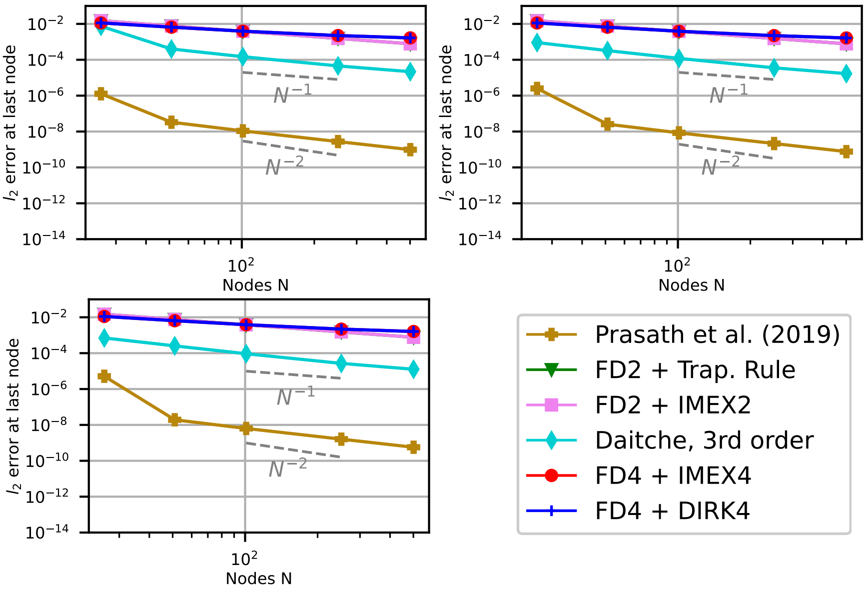

Figure 6.2: Convergence plots for a particle moving for 1 s in the quiescent flow with $S = 0.1$ and for three different values of the effective density ratio: $R = 7/9$ (top-left), $R = 1$ (top-right) and $R = 4/3$ (bottom-left). The initial conditions of the particle are $\boldsymbol{y}_0 = (0,0)^T$ and $\boldsymbol{q}(0,t_0) = (0.1,0)^T$.

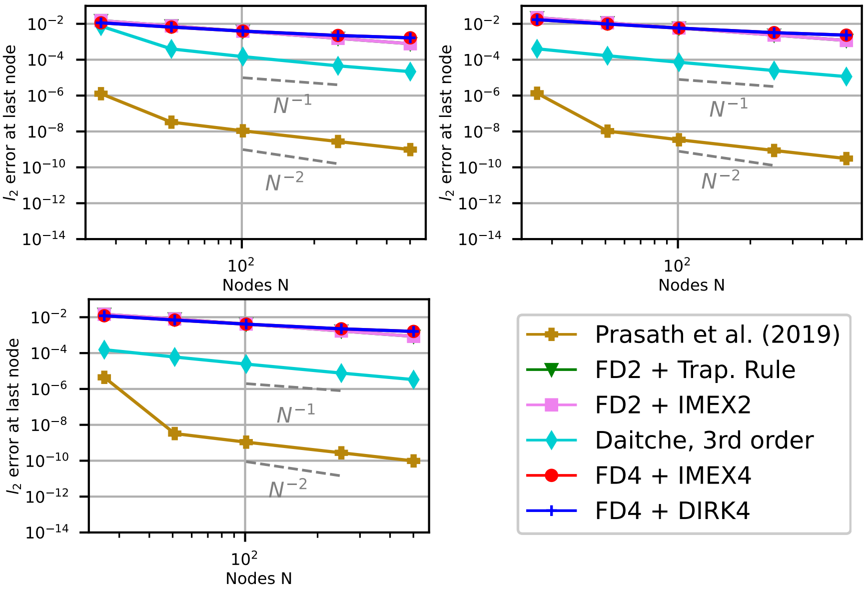

Figure 6.3: Convergence plots for a particle moving for 1 s in a quiescent flow with $R = 7/9$ and three different Stoke numbers: $S = 0.1$ (top-left), $S = 1$ (top-right) and $S = 10$ (bottom-left). The initial conditions of the particle are $\boldsymbol{y}_0 = (0,0)^T$ and $\boldsymbol{q}(0,t_0) = (0.1,0)^T$.

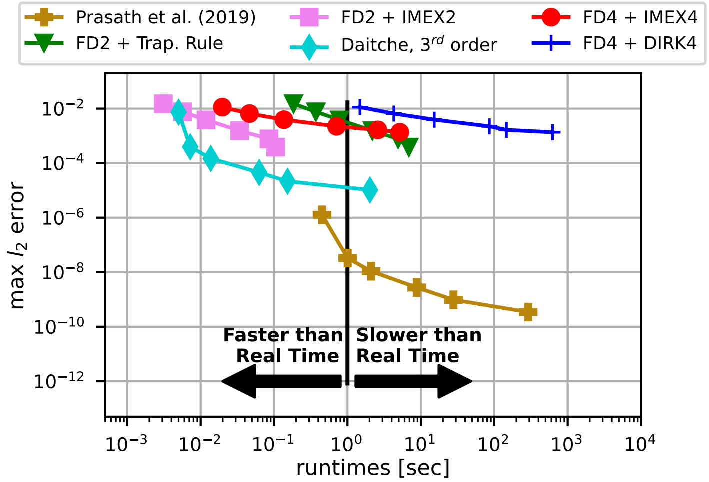

Figure 6.4: Work-precision plot for a particle moving for 1 s in a quiescent flow with $R = 7/9$ and $S = 0.1$. The initial conditions of the particle are $\boldsymbol{y}_0 = (0, 0)^T$ and $\boldsymbol{q}(0, t_0) = (0.1, 0)^T$.

is simulated for 1 s, so runtimes smaller than 1 are considered "*faster than real-time*". Daitche's 3^{rd} order method overtakes all the FD implementations, achieving low errors faster than the FD schemes, except for errors above 10^{-2}, where FD2 + IMEX2 becomes more efficient. Lowest errors ($< 10^{-6}$) are achieved by Prasath et al.'s scheme at a relatively high computational cost, remaining either very close or above real-time.

Figure 6.5 shows the l_2-norm error at the last node for different values of the parameter c for the FD methods from chapter 5. Errors reduce as c decreases for both the second and fourth order methods. Second order methods show first order linear convergence with respect to c, whereas fourth order methods present nonlinear convergence, becoming parallel to the line of the second order methods for the largest values of c. All lines cross at $c = 20$, which is the value of c used in the previous calculations. For $c < 20$ second order methods attain a smaller error, opposite to the behaviour for $c > 20$.

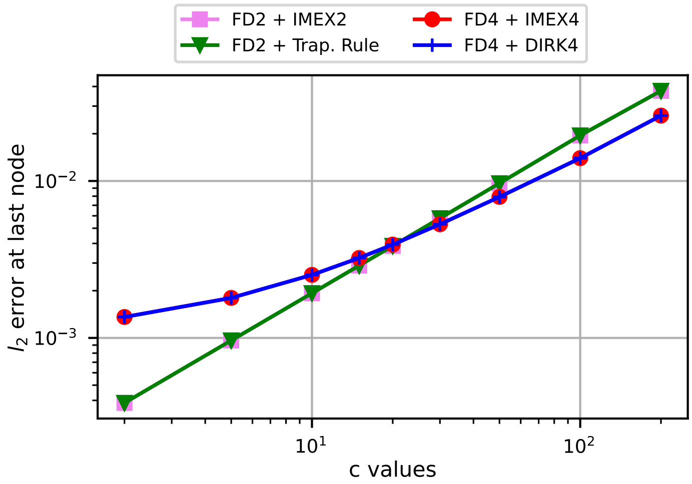

Figure 6.5: Convergence of the FD methods with respect to parameter c for a particle moving for 1 s in a quiescent flow with $R = 7/9$ and $S = 0.1$. The initial conditions of the particle are $\boldsymbol{y}_0 = (0,0)^T$ and $\boldsymbol{q}(0, t_0) = (0.1, 0)^T$.

6.1.2 A steady flow: The vortex

The second flow field with an existing analytical solution is the steady vortex presented in Candelier et al. (2004) [12]. This vortex depicts a flow field that rotates with constant angular velocity around a point called center or origin. The nondimensional expression of the flow field is given by the following formula

$$\boldsymbol{u}(\boldsymbol{y}(t), t) = T\omega \, \|\boldsymbol{y}(t)\|_2 \, \vec{\boldsymbol{e}}_\theta = T\omega \begin{bmatrix} -y^{(2)} \\ y^{(1)} \end{bmatrix}, \tag{6.11}$$

where $\omega \in \mathbb{R}$ is the angular velocity of the field given in radians per second and T is the time scale of the flow field. Note that the velocity of this vortex becomes larger with the radial distance from the center, i.e. $\boldsymbol{u} \to \infty$ as $\|\boldsymbol{y}\|_2 \to \infty$, in contrast to the vortex given in Prasath et al. (2019) [53]. Particles denser than the fluid are expelled from the center, contrary to those lighter than the fluid. This phenomenon can be observed in figure 6.6, that portraits the trajectories of three particles with different density ratios: (1) a particle lighter than the fluid that is captived into the center, (2) a neutrally buoyant one, i.e. $\beta = 1$, that rotates around the center always at constant distance and (3) a heavier particle that is ejected further away from the center.

The analytical expression for a particle moving in this vortex with zero initial relative velocity, i.e. $\boldsymbol{q}(0, t_0) = \boldsymbol{v}(t_0) - \boldsymbol{u}(\boldsymbol{y}(t_0), t_0) = (0,0)^T$, is given in Candelier et al. [12] as

$$Z(t) = \sum_{i=1}^{4} \frac{A_i}{X_i} \exp(X_i^2 t) \operatorname{erfc}(-X_i \sqrt{t}), \tag{6.12}$$

where $Z(t) := y^{(1)}(t) + i y^{(2)}(t)$ is a complex number holding both trajectory components,

$$A_i := \frac{U(t_0)(X_i^2 - C\sqrt{\pi} X_i) - BZ(t_0)}{\prod_{\substack{j=1 \\ j \neq i}}^{j=4} (X_i - X_j)}, \tag{6.13}$$

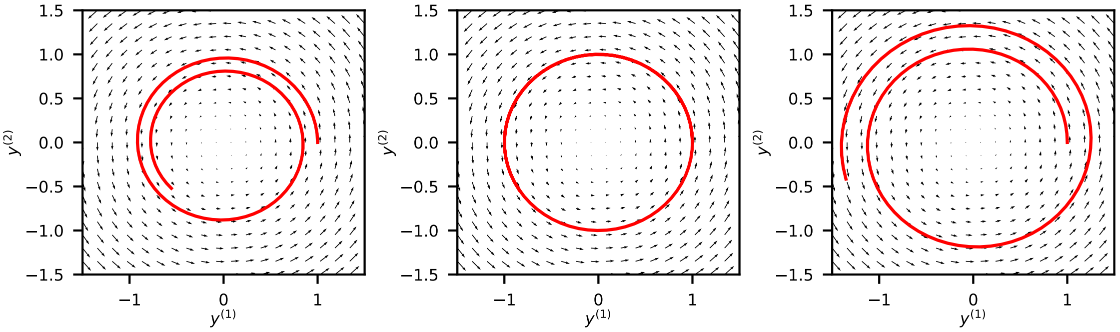

Figure 6.6: Trajectories of three particles moving in the vortex with $\omega = 1\,\mathrm{rad\,s^{-1}}$ for 10 s with different effective density ratios: $R = 7/9$ (left), $R = 1$ (center), $R = 4/3$ (right) with $S = 0.3$ and initial conditions $\boldsymbol{y}_0 = (1,0)^T$ and $\boldsymbol{q}(0,t_0) = (0,0)^T$.

$U(t) := v^{(1)}(t) + iv^{(2)}(t)$ is a complex number holding both absolute velocity components, X_i are the roots of the following fourth order polynomial

$$X^4 - C\sqrt{\pi}X^3 + AX^2 + iC\sqrt{\pi}X + B = 0, \tag{6.14}$$

whose coefficients are defined as

$$A := \frac{3}{S(2\beta+1)}, \quad B := \frac{3(S-i)}{S(2\beta+1)}, \quad C := -\frac{9}{(2\beta+1)\sqrt{\pi S}}. \tag{6.15}$$

These expressions are based on those provided in Candelier et al. (2004), although a few modifications were introduced to account for the differences in the definition of the parameters β and S and make it consistent with the definitions given in this paper.

Figure 6.6 shows the trajectories of three particles with different density ratios that move in a vortex with angular velocity, $\omega = 1\,\mathrm{rad\,s^{-1}}$. All particles have the same Stokes number, S, and start at $\boldsymbol{y}(t_0) = (1,0)^T$ with the same velocity of the fluid, i.e. $\boldsymbol{v}(t_0) = (0,1)^T$, so their relative velocity is zero, $\boldsymbol{q}(0,t_0) = (0,0)^T$. For simplicity, the timescale is chosen to be the inverse of the angular velocity, $T = 1/\omega$, and the spatial scale is chosen to be the unit, $L = 1\,\mathrm{m}$.

Table 6.2 presents the experimentally-computed convergence orders of our implementations of the schemes given in chapter 5 against the analytical solution given in equation (6.12) for different values of R and S. All implementations reach their expected convergence rates or remain very close to them. Prasath et al.'s scheme converges with order higher than two, steadily increasing as R and S increase. Machine precision is reached for the case $R = 1$, maybe due to the cancellation of the material derivative term in the forcing term $\boldsymbol{f}$. Second order FD methods reach second order independently of R and S. Daitche's 3^{rd} order approach attains superquadratic convergence, only reaching third order for $R = 1$. Daitche's convergence order increases with S, similarly to Prasath et al.'s approach. The difference between the experimentally-computed convergence with its theoretical one is most likely due to the fact that the method's coefficients are calculated in double and not quadruple precision. This was already observed in Daitche (2013) [20] and Moreno-Casas and Bombardelli (2016) [47]. Like in the quiescent flow, Daitche's scheme becomes unstable for the lowest values of the effective density ratio, R, and Stokes number,

Vortex flow field with zero initial relative velocity and $S = 0.1$					
Method	$R = 1/3$	$R = 7/9$	$R = 1$	$R = 4/3$	$R = 7/3$
Prasath et al. [53]	2.1	2.3	machine-ε	2.5	3.1
FD2 + Trap. or IMEX2	2.0	2.0	2.0	2.0	2.0
Daitche 3^{rd} order [20]	unstable	2.6	3.1	2.4	2.4
FD4 + IMEX4	**3.2**	**3.4**	**4.0**	**3.6**	**3.7**
FD4 + DIRK4	**3.2**	**3.4**	3.4	**3.6**	**3.7**

Vortex flow field with zero initial relative velocity and $R = 4/3$						
Method	$S = 0.01$	$S = 0.1$	$S = 0.5$	$S = 1$	$S = 2$	$S = 4$
Prasath et al. [53]	2.0	2.3	2.4	2.4	2.4	2.5
FD2 + Trap. or IMEX2	2.0	2.0	2.0	2.0	2.0	2.0
Daitche 3^{rd} order [20]	unstable	2.6	2.3	2.3	2.4	2.5
FD4 + IMEX4 or DIRK 4	**2.9**	**3.4**	**3.7**	**3.8**	**3.8**	**3.9**

Table 6.2: Experimentally-computed convergence orders for a particle moving for 1 s in the steady vortex given by equation (6.11) with $\omega = 1$, for different values of R and S. The initial conditions are $\boldsymbol{y} = (0, 1)^T$ and $\boldsymbol{q}(0, t_0) = (0, 0)^T$.

S. Fourth order FD methods converge with orders between 3 and 4, slightly lower than what is theoretically expected, except for $R = 1$, case in which order four is reached for the FD4 + IMEX4 method.

Figure 6.7 shows the convergence plots of the schemes for this velocity flow field for different values of R. The top right plot corresponds to the convergence plot for the special case $R = 1$, where all methods achieve their expected convergence orders.

Figure 6.8 shows the maximum l_2 error versus runtimes for a particle moving in the vortex for 1 s with $S = 0.1$ and $R = 7/9$, initialized at $\boldsymbol{y} = (1, 0)^T$ with $\boldsymbol{q}(0, t_0) = (0, 0)^T$. In this case, Daitche and the IMEX's methods are the best performing methods. Daitche's scheme provides the best runtimes for errors between 10^{-4} and 10^{-8}, whereas the second order IMEX performs better for errors higher than 10^{-4} and fourth order IMEX for errors lower than 10^{-8}.

Figure 6.9 shows the maximum l_2-norm error for different values of the parameter c for the FD methods from chapter 5 applied to the steady vortex. Second order FD methods show a higher error than the fourth order ones for all the values of c. They present second order convergence with respect to c until they reach 10^{-5} for $c = 10$ and remain constant for smaller values of c. On the other hand, fourth order methods show third order convergence with respect to c until they achieve 10^{-8} for the smallest values of c, i.e. $c = 2$ an $c = 5$. Decreasing the value of c, from 20 to 10 or lower, will therefore translate in a decrease of the error of the FD methods, specially for the fourth order one.

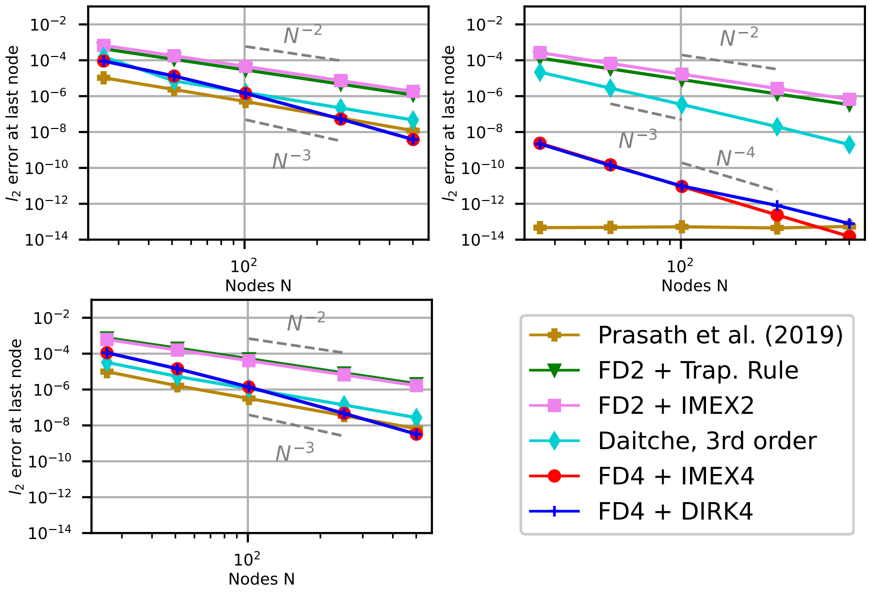

Figure 6.7: Convergence plots for a particle moving for 1 second in the vortex given by equation (6.11) with $\omega = 1\,\mathrm{rad\,s^{-1}}$, $S = 0.1$ and three different values of the effective density ratio: $R = 7/9$ (top-left), $R = 1$ (top-right) and $R = 4/3$ (bottom-left). The initial conditions of the particle are $\boldsymbol{y}_0 = (1,0)^T$ and $\boldsymbol{q}(0,t_0) = (0,0)^T$.

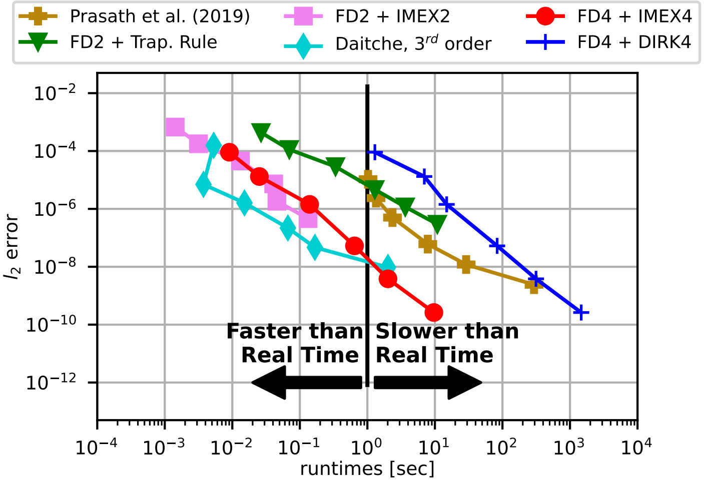

Figure 6.8: Work-precision plot for a particle moving for 1 s in the vortex given by equation (6.11) with $\omega = 1\,\mathrm{rad\,s^{-1}}$, $R = 7/9$ and $S = 0.1$. The initial conditions of the particle are $\boldsymbol{y}_0 = (0,0)^T$ and $\boldsymbol{q}(0,t_0) = (0,0)^T$.

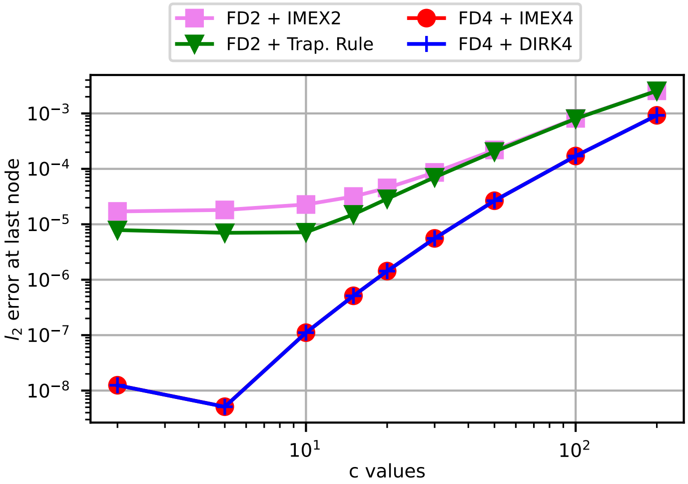

Figure 6.9: Convergence of the FD methods with respect to the parameter c for a particle moving for 1 s in the steady vortex given by equation (6.11) with $\omega = 1\,\mathrm{rad\,s^{-1}}$, $R = 7/9$ and $S = 0.1$. The initial conditions of the particle are $\boldsymbol{y}_0 = (1, 0)^T$ and $\boldsymbol{q}(0, t_0) = (0, 0)^T$.

6.1.3 A spatially homogeneous case: The oscillatory background

The last flow field with an analytical solution considered here is the oscillatory background described in Prasath et al. (2019) [53, Example 3]. This is a spatially-homogeneous but time-dependent (unsteady) field whose velocity is given by a sinusoidal function. The expression

$$\boldsymbol{u}(\boldsymbol{y}(t), t) = \begin{bmatrix} 1 \\ \sin(t) \end{bmatrix}, \tag{6.16}$$

corresponds to the nondimensional velocity field of the oscillatory background.

Note that the sinusoidal function is only present on the second (or vertical) component, whereas the first (or horizontal) component is given by a constant parameter. This configuration was chosen for representation purposes in figure 6.10, since the oscillatory behaviour is better noted if horizontal movement is included. All errors are therefore calculated with respect to the second component.

The analytical expression for the nondimensional a particle moving in this flow field is given by

$$y^{(1)}(t) = y_0^{(1)} + t + 2\frac{v_0^{(1)}}{\pi} \int_0^\infty \frac{\gamma(1 - e^{-k^2 t})}{(\alpha - k^2)^2 + (k\gamma)^2} dk, \tag{6.17a}$$

$$\begin{aligned} y^{(2)}(t) = y_0^{(2)} &+ (1 - \cos(t)) + 2\frac{v_0^{(2)}}{\pi} \int_0^\infty \frac{\gamma(1 - e^{-k^2 t})}{k^2\gamma^2 + (k^2 - \alpha)^2}\, dk + \\ &+ \frac{2}{\pi}\frac{(1-R)}{R} \int_0^\infty \frac{k^2 \gamma e^{-k^2 t}}{(k^2\gamma^2 + (k^2 - \alpha)^2)(k^4 + 1)} dk + \\ &+ \frac{2}{\pi}\frac{(1-R)}{R} \int_0^\infty \frac{k^4 \gamma \sin(t)}{(k^2\gamma^2 + (k^2 - \alpha)^2)(k^4 + 1)} dk + \\ &- \frac{2}{\pi}\frac{(1-R)}{R} \int_0^\infty \frac{k^2 \gamma \cos(t)}{(k^2\gamma^2 + (k^2 - \alpha)^2)(k^4 + 1)} dk. \end{aligned} \tag{6.17b}$$

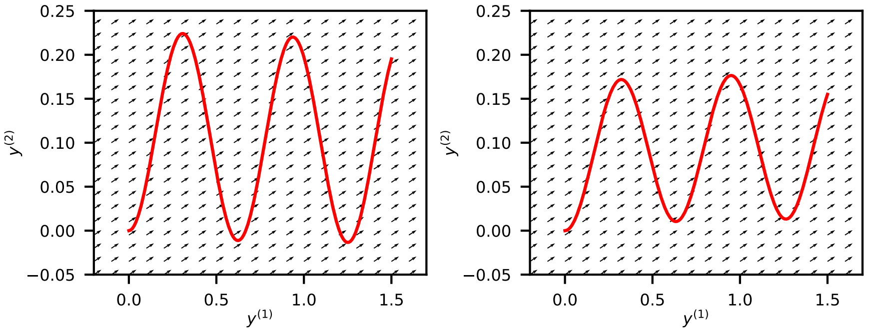

Figure 6.10: Trajectory of two particles moving for 3 s in the oscillatory background (6.16) with $S = 10$ and two different values of the effective density ratio: $R = 7/9$ (left) and $R = 4/3$ (right). The initial conditions of the particle are $\boldsymbol{y}_0 = (0,0)^T$ and $\boldsymbol{q}(0,t_0) = (0,0)^T$.

where the first component (6.17a) corresponds to the solution of a particle relaxing in a field with constant velocity and the second component (6.17b) corresponds to the solution of a particle moving in a purely oscillatory field. This solution was not provided in Prasath et al. (2019), but calculated using equation (6.16) on the formula for $\boldsymbol{f}$ (equation (2.12)), obtaining

$$\boldsymbol{f}(\boldsymbol{q}(0,t),\boldsymbol{y}(t),t) = \left(\frac{1}{R}-1\right)\frac{D}{Dt}\begin{bmatrix}1\\ \sin(t)\end{bmatrix} - \boldsymbol{q}(0,t)\cdot\cancelto{\mathbf{0}}{\nabla_y\begin{bmatrix}1\\ \sin(t)\end{bmatrix}} \tag{6.18a}$$

$$= \left(\frac{1}{R}-1\right)\left(\partial_t\begin{bmatrix}1\\ \sin(t)\end{bmatrix} + \boldsymbol{u}\cdot\cancelto{\mathbf{0}}{\nabla_y\begin{bmatrix}1\\ \sin(t)\end{bmatrix}}\right) \tag{6.18b}$$

$$= \left(\frac{1}{R}-1\right)\begin{bmatrix}0\\ \cos(t)\end{bmatrix}, \tag{6.18c}$$

where all the spatial derivatives disappear because the field is constant in space. Analytical solution (3.62) is obtained by plugging this result into equation (3.56) and integrating.

Figure 6.10 shows the trajectory of two particles with different density ratios, β, moving in the oscillatory flow field described in equation 6.16.

Table 6.3 presents the experimentally-computed convergence orders of a particle moving in the oscillatory background with zero initial relative velocity for different values of R and S. The 4^{th} order FD methods are the best performing schemes in all cases. Daitche's scheme is unstable in many of the cases considered, but presents good convergence in those cases in which there are no instabilities, except for the special case $R = 1$ in which Prasath et al.'s method achieves machine precision. Note that the "*unstable*" mark on the table indicates that Daitche's method was unstable for at least one of the meshes considered, so that one could still obtain a stable solution using Daitche's method by just using the right mesh. The convergence of Prasath et al.'s scheme ranges from 1.4 to 1.9, increasing as R and S increase. Second order FD methods behave slightly worse than expected, reaching an order of 1.5 for all the pairs of parameters considered.

Table 6.4 shows the empirically-computed convergence orders for a particle moving in the oscillatory background with nonzero initial relative velocity for several values of R and S. Prasath et al.'s method is the best performing method, obtaining convergence orders

Oscillatory field with zero initial relative velocity and $S = 0.1$					
Method	$R = 1/3$	$R = 7/9$	$R = 1$	$R = 4/3$	$R = 7/3$
Prasath et al. [53]	1.4	1.6	machine-ε	1.8	1.9
FD2 + Trap. or IMEX2	1.5	1.5	1.5	1.5	1.5
Daitche 3^{rd} order [20]	unstable	unstable	2.5	unstable	unstable
FD4 + IMEX4 or DIRK4	**2.3**	**2.8**	**3.5**	**3.0**	**3.2**

Oscillatory field with zero initial relative velocity and $R = 7/9$						
Method	$S = 0.01$	$S = 0.1$	$S = 0.5$	$S = 1$	$S = 2$	$S = 4$
Prasath et al. [53]	1.2	1.6	1.8	1.9	1.9	1.9
FD2 + Trap. or IMEX2	1.5	1.5	1.5	1.5	1.5	1.5
Daitche 3^{rd} order [20]	unstable	unstable	2.2	2.2	2.3	2.3
FD4 + IMEX4 or DIRK4	**1.6**	**2.8**	**3.2**	**3.3**	**3.4**	**3.4**

Table 6.3: Experimentally-computed convergence orders for particles moving for 1 s in the oscillatory background given by equation (6.16), with different values of R and S. The initial conditions are $\boldsymbol{y} = (0,0)^T$ and $\boldsymbol{q}(0,t_0) = (0,0)^T$.

between 1.2 and 1.9. Daitche's scheme is the second best performing method for those cases in which there are no instabilities. However, instabilities are present in many of the cases. Daitche's method achieves superquadratic order for the highest R considered, whereas it barely reaches linear convergence in all the other cases. Second order FD methods achieve half order, whereas fourth order methods have a constant error of about 10^{-1}.

The work-precision plots for a particle with zero as well as nonzero initial relative velocity in the oscillatory background are provided in figure 6.11. With zero initial relative velocity, IMEX methods are the optimal ones, with errors expanding between 10^{-2} and 10^{-8}, always faster than realtime. Daitche's approach performs fairly well when instabilities do not appear, which in this case that is half of the grids considered. Fourth order DIRK method performs fairly well regarding errors, but stays slower than realtime in five out of the six meshes considered. FD2 + Trap. Rule performs fairly well, with a similar score as Prasath et al.'s method, and with errors of the same magnitude as the second order IMEX. Prasath et al.'s performs quite slow, but reaches an error between 10^{-3} and 10^{-6}.

The nonzero initial relative velocity has a remarkable influence in the errors of all methods, except for Prasath et al.'s method, which remains exactly the same. All other methods present a considerable increase in their errors. This is a good indicator that the discontinuity in the initial condition is a big error driver in the FD and Daitche's methods. In this situation, it is not so easy to point out which method is the best, since the second order IMEX provides faster than realtime solutions but at relatively high errors, i.e. between 10^{-1} and 10^{-2} and Prasath et al.'s solutions are accurate (errors are between 10^{-3} and 10^{-6}) but very slow. Daitche's approach again shows instabilities for half of the meshes considered. The remaining FD methods perform worse both with respect to accuracy and runtimes.

Figure 6.12 shows convergence with respect to the parameter c. For zero initial relative

Oscillatory field with non-zero initial relative velocity and $S = 0.1$					
Method	$R = 1/3$	$R = 7/9$	$R = 1$	$R = 4/3$	$R = 7/3$
Prasath et al. [53]	**1.4**	**1.6**	**1.1**	**1.8**	**1.9**
FD2 + Trap.	0.4	0.4	0.4	0.4	0.4
FD2 + IMEX2	0.5	0.5	0.5	0.5	0.5
Daitche 3^{rd} order [20]	unstable	unstable	unstable	unstable	2.2
FD4 + IMEX4 or DIRK 4	0.0	0.0	0.0	0.0	0.0

Oscillatory field with non-zero initial relative velocity and $R = 7/9$						
Method	$S = 0.01$	$S = 0.1$	$S = 0.5$	$S = 1$	$S = 2$	$S = 4$
Prasath et al. [53]	**1.2**	**1.6**	**1.8**	**1.9**	**1.9**	**1.9**
FD2 + Trap.	0.3	0.4	0.5	0.5	0.5	0.5
FD2 + IMEX2	0.6	0.5	0.5	0.5	0.5	0.5
Daitche 3^{rd} order [20]	unstable	unstable	0.9	0.7	0.7	0.8
FD4 + IMEX4 or DIRK 4	0.0	0.0	0.0	0.0	0.0	0.0

Table 6.4: Experimentally-computed convergence orders for particles moving for 1 s in the oscillatory background given by equation (6.16). The initial conditions are $\boldsymbol{y} = (0,0)^T$ and $\boldsymbol{q}(0,t_0) = (0,0.1)^T$.

velocity, second and fourth order FD methods behave differently. Second order methods always have a higher error and even though it decreases as c decreases, the minimum error is found around $2 \cdot 10^{-3}$ for $c < 50$. The error for the fourth order methods decreases with c until $c = 15$ and an error of approximately $5 \cdot 10^{-7}$. After that, errors grow until 10^{-4} with $c = 2$. Nonzero initial relative velocity solutions show faster convergence for the second order methods. Fourth order methods do not only have a smaller convergence, but they seem to reach a plateau for the smallest values of c. A decrease of the value of c used, from $c = 20$ to a lower c, would have had almost no influence in the solutions with zero initial relative velocity, whereas the solutions with non-zero initial relative velocity would have achieved a smaller error.

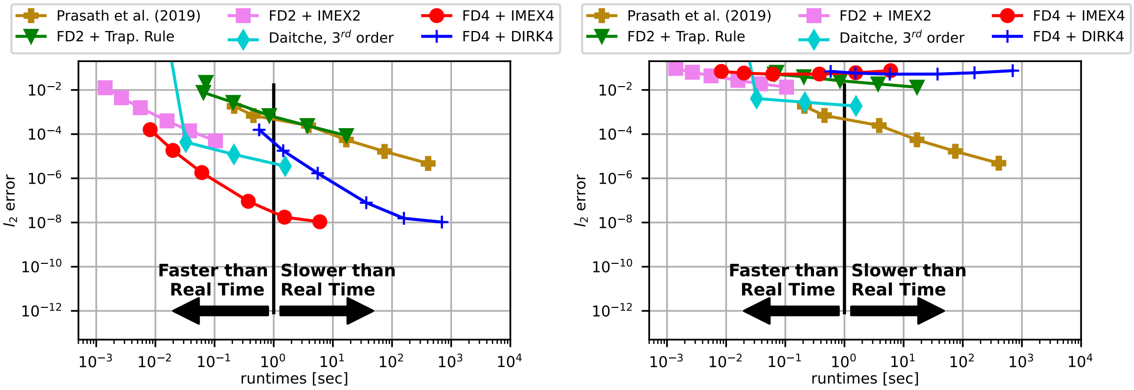

Figure 6.11: Work-precision plots for a particle moving for 1 s in the oscillatory background described in equation (6.16), with $R = 7/9$ and $S = 0.1$. The initial conditions of the particle are $\boldsymbol{y}_0 = (0,0)^T$ and $\boldsymbol{q}(0,t_0) = (0,0)^T$ (left) and $\boldsymbol{q}(0,t_0) = (0,0.1)^T$ (right).

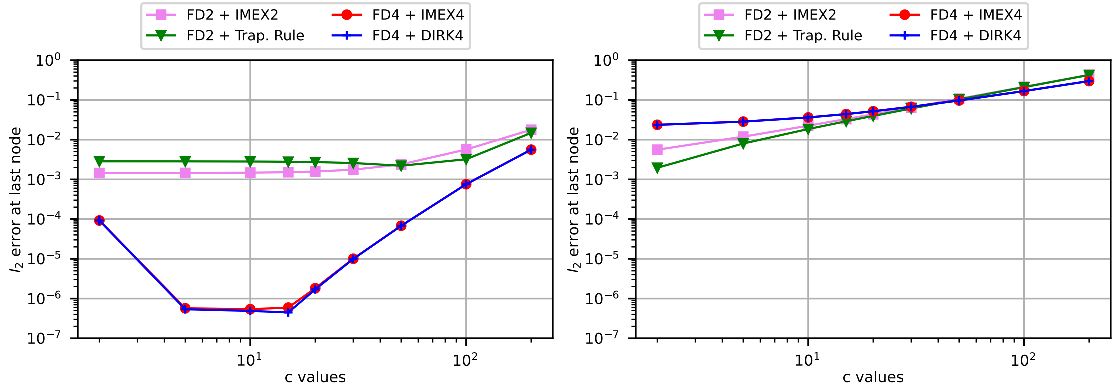

Figure 6.12: Convergence with respect to the parameter c of the finite difference methods for a particle moving for 1 s in the oscillatory background, with $R = 7/9$ and $S = 0.1$. The initial conditions of the particles are $\boldsymbol{y}_0 = (0,0)^T$ and $\boldsymbol{q}(0,t_0) = (0,0)^T$ (left) and $\boldsymbol{q}(0,t_0) = (0,0.1)^T$ (right).

6.2 Numerical efficiency for spatially inhomogeneous and unsteady flow fields

This section investigates the behaviour of the numerical implementations described in chapter 5 on complex fields that change both in time (unsteady) and space (spatially inhomogeneous). The first complex field described here is the double gyre, which is a typical toy example used in the study of mixing patterns in a fluid [62]. The second flow field is the Bickley jet proposed in Rypina et al. (2007) [57], which represents an idealised model of the stratospheric flow [51].

The third field is an experimentally-measured flow called the Faraday flow. The velocity data was recorded in the course of the master thesis of J. Tenhaus under the supervision of A.v.Kameke. This field was obtained by shaking a cylindrical container of 290 mm diameter filled with 2 mm of distilled water at a frequency of 50 Hz at a measured forcing acceleration of $a = 1.6g$, which corresponds to a supercriticality of $\varepsilon = 0.04$ [14]. This creates Faraday waves, which appear as quasi-standing waves on the surface of the fluid. The flow field is then recorded by using Particle Image Velocimetry (PIV) with floating white, hollow, glass microspheres of diameter 70 µm and density $0.15\,\mathrm{g\,cm^{-1}}$ as flow tracers to visualise horizontal motion. Particle positions were recorded with a high-speed camera triggered at 400 Hz, obtaining a dataset of 115×86 gridpoints over an area of 70.395 mm by 52.487 mm. 1056 snapshots were generated over 42.24 s. More detailed explanations of the experiment are given in Colombi et al. (2021) [14] and (2022) [15].

To our knowledge, there exist no analytical solutions for the trajectories of a particle moving in any of the two analytically-given flow fields (the double gyre and Bickley jet). Obviously, there is no reference solution for a particle trajectory on the experimentally-obtained flow field. For this reason, an accurate-enough numerical solution calculated with Prasath et al.'s method and $1,000$ time nodes, is used as a reference for the calculation of the errors. Even though Prasath et al.'s scheme is slow, it showed constant low errors for all the simple fields from section 6.1 and good stability, therefore providing a good reference solution. This will also ensure that all methods converge to the same solution.

6.2.1 The Double Gyre

The velocity field of the double gyre is taken from Shadden et al. (2005) [62, Example 1]. This flow field is described by the streamfunction

$$\varphi(\boldsymbol{y}, t) = A \sin(\pi f(y^{(1)}, t)) \sin(\pi y^{(2)}) \tag{6.19}$$

where

$$\begin{aligned} f(y^{(1)}, t) &= a(t)(y^{(1)})^2 + b(t) y^{(1)}, &(6.20)\\ a(t) &= \varepsilon \sin(\omega t), &(6.21)\\ b(t) &= 1 - 2\varepsilon \sin(\omega t), &(6.22) \end{aligned}$$

with constants $A = 0.1$, $\varepsilon = 0.25$ and $\omega = \frac{2\pi}{T} = \frac{2\pi}{10}$, where T is the timescale. The lengthscale of the flow field is considered to be unity. The values of the constants are taken from the tutorial given by Shadden and available online [61, Movie 11]. The spatial domain presented here is restricted to $[0, 2] \times [0, 1]$ although particles can move beyond it since the field is defined for all $\boldsymbol{y} \in \mathbb{R}^2$.

The velocity field is obtained using Hamilton's equations [82], i.e. derivating the streamfunction (6.19), as follows

$$u^{(1)}(\boldsymbol{y}, t) = -\frac{\partial \psi}{\partial y^{(2)}} \qquad u^{(2)}(\boldsymbol{y}, t) = \frac{\partial \psi}{\partial y^{(1)}} \tag{6.23}$$

obtaining

$$u^{(1)}(\boldsymbol{y}, t) = -A\pi \cos(\pi y^{(2)}) \sin(\pi y^{(1)}((y^{(1)} - 2)\varepsilon \sin(t\omega) + 1)) \tag{6.24}$$

for the horizontal component and

$$u^{(2)}(\boldsymbol{y}, t) = A \sin(\pi y^{(2)})(2\pi(y^{(1)} - 1)\varepsilon \sin(t\omega) + \pi) \cos(\pi y^{(1)}((y^{(1)} - 2)\varepsilon \sin(t\omega) + 1)) \tag{6.25}$$

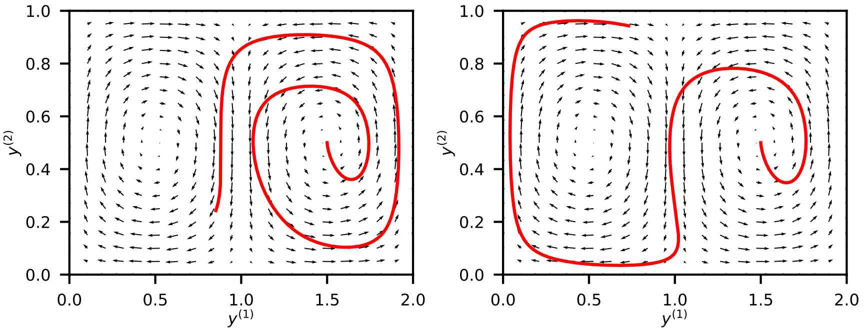

Figure 6.13: Trajectories of two particles moving for 200 s in the double gyre, calculated with FD4 + IMEX4 and a timestep of 0.01. The particles' Stokes number is $S = 1/3$ and the effective density ratios are $R = 7/9$ (left) and $R = 4/3$ (right). The initial position and velocity is common for both particles: $\boldsymbol{y}(t_0) = (1.5, 0.5)$ and $\boldsymbol{q}(0, t_0) = \boldsymbol{0}$.

for the vertical one.

Figure 6.13 shows the trajectory of two particles with different density ratios. As it can be observed, a small change in one parameter introduces a drastic change in the trajectory.

Table 6.5 shows the computed convergence orders for a particle moving in the double gyre with zero initial velocity. The fourth order methods are the best performing methods for all the values of R and S considered. For $R = 1$, all methods achieve their expected convergence, except the fourth order methods that achieve machine precision (10^{-15}). Although this phenomenon is due to the fact that the reference solution's error is achieved. Prasath et al.'s as well as Daitche's third order method behave fairly similar, obtaining convergence orders between 2.3 and 4.8. However, Daitche's method reaches bigger values for $S \geq 0.5$. Interestingly, no instabilities show up for the smallest values of the parameters in contrast to the previous examples seen. Second order methods perform fairly well, reaching convergence orders greater than 1.7.

Table 6.6 shows the experimentally-computed convergence orders for a particle moving in the double gyre with nonzero initial velocity, i.e. $\boldsymbol{q}(0, t_0) \neq \boldsymbol{0}$. Prasath et al.'s method is the best performing method in all the ranges of R and S, obtaining a supercubic convergence rate in all cases, reaching a maximum of 6.5 for the largest R. Convergence increases along with R and S. The second best performing method is Daitche's method, reaching superlinear convergence in all cases. This is however closely followed by the FD methods that almost reach first order convergence for all cases.

Figure 6.14 presents the work-precision plots for a particle with zero (left) and nonzero (right) relative initial velocity moving in the double gyre. For the case of zero initial relative velocity, Daitche's approach is the best performing method, obtaining the lowest error at the fastest runtimes, always faster than realtime. It is not so easy to tell which one is the second best performing method, since it depends on whether the error or the runtimes must be minimised. Second order IMEX method reaches fairly low errors (between 10^{-5} and 10^{-8}), always faster than realtime. Fourth order IMEX reaches lower marks in the error (between 10^{-5} and 10^{-10}) but at a cost of larger runtimes, sometimes greater than realtime. Prasath et al.'s approach obtains similar errors as Daitche's approach, but its runtimes are always greater than realtime (between 1 and 10^2 seconds). Implicit methods are ranked as the worst ones, due to their long runtimes, compared to their IMEX counterparts. However,

Double Gyre with zero initial relative velocity and $S = 0.1$					
Method	$R = 1/3$	$R = 7/9$	$R = 1$	$R = 4/3$	$R = 7/3$
Prasath et al. [53]	2.4	2.6	machine-ε	3.7	4.8
FD2 + Trap. / IMEX2	1.7	1.7	2.0	1.8	1.8
Daitche 3^{rd} order [20]	2.3	2.6	3.1	2.8	2.9
FD4 + IMEX4 or DIRK4	**3.4**	**3.4**	machine-ε	**3.3**	**3.3**

Double Gyre with zero initial relative velocity and $R = 7/9$						
Method	$S = 0.01$	$S = 0.1$	$S = 0.5$	$S = 1$	$S = 2$	$S = 4$
Prasath et al. [53]	2.4	2.6	2.5	2.5	2.4	2.8
FD2 + Trap. / IMEX2	1.8	1.7	1.7	1.8	1.8	1.8
Daitche 3^{rd} order [20]	2.5	2.6	2.8	2.9	3.0	3.1
FD4 + IMEX4 / DIRK4	**3.6**	**3.4**	**3.3**	**3.3**	**3.3**	**3.3**

Table 6.5: Experimentally computed convergence orders for particles moving for 1 s in the double gyre for different values of S and R. The initial conditions are $\boldsymbol{y} = (1, 0.5)^T$ and $\boldsymbol{q}(0, t_0) = (0, 0)^T$.

trapezoidal rule has similar errors as the second order IMEX method and is in almost all the cases, faster than real time. For the nonzero initial relative velocity, a general increase in the errors occurs. In this case there is no clear winner and a compromise between errors and runtimes must be met. Daitche's approach achieves relatively low errors (between 10^{-5} and 10^{-7}) at runtimes always faster than realtime. Prasath et al.'s approach reaches the smallest errors (between 10^{-5} and 10^{-11}) with a cost on runtimes, mostly greater than realtime (between 0.5 and 10^{-11} seconds). FD methods achieve very similar errors among themselves, always between 10^{-3} and 10^{-4}, but runtimes are only always faster than realtime for the second order IMEX method. Fourth order IMEX method and the trapezoidal rule have similar runtimes, faster than realtime for all the meshes considered, except for the largest one with 501 nodes.

Figure 6.15 shows convergence of the FD methods with respect to the parameter c for a particle moving in the double gyre with zero and nonzero initial relative velocity. Like seen in the oscillatory background, errors are smaller in the case of zero initial relative velocities. In the case with zero initial relative velocity, fourth order methods achieve smaller errors than the fourth order ones for almost all values of c. Although errors generally decrease as c decreases, a minimum is found at around 10^{-9}. In the case with nonzero initial relative velocity, the errors are very similar for all methods and values of c. Again, errors decrease with c and are kept between 10^{-3} and 10^{-5}. In this example, a decrease in the value of c from 20 to 5 or lower would decease the errors for all the methods, except for the trapezoidal rule if was smaller than 5.

Double Gyre with non-zero initial relative velocity and $S = 0.1$					
Method	$R = 1/3$	$R = 7/9$	$R = 1$	$R = 4/3$	$R = 7/3$
Prasath et al. [53]	**3.1**	**4.0**	**4.1**	**4.9**	**6.5**
FD2 + Trap. / IMEX2	0.9	0.9	0.9	0.9	0.8
Daitche 3^{rd} order [20]	1.1	1.2	1.2	1.2	1.3
FD4 + IMEX4 / DIRK4	0.8	0.8	0.8	0.8	0.8

Double Gyre with non-zero initial relative velocity and $R = 7/9$						
Method	$S = 0.01$	$S = 0.1$	$S = 0.5$	$S = 1$	$S = 2$	$S = 4$
Prasath et al. [53]	**3.3**	**4.0**	**4.0**	**4.0**	**4.0**	**4.1**
FD2 + Trap. / IMEX2	1.0	0.9	0.8	0.8	0.8	0.8
Daitche 3^{rd} order [20]	1.8	1.2	1.3	1.3	1.3	1.4
FD4 + IMEX4 / DIRK4	0.8	0.8	0.8	0.8	0.7	0.7

Table 6.6: Experimentally-computed convergence orders for particles moving for 1 s in the double gyre with different values of S and R. The initial conditions are $\boldsymbol{y} = (1, 0.5)^T$ and $\boldsymbol{q}(0, t_0) = (0, -0.0314159265)^T$.

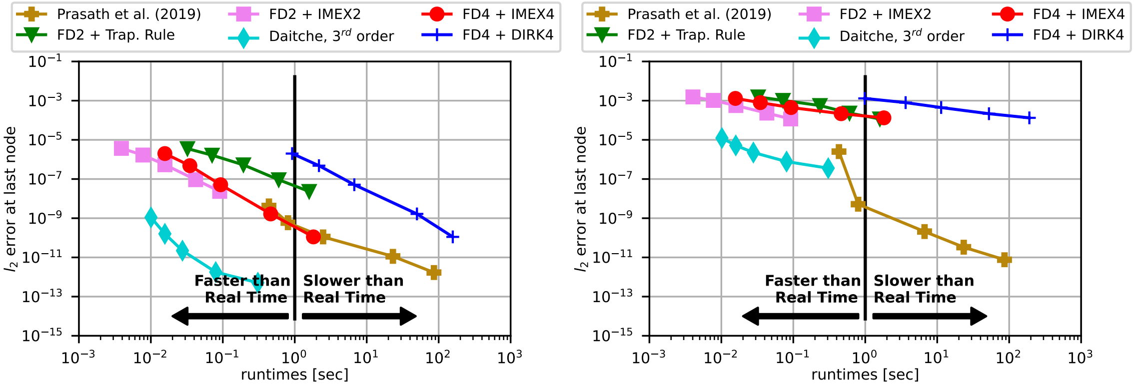

Figure 6.14: Work-precision plots for a particle moving for 1 s in the double gyre with $R = 7/9$ and $S = 0.1$. The initial conditions of the particle are $\boldsymbol{y}_0 = (1, 0.5)^T$ and $\boldsymbol{q}(0, t_0) = (0, 0)^T$ (left) and $\boldsymbol{q}(0, t_0) = (0, 0.0314159265)^T$ (right)

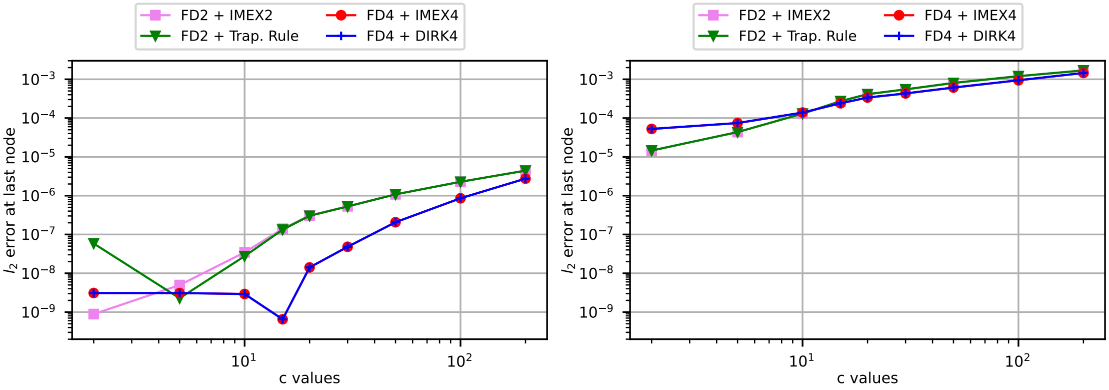

Figure 6.15: Convergence of the finite difference methods with respect to the parameter c for a particle moving for 1 s in the double gyre with $R = 7/9$ and $S = 0.1$. The initial conditions of the particle are $\boldsymbol{y}_0 = (1, 0.5)^T$ and $\boldsymbol{q}(0, t_0) = (0, 0)^T$ (left) and $\boldsymbol{q}(0, t_0) = (0, 0.0314159265)^T$ (right)

6.2.2 The Bickley Jet

The Bickley jet was proposed in Rypina et al. (2007) [57] as an idealized model of stratospheric flow. This flow field is defined by the following streamfunction,

$$\Psi(\boldsymbol{y},t) = -U_0 L \tanh\left({}^{y^{(2)}}\!/\!{}_{L}\right) + \sum_{i=1}^{3} A_i U_0 L \operatorname{sech}^2\left({}^{y^{(2)}}\!/\!{}_{L}\right) \cos\Big(k_i y^{(1)} - \sigma_i, t\Big) \tag{6.26}$$

where U_0 and L are the velocity and lengthscales of the flow. The parameter values are taken from Padberg-Gehle and Schneide (2017) [51], who used the parameter values from Hadjighasem et al. (2016) [32].

The velocity field is obtained in the same way as in the double gyre, i.e. using Hamilton's equations. The horizontal component of the flow velocity is therefore given by

$$u^{(1)}(\boldsymbol{y},t) = U_0\left(1 - \tanh^2\left({}^{y^{(2)}}\!/\!{}_{L}\right)\right) + \tag{6.27a}$$

$$+\, 2\, U_0 \operatorname{sech}^2\left({}^{y^{(2)}}\!/\!{}_{L}\right) \tanh\left({}^{y^{(2)}}\!/\!{}_{L}\right) \sum_{i=1}^{3} A_i \cos\Big(k_i y^{(1)} - \sigma_i t\Big) \tag{6.27b}$$

and the vertical component by

$$u^{(2)}(\boldsymbol{y},t) = -U_0 L \operatorname{sech}^2\left({}^{y^{(2)}}\!/\!{}_{L}\right) \sum_{i=1}^{3} A_i k_i \sin\Big(k_i y^{(1)} - \sigma_i t\Big)\,. \tag{6.28}$$

Plots in figure 6.16 show the trajectory of two particles with different effective density ratios moving in the Bickley jet. Note that the background shown in the plots corresponds to the field evaluated at final time, i.e. $\boldsymbol{u}_f := \boldsymbol{u}(\boldsymbol{y}(t_f), t_f)$ with $t_f = 10\,\mathrm{d}$.

Table 6.7 shows the empirically-obtained convergence orders for a particle in the Bickley jet with zero initial relative velocity. Like in previous cases with zero initial relative velocity, fourth order methods achieve the highest convergence orders in almost all cases, except for the smallest values of R and S considered, followed by Daitche's. Daitche's method reaches cubic or supercubic convergence and presents instabilities for many parameter sets. Instabilities are more predominant for the smallest values of the parameters,

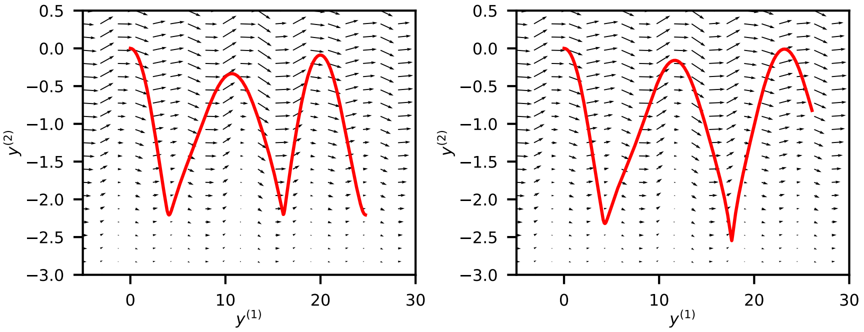

Figure 6.16: Trajectory of particles with Stokes number $S = 0.3$ and effective density ratio $R = {}^{7}\!/\!{}_{9}$ (left) and $R = {}^{4}\!/\!{}_{3}$ (right) moving for 10 d in the Bickley jet. The initial conditions are $\boldsymbol{y}(t_0) = (0,0)^T$ and $\boldsymbol{q}(0,t_0) = (0,0)^T$.

Bickley jet with zero initial relative velocity and $S = 0.1$					
Method	$R = 1/3$	$R = 7/9$	$R = 1$	$R = 4/3$	$R = 7/3$
Prasath et al. [53]	**2.0**	2.2	machine-ε	2.3	2.5
FD2 + Trap. / IMEX2	1.9	2.0	2.0	2.0	2.0
Daitche 3^{rd} order [20]	unstable	unstable	3.0	unstable	2.9
FD4 + IMEX4 / DIRK4	1.8	**2.3**	**4.1**	**2.7**	**3.1**

Bickley jet with zero initial relative velocity and $R = 7/9$						
Method	$S = 0.01$	$S = 0.1$	$S = 0.5$	$S = 1$	$S = 2$	$S = 4$
Prasath et al. [53]	1.8	2.2	2.4	2.4	2.5	2.5
FD2 + Trap. or IMEX2	**2.0**	2.0	2.0	2.0	2.0	2.0
Daitche 3^{rd} order [20]	unstable	unstable	2.9	3.0	3.3	3.4
FD4 + IMEX4 / DIRK4	0.8	**2.3**	**3.2**	**3.3**	**3.5**	**3.8**

Table 6.7: Experimentally-computed convergence orders for particles moving for approximately 1 d in the Bickley jet for different values of R and S. The initial conditions are $\boldsymbol{y} = (0,0)^T$ and $\boldsymbol{q}(0,t_0) = (0,0)^T$.

meaning that they appear for many of the meshes considered, whereas instabilities appear for fewer meshes as the parameters grow. Prasath et al.'s method follows with quadratic and superquadratic orders, increasing with R and S. Second order FD methods always achieve their expected theoretical convergence order.

Table 6.8 shows the experimentally-computed convergence orders for a particle moving the Bickley jet with nonzero initial velocity. Like in the previous examples with nonzero initial relative velocity, Prasath et al.'s is the method with best convergence for every single one of the values of R and S considered, obtaining a superquadratic convergence rate that increases as R and S increase. Second order FD methods are the second best performing methods, although they only achieve first order convergence. Instabilities are predominant in Daitche's method, specially for the smallest values of the parameters. Fourth order FD methods only obtain a maximum of 0.6 of convergence order.

Figure 6.17 shows the work-precision plots for particles moving in the Bickley jet for zero (left) and nonzero (right) initial relative velocity. On the left plot, IMEX methods perform very well, overpassing real-time for almost all the meshes considered and without any instability. Daitche's method demonstrates a similar behaviour as IMEX methods, although instabilities are present for half of the meshes considered. Fully implicit FD as well as Prasath et al.'s methods show very long runtimes for equivalent errors and are not competitive in this case.

Again, for the case of particles with nonzero initial relative velocity there is a considerable increase in the error for all methods except for Prasath et al.'s approach. Prasath et al.'s method attains the smallest errors (between 10^{-4} and 10^{-7}) but exceeds the realtime threshold for all the meshes used. Daitche's scheme performs fairly well, obtaining the smallest errors within the methods that are faster than realtime. However, instabilities are again present for half of the grids used. Second order IMEX implementation remains

Bickley jet with non-zero initial relative velocity and $S = 0.1$					
Method	$R = 1/3$	$R = 7/9$	$R = 1$	$R = 4/3$	$R = 7/3$
Prasath et al. [53]	**2.0**	**2.2**	**2.3**	**2.3**	**2.5**
FD2 + Trap. / IMEX2	1.1	1.1	1.1	1.1	1.0
Daitche 3^{rd} order [20]	unstable	unstable	unstable	unstable	2.0
FD4 + IMEX4 / DIRK4	0.4	0.5	0.5	0.5	0.5

Bickley jet with non-zero initial relative velocity and $R = {}^7/_9$						
Method	$S = 0.01$	$S = 0.1$	$S = 0.5$	$S = 1$	$S = 2$	$S = 4$
Prasath et al. [53]	**1.9**	**2.2**	**2.4**	**2.4**	**2.5**	**2.5**
FD2 + Trap. or IMEX2	1.1	1.1	1.1	1.1	1.1	1.1
Daitche 3^{rd} order [20]	unstable	unstable	1.0	1.0	1.1	1.1
FD4 + IMEX4 or DIRK4	0.4	0.5	0.5	0.6	0.6	0.6

Table 6.8: Experimentally-computed convergence orders for particles moving for approximately 1 d in the Bickley jet for different values of R and S. The initial conditions are $\boldsymbol{y} = (0, 0)^T$ and $\boldsymbol{q}(0, t_0) = (0.1, 0)^T$.

competitive in time but attains fairly not too small errors, between 10^{-2} and 10^{-3}. Fourth order IMEX method, the trapezoidal rule and fully implicit FD methods perform poorly. In fact, DIRK method is always slower than realtime.

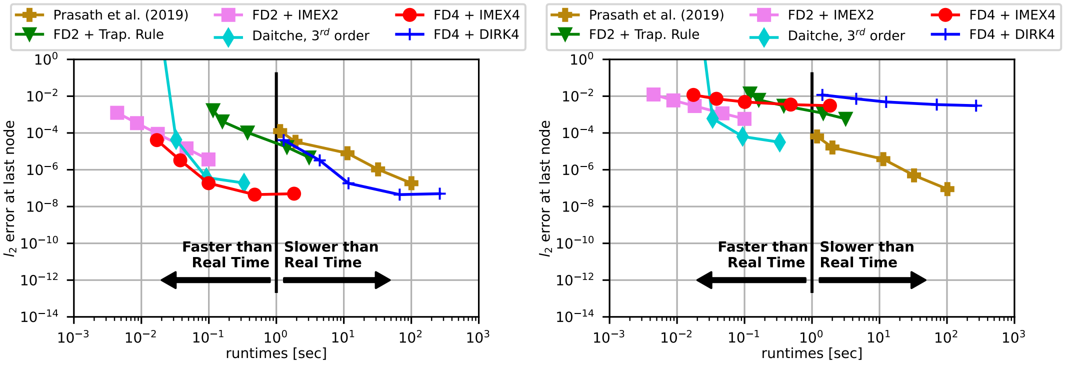

Figure 6.17: Work-precision plots for a particle moving for 1 d in the Bickley jet with $R = {}^7/_9$ and $S = 0.1$. The initial conditions of the particle are $\boldsymbol{y}_0 = (0, 0)^T$ and $\boldsymbol{q}(0, t_0) = (0, 0)^T$ (left) and $\boldsymbol{q}(0, t_0) = (0.1, 0.)^T$ (right)

Figure 6.18 shows convergence of the FD methods with respect to the parameter c for a particle moving in the Bickley jet with zero and nonzero initial relative velocity. For the examples with zero initial relative velocity, fourth order methods as well as the trapezoidal rule have a constant error for most of the values of c studied. Second order IMEX is the only one for which the error decreases as c decreases, with an approximately second order convergence with respect to c. The plot with nonzero initial relative velocity shows that the methods slowly converge with c, and that second order methods maximise that convergence. Hence, a decrease in the value of the parameter c, from 20 to 5, would have achieved a smaller error in most of the cases.

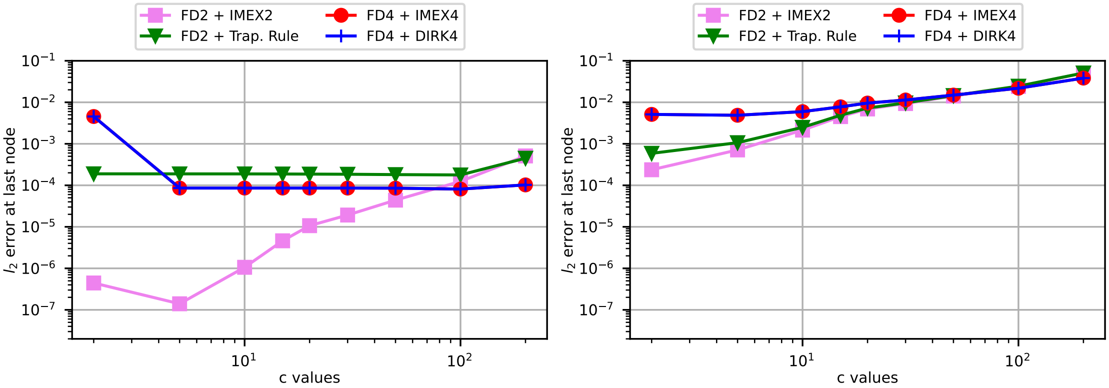

Figure 6.18: Convergence with respect to the parameter c of the finite difference methods for a particle with $R = 7/9$ and $S = 0.1$ moving in the Bickley jet with zero (left) and nonzero (right) initial relative velocity. The initial conditions of the particle are $\boldsymbol{y}_0 = (0,0)^T$ and $\boldsymbol{q}(0,t_0) = (0,0)^T$ (left) and $\boldsymbol{q}(0,t_0) = (0.1, 0.)^T$ (right)

6.2.3 The experimental case: The Faraday flow

This section studies the efficiency of the implementations presented in chapter 5 on a experimentally-obtained velocity field, called the Faraday flow. The Faraday flow is generated in a cylindrical glass container of 290 mm diameter, filled with a 2 mm-deep layer of distilled water in a cylindrical container, like the one shown in figure 6.19. The container is shaken vertically with a frequency of 50 Hz at a measured forcing acceleration of $a = 1.6g$ by an electromagnetic shaker, corresponding to a supercriticality of $\varepsilon = 0.04$ and generating quasi-standing waves over the fluid's surface, called Faraday waves. The Faraday waves correspond to a turbulent space- and time-dependent $2D$-velocity field. The flow field is recorded by using particle image velocimetry (PIV) on uniformly-distributed white, hollow, glass microspheres of diameter 70 μm and density 0.15 g/cm^3. Further details about the experiment can be found in Colombi et al. (2021) [14] and (2022) [15].

As explained in Urizarna et al. (2023) [74], PIV data consists on a data set of values for the horizontal and vertical components of the absolute velocity at discrete grid points over an area of approximately 7.0395 cm by 5.2487 cm. A total amount of 1056 discrete data sets are recorded over a time period of 42.24 s. Spatial interpolation between data points is carried out by SciPy's bivariate rectangular spline interpolation [77]. On the other hand, time interpolation is done by using linear interpolation.

Figure 6.20 depicts the trajectory of two particles with different effective density ratios, R, moving in the Faraday flow. Both trajectories do not differ much, although there is a clear difference in the size of the loop done by the particle on the bottom left side of the plots.

Table 6.9 shows the experimentally-computed convergence plots for particles moving in the Faraday flow with zero initial relative velocity. In opposition to what it happened in the previous flow fields, there is not a clear method that wins over the others as R varies.

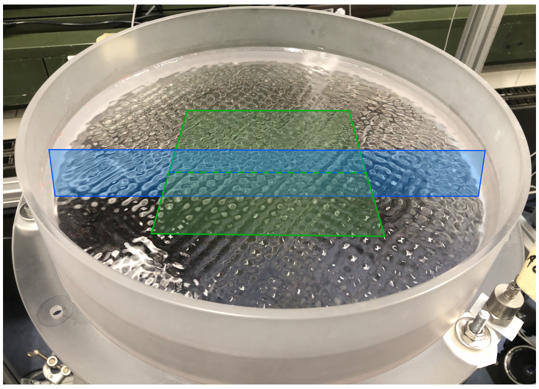

Figure 6.19: Device used on the experiment described in [15]. Faraday waves for a frequency of 50 Hz can be observed on the surface of the cylinder. Colored planes indicate the scanned areas for the horizontal and vertical PIV measurements.

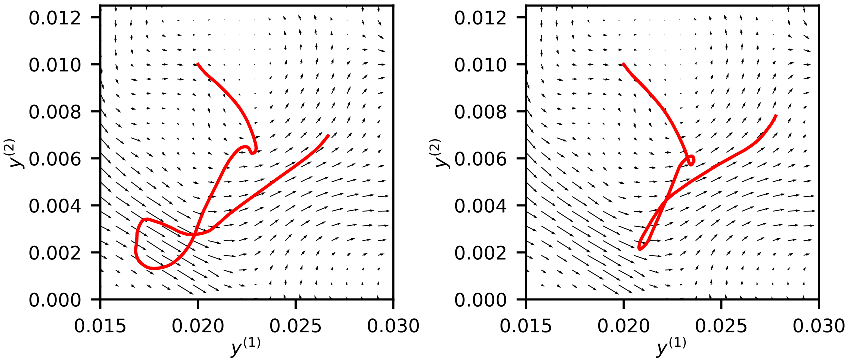

Figure 6.20: Trajectories of two particles with $S = 0.3$ and $R = 7/9$ (left) and $R = 4/3$ (right) moving in the Faraday flow for 5 s. The initial conditions are $\boldsymbol{y}(t_0) = (0.02, 0.01)^T$ and $\boldsymbol{q}(0, t_0) = (0, 0)^T$.

Faraday flow with zero initial relative velocity and $S = 0.1$

Method	$R = 1/3$	$R = 7/9$	$R = 1$	$R = 4/3$	$R = 7/3$
Prasath et al. [53]	**1.9**	1.0	**7.3**	1.6	**2.3**
FD2 + Trap.	1.2	1.3	2.8	1.2	1.0
FD2 + IMEX2	1.5	**1.6**	2.0	**1.7**	1.8
Daitche 3^{rd} order [20]	**1.9**	0.6	1.1	1.1	1.1
FD4 + IMEX4	1.7	1.3	6.5	1.3	1.0
FD4 + DIRK4	**1.9**	1.5	3.6	1.5	1.2

Faraday flow with zero initial relative velocity and $R = 7/9$

Method	$S = 0.01$	$S = 0.1$	$S = 0.5$	$S = 1$	$S = 2$	$S = 4$
Prasath et al. [53]	**2.0**	1.0	0.9	0.9	0.8	0.8
FD2 + Trap.	1.5	1.3	1.2	1.1	1.1	1.0
FD2 + IMEX2	1.8	**1.6**	**1.6**	**1.6**	**1.6**	**1.7**
Daitche 3^{rd} order [20]	1.3	0.6	1.2	1.3	1.4	1.4
FD4 + IMEX4	1.3	1.3	1.2	1.1	1.1	1.0
FD4 + DIRK4	1.3	1.5	1.4	1.3	1.3	1.2

Table 6.9: Experimentally-computed convergence orders for particles moving for approximately 1 s in the Faraday flow, with different values of S and R. The initial conditions are $\boldsymbol{y} = (0.3810451, 0.19052255)^T$ and $\boldsymbol{q}(0, t_0) = (0, 0)^T$.

On the other hand, second order IMEX method achieves maximum convergence for all $S \geq 0.1$ and $R = 7/9$. All methods perform fairly well in this case, reaching superlinear convergence in most methods, except Prasath et al.'s for $S \geq 0.1$ and $R = 7/9$, that barely reaches linear convergence.

Table 6.10 shows the experimentally-computed convergence plots for particles moving in the Faraday flow with nonzero initial relative velocity. Prasath et al.'s method dominates here for $S = 0.1$ and all different values of R. It is only surpassed by the second order IMEX method by a difference of 0.4 orders of convergence for $R = 7/9$ and $S \geq 0.5$. For all methods and most of the parameter combinations, convergence ranges between 0.5 and 1.8.

Figure 6.21 consists of two work-precision plots for particles moving in the Faraday flow, again for the case with zero (left) and nonzero (right) initial relative velocity. The performance of the methods in both cases is qualitatively the same. For the case with zero initial relative velocity, the second order IMEX method is the fastest method, achieving errors between 10^{-2} and 10^{-5}. Fourth order IMEX method and Daitche's method attain similar errors with slightly slower runtimes. FD4 + IMEX4's last node is slower than realtime. The trapezoidal rule obtains also similar errors with slower runtimes, but only surpasses realtime at the last node. The fourth order fully implicit method is the worse performing method, obtaining the same errors at runtimes almost three orders of magnitude larger. Prasath et al's method is in all cases slower than realtime, but attains the smallest errors, between 10^{-5} and 10^{-7}.

Faraday flow with non-zero initial relative velocity and $S = 0.1$					
Method	$R = 1/3$	$R = 7/9$	$R = 1$	$R = 4/3$	$R = 7/3$
Prasath et al. [53]	**1.9**	**1.2**	**3.1**	**1.8**	**2.4**
FD2 + Trap.	1.3	1.0	0.9	0.8	0.9
FD2 + IMEX2	1.6	**1.2**	1.0	0.6	1.0
Daitche 3^{rd} order [20]	1.8	0.8	1.1	1.2	1.3
FD4 + IMEX4	1.5	0.9	0.8	0.5	0.8
FD4 + DIRK4	1.5	0.9	0.8	0.6	0.7

Faraday flow with non-zero initial relative velocity and $R = 7/9$						
Method	$S = 0.01$	$S = 0.1$	$S = 0.5$	$S = 1$	$S = 2$	$S = 4$
Prasath et al. [53]	**2.1**	**1.2**	0.8	0.8	0.8	0.8
FD2 + Trap.	1.0	1.0	1.1	1.1	1.1	1.1
FD2 + IMEX2	1.1	**1.2**	**1.2**	**1.2**	**1.2**	**1.2**
Daitche 3^{rd} order [20]	1.3	0.8	0.9	1.0	1.0	1.0
FD4 + IMEX4	0.8	0.9	1.0	1.0	1.0	1.0
FD4 + DIRK4	0.8	0.9	1.0	1.0	1.0	1.0

Table 6.10: Experimentally-computed convergence orders for particles moving for approximately 1 s in the Faraday flow for different values of R and S. The initial conditions are $\boldsymbol{y} = (0.3810451, 0.19052255)^T$ and $\boldsymbol{q}(0, t_0) = (0.10848, -0.13324066)^T$.

In the nonzero initial relative velocity, the performance of all the methods is basically the same, except that errors are slightly higher (except for Prasath et al.'s approach), approximately one order higher and that Daitche's method ties with the second order IMEX as the best performing method. Prasath et al.'s approach is basically the same in both cases.

Figure 6.22 shows the convergence plots with respect to the parameter c. Convergence is very similar for all methods for the case with nonzero initial relative velocity, reaching superlinear convergence. When the particle starts with zero initial relative velocity, the behaviours of the methods changes depending on the value of c. For $c \geq 20$, all methods converge with c. Errors for the second order methods are higher than for the fourth order ones and they present first order convergence. Fourth order methods converge faster, with approximately second order convergence. For $c < 20$, the implicit second order and the fourth order methods remain with constant error. On the other hand, the error of the second order IMEX method greatly decreases from approximately $2 \cdot 10^{-4}$ to 10^{-6}, achieving the smallest error among all methods. In this field, a decrease in the value of c, from 20 to 2, would have generally decreased the error of all the methods.

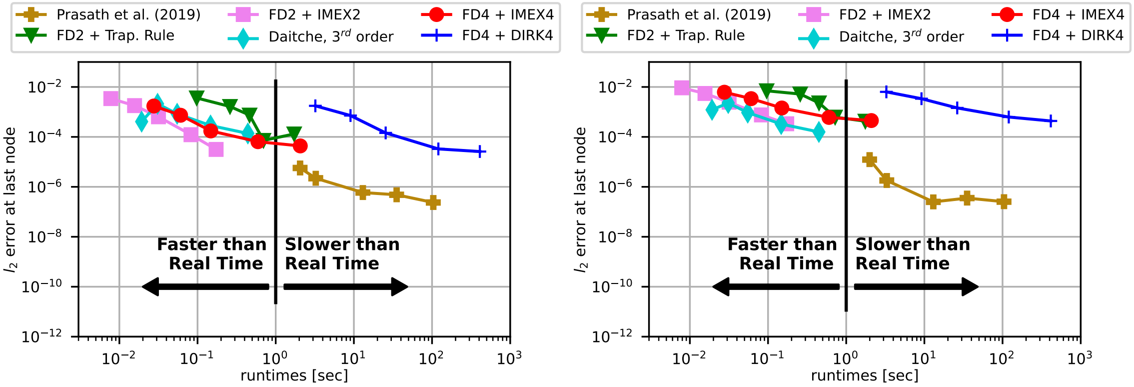

Figure 6.21: Work-precision plots for a particle moving in the Faraday flow for approximately 1 s with $R = 7/9$ and $S = 0.1$. The initial conditions of the particle are $\boldsymbol{y}_0 = (0.3810451, 0.19052255)^T$ and $\boldsymbol{q}(0,t_0) = (0,0)^T$ (left) and $\boldsymbol{q}(0,t_0) = (0.10848, -0.13324066)^T$ (right).

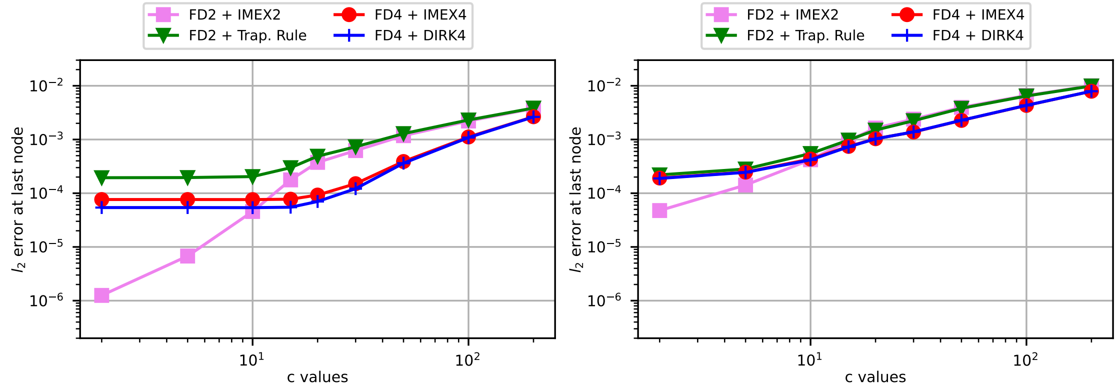

Figure 6.22: Convergence with respect to the parameter c of the finite difference methods for a particle moving in the Faraday flow for approximately 1 s with $R = 7/9$ and $S = 0.1$. The initial conditions of the particle are $\boldsymbol{y}_0 = (0.3810451, 0.19052255)^T$ and $\boldsymbol{q}(0,t_0) = (0,0)^T$ (left) and $\boldsymbol{q}(0,t_0) = (0.10848, -0.13324066)^T$ (right).

7

The effect of the Basset history term

This chapter uses the numerical implementations seen in chapter 5 to study in which cases the BHT has a major influence in particle trajectories. The code needed to reproduce the figures and the tables from this chapter can be found in the code repository in GitHub [72]. This information provides orientation about when neglecting it would translate into an important disparity between the obtained and the actual trajectory. The influence of the BHT is first studied on single particle trajectories, later on clusters of particles and finally on large scale features of the flow fields called Lagrangian Coherent Structures (LCS).

The shape of the MRGE, provided in equation (2.6), indicates that the Stokes number affects the Stokes drag and the BHT in a different manner. The Stokes drag is scaled by the constant $1/S$, whereas the BHT is multiplied by $\sqrt{1/S}$. This indicates that smaller values of the Stokes number, i.e. $0 < S << 1$, will make the influence of the Stokes drag predominant over the BHT. Little difference is therefore expected between trajectories calculated with and without BHT for a sufficiently small Stokes numbers. On the other hand, bigger Stokes numbers, i.e. $S \geq 1$, will make the difference between trajectories more noticeable, since the BHT will be multiplied by a larger coefficient than the Stokes drag.

Up to the author's knowledge, there is limited information regarding perturbation theory for the MRGE with BHT. Langlois et al. (2015) showed algebraic decay for the MRGE with memory term, instead of the exponential decay observed in the absence of it [39]. More information is available for approximations of the MRGE in the absence of BHT, like the one in Mograbi and Bar-Ziv (2006) [46] and Beron-Vera et al. (2019) [10].

The coming sections of this chapter present and compare the trajectories of single particles as well as particle clusters calculated with and without BHT on the flow fields given in chapter 6.

7.1 Influence of the BHT on individual particle trajectories

This section studies the influence of the BHT in the trajectory of individual particles. These examples consider a particle placed arbitrarily in the velocity fields given in chapter 6.

The study of individual particles is more insightful for the first three fields, since their symmetries and similarities makes all particle trajectories similar to each other. Initial

	$S = 0.01$	$S = 0.1$	$S = 1$	$S = 10$
$y_{radial}(t_f = 15)$	0.0076	0.0716	0.5901	3.1928

Table 7.1: Absolute radial distance at final time calculated with BHT, $y_{radial}(t_f)$, of a particle moving in the quiescent flow for 15 s with $R = 7/9$ and four different values of S. The initial conditions of the particle are $\boldsymbol{y}(t_0) = (0, 0)^T$ and $\boldsymbol{q}(0, t_0) = (1, 0)^T$.

conditions have a large effect on the particle's path for last three fields, since they are time dependent inhomogeneous flow fields. The study of individual particles for these fields feels incomplete but it provides a good base to state assumptions for the clusters of particles that will be shown in the following sections.

7.1.1 A Relaxing particle

Figure 7.1 presents the relative distance with respect to their initial position travelled by several particles with different Stokes numbers in the quiescent flow. Each plot has two lines: (1) A blue dashed line representing the relative distance travelled by a particle when the BHT is neglected and (2) a red line showing the relative distance travelled when the trajectory is calculated with the full MRGE.

The relaxing particle example corresponds to a particle that moves in a still fluid, so that the fluid forces only act on the particle to reduce its velocity until it reaches a halt. A $2D$ spatial plot of the particle's trajectory will always show a straight line, whose only relevant information would then be the final position of the particle. On the other hand, distance vs time plots show how far from its starting point the particle is at each single time and are therefore more insightful.

The scales of the distances in the y-axis in the plots in figure 7.1 are normalised by dividing all distances by the final position at $t_f = 15$ s, calculated with the full MRGE, so that all plots show relative distances and have the same range in the y axis. This makes the four plots of figure 7.1 easier to compare. Note that the values of the absolute distance travelled by the particle differ considerably for the different values of the Stokes number (see table 7.1.1). For instance, the final-time distance travelled by the particle without History Term for $S = 10$ is twice as big as when it is calculated with BHT, whereas for $S = 0.01$, the difference is barely appreciable.

Figure 7.2 shows maximum normalised difference against the Stokes number for four values of R. The normalised difference is the l_2-norm of the difference between the trajectories calculated with and without BHT divided by the l_2-norm of the radial distance calculated with BHT. Equation (7.1) exhibits the expression used to obtain the maximum normalised distance difference.

$$\Delta\tilde{y}_{max} := \max_{t\in[t_0,t_f]} \left\{ \frac{||\boldsymbol{y}_{Stokes}(t) - \boldsymbol{y}_{BHT}(t)||_2}{||\boldsymbol{y}_{BHT}(t) - \boldsymbol{y}_{BHT}(t_0)||_2} \right\}. \tag{7.1}$$

This quantity can be understood as the maximum relative effect of the BHT on the particle over the whole time domain. Using the relative magnitude instead of the absolute one, maximises differences at the beginning and minimises them as time goes by, accounting for the fact that it is normal that trajectories differ as time passes by. In fact, it would be

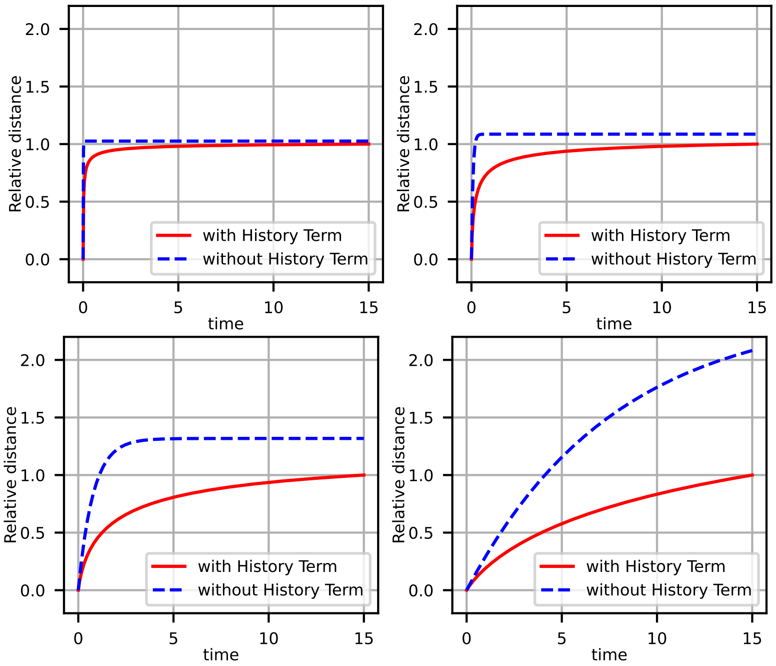

Figure 7.1: Relative distance to the starting point with and without BHT of particles moving in the quiescent flow for 15 s with different Stokes numbers, $S = 0.01$ (top left), $S = 0.1$ (top right), $S = 1$ (bottom left) and $S = 10$ (bottom right). The effective density ratio is $R = 7/9$ and the initial conditions are $\boldsymbol{y}(t_0) = (0,0)^T$ and $\boldsymbol{q}(0,t_0) = (1,0)^T$.

more precise to divide by the length of the full trajectory instead of the final time position, but it is still a good approximation.

Figure 7.2 confirms that the smaller the Stokes number is, the smaller the differences in the trajectories with and without History Term are. Additionally, R also influences the differences between the trajectories, having the smaller difference for the larger values of R. However, R is not a main driver, like S; and its influence is not noticeable when S is small.

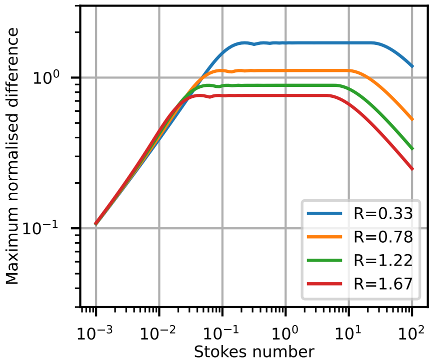

Figure 7.2: Maximum normalised difference between the trajectories calculated with and without BHT against the Stokes number in the quiescent flow. The initial conditions are $\boldsymbol{y}(t_0) = (0,0)^T$ and $\boldsymbol{q}(0,t_0) = (1,0)^T$. Trajectories are calculated for 10 s.

7.1.2 The Vortex

Figures 7.3 and 7.4 display trajectories calculated with and without BHT of a particle moving in the vortex described by equation (6.11) for three values of the Stokes number and two values of the effective density ratio. Independently of the consideration of the BHT, the plots show the expected rotating behaviour: Accumulation of particles around the origin for $R < 1$ and ejection for $R > 1$.

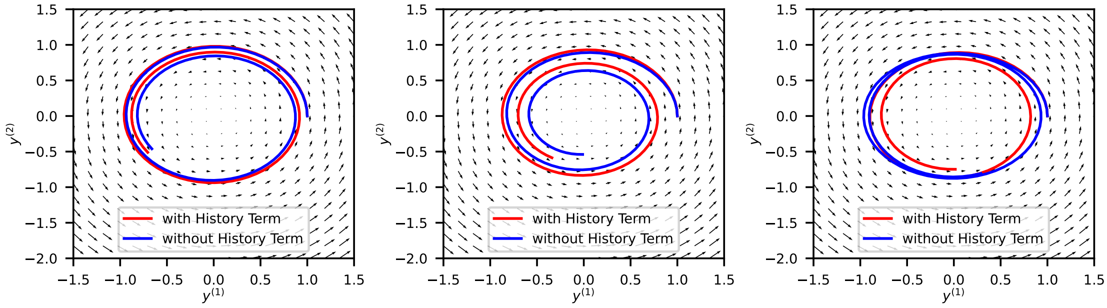

Figure 7.3: Exact trajectories calculated with and without BHT of two particles with three different Stokes numbers, $S = 0.1$ (left), $S = 1$ (center) and $S = 10$ (right), moving in the vortex for 10 s. The effective density ratio is $R = {}^{7}/_{9}$ and the initial conditions are $\boldsymbol{y}(t_0) = (1, 0)^T$ and $\boldsymbol{q}(0, t_0) = (0, 0)^T$.

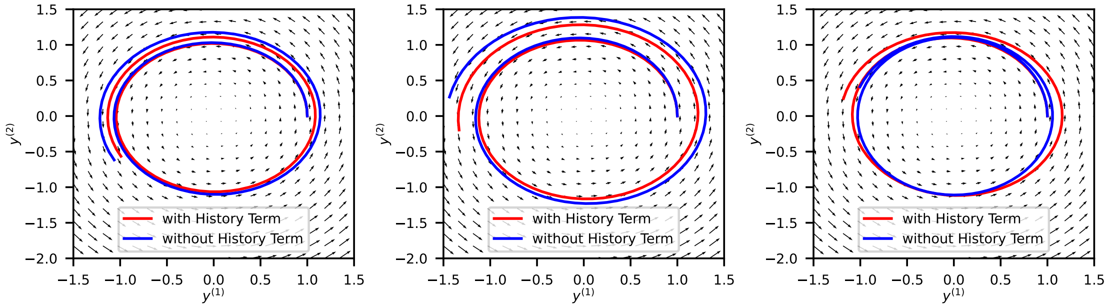

Figure 7.4: Exact trajectories calculated with and without BHT of two particles with three different Stokes numbers, $S = 0.1$ (left), $S = 1$ (center) and $S = 10$ (right), moving in the vortex for 10 s. The effective density ratio is $R = {}^{11}/_{9}$ and the initial conditions are $\boldsymbol{y}(t_0) = (1, 0)^T$ and $\boldsymbol{q}(0, t_0) = (0, 0)^T$.

Figures 7.5 and 7.6 show radial distance vs. time. Accumulative behaviour is presented when the radial distance decreases with time, whereas ejection is observed when the radial distance increases with time. The figures show linear behaviour for $S \in \{0.1, 1\}$, while this linear behaviour is affected by oscillations for $S = 10$. Pure oscillations occur when both the Stokes drag and the BHT are neglected in the MRGE, i.e. only with the material derivative term, also called a perfect tracer, so it makes sense that these oscillations occur as S grows and these terms tend to zero (see figure 7.7). Note that the Stokes number appears in a square root in the BHT. Hence the BHT does not decay as fast as $S \to \infty$ and its inclusion has a damping effect on the perfect tracer oscillations.

The neglect of the BHT overestimates the accumulative and ejective behaviour for

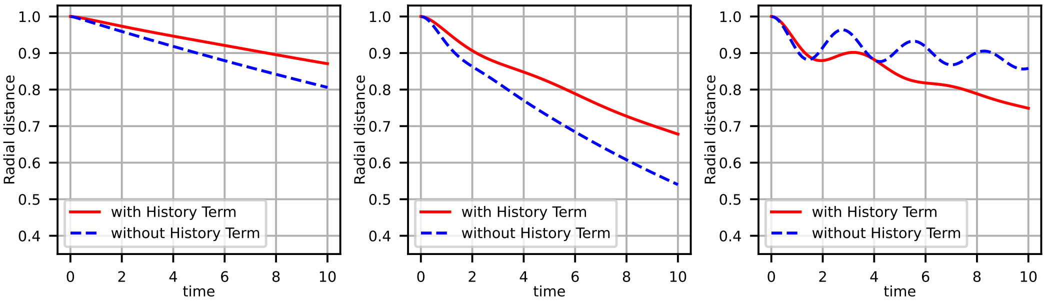

Figure 7.5: Radial distance calculated with and without BHT of two particles with three different Stokes numbers, $S = 0.1$ (left), $S = 1$ (center) and $S = 10$ (right), moving in the vortex for 10 s. The effective density ratio is $R = {}^{7}/_{9}$ and the initial conditions are $\boldsymbol{y}(t_0) = (1, 0)^T$ and $\boldsymbol{q}(0, t_0) = (0, 0)^T$.

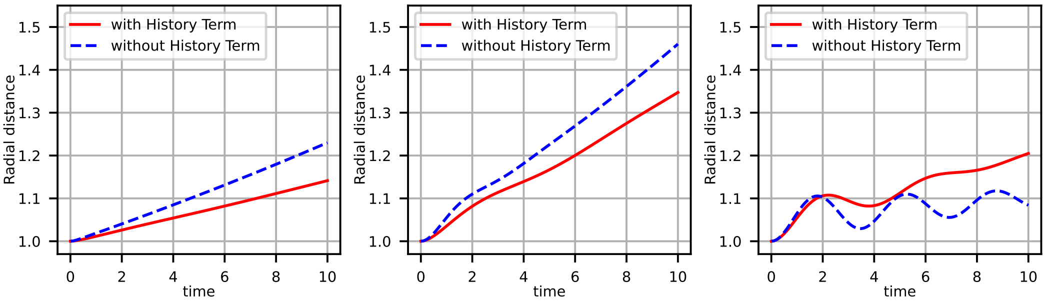

Figure 7.6: Radial distance calculated with and without BHT of two particles with three different Stokes numbers, $S = 0.1$ (left), $S = 1$ (center) and $S = 10$ (right), moving in the vortex for 10 s. The effective density ratio is $R = {}^{11}/_{9}$ and the initial conditions are $\boldsymbol{y}(t_0) = (1, 0)^T$ and $\boldsymbol{q}(0, t_0) = (0, 0)^T$.

$S \in \{0.1, 1\}$, whereas this is underestimated for $S = 10$. Figure 7.8 indicates that the threshold value where the behaviours are reversed are found for values of the Stokes number in a neighbourhood of $S = 2$. For $S > 2$, the influence of the Stokes drag starts to be small compared to the material derivative term. The BHT softens this effect because its coefficient includes the Stokes number in a square root, i.e. $\sqrt{{}^{1}/_{S}}$, in comparison to the ${}^{1}/_{S}$ coefficient multiplying the Stokes drag.

Figure 7.9 shows a decrease in the maximum normalised difference as S decreases and increases, obtaining its global maximum for intermediate values of S. Extending the plot for smaller values of S was not possible in this plot due to stability issues. The behaviour for different values of R is qualitatively similar, observing the minimum for $R = 1.22$.

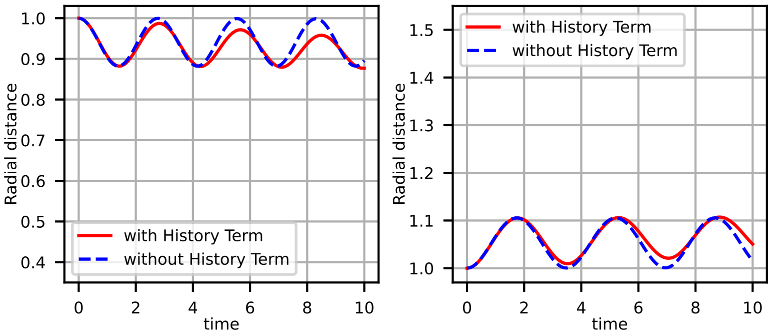

Figure 7.7: Radial distance calculated with and without BHT of two particles moving in the vortex for 10 s with $S = 1000$ and two effective density ratios, $R = 7/9$ (left) and $R = 11/9$ (right). The initial conditions are $\boldsymbol{y}(t_0) = (1, 0)^T$ and $\boldsymbol{q}(0, t_0) = (0, 0)^T$.

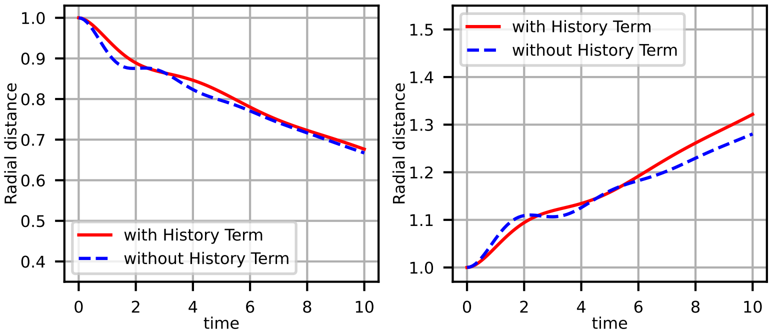

Figure 7.8: Radial distance calculated with and without BHT of two particles moving in the vortex with $S = 2$ and two effective density ratios, $R = 7/9$ (left) and $R = 11/9$ (right). The initial conditions are $\boldsymbol{y}(t_0) = (1, 0)^T$ and $\boldsymbol{q}(0, t_0) = (0, 0)^T$.

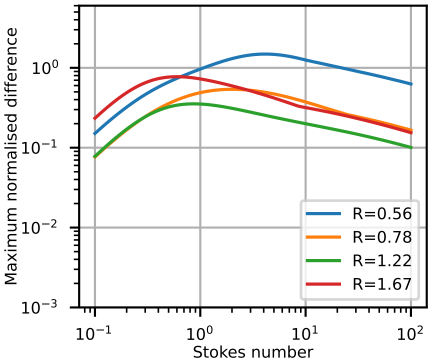

Figure 7.9: Maximum normalised difference between the trajectories calculated with and without BHT against the Stokes number in the vortex. The initial conditions are $\boldsymbol{y}(t_0) = (1, 0)^T$ and $\boldsymbol{q}(0, t_0) = (0, 0)^T$. Trajectories are calculated for 10 s.

7.1.3 Oscillatory Background

Figures 7.10 and 7.11 show the trajectories of particles moving in the oscillatory background. There is a considerable difference in the particle's trajectory if the memory term is omitted: The amplitude of the oscillation of the particles with BHT is four times bigger than without the history term. No large differences are observed as the parameters change. For $R = 7/9$, the amplitude of the oscillation increases with S, opposite to the $R = 11/9$ case, in which the amplitude gets reduced with S. Interestingly, the amplitude of the oscillation is smaller for the larger R case for the same Stokes number.

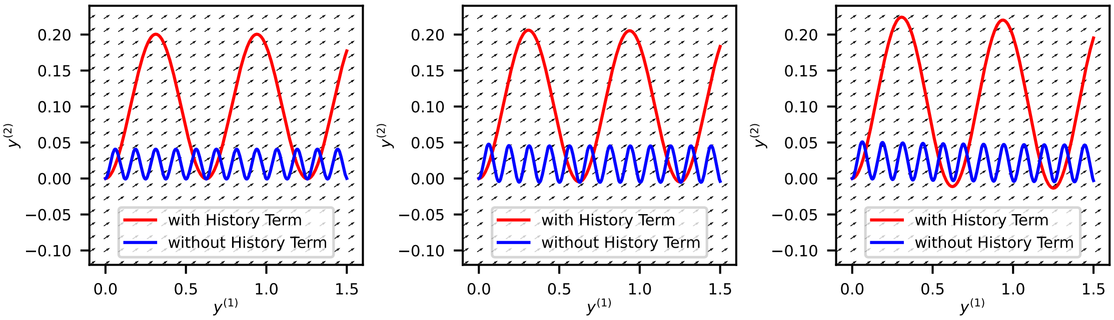

Figure 7.10: Exact trajectories with and without BHT of two particles with $R = 7/9$ and three different Stokes numbers, $S = 0.1$ (left), $S = 1$ (center) and $S = 10$ (right), moving in the oscillatory background for 3 s. The initial conditions are $\boldsymbol{y}(t_0) = (0, 0)^T$ and $\boldsymbol{q}(0, t_0) = (0, 0)^T$.

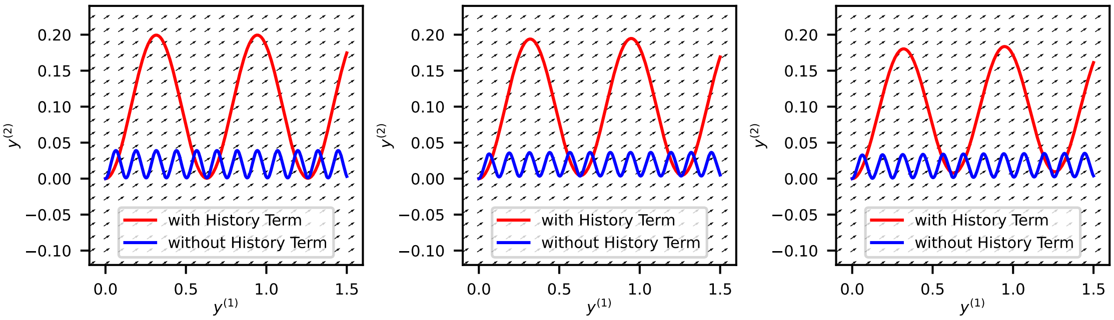

Figure 7.11: Exact trajectories with and without BHT of two particles with $R = 11/9$ and three different Stokes numbers, $S = 0.1$ (left), $S = 1$ (center) and $S = 10$ (right), moving in the oscillatory background for 3 s. The initial conditions are $\boldsymbol{y}(t_0) = (0, 0)^T$ and $\boldsymbol{q}(0, t_0) = (0, 0)^T$.

Figure 7.12 presents the maximum normalised distance difference against the Stokes number. This normalised difference is constant for all $S \leq 0.1$, independently of the values of R. For $S > 0.1$, the differences are more noticeable but not too large, reaching its maximum for $R = 1/3$. These results aline with the trajectories shown in figures 7.10 and 7.11, where plots are the most similar for the smallest values of S and start differing as S increases.

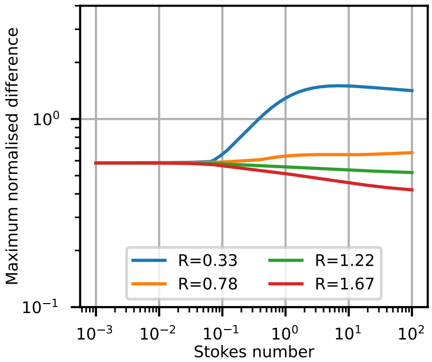

Figure 7.12: Maximum normalised difference between trajectories of particles calculated with and without BHT against the Stokes number in the oscillatory background. The initial conditions are $\boldsymbol{y}(t_0) = (0,0)^T$ and $\boldsymbol{q}(0,t_0) = (0,0)^T$ and trajectories are calculated for 0.6 s with a step of $\Delta t = 0.05$.

7.1.4 Double Gyre

Figures 7.13 and 7.14 show the trajectories with and without BHT of particles moving in the double gyre for two different effective density ratios, $R \in \{7/9, 11/9\}$, and three values of the Stokes number, $S \in \{0.1, 1, 10\}$. Particle paths for $R = 7/9$ (figure 7.13) present differences for $S = 1$ and $S = 10$ but they are specially noticeable for $S = 10$. The case of particles denser than the fluid, i.e. $R = 11/9$ (figure 7.14), exhibits a noticeable divergence in the particle paths for $S = 1$, which gets stronger for $S = 10$. Hence, in the double gyre the BHT seems to have a larger influence on the trajectories of particles denser than the fluid.

The same behaviour is observed when the radial distance from the initial position with respect to time is studied. Plots of particles lighter than the fluid, $R < 1$, in figure 7.15 show a good match between both solutions for all the values of the Stokes number considered, whereas plots in figure 7.16 exhibit an obvious mismatch at final times for the cases $S \geq 1$. It is then fair to assume that denser-than-fluid particles moving in fluid flows with time-dependent vortices will be more susceptible to the inclusion of the BHT. On the other

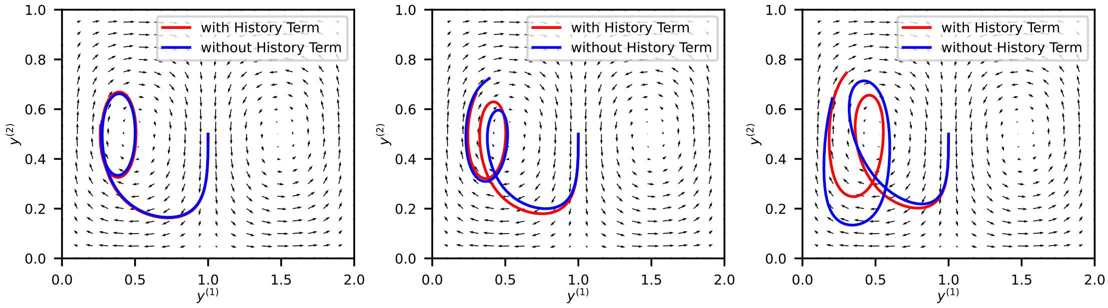

Figure 7.13: Exact trajectories with and without BHT of particles with different Stokes numbers, $S = 0.1$ (left), $S = 1$ (center) and $S = 10$ (right), moving in the double gyre for 10 s. The effective density ratio is $R = 7/9$ and the initial conditions are $\boldsymbol{y}(t_0) = (1, 0.5)^T$ and $\boldsymbol{q}(0,t_0) = (0,0)^T$.

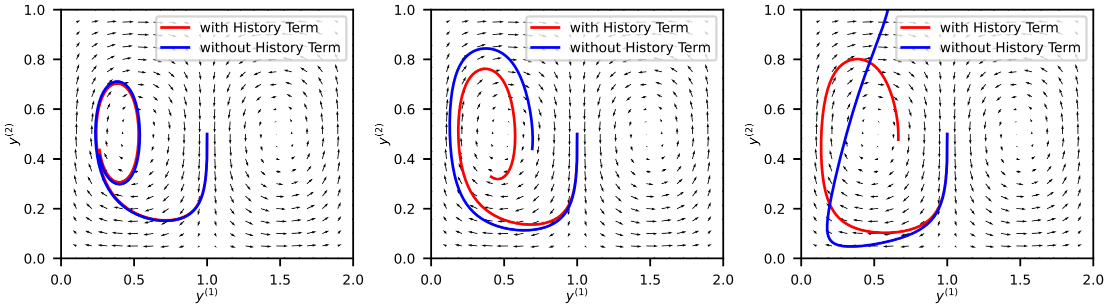

Figure 7.14: Exact trajectories with and without BHT of particles with different Stokes numbers, $S = 0.1$ (left), $S = 1$ (center) and $S = 10$ (right), moving in the double gyre for 10 s. The effective density ratio is $R = {}^{11}\!/_{9}$ and the initial conditions are $\boldsymbol{y}(t_0) = (1, 0.5)^T$ and $\boldsymbol{q}(0, t_0) = (0, 0)^T$.

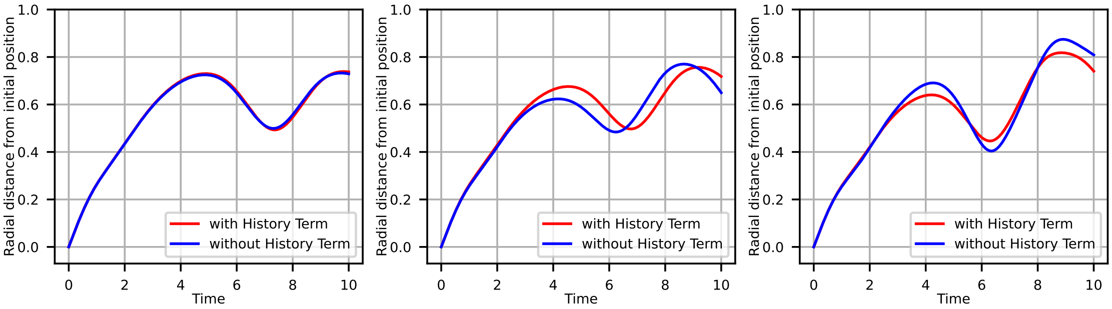

Figure 7.15: Radial distance from the initial position with and without BHT of particles with different Stokes numbers, $S = 0.1$ (left), $S = 1$ (center), and $S = 10$ (right), moving in the double gyre for 10 s. The effective density ratio is $R = {}^{7}\!/_{9}$ and the initial conditions are $\boldsymbol{y}(t_0) = (1, 0.5)^T$ and $\boldsymbol{q}(0, t_0) = (0, 0)^T$.

hand, figure 7.17 shows that the biggest maximum relative distance difference is achieved for very small values of the effective density ratio, $R = {}^{1}\!/_{3}$, so that the BHT will also play a significant role for particles of gases with small R values.

Again, maximum normalised relative difference, as shown in figure 7.17, presents a big decrease with S, independently of the value of R. For Stokes numbers higher than 0.2, the difference remains between 0.1 and 1, remaining relatively constant for most of the values of R, reaching its maximum variability for $R = {}^{11}\!/_{9}$.

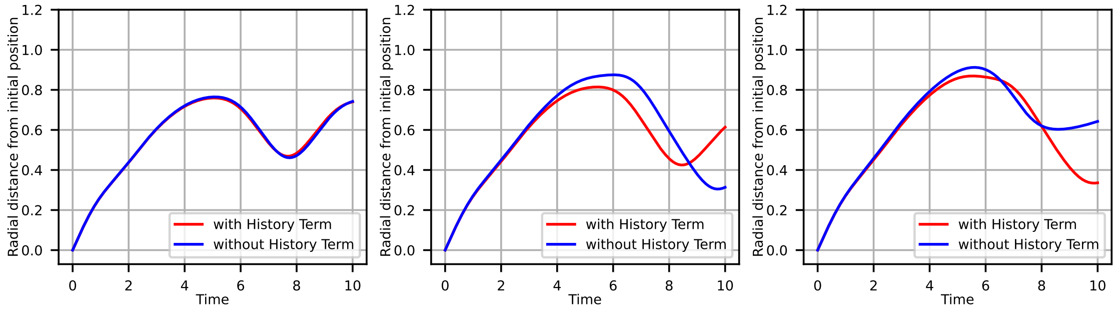

Figure 7.16: Radial distance from the initial position with and without BHT of particles with different Stokes numbers, $S = 0.1$ (left), $S = 1$ (center), and $S = 10$ (right), moving in the double gyre for 10 s. The effective density ratio is $R = {}^{11}/_{9}$ and the initial conditions are $\boldsymbol{y}(t_0) = (1, 0.5)^T$ and $\boldsymbol{q}(0, t_0) = (0, 0)^T$.

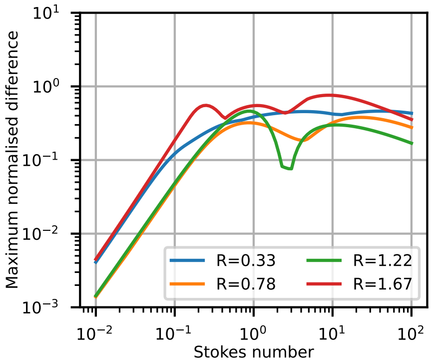

Figure 7.17: Maximum normalised difference between the trajectories of particles calculated with and without BHT against the Stokes number in the double gyre. The initial conditions are $\boldsymbol{y}(t_0) = (1, 0.5)^T$ and $\boldsymbol{q}(0, t_0) = (0, 0)^T$. Trajectories are calculated for 10 s with a step of $\Delta t = 0.01$.

7.1.5 Bickley Jet

Figures 7.18 and 7.20 show the paths of particles moving in the Bickley jet for different values of R and S. This figure shows that the BHT has a larger impact for largest values of the Stokes number and specially for the largest value of R.

Figures 7.21 and 7.19 show the radial distance from the initial position calculated with and without BHT for particles with different values of R and S. Radial distance is well-conserved in both cases, although it reaches a major disparity for $S = 1$ of the denser-than-fluid particle.

Figure 7.22 presents the maximum relative distance difference against the Stokes number for four effective density ratios. The plot shows for the values of $R \in \{{}^{1}/_{3}, {}^{7}/_{9}, {}^{11}/_{9}\}$ two humps at intermediate values of S. For the largest value of R, there is no specific pattern in this quantity, apart from a fluctuating behaviour between $[10^{-1}, 10^{0}]$. For all the values of R considered, there is a considerable decrease in this quantity with S.

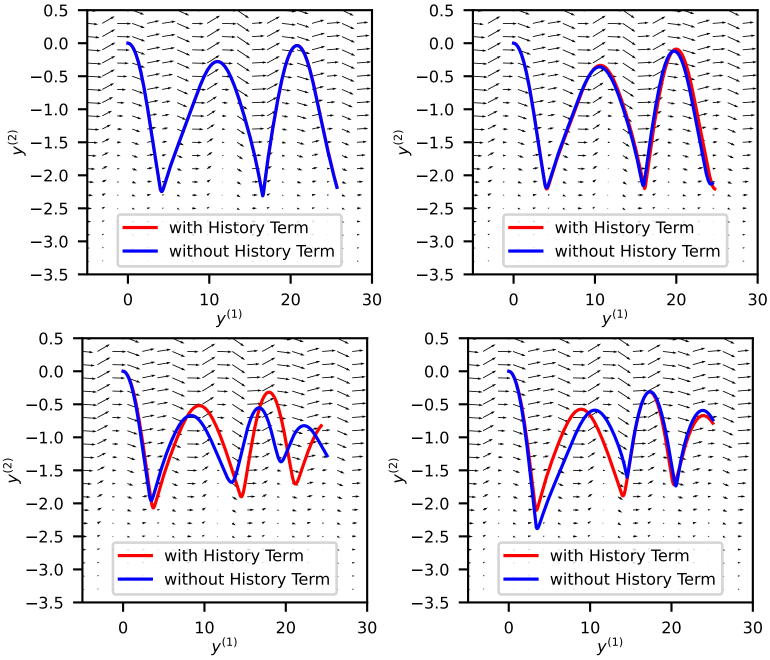

Figure 7.18: Exact trajectories with and without BHT of particles with different Stokes numbers, $S = 0.01$ (top left), $S = 0.1$ (top right), $S = 1$ (bottom left) and $S = 10$ (bottom right), moving in the Bickley jet for approximately 10 d. The effective density ratio is $R = 7/9$ and the initial conditions are $\boldsymbol{y}(t_0) = (0, 0)^T$ and $\boldsymbol{q}(0, t_0) = (0, 0)^T$.

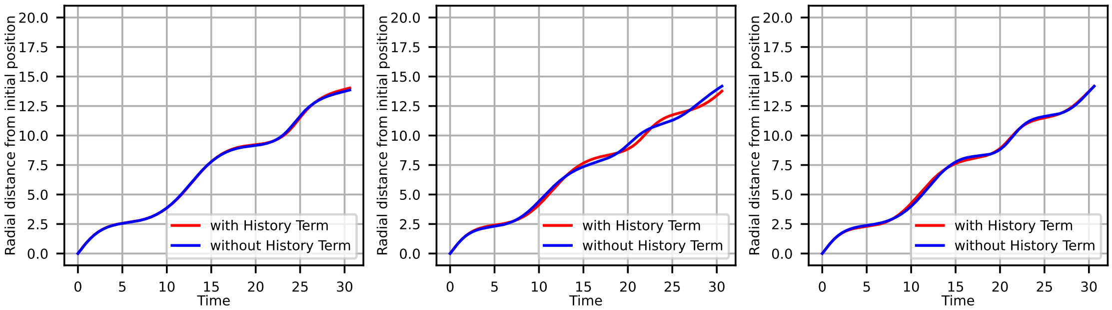

Figure 7.19: Radial distance from the initial position with and without BHT of particles with different Stokes numbers, $S = 0.1$ (left), $S = 1$ (center), and $S = 10$ (right), moving in the Bickley Jet. The effective density ratio is $R = 7/9$ and the initial conditions are $\boldsymbol{y}(t_0) = (0, 0)^T$ and $\boldsymbol{q}(0, t_0) = (0, 0)^T$.

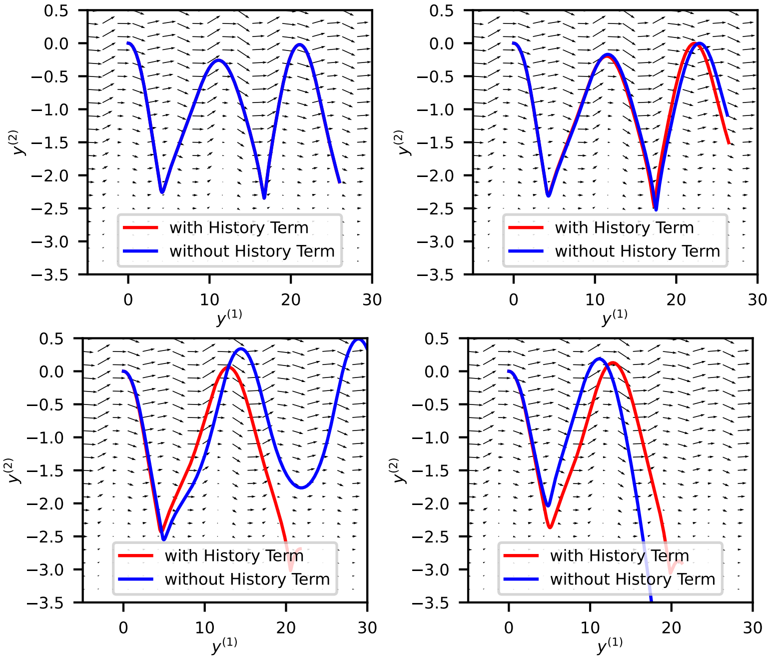

Figure 7.20: Exact trajectories with and without BHT of particles with different Stokes numbers, $S = 0.01$ (top left), $S = 0.1$ (top right), $S = 1$ (bottom left) and $S = 10$ (bottom right), moving in the Bickley jet for approximately 10 d. The effective density ratio is $R = {}^{11}\!/_{9}$ and the initial conditions are $\boldsymbol{y}(t_0) = (0,0)^T$ and $\boldsymbol{q}(0,t_0) = (0,0)^T$.

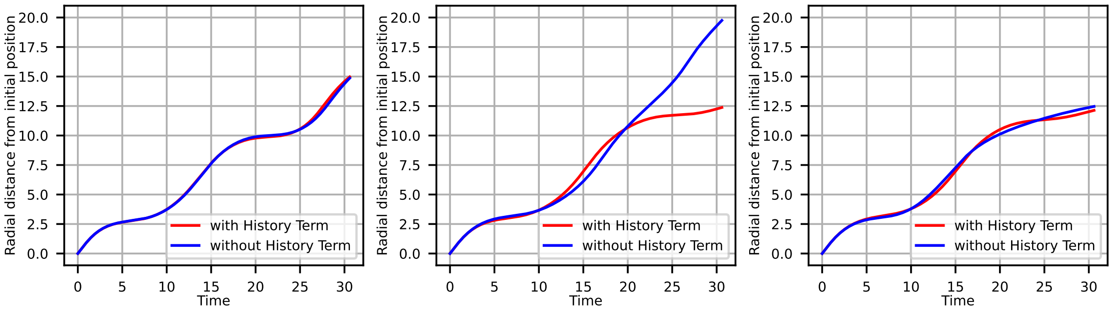

Figure 7.21: Radial distance from the initial position with and without BHT of particles with different Stokes numbers, $S = 0.1$ (left), $S = 1$ (center), and $S = 10$ (right), moving in the Bickley Jet. The effective density ratio is $R = {}^{11}\!/_{9}$ and the initial conditions are $\boldsymbol{y}(t_0) = (0,0)^T$ and $\boldsymbol{q}(0,t_0) = (0,0)^T$.

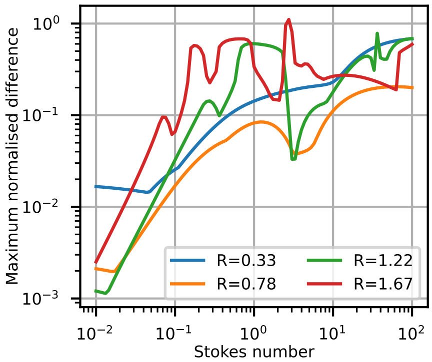

Figure 7.22: Maximum normalised difference between the trajectories calculated with and without BHT against the Stokes number in the Bickley jet for approximately 10 d. The initial conditions are $\boldsymbol{y}(t_0) = (0,0)^T$ and $\boldsymbol{q}(0,t_0) = (0,0)^T$. Trajectories are calculated with a step of $\Delta t \approx 0.0305876$.

7.1.6 Experimental flow: The Faraday flow

The Faraday flow corresponds to a flow field made up of many time-variant rotating vortices. Figures 7.23 and 7.25 show the paths of particles moving in the Faraday flow for different values of R and S. Again, trajectories with and without BHT remain more similar for smaller values of S and start diverging for $S \geq 1$. This divergence is specially clear for particles lighter than the fluid, but it is difficult to draw conclusions from a single particle movement, considering how turbulent this field is.

Figures 7.24 and 7.26 show the radial distance from the initial position against time for a particle moving in the Faraday flow for two effective density ratios and four Stokes numbers. Radial distance is similar for both solutions for $R > 1$ for all the Stokes numbers considered. Disparities are larger for the $R < 1$ case.

No clear conclusion can be drawn from figure 7.27 where the maximum normalised distance difference is plotted against the Stokes number. The four lines presented, corresponding to solutions calculated with four different parameters of R, have very different patterns. The limit case $R = 1/3$ presents the interval with the largest minimum, ranging about $[0.8, 100]$, approximately. The line corresponding to $R = 7/9$ has the largest range for the difference, from 10^{-1} at $S \approx 10^{-2}$ to over 10^2 at approximately $3 \cdot 10^0$. The two remaining lines oscillate around the interval $[0.04, 6]$. The difference decreases for the smallest values of S in all cases, except for the limit case, $R = 1/3$.

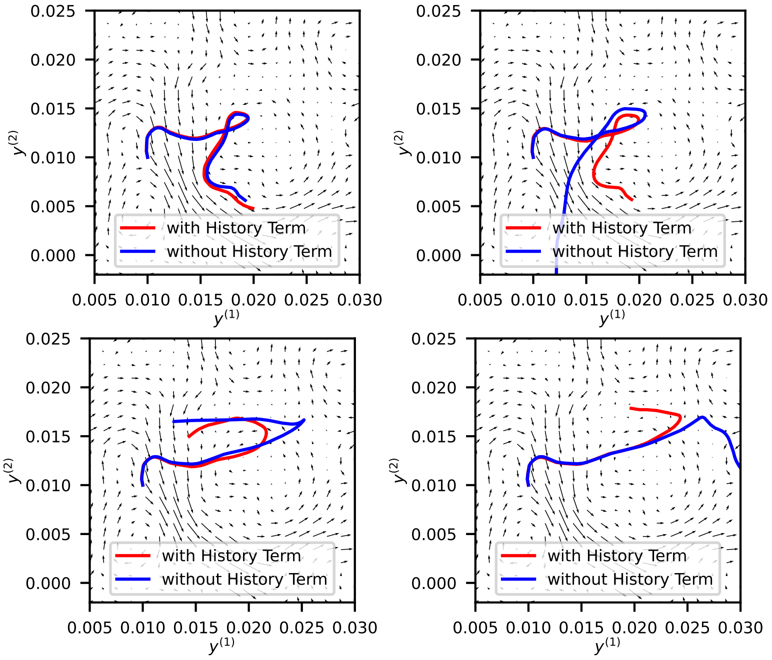

Figure 7.23: Exact trajectories with and without BHT of particles with different Stokes numbers, $S = 0.01$ (top left), $S = 0.1$ (top right), $S = 1$ (bottom left) and $S = 10$ (bottom right), moving in the experimental flow for approximately 5 s. The effective density ratio is $R = 7/9$ and the initial conditions (in dimensional units) are $\boldsymbol{y}(t_0) = (0.01, 0.01)^T$ and $\boldsymbol{q}(0, t_0) = (0, 0)^T$.

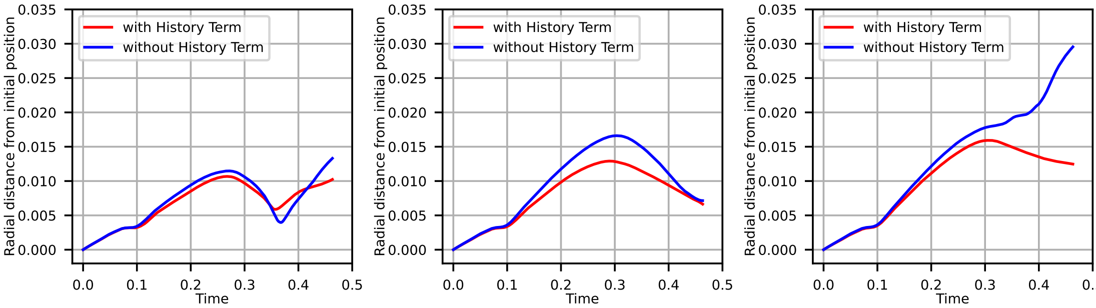

Figure 7.24: Radial distance from the initial position with and without BHT of particles with different Stokes numbers, $S = 0.1$ (left), $S = 1$ (center) and $S = 10$ (right), moving in the experimental flow for 5 s. The effective density ratio is $R = 7/9$ and the initial conditions (in dimensional units) are $\boldsymbol{y}(t_0) = (0.01, 0.01)^T$ and $\boldsymbol{q}(0, t_0) = (0, 0)^T$.

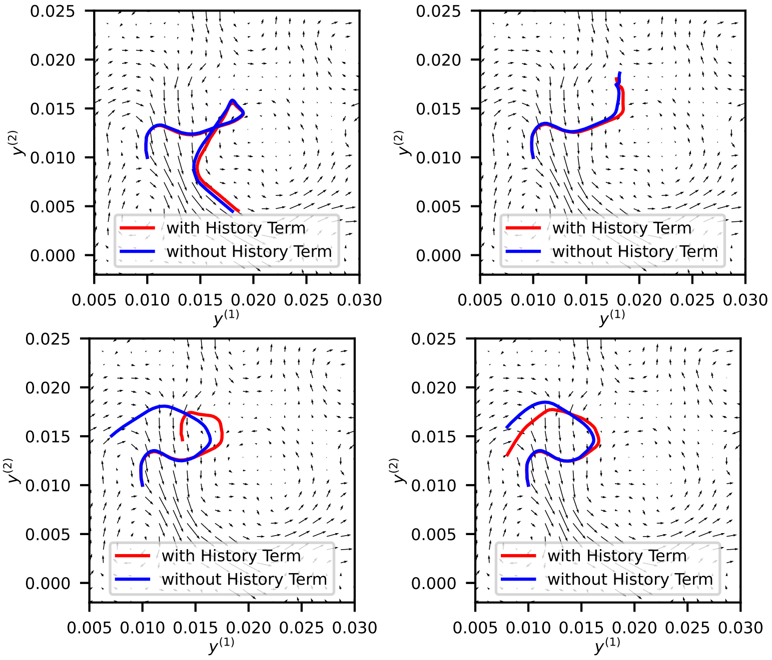

Figure 7.25: Exact trajectories with and without BHT of particles with different Stokes numbers, $S = 0.01$ (top left), $S = 0.1$ (top right), $S = 1$ (bottom left) and $S = 10$ (bottom right), moving in the experimental flow for 5 s. The effective density ratio is $R = {}^{11}\!/_{9}$ and the initial conditions (in dimensional units) are $\boldsymbol{y}(t_0) = (0.01, 0.01)^T$ and $\boldsymbol{q}(0, t_0) = (0, 0)^T$.

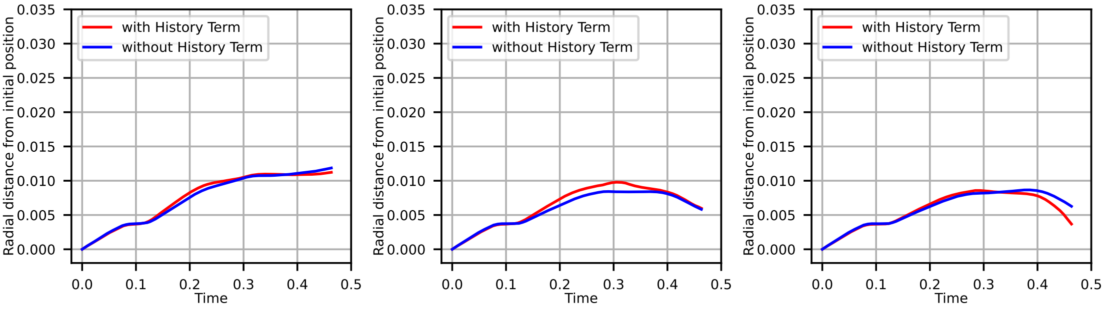

Figure 7.26: Radial distance from the initial position with and without BHT of particles with different Stokes numbers, $S = 0.1$ (left), $S = 1$ (center) and $S = 10$ (right), moving in the experimental flow for 5 s. The effective density ratio is $R = {}^{11}\!/_{9}$ and the initial conditions (in dimensional units) are $\boldsymbol{y}(t_0) = (0.01, 0.01)^T$ and $\boldsymbol{q}(0, t_0) = (0, 0)^T$.

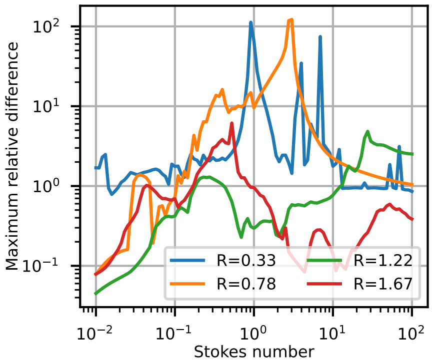

Figure 7.27: Maximum normalised difference between the trajectories calculated with and without BHT against the Stokes number in the experimental flow for 5 s. The initial conditions are $\boldsymbol{y}(t_0) = (0.381045, 0.190523)^T$ and $\boldsymbol{q}(0, t_0) = (0, 0)^T$. Trajectories are calculated for 5 s with a step of $\Delta t = 0.005$ s.

7.2 Influence of the BHT on the clustering behaviour of the particles

The study of individual trajectories overlooks the fact that the initial conditions of the particle strongly influence the particle's path in flows for which there is no spatial symmetry or similarity.

Fluid flows like the quiescent flow, the vortex and the oscillatory background, have some kind of symmetry or similarity and all particle paths are similar to each other independently of the starting point. In the quiescent flow, any particle with a given initial velocity will have the same trajectory and velocity pattern independently of their initial position, since the field is equal anywhere. In the oscillatory background, this also holds true for particles starting at the same initial time, since it is a time-dependent flow that changes with time. The vortex is a point symmetric field and the particle's trajectory depends only on its initial velocity and the distance from the origin. Since initial velocities are equal to the one of the fluid at the initial position and this one grows together with the distance from the origin, all particles are similar from each other, i.e. a particle starting at a given distance from the origin with a given velocity will have a similar trajectory pattern as another one starting at double the distance from the origin, since the velocity also doubles.

In the previous examples, all particle paths are similar to each other and studying a single particle's movement provides a lot of information about how all other particles would move in the field.

Similarity is a rare property in velocity fields but specially in those obtained from experiments and real-world measurements. The double gyre, the Bickley jet and the Faraday flow are examples of flow fields for which there is no clear similarity. In these flows, paths calculated with and without BHT may look more similar for some initial conditions but strongly diverge for others. The study of clusters of particles thus seems more appropriate for these fields, since the exceptional behaviour of a single particle is averaged within the cluster's behaviour.

The relative average difference in the final position of particles computed with and without BHT,

$$\tilde{d} := \frac{1}{N}\sum_{i=1}^{N}\left(\frac{\left\|x_i(t_{\mathrm{end}}) - x_i^{\mathrm{nobht}}(t_{\mathrm{end}})\right\|_2}{\frac{1}{N}\sum_{j=1}^{N}\left\|x_j(t_{\mathrm{end}}) - x_j(t_0)\right\|_2}\right), \tag{7.2}$$

is used in the following subsections as a way to measure the influence of the BHT in the trajectory of a cluster of particles.

7.2.1 Double Gyre

The double gyre presents two time-dependent vortices that move in the x-direction. From the results obtained from the vortex, it is expected that due to the rotating nature of the double gyre, particles will accumulate or scatter around the vortices depending on their density with respect to the one of the fluid: Particles denser than the fluid will scatter, whereas lighter particles will accumulate. These behaviours can be observed in figure 7.28 for lighter particles and figure 7.29 for denser particles at the intermediate and largest Stokes numbers, $S \geq 1$. Figures also show that particle dynamics accelerates in a more chaotic way when BHT is ignored.

All the plots and tables shown here are obtained by calculating the trajectory of $20,301$ particles distributed on a mesh of 101×201 equidistant nodes in the domain $[0,2] \times [0,1]$ for 10 nondimensional time units with a timestep of $\Delta t = 0.01$. The distance between particles is then 0.01. Regarding the initial velocities, particles are initialised with the same velocity as the flow field at the initial position, meaning that they start with zero initial relative velocity.

An initial visual comparison between the final-time positions obtained with and without BHT in figures 7.28 and 7.29 indicates that final positions barely differ for the lowest Stokes number considered, $S = 0.1$, but disparities become clearer for the other values of S used. Data in tables 7.2 confirms this observation. The lowest absolute average distances between solutions are found for the smallest value of S for the two density ratios considered. Average distances grow with S for all density ratios, although growth is faster for the denser particles until they reach similar absolute values. Relative average distance follows the same pattern, although for lighter-than-fluid particles with $S = 10$ the disparity between the solutions represents on average 65 % of the average radial distance.

Table 7.3 exhibits the number of particles that leave the initial domain of the double gyre, i.e. $[0,2] \times [0,1]$, after 10 time units. This table shows that the larger the Stokes number, the more particles leave the initial domain, independently of the value of R. Generally, more particles leave the initial domain when the BHT is neglected, except for $S = 0.1$ where less than 2 % of the particles leave the domain. Denser-than-fluid particles have a higher tendency to leave the domain due to the rotating behaviour of the field.

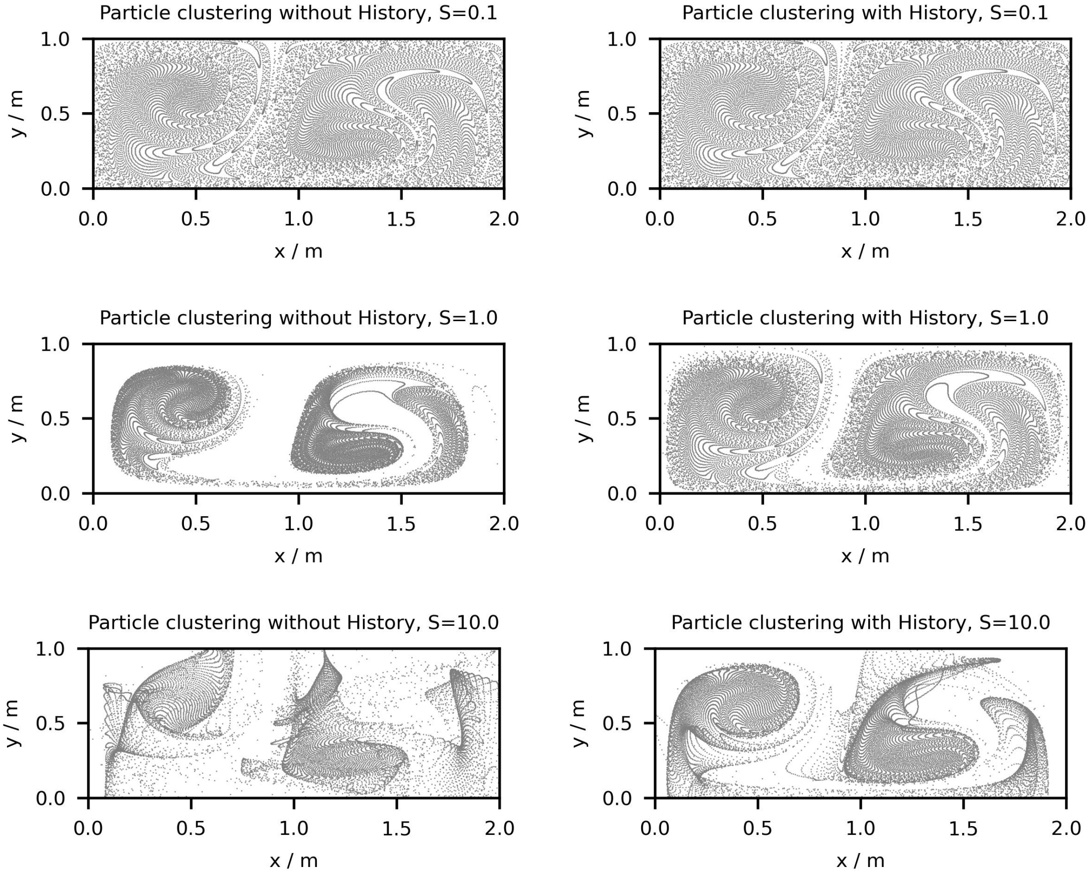

Figure 7.28: Particle positions at final time $t = 10$ time units in the Double Gyre calculated without (left) and with BHT (right). All particles have the same effective density ratio $R = 7/9$. Stokes numbers increase from top to bottom: $S = 0.1$ (top), $S = 1$ (center) and $S = 10$ (bottom).

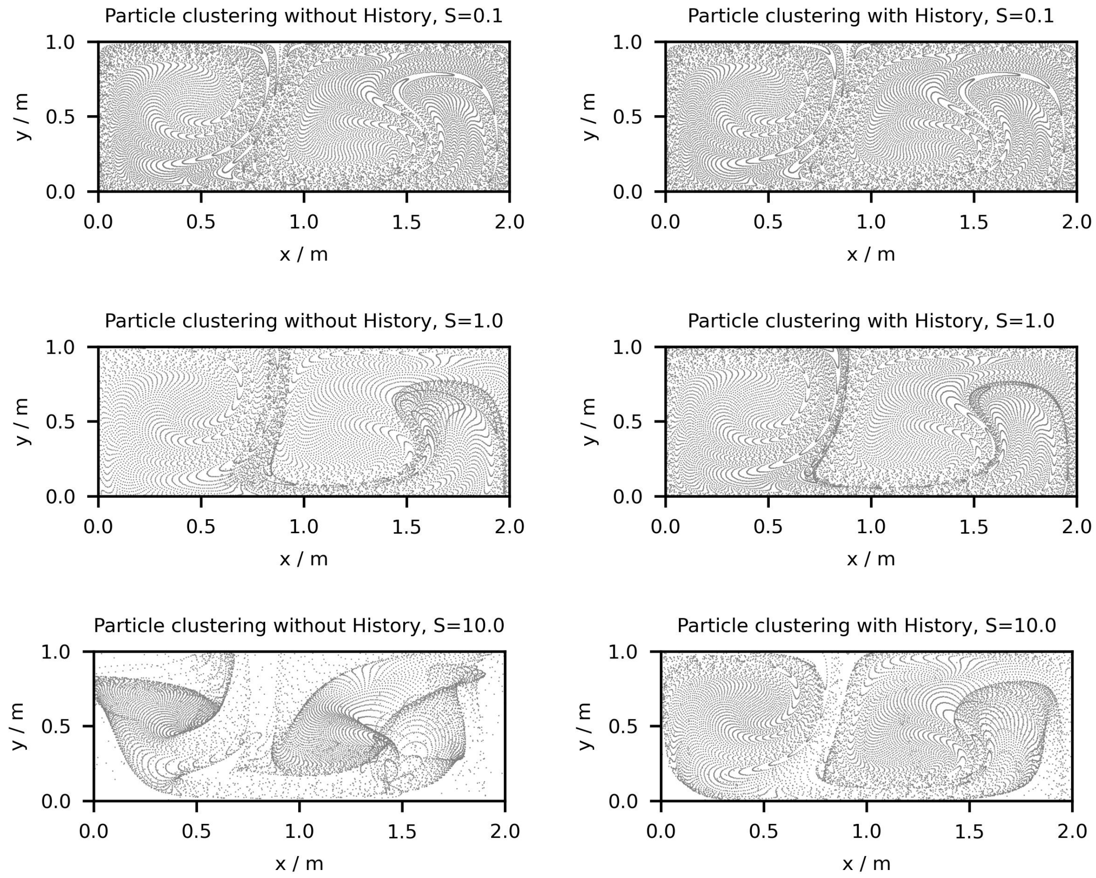

Figure 7.29: Particle positions at final time $t = 10$ time units in the Double Gyre calculated without (left) and with BHT (right). All particles have the same effective density ratio $R = {}^{11}\!/_{9}$. Stokes numbers increase from left to right: $S = 0.1$ (top), $S = 1$ (center) and $S = 10$ (bottom).

Average relative distance and standard deviation			
	$S = 0.1$	$S = 1$	$S = 10$
$R = 7/9$	0.03 ± 0.06	0.34 ± 0.38	0.65 ± 0.75
$R = 11/9$	0.03 ± 0.05	0.53 ± 0.63	0.44 ± 0.56

Average absolute distance and standard deviation			
	$S = 0.1$	$S = 1$	$S = 10$
$R = 7/9$	0.02 ± 0.04	0.23 ± 0.25	0.45 ± 0.52
$R = 11/9$	0.02 ± 0.04	0.41 ± 0.49	0.43 ± 0.55

Table 7.2: Average relative and absolute differences of the final-time positions of particle trajectories in the double gyre calculated with and without the inclusion of the Basset history term.

	History included	$S = 0.1$	$S = 1$	$S = 10$
$R = 7/9$	Yes	0 %	0 %	4.5 %
	No	0 %	0 %	26.4 %
$R = 11/9$	Yes	1.6 %	17.6 %	36.3 %
	No	0 %	39.8 %	44.9 %

Table 7.3: Percentage of particles that leave the initial spatial domain, $[0, 2] \times [0, 1]$, at final time in the double gyre.

7.2.2 Bickley Jet

The data utilised in the plots and tables of this section for the Bickley jet is obtained by calculating the trajectory of 16,281 particles initialised on a grid of 81×201 equidistant nodes on the domain $[0, 20] \times [-4, 4]$ Mm^2. Particles are therefore separated by a distance of approximately $0.1\,\mathrm{Mm}$. The time interval considered is approximately $[10, 30] \cdot T$ d and the timestep $\Delta t = 0.02 \cdot T$ d, where $T = 1.77/5.414$. Horizontal symmetry is implemented, so that particles leaving the domain on the right appear again on the left hand side. Like in the previous field, particles start with the same velocity as the fluid at their initial position.

Figures 7.30 and 7.31 show the final time positions for particles with different characteristics moving in the Bickley jet. In the example with lighter-than-fluid particles, figures clearly show a stronger clustering effect when the BHT is ignored already for $S \geq 1$. On the other hand, heavier particles exit the vortices and accumulate around the middle jet. In both cases and as observed for the double gyre, particle clusters seem more erratic when the BHT is not used in the calculation of the particle paths.

Tables 7.4 show that the minimum (absolute and relative) average distance between solutions is found again for the smallest value of S, constantly growing with S. In contrast to the double gyre, distances between the final time positions grow at a similar rate for both density ratios, reaching both maximums for $S = 10$.

The number of particles leaving the initial vertical domain, $[-4, 4]$, showed in table 7.5, remains low for low and medium Stokes numbers and grows considerably at the highest Stokes number. For $S \leq 1$ the number of particles outside the domain at final time remains

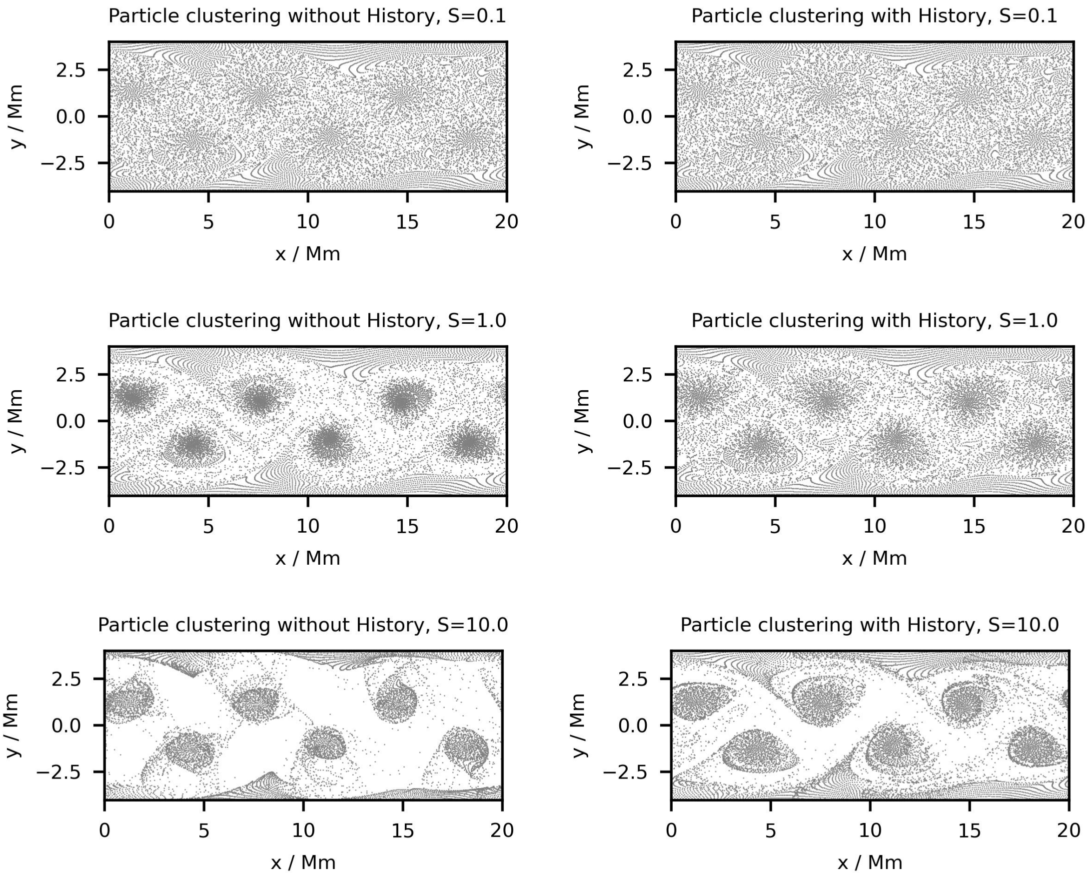

Figure 7.30: Particle positions at final time $t = 10\,\mathrm{d}$ (approximately 30.58 nondimensional time units) in the Bickley jet, calculated without (left) and with BHT (right). All particles have the same effective density ratio $R = 7/9$. Stokes numbers increase from top to bottom: $S = 0.1$ (top), $S = 1$ (center) and $S = 10$ (bottom).

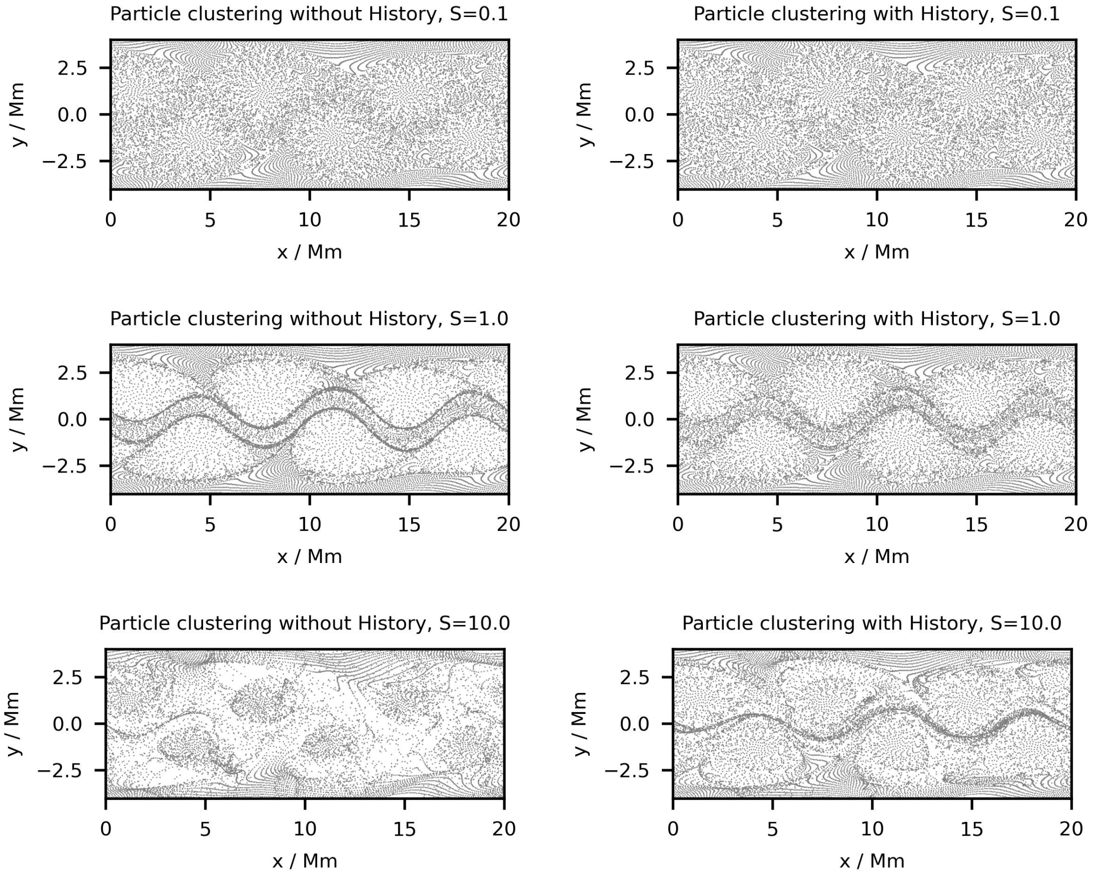

Figure 7.31: Particle positions at final time $t = 10\,\mathrm{d}$ (approximately 30.58 nondimensional time units) in the Bickley jet, calculated without (left) and with BHT (right). All particles have the same effective density ratio $R = {}^{11}\!/_{9}$. Stokes numbers increase from top to bottom: $S = 0.1$ (top), $S = 1$ (center) and $S = 10$ (bottom).

Average relative distance and standard deviation			
	$S = 0.1$	$S = 1$	$S = 10$
$R = 7/9$	0.04 ± 0.23	0.28 ± 0.56	0.45 ± 0.69
$R = 11/9$	0.04 ± 0.23	0.26 ± 0.54	0.48 ± 0.73

Average absolute distance and standard deviation			
	$S = 0.1$	$S = 1$	$S = 10$
$R = 7/9$	0.46 ± 2.68	3.10 ± 6.25	5.04 ± 7.76
$R = 11/9$	0.48 ± 2.70	3.02 ± 6.21	5.58 ± 8.54

Table 7.4: Average relative as well as absolute distances between the final time positions calculated with and without History term.

	History included	$S = 0.1$	$S = 1$	$S = 10$
$R = 7/9$	Yes	1.7 %	1.7 %	4.6 %
	No	1.7 %	1.6 %	26.1 %
$R = 11/9$	Yes	1.7 %	1.7 %	3.3 %
	No	1.7 %	1.8 %	24.8 %

Table 7.5: Percentage of particles that are outside the initial vertical domain $[-4, 4]$ Mm at final time in the Bickley jet.

basically constant. These numbers largely increases for $S = 10$, reaching similar values for both density ratios when the BHT is present: 4.6 % particles for $R = 7/9$ and 3.3 % for $R = 11/9$; and overshooting when the BHT is not present: 26.1 % particles for $R = 7/9$ and 24.8 % for $R = 11/9$.

7.2.3 Experimental flow

Data for the Faraday flow is obtained by initialising 40.401 particles on a mesh of 201×201 equidistant nodes, separated by approximately 0.000 352 m, on the domain $[0, 0.07039433] \times [0, 0.052487]$ m^2. Solutions are run for 10 s, with a timestep of $\Delta t = 0.01$ s. Like in the previous two examples, particles start with zero initial relative velocity.

Figures 7.32 and 7.33 show the final time positions for particles with different characteristics moving in the experimentally-obtained velocity field. Although the field data is restricted to the domain $[0, 0.07039433] \times [0, 0.052487]$ m^2, particles are allowed to leave this initial domain, where the field is set to zero. This makes particle dynamics to suddenly change and continue as relaxing particles as soon as they reach the boundary, so that it is impossible for particles to come back to the initial domain once they are outside it. There is thus a tendency for particles to accumulate around the boundaries of the domain, which is not shown in these plots. However, these plots show that the dispersive dynamics accelerates if the BHT is omitted in the calculations.

Table 7.6 shows very large average distances for $S = 10$, reaching 0.0503 and 0.0478 in absolute numbers for $R = 7/9$ and $R = 11/9$, respectively. These values almost correspond to the value of the width/height of the initial spatial domain and represent over twice the

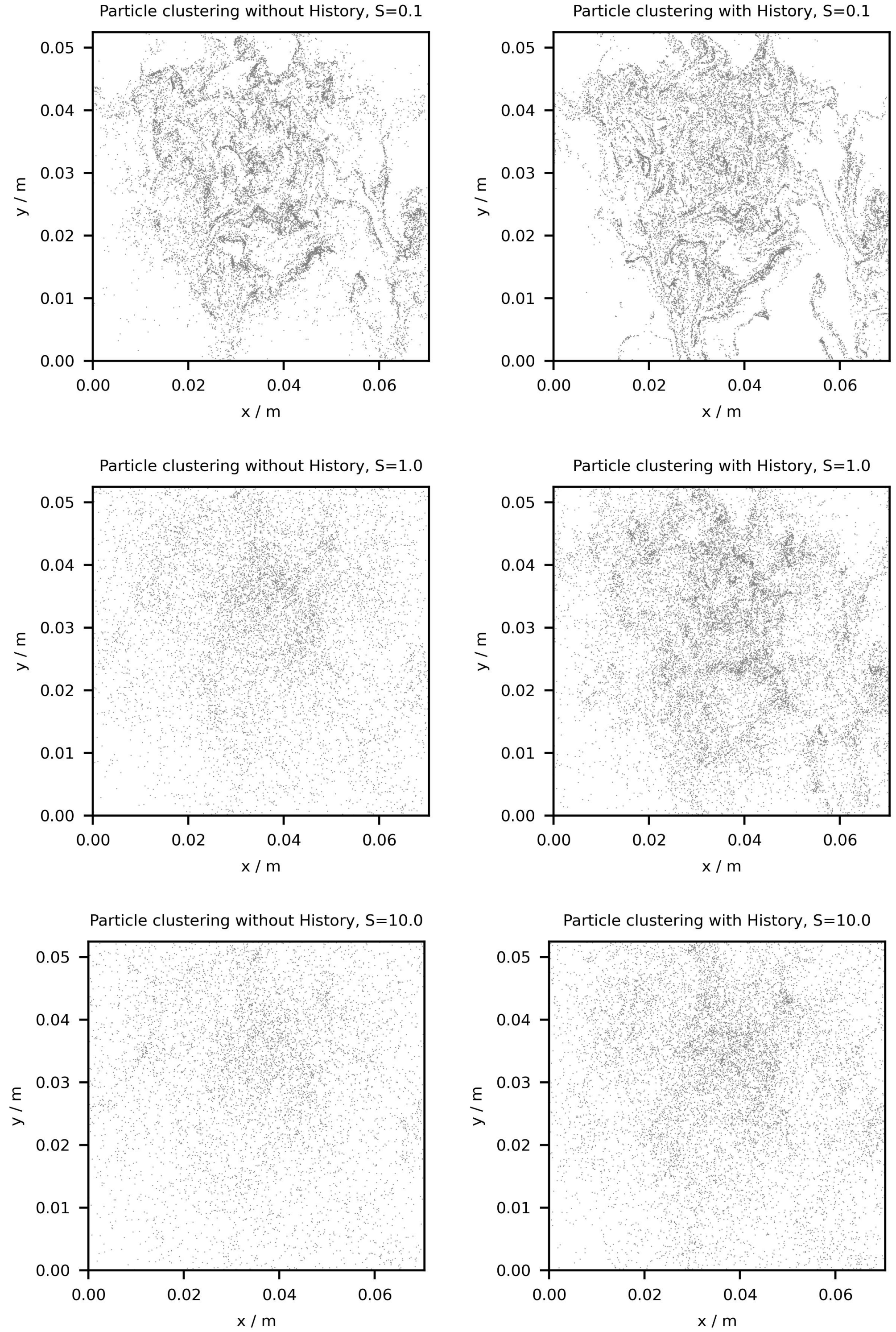

Figure 7.32: Particle positions at final time $t = 10$ time units in the Faraday flow calculated without (left) and with BHT (right). All particles have the same effective density ratio $R = 7/9$. Stokes numbers increase from top to bottom: $S = 0.1$ (top), $S = 1$ (center) and $S = 10$ (bottom).

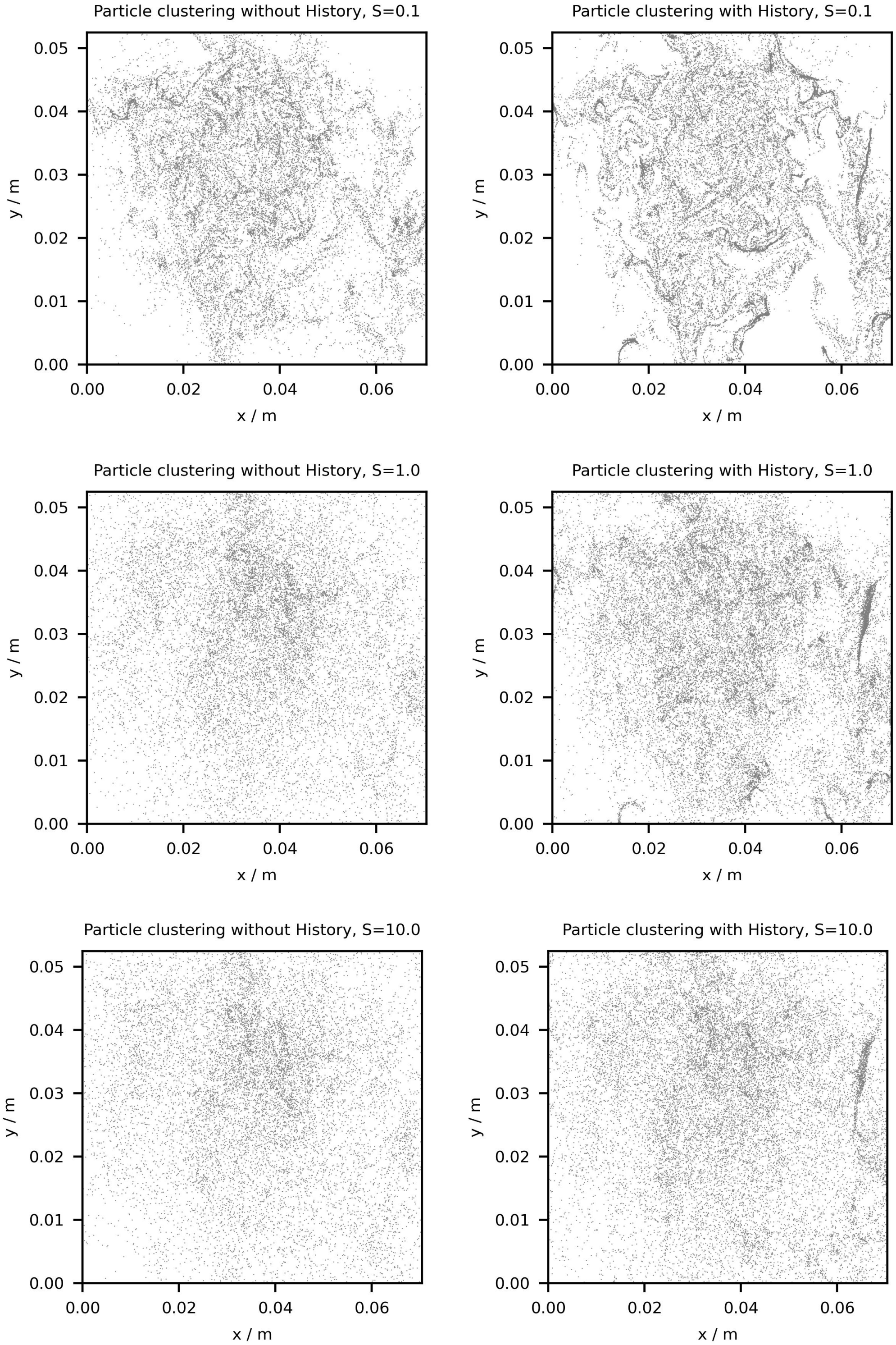

Figure 7.33: Particle positions at final time $t = 10$ time units in the Faraday flow calculated without (left) and with BHT (right). All particles have the same effective density ratio $R = {}^{11}/_{9}$. Stokes numbers increase from top to bottom: $S = 0.1$ (top), $S = 1$ (center) and $S = 10$ (bottom).

Average relative distance and standard deviation			
	$S = 0.1$	$S = 1$	$S = 10$
$R = 7/9$	0.69 ± 0.58	2.45 ± 1.59	1.63 ± 1.13
$R = 11/9$	0.75 ± 0.62	1.99 ± 1.49	1.47 ± 1.20

Average absolute distance and standard deviation			
	$S = 0.1$	$S = 1$	$S = 10$
$R = 7/9$	0.0005 ± 0.0004	0.0024 ± 0.0016	0.0033 ± 0.0023
$R = 11/9$	0.0005 ± 0.0004	0.0018 ± 0.0014	0.0022 ± 0.0018

Table 7.6: Average relative and absolute distances between the final time positions calculated with and without history.

	History included	$S = 0.1$	$S = 1$	$S = 10$
$R = 7/9$	Yes	50.8 %	56.9 %	73.6 %
	No	56.1 %	78.6 %	84.4 %
$R = 11/9$	Yes	26.5 %	35.5 %	50.9 %
	No	52.1 %	64.6 %	68.2 %

Table 7.7: Percentage of particles that are outside the initial domain at final time in the Faraday Flow.

average distance travelled by the particle. Like in the other fields, the difference between both solutions grows with S.

The percentages of particles leaving the initial domain of the Faraday flow are provided in table 7.7. It is interesting that in almost all cases, half or more than half of the particles leave the initial domain. This could be due to the no-way-back effect at the boundary, although it is still surprising because it indicates that a high number of particles reach the boundary of the domain. The high turbulent behaviour of the field must be one of the drivers. The amount of particles leaving the domain gets incremented when the BHT is not used. This number doubles for the heaviest particle case with $S = 0.1$, compared to the 6% increase for the lightest particle. For the other Stokes numbers considered, the percentages increase between a 10 to a 20%.

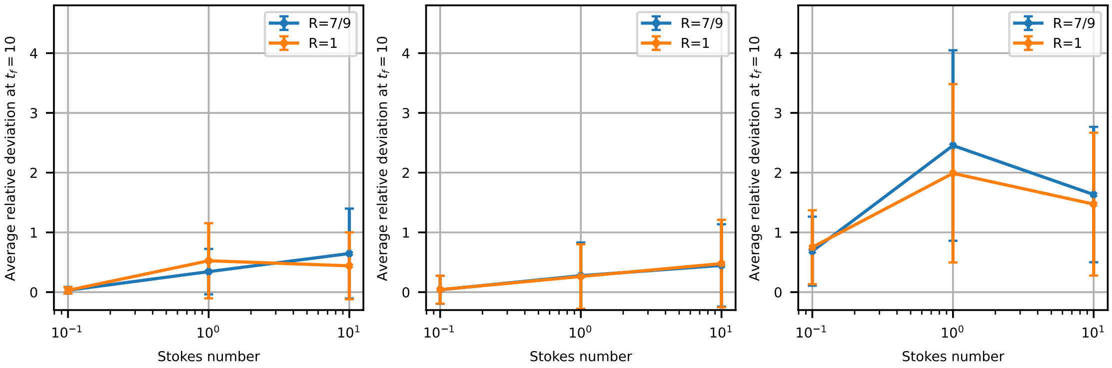

Figure 7.34: Average relative difference in the final time trajectories calculated with and without BHT for particles in the double gyre (left), the Bickley jet (center) and the Faraday flow (right).

7.3 Lagrangian Coherent Structures

The study of transport within a flow field with Lagrangian Coherent Structures (LCS) is a widely-investigated subject in fluid dynamics. Examples of these are the studies of oil spills in the ocean [9, 48, 49, 45], urban pollution dispersion [68] and more (see Sudharsan et al. (2016) [66] for more references).

Shadden et al. (2005) [62] defines the LCSs as “ridges of Finite-Time Lyapunov Exponents (FTLE) fields” or “special gradient lines of the FTLE field that are transverse to the direction of minimum curvature”. In the online tutorial created by the Shadden lab of the University of California Berkeley [63], an FTLE is defined as a “scalar value which characterizes the amount of stretching about the trajectory of point $\boldsymbol{y} \in D$ over the time interval $[t_0, t]$”. The appropriate definitions are provided below.

Definition 7.1 (Flow map)**.** Let the open set $D \subset \mathbb{R}^n$ be the spatial domain covered by a fluid, with typically $n = 2$ or $n = 3$ and $[t_0, t]$ be the time interval in which the particle's trajectory is calculated. Then, given a velocity field $\boldsymbol{u}$ in D, the function

$$\phi_{t_0}^{t} : D \to D \tag{7.3a}$$

$$\boldsymbol{y}_0 \mapsto \phi_{t_0}^{t}(\boldsymbol{y}_0) = \boldsymbol{y}(t; t_0, \boldsymbol{y}_0), \tag{7.3b}$$

that maps particles starting at points $\boldsymbol{y}_0 \in D$ at time t_0 to their position at time t within D, is called the *flow map.*

The flow map is therefore the function that outcomes the particle trajectories given their initial conditions. Depending on the nature of the FTLEs, trajectories should be calculated by using different types of formulas. In this chapter, the flowmap consists on integrating the Maxey-Riley equation (2.6) twice for the case of zero initial relative velocity, i.e. $\boldsymbol{v}(t_0) = \boldsymbol{u}(\boldsymbol{y}(t_0), t_0)$. The integration of the full MRGE (with BHT) is carried out by using the FD2 + IMEX2 scheme presented in chapter 5. On the other hand, the MRGE without BHT is integrated by using the Explicit Runge-Kutta method of order 5(4) provided within the *solve_ ivp* solver within Python's SciPy library [77].

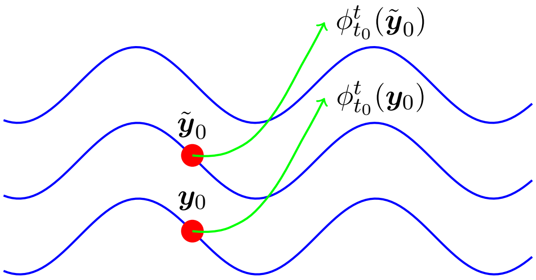

Figure 7.35: Representation of the flow map function applied on two points, $\boldsymbol{y}_0$ and $\tilde{\boldsymbol{y}}_0$.

Definition 7.2 (Deformation gradient tensor [61])**.** Consider a flow map $\phi^t_{t_0}$. The *deformation gradient tensor* is defined as the Jacobian of the flow map with respect to the spatial variables, namely

$$D\phi^t_{t_0} := \begin{bmatrix} \frac{\partial(\phi^t_{t_0}(\boldsymbol{y}_0))^{(1)}}{\partial y^{(1)}} & \cdots & \frac{\partial(\phi^t_{t_0}(\boldsymbol{y}_0))^{(1)}}{\partial y^{(n)}} \\ \vdots & \ddots & \vdots \\ \frac{\partial(\phi^t_{t_0}(\boldsymbol{y}_0))^{(n)}}{\partial y^{(1)}} & \cdots & \frac{\partial(\phi^t_{t_0}(\boldsymbol{y}_0))^{(n)}}{\partial y^{(n)}} \end{bmatrix}. \tag{7.4}$$

Following Garaboa-Paz and Pérez-Muñuzuri (2015)'s example [30], the Jacobian is approximated using finite-difference methods.

Definition 7.3 (Finite-Time Lyapunov Exponents [61])**.** Given a velocity field $\boldsymbol{u}$ extended over an open set $D \subset \mathbb{R}^n$ and a flow map $\phi^t_{t_0}$, the *Finite-Time Lyapunov Exponent* (FTLE) at a point $\boldsymbol{y}_0$ is defined as

$$\sigma^t_{t_0}(\boldsymbol{y}_0) := \frac{1}{(t-t_0)} \ln \sqrt{\lambda_{max}(\Delta)}, \tag{7.5}$$

where $\lambda_{max}(\Delta)$ is the largest eigenvalue of the Cauchy-Green deformation tensor, $\Delta = (D\phi^t_{t_0})^* \, D\phi^t_{t_0}$.

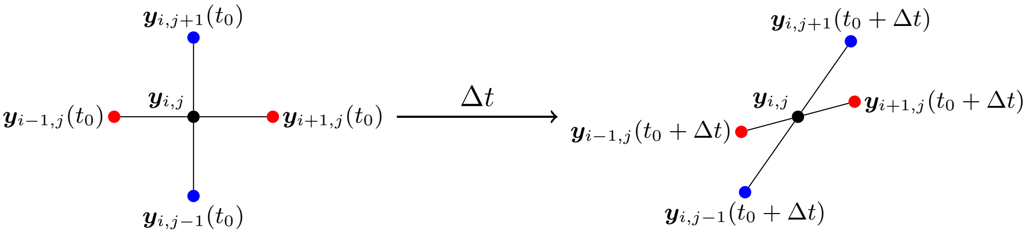

Figure 7.36: Example of the general stencil used for the calculation of the FTLE, $\sigma^t_{t_0}(\boldsymbol{y}_{i,j})$, at position $\boldsymbol{y}_{i,j}$ and the movement of the particles in the stencil after a time Δt.

Definition 7.4 (Lagrangian Coherent Structures (LCS))**.** Given a velocity field $\boldsymbol{u}$ extended over an open set $D \subset \mathbb{R}^n$, a flow map $\phi^t_{t_0}$ and its correspondent FTLE field, the *Lagrangian Coherent Structures* (LCS) are defined as the "ridges in the FTLE field". These ridges are "special gradient lines of the FTLE field that are transverse to the direction of minimum curvature" [62].

Most of the available analysis of the FTLE for inertial particles available in the literature to our knowledge is done using the Maxey-Riley-Gatignol Equation without History Term [7, 21, 30, 66] or directly integrating the velocity field [62, 61]. The study done in the sections 7.1 and 7.2 indicates that neglecting the History Term has a direct influence on the particle trajectories for some parameter values. Hence, the BHT will most likely have an indirect influence in the FTLE and the LCS.

The following subsections present a study of the influence of the BHT in the calculation of the FTLEs for inertial particles for the three velocity fields from section 6: the double gyre, the Bickley jet and the Faraday flow. In all these three fields, the calculation of the FTLE is done by recycling the data used in the previous section for plotting the final time particle position, so that the particle settings are the same as in that section. The double gyre is a typical toy example in the calculation of the FTLEs and LCS and hence, there exists an extended literature available about it in which the FTLEs and LCS for this field are studied. [61, 62, 66, 6].

For each single one of the flow fields, two figures with nine plots are shown. Each figure corresponds to a different density ratio. There will always be one figure for lighter-than-fluid particles ($R < 1$) and another one for denser-than-fluid particles ($R > 1$). Within each figure there are three columns. The left column corresponds to the case of FTLEs calculated without BHT, the central one to the FTLEs with BHT and the right column to the relative difference between both plots. Plots with the lowest Stokes number are placed on the top row ($S = 0.1$), plots with middle Stokes number ($S = 1$) on the middle row and plots with the largest Stokes numbers on the bottom row ($S = 10$).

The relative FTLE difference for inertial particles in % are calculated as follows

$$\Delta\sigma^t_{t_0,relative}(\boldsymbol{y}) := 100\, \frac{\sigma^t_{t_0,History}(\boldsymbol{y}) - \sigma^t_{t_0,Stokes}(\boldsymbol{y})}{||\sigma^t_{t_0,History}||_{l_\infty(D)}} \tag{7.6}$$

where $D \subset \mathbb{R}^2 \times [0, T]$.

7.3.1 The Double Gyre

The double gyre is a typical example in the study of LCS. Examples of papers in which FTLE and LCS in the double gyre were studied are Shadden et al. (2005) [62] and Sudharsan et al. (2016) [66]. Shadden et al. (2005) calculated the FTLEs by numerically integrating the field directly, whereas Sudharsan et al. (2016) used the MRGE without BHT.

Figure 7.37 shows the FTLE plots for lighter-than-fluid particles ($R = 7/9$). Like in the case of particle clustering, plots for $S = 0.1$ remain quite unchanged independently of whether the BHT is included or not. Differences start to be noticeable for $S \geq 1$. FTLEs for the case $S = 1$ with and without history term are similar but start presenting disparities in the areas with the lowest FTLE values as well as in the most left path of the LCS, showing a slight shift to the left when the BHT is excluded. Discrepancies become substantial for the largest Stokes number considered, $S = 10$. Without BHT, additional LCS appear in distinct areas and the previous LCS observed in the plots with lower S splits into two. Interestingly, at the highest Stokes number, these new LCS do not appear when the BHT is considered and a similar pattern to the previous ones remains. Differences between both FTLE plots are substantial in certain areas, reaching up to ±100%.

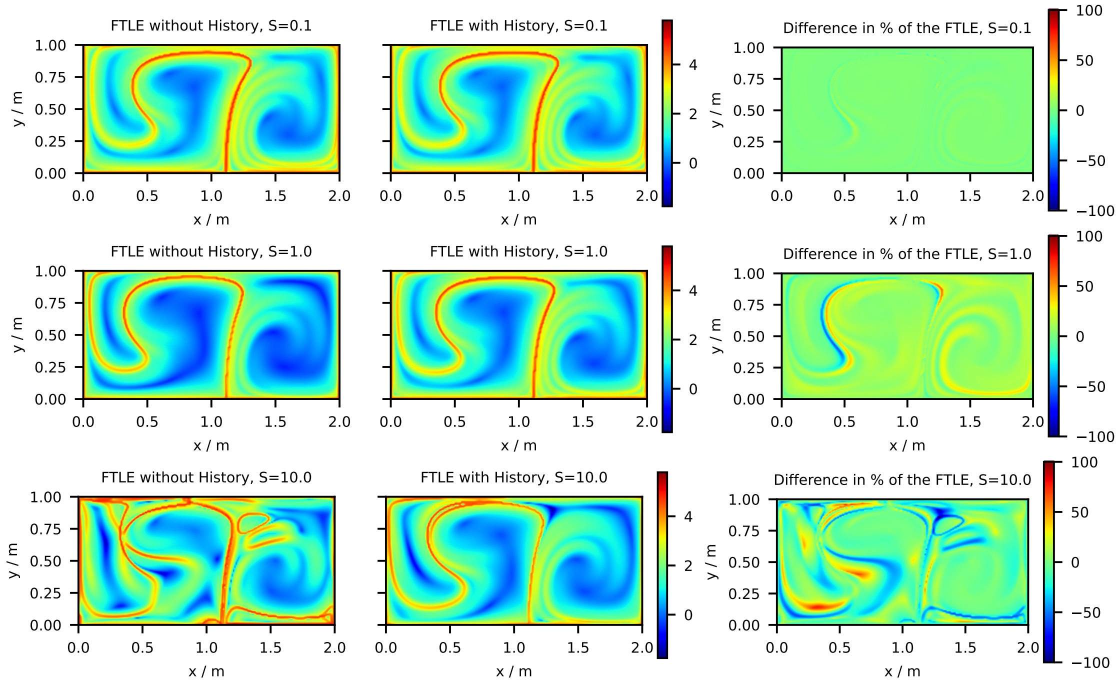

Figure 7.37: FTLEs for lighter-than-fluid particles ($R = 7/9$) and three Stokes numbers, $S = 0.1$ (top), $S = 1$ (center), $S = 10$ (bottom), moving in the double gyre. Particle settings are the same as the ones used in figure 7.28. Left and center columns show the FTLEs computed with trajectories calculated without (left) and with BHT (middle). The right-most column shows the relative difference in % of the FTLE.

Figure 7.37 displays the same plots for the heavier particle with $R = 11/9$. Again, disparities are barely noticeable for $S = 0.1$. This changes noticeably for larger Stokes numbers, since the LCS patterns start to change even for $S = 1$. This makes sense since heavier particles tend to be ejected by the vorteces and scatter more. For $S = 1$, the central LCS splits into three and differences are clearly visible over M. The difference plot on the right most column indicates a clear dominance of the blue areas, that demonstrate a more powerful overestimate of the FTLE when BHT is ignored. For the largest Stokes number $S = 10$, LCS overtake many areas of the domain M with and without BHT. However the FTLE plots without BHT again show a more disorderly pattern, manifesting a stabilising behaviour of the BHT.

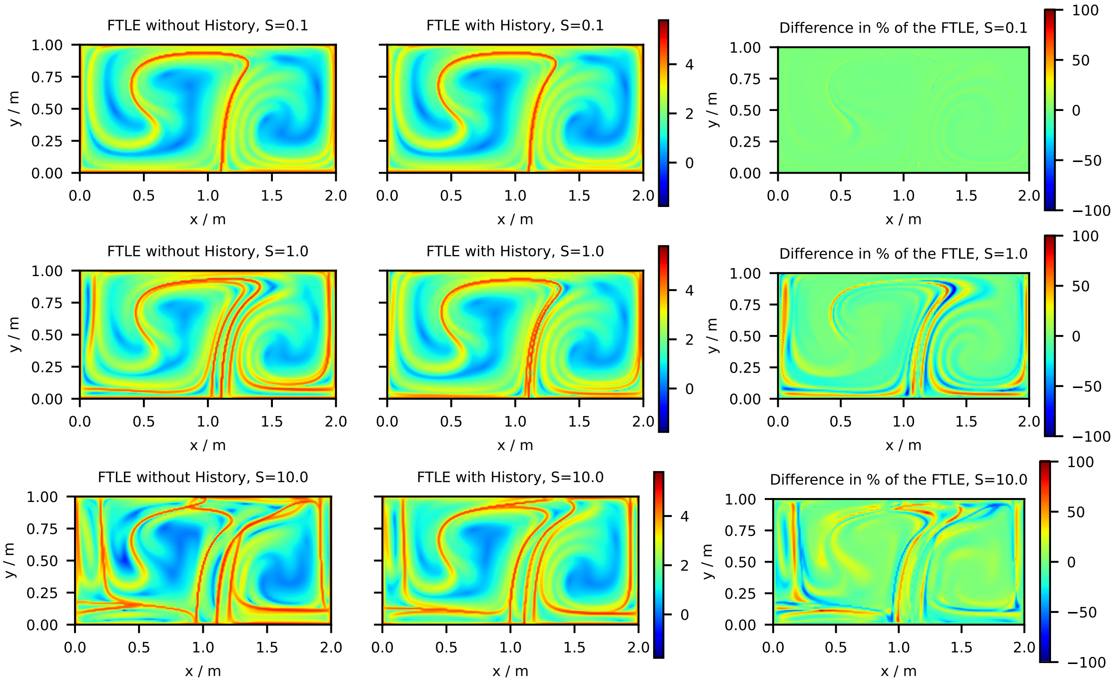

Figure 7.38: FTLEs for heavier-than-fluid particles ($R = 11/9$) and three Stokes numbers, $S = 0.1$ (top), $S = 1$ (center), $S = 10$ (bottom), moving in the Double Gyre. Particle settings are the same as the ones used in figure 7.29. Left and center columns show the FTLEs computed with trajectories calculated without (left) and with BHT (middle). The right-most column shows the relative difference in % of the FTLE.

7.3.2 LCS in the Bickley Jet

Figures 7.39 and 7.40 show the FTLE field and their differences in the same way as shown for the Double Gyre. For $S = 0.1$ and independently of R, differences in the FTLE fields with and without BHT are mostly small, although more noticeable than for the double gyre. This could indicate that the BHT becomes more relevant in more complex flow fields, even if S is small.

For $R = 7/9$ and $S = 1$, disagreements in the FTLE are small and they mainly accumulate on one of the vortices and along the central jet. For the highest Stokes number, $S = 10$, the FTLE start to present an erratic behaviour, with many LCS with small filaments, that accumulate around the central jet and one of the vortices. Without BHT these filaments appear close to each other in small areas, whereas with BHT these filaments form ovals within the central jet. Differences spread out over the whole domain, accumulating around the vortices and the middle jet but without a clear tendency.

On the other hand, the FTLE patter for heavier particles with $R = 11/9$ is different. For $S = 1$, differences in the FTLE are small and accumulate around the vortices. On the contrary, for the largest Stokes number, differences concentrate around the central jet with a clear overestimation of the FTLE when the BHT is neglected. In fact, the FTLE pattern without history are more chaotic than the ones with history. The LCS in this case start to overtake more areas of the domain, whereas the FTLE patter with BHT is very similar to the one for $S = 1$, indicating a smoother transition in the FTLE when the BHT is included.

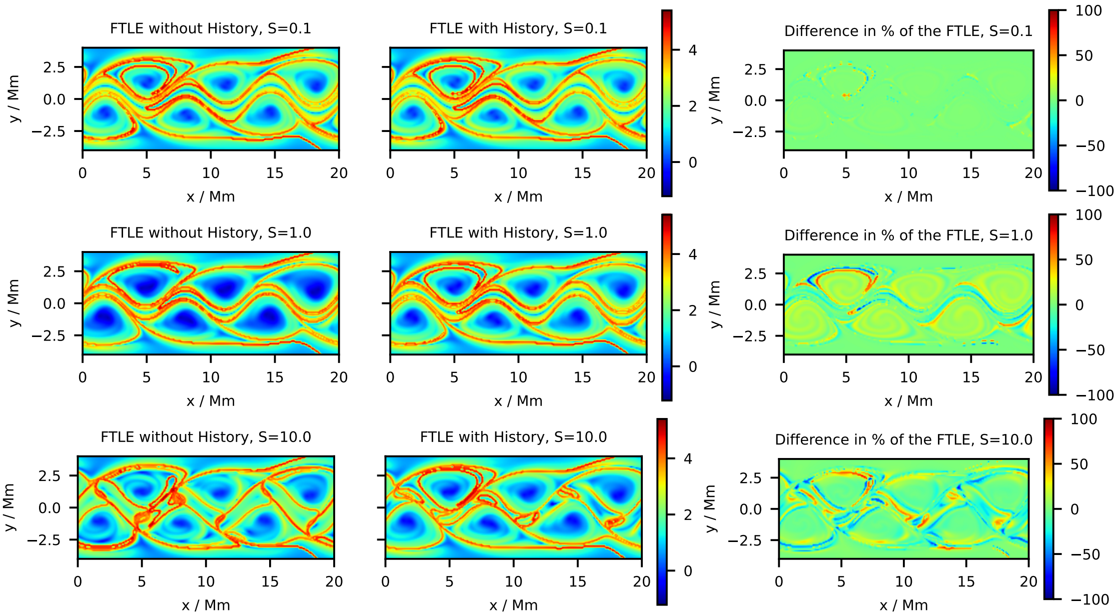

Figure 7.39: FTLEs for lighter-than-fluid particles ($R = 7/9$) and three Stokes numbers, $S = 0.1$ (top), $S = 1$ (center), $S = 10$ (bottom), moving in the Bickley jet. Particle settings are the same as the ones used in figure 7.30. Left and center columns show the FTLEs computed with trajectories calculated without (left) and with BHT (middle). The right-most column shows the relative difference in % of the FTLE.

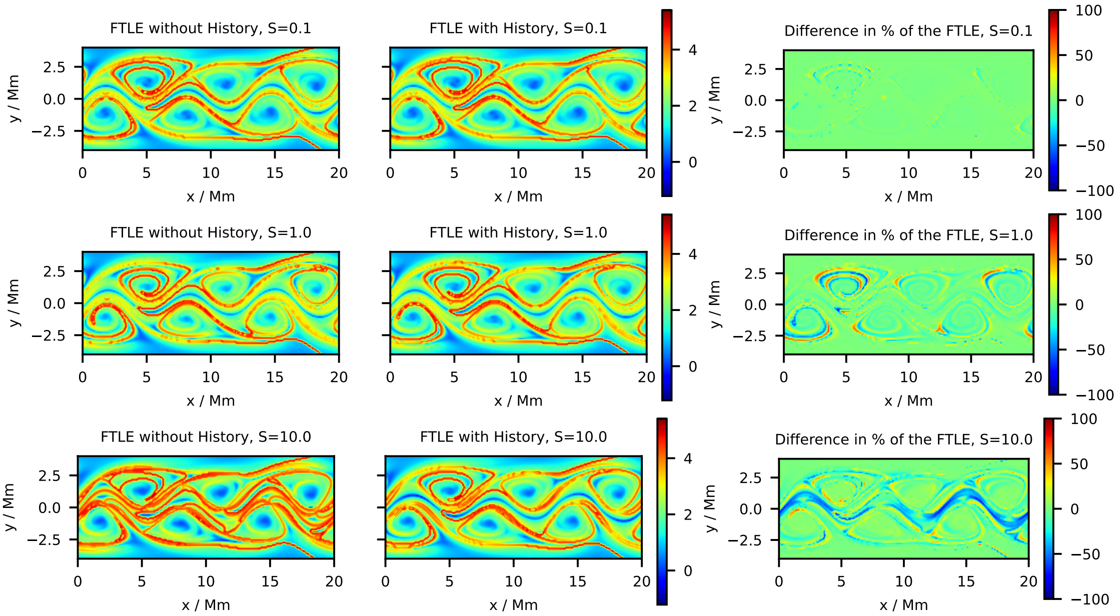

Figure 7.40: FTLEs for heavier-than-fluid particles ($R = 11/9$) and three Stokes numbers, $S = 0.1$ (top), $S = 1$ (center), $S = 10$ (bottom), moving in the Bickley Jet. Particle settings are the same as the ones used in figure 7.31. Left and center columns show the FTLEs computed with trajectories calculated without (left) and with BHT (middle). The right-most column shows the relative difference in % of the FTLE.

7.3.3 LCS in the Faraday flow

Figures 7.41 and 7.42 show the FTLE and difference plots for the Faraday flow.

For the lighter-than-fluid particles (Figure 7.41) with $S = 0.1$, the FTLE plots are already different, with higher FTLE values without BHT than with BHT. In fact, the difference plot shows a predominantly green and blue plot, meaning that there is a general tendency to overestimate the FTLE without BHT.

Differences are also obvious for $S = 1$, where there is a generalised increase on the FTLE, but specially for the case without BHT, where red colours are already predominant over the initial domain. The difference plot is mainly covered with blue areas, indicating again an overestimate of the FTLE when the BHT is neglected. For $S = 10$, the change in the FTLE plot, with respect to the $S = 1$ plot, for the case without history is not very sudden, whereas an overtake of the high FTLE is already noticeable on the plot with history. The percentages of particles leaving the initial domain are very high, $73.6\% and 84.4\%$, and it is therefore clear that the no-return feature of the boundary has a clear influence on the increase of the FTLE values. In this case, differences in the FTLE values are small.

For the denser-than-fluid particles (Figure 7.42) and $S = 0.1$, disparities seem small, with some higher FTLE values for the case without history, that is verified with the green and blue areas in the difference plot. Some of these areas show a very intense blue, indicating differences of about $-+100\%$ in some areas. For $S = 1$, the plot presents a very similar pattern as for the lighter-than-fluid particles: A general increase in the FTLE. The difference plot shows many zones with deep blue, pointing out many areas where the FTLE without BHT are larger than the ones with BHT. For the largest Stokes number, $S = 10$, the increase in the FTLE is generalised and plots are quite similar with and without BHT. Red areas therefore appear within most of the domain. The differences plot displays an overtake of light blue areas (small negative FTLE difference) together with some areas in yellow, demonstrating some convergence between both FTLE plots.

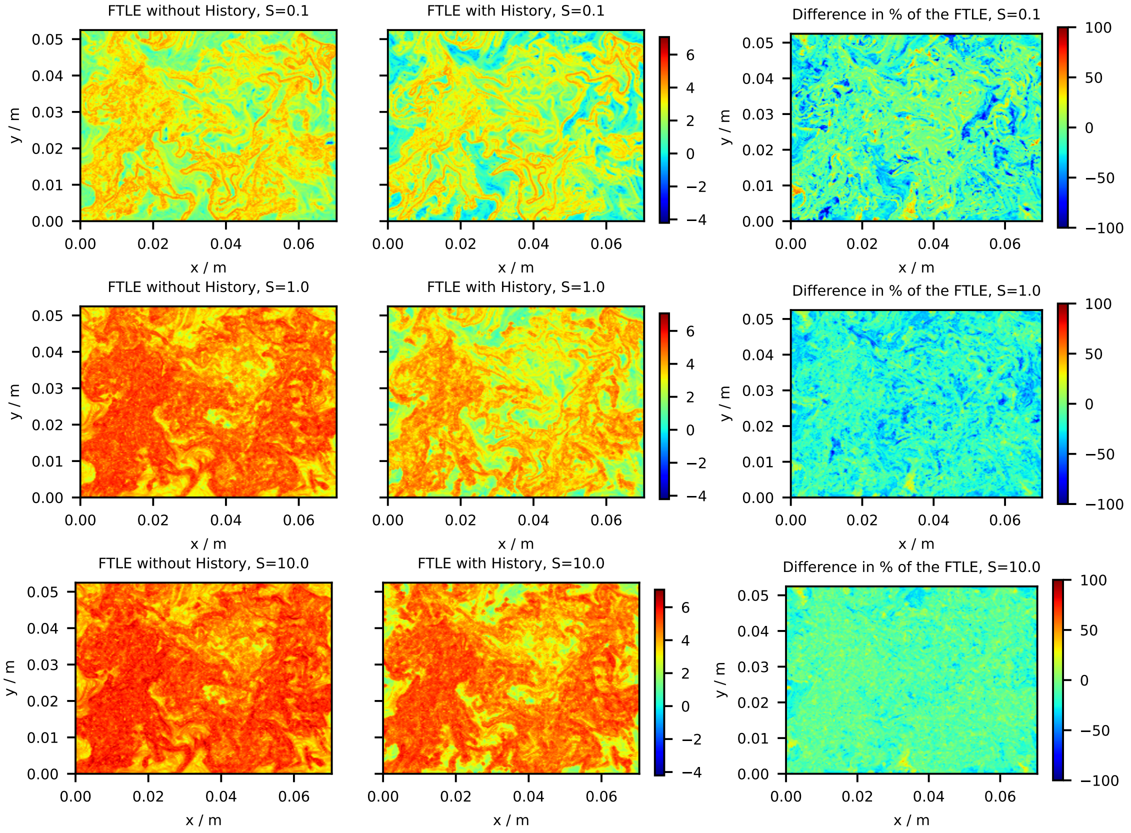

Figure 7.41: FTLEs for lighter-than-fluid particles ($R = 7/9$) and three Stokes numbers, $S = 0.1$ (top), $S = 1$ (center), $S = 10$ (bottom), moving in the Faraday flow. Particle settings are the same as the ones used in figure 7.32. Left and center columns show the FTLEs computed with trajectories calculated without (left) and with BHT (middle). The right-most column shows the relative difference in % of the FTLE.

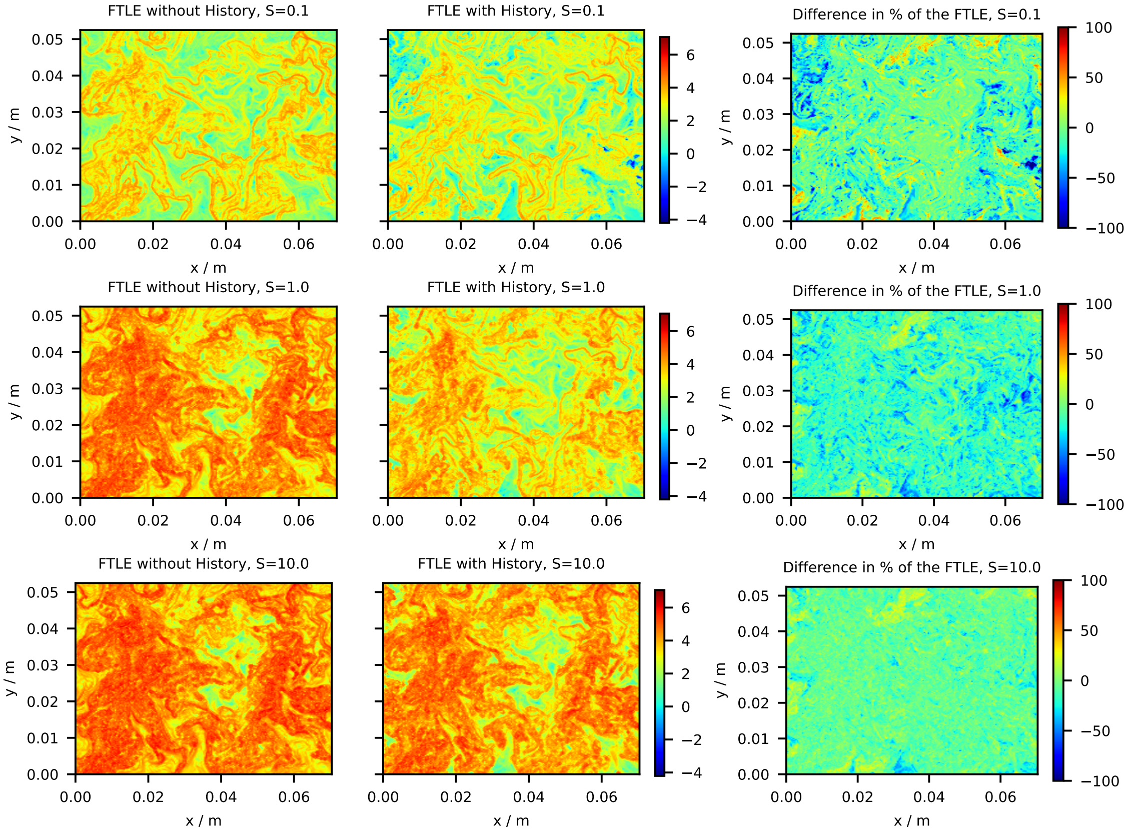

Figure 7.42: FTLEs for heavier-than-fluid particles ($R = {}^{11}\!/_{9}$) and three Stokes numbers, $S = 0.1$ (top), $S = 1$ (center), $S = 10$ (bottom), moving in the Faraday flow. Particle settings are the same as the ones used in figure 7.33. Left and center columns show the FTLEs computed with trajectories calculated without (left) and with BHT (middle). The right-most column shows the relative difference in % of the FTLE.

8

Conclusions

This dissertation investigates the development and analysis of novel finite difference-based numerical methods for solving the Maxey-Riley-Gatignol equation with Basset-Boussinesq history term and compares accuracy and runtimes against the already-existing numerical schemes provided in Prasath et al. (2019) [53] and Daitche (2013) [20]. Additionally, the influence of the BHT on particle trajectories and large-scale features for different flows is examined and evaluated, providing a reference for future research on when the BHT can be neglected with a minor impact.

The numerical schemes were programmed in Python, calculating and storing all data with double precision. Python is a high level language suitable for programming Toolbox prototypes. Using a lower level language will decrease runtimes and using quad precision should provide a lower error for Daitche's method.

The study of the accuracy revealed a big impact of the initial relative velocity on the convergence of the schemes. In the case of particles starting with zero initial relative velocity, the schemes achieve higher convergence rates and on smoother velocity fields their convergence achieves or is close to their expected order of convergence. Second order FD methods are usually well-behaved, reaching in many cases their expected second order convergence, whereas fourth order methods achieve values between three and four, reaching four in very rare cases. Even so, fourth order methods attain the best convergence rates for the solutions of particle trajectories starting with zero initial relative velocity in all the fields, except the Faraday flow. Prasath et al.'s and Daitche's methods are in many cases the second best methods, having in these cases orders higher than two. Second order methods achieve in most cases first or second order. Second order IMEX method behave exceptionally good in the Faraday flow, being the method with the highest order for many sets of parameters.

The convergence of Daitche's third order method is in most cases smaller than expected. This was already expected, since Daitche (2013) [20] and Moreno-Casas and Bombardelli (2016) [47] already record a slightly loss in the convergence order when the coefficients are obtained and calculated using double precision instead of quad precision. Hence, an improvement in the convergence is to be expected if the coefficients were calculated with more precision. Daitche's method presents in many cases instabilities

For neutrally buoyant particles, i.e. $R = 1$, and zero initial relative velocity, all methods achieve some of their best convergence order and in some cases, their theoretical convergence, obtaining machine precision for Prasath et al's scheme. Prasath et al.'s scheme's convergence also improves as the values of R and S increase.

For trajectories calculated with non-zero initial relative velocity, the experimentally-computed convergence orders decrease considerably. Despite being a generalised behaviour, FD-based methods are the most affected methods. Second order FD methods often lose one order, while fourth order methods lose three or more convergence orders from their expected ones. This loss in convergence is expected, since a non-zero initial relative velocity introduces a discontinuity in the initial condition of the diffusive problem obtained after applying the transformation from Prasath et al. (2019) [53] and FD methods are known to perform badly with discontinuities. Daitche's 3^{rd} order scheme is also affected but the loss in convergence is not so drastic but it can be large, losing from one to almost two orders. On the other hand, Prasath et al.'s method's convergence order remains unchanged despite the discontinuity. This is most likely due to the integral nature of Prasath et al.'s solution formula. Integral methods usually perform well with discontinuities.

Regarding precision plots, a winner is only found for the cases with zero initial relative velocity. Daitche's method is the best performing method for the calculation of a particle trajectory in the vortex and in the double gyre with zero initial relative velocity. Second order IMEX method wins in the oscillatory background with zero initial relative velocity and ties for the best with the fourth order IMEX in Bickley jet. In these two fields, Daitche's approach presented instabilities in half of the meshes observed. Daitche is therefore better in rotating fields, whereas IMEX methods perform better in oscillatory fields. The methods that used nonlinear solvers, such as the implicit methods and Prasath et al.'s method, exceeded the real-time threshold for most of the grids used. In those grids in which the real-time threshold was not exceeded, the errors were greater than those in other methods. FD + IMEX methods as well as 3^{rd} order Daitche's method achieved faster-than-real-time times for more than half of the grids studied in all fields. The second order IMEX method was the only case in which all runtimes were faster than real-time for the grids considered.

In the problems with non-zero initial relative velocity there is no an indisputable winner. A compromise between short runtimes and small error must be found. Short runtimes at relatively high errors can be found with Daitche's third order method, whilst small runtimes at relatively long times can be achieved with Prasath et al.'s scheme.

Regarding convergence with respect to the value of the parameter c, a general reduction in error can be achieve by reducing c. The parameter c was set to 20 in the calculation of all the trajectories, convergence plots and orders as well as precision plots, so a reduction in the errors of the FD schemes could be achieved by setting a smaller value of c. In some very special cases, like a particle in either the oscillatory background or the double gyre or the Bickley jet with zero initial relative velocities, error increases when c is reduced from 5 to 2, so a big reduction in the value of c could be counterproductive.

It is impossible to indicate a globally best-performing scheme, since the scheme's behaviour changes with the initial conditions as well as the field considered. When the initial relative velocity is zero, the best performing method is the fourth order IMEX method, followed by Daitche's approach and the second IMEX method. Note that in the experimental field considered, FD2 + IMEX2 method behaved better for many of the parameter sets considered, obtaining lower errors for equal runtimes. For large grids, it is advisable not to use Daitche's method, since its computational costs (and therefore runtimes) grow "*with the square of the number of time-steps and can become quite substantial for long in-*

tegration periods" [20]. On the other hand, when the initial relative velocity is non-zero, it is recommendable to use either Daitche's third order scheme or Prasath et al.'s method, depending on whether accuracy or runtimes are a priority. Prasath et al.'s method achieves lower errors but it is almost never faster-than-real-time. Daitche's third order scheme is faster-than-realtime in all the cases, but its accuracy is not as good. Daitche's third order method has the limitation that it is unstable for many the sets of R and S studied. Many of these parameter sets correspond to feasible values in experiments.

Candelier et al. (2004) [12] showed experimentally that the influence of the BHT is not neglectable. Thanks to the implementations of efficient methods for solving the MRGE with history term, this influence was measured. For the simplest flow fields, such as the quiescent flow, the vortex and the oscillatory background, only one set of initial conditions is enough, whilst more particles were required to study the more complex fields. The simplest fields considered in this paper are given by short analytic formulas and are either symmetric or each spatial position is similar in some way.

In the absence of background flow (a quiescent flow field), final-time relative distances are not too different for the smallest Stokes numbers, $S \leq 0.1$, although particle trajectories calculated without BHT tend to come to a halt in a shorter time. Differences start to accentuate for $S \geq 1$, reaching over twice the final-time distance for $S = 10$. Maximum normalised distance difference is obtained for small and large enough values of S. It is important to note that for large S, some of our assumptions like are not applicable anymore and an experimentally-accurate solution may not be achieved if the Fàxen corrections are neglected.

In the vortex, radial distance changes (decreases for $R < 1$ and increases for $R > 1$) linearly for $S < 2$, while oscillations appear for the Stokes numbers larger than one. Neglecting the BHT overestimates the effect of the vortex for approximately $S < 2$ and underestimates it for approximately $S > 2$. Additionally, the inclusion of the BHT has a damping effect on the oscillations that appear for the larger Stokes numbers.

In the oscillatory background, the effect of the BHT in the particle's trajectory is very noticeable: The amplitude of the oscillation of the particles with BHT is four times larger than without the history term. Interestingly, the change in the trajectories is minimal as we change the Stokes number for values of $R \in \{7/9, 11/9, 5/3\}$. The only significant change is found for $R = 1/3$, which is a limit case, for an unrealistic particle with zero density.

On the fields given by the most complicate expressions, such as the double gyre, the Bickley jet and the Faraday flow, clusters of many particles are more useful. Single particle trajectories are not very characteristic, since these flows are unsteady and spatially-inhomogeneous and particle trajectory will be greatly influenced by its initial conditions.

Due to the rotating behaviour of the double gyre, a similar dynamics to the one of the vortex can be observed, with particles clustering or dispersing depending on the value of R. This behaviour gets accelerated when the BHT is ignored. Average relative distances between solutions with and without BHT typically grow with S for the two density ratios considered. Regarding relative average distances in lighter-than-fluid particles with $S = 10$, the difference between the solutions represents on average a substantial 65% of the average radial distance, which is the maximum relative average distance. In all the cases considered, more than half of the particles remain within the initial spatial domain, increasing this value with S. Generally, more particles leave the initial domain when the BHT is neglected,.

In the Bickley jet, erratic clusters are also observed when the BHT is neglected. The deviation between solutions grows steadily with the Stokes number and at a similar rate for all the values of R. The ratio of particles leaving the vertical domain remains low for $S \in \{0.1, 1\}$ and escalates quickly for $S = 10$, when it reaches less than 5% with BHT and about 25% without BHT. The number of particles leaving the vertical domain is then influenced by the BHT for the largest values of S.

In the experimental field a big percentage of particles leave the initial domain, ranging from 26.5% to 78.6%. In fact, more than half of the particles leave the initial domain in 10 out of the 12 cases analysed. When the BHT is ignored, this number increases, accelerating for the larger values of the Stokes number.

According to the previous observations, the BHT seems to have a large influence in trajectories of particles in the oscillatory fields than in fields of rotating nature and when it does have an influence, the BHT has a stabilising nature on the particle's trajectory. This stabilising behaviour can also be observed in the transporting features of the flow or LCS. The patterns of the FTLE colourmaps are more stable when the BHT is included. Neglecting the BHT produces patterns that correspond to ones with a higher Stokes number, namely larger particles.

In the double gyre and Bickley jet, there is little difference between the dynamics computed with and without BHT for Stokes number of $S = 0.1$. In the more turbulent Faraday flow, omitting the BHT already has a visible impact on the FTLE field for $S = 0.1$. For $S \in \{1, 10\}$, significant differences start to emerge for the double gyre and the Bickley jet, whilst differences reduce in the Faraday flow. Ignoring the BHT overestimates some of the FTLE, altering the positions of the LCS, even when the general patterns still look similar and produces patterns that would correspond to ones for a larger Stokes number if the BHT was considered.

To wrap up, a good approximation of a particle dynamics may be obtained without BHT at low Stokes numbers, $S \leq 0.1$. The full MRGE is adviced for medium and high Stokes numbers, $S \geq 1$. The MRGE without BHT may however behave well in flows with a high rotating component and poorly in highly oscillatory or turbulent flows.

Hopefully, the methods and findings presented in this paper will serve other scientists and researchers in accurately modeling particle movements and making appropriate decisions on when to neglect the history term. In addition, many unresolved questions and unfinished actions are left open in this research and we hope to inspire other scientist to continue them. Some of the unfinished actions consisted in extending the models to three-dimensional flows, including the buoyancy force, that is neglected in our models. A full solution of the MRGE could also be provided by including Fàxen corrections in Prasath et al.'s transformation. The numerical resolution could also be improved by providing some way to avoid the discontinuous initial condition when the initial relative velocity is nonzero. To add on, a continuous study of the errors could be done for continuous values of the parameters R and S.

A

Coefficients for Daitche (2013)'s method

Coefficients η_j^n for the three methods provided in Daitche (2013) are provided here. Note that the coefficients differ depending on the convergence order of the method. More information about the coefficients and their calculation can be obtained from Daitche (2013) [20].

- For the first order method ($\nu = 1$):

$$\eta_j^n = \frac{4}{3}\begin{cases} 1 & j = 0 \\ (j-1)^{3/2} + (j+1)^{3/2} - 2j^{3/2} & 0 < j < n \\ (n-1)^{3/2} - n^{3/2} + \frac{6}{4}\sqrt{n} & j = n. \end{cases} \tag{A.1}$$

- For the second order method ($\nu = 2$):
  - For $n = 2$:

$$\eta^2_{j=0,1,2} = \frac{12}{15}\sqrt{2};\, \frac{16}{15}\sqrt{2};\, \frac{2}{15}\sqrt{2} \tag{A.2}$$

.

  - For $n = 3$:

$$\eta^3_{j=0,1,2,3} = \frac{4}{5}\sqrt{2};\, \frac{14}{5}\sqrt{3} - \frac{12}{5}\sqrt{2};\, -\frac{8}{5}\sqrt{3} + \frac{12}{5}\sqrt{2};\, \frac{4}{5}\sqrt{3} - \frac{4}{5}\sqrt{2} \tag{A.3}$$

.

  - For $n \geq 4$:

$$\eta_j^n = \begin{cases} \frac{4}{5}\sqrt{2}, & j = 0, \\ \frac{14}{5}\sqrt{3} - \frac{12}{5}\sqrt{2}, & j = 1, \\ \frac{176}{15} - \frac{42}{5}\sqrt{3} + \frac{12}{5}\sqrt{2}, & j = 2, \\ \frac{8}{15}((j+2)^{5/2} - 3(j+1)^{5/2} + 3j^{5/2} - (j-1)^{5/2}) + & \\ \quad + \frac{2}{3}(-(j+2)^{3/2} + 3(j+1)^{3/2} - 3j^{3/2} + (j-1)^{3/2}), & 2 < j < n-1, \\ \frac{8}{15}(-2n^{5/2} + 3(n-1)^{5/2} - (n-2)^{5/2}) + & \\ \quad + \frac{2}{3}(4n^{3/2} - 3(n-1)^{3/2} + (n-2)^{3/2}), & j = n-1, \\ \frac{8}{15}(n^{5/2} - (n-1)^{5/2}) + \frac{2}{3}(-3n^{3/2} + (n-1)^{3/2}) + 2\sqrt{n}, & j = n. \end{cases} \tag{A.4}$$

- And for the third order method ($\nu = 3$):
  - For $3 \leq n \leq 6$:

$$\eta^3_{j=0,\dots,3} = \frac{68}{105}\sqrt{3};\ \frac{6}{7}\sqrt{3};\ \frac{12}{35}\sqrt{3};\ \frac{16}{105}\sqrt{3}, \tag{A.5}$$

$$\begin{aligned}\eta^4_{j=0,\dots,4} = {} & \frac{244}{315}\sqrt{2};\ \frac{1888}{315} - \frac{976}{315}\sqrt{2};\ -\frac{656}{105} + \frac{488}{105}\sqrt{2};\\ & \frac{544}{105} - \frac{976}{315}\sqrt{2};\ -\frac{292}{315} + \frac{244}{315}\sqrt{2},\end{aligned} \tag{A.6}$$

$$\begin{aligned}\eta^5_{j=0,\dots,5} = {} & \frac{244}{315}\sqrt{2};\ \frac{362}{105}\sqrt{3} - \frac{976}{315}\sqrt{2};\ \frac{500}{63}\sqrt{5} - \frac{1448}{105}\sqrt{3} + \frac{488}{105}\sqrt{2};\\ & -\frac{290}{21}\sqrt{5} + \frac{724}{35}\sqrt{3} - \frac{976}{315}\sqrt{2};\ \frac{220}{21}\sqrt{5} - \frac{1448}{105}\sqrt{3} + \frac{244}{315}\sqrt{2};\\ & -\frac{164}{63}\sqrt{5} + \frac{362}{105}\sqrt{3},\end{aligned} \tag{A.7}$$

$$\begin{aligned}\eta^6_{j=0,\dots,6} = {} & \frac{244}{315}\sqrt{2};\ \frac{362}{105}\sqrt{3} - \frac{976}{315}\sqrt{2};\ \frac{5584}{315} - \frac{1448}{105}\sqrt{3} + \frac{488}{105}\sqrt{2};\\ & \frac{344}{21}\sqrt{6} - \frac{22336}{315} + \frac{724}{35}\sqrt{3} - \frac{976}{315}\sqrt{2};\\ & -\frac{1188}{35}\sqrt{6} + \frac{11168}{105} - \frac{1448}{105}\sqrt{3} + \frac{244}{315}\sqrt{2};\\ & \frac{936}{35}\sqrt{6} - \frac{22336}{315} + \frac{362}{105}\sqrt{3};\ -\frac{754}{105}\sqrt{6} + \frac{5584}{315}.\end{aligned} \tag{A.8}$$

  - For $n \geq 7$:

$$\eta^n_j = \begin{cases} \frac{244}{315}\sqrt{2}, & j = 0,\\ \frac{362}{105}\sqrt{3} - \frac{976}{315}\sqrt{2}, & j = 1,\\ \frac{5584}{315} - \frac{1448}{105}\sqrt{3} + \frac{488}{105}\sqrt{2}, & j = 2,\\ \frac{1130}{63}\sqrt{5} - \frac{22336}{315} + \frac{724}{35}\sqrt{3} - \frac{976}{315}\sqrt{2}, & j = 3,\\ \frac{16}{105}((j+2)^{7/2} + (j-2)^{7/2} - 4(j+1)^{7/2} + & \\ - 4(j-1)^{7/2} + 6j^{7/2}) + \frac{2}{9}(4(j+1)^{3/2} + & \\ + 4(j-1)^{3/2} - (j+2)^{3/2} - (j-2)^{3/2} - 6j^{3/2}), & 3 < j < n-3,\\ \frac{16}{105}(n^{7/2} - 4(n-2)^{7/2} + 6(n-3)^{7/2} + & \\ - 4(n-4)^{7/2} + (n-5)^{7/2}) - \frac{8}{15}n^{5/2} + \frac{4}{9}n^{3/2} + & \\ + \frac{8}{9}(n-2)^{3/2} - \frac{4}{3}(n-3)^{3/2} + \frac{8}{9}(n-4)^{3/2} + & \\ - \frac{2}{9}(n-5)^{3/2}, & j = n-3,\\ \frac{16}{105}((n-4)^{7/2} - 4(n-3)^{7/2} + 6(n-2)^{7/2} - 3n^{7/2}) + & \\ + \frac{32}{15}n^{5/2} - 2n^{3/2} - \frac{4}{3}(n-2)^{3/2} + \frac{8}{9}(n-3)^{3/2} + & \\ - \frac{2}{9}(n-4)^{3/2}, & j = n-2,\\ \frac{16}{105}(3n^{7/2} - 4(n-2)^{7/2} + (n-3)^{7/2}) - \frac{8}{3}n^{5/2} + 4n^{3/2} + & \\ + \frac{8}{9}(n-2)^{3/2} - \frac{2}{9}(n-3)^{3/2}, & j = n-1,\\ \frac{16}{105}((n-2)^{7/2} - n^{7/2}) + \frac{16}{15}n^{5/2} - \frac{22}{9}n^{3/2} - \frac{2}{9}(n-2)^{3/2} + & \\ + 2\sqrt{n}, & j = n. \end{cases} \tag{A.9}$$

B

Matrices for the fourth order formulation

The matrices used in the system (5.32a) and (5.32b) of the FD numerical schemes and implemented in the Python Toolbox [72] are shown below.

$$M_1 := \begin{bmatrix} c & 0 & \frac{Nc}{N-1} & 0 & 0 & 0 & 0 & \dots & 0 \\ 0 & c & 0 & \frac{Nc}{N-1} & 0 & \ddots & \ddots & \ddots & 0 \\ c & 0 & \frac{4Nc}{N-1} & 0 & \frac{Nc}{N-2} & 0 & \ddots & \ddots & 0 \\ 0 & c & 0 & \frac{4Nc}{N-1} & 0 & \frac{Nc}{N-2} & 0 & \ddots & 0 \\ \vdots & 0 & \frac{Nc}{N-1} & 0 & \frac{4Nc}{N-2} & 0 & \frac{Nc}{N-3} & \ddots & 0 \\ \vdots & \ddots & \ddots & \ddots & \ddots & \ddots & \ddots & \ddots & \vdots \\ \vdots & \ddots & \ddots & \frac{Nc}{4} & 0 & \frac{4Nc}{3} & 0 & \frac{Nc}{2} & 0 \\ \vdots & \ddots & \ddots & \ddots & \frac{Nc}{4} & 0 & \frac{4Nc}{3} & 0 & \frac{Nc}{2} \\ 0 & \ddots & \ddots & \ddots & \ddots & \frac{Nc}{3} & 0 & \frac{4Nc}{2} & 0 \\ 0 & 0 & \dots & \dots & \dots & 0 & \frac{Nc}{3} & 0 & \frac{4Nc}{2} \end{bmatrix},$$

$$M_2 := \begin{bmatrix} c & 0 & 3\frac{Nc}{N-1} & 0 & 0 & 0 & 0 & 0 & \dots & 0 \\ 0 & c & 0 & 3\frac{Nc}{N-1} & 0 & \ddots & \ddots & \ddots & \ddots & 0 \\ c & 0 & \frac{4Nc}{N-1} & 0 & \frac{Nc}{N-2} & 0 & \ddots & \ddots & \ddots & 0 \\ 0 & c & 0 & \frac{4Nc}{N-1} & 0 & \frac{Nc}{N-2} & 0 & \ddots & \ddots & 0 \\ 0 & 0 & \frac{Nc}{N-1} & 0 & \frac{4Nc}{N-2} & 0 & \frac{Nc}{N-3} & 0 & \ddots & 0 \\ \vdots & \ddots & \ddots & \ddots & \ddots & \ddots & \ddots & \ddots & \ddots & \vdots \\ \vdots & \ddots & \ddots & \ddots & \frac{Nc}{4} & 0 & \frac{4Nc}{3} & 0 & \frac{Nc}{2} & 0 \\ \vdots & \ddots & \ddots & \ddots & 0 & \frac{Nc}{4} & 0 & \frac{4Nc}{3} & 0 & \frac{Nc}{2} \\ 0 & \ddots & \ddots & \ddots & \ddots & 0 & \frac{Nc}{3} & 0 & \frac{4Nc}{2} & 0 \\ 0 & 0 & \dots & \dots & \dots & \dots & 0 & \frac{Nc}{3} & 0 & \frac{4Nc}{2} \end{bmatrix},$$

$$B_1 := \frac{1}{d}\begin{bmatrix} \frac{12\alpha dc-17\gamma}{18\gamma} & 0 & {}^1\!/_2 & 0 & {}^1\!/_2 & 0 & -{}^1\!/_{18} & 0 & \dots & 0 \\ 0 & \frac{12\alpha dc-17\gamma}{18\gamma} & 0 & {}^1\!/_2 & 0 & {}^1\!/_2 & 0 & -{}^1\!/_{18} & \ddots & 0 \\ -3 & 0 & 0 & 0 & 3 & 0 & 0 & 0 & \dots & 0 \\ 0 & -3 & 0 & 0 & 0 & 3 & 0 & 0 & \ddots & 0 \\ \vdots & \ddots & \ddots & \ddots & \ddots & \ddots & \ddots & \ddots & \ddots & \vdots \\ \vdots & \ddots & \ddots & \ddots & \ddots & 0 & -3 & 0 & 0 & 0 \\ 0 & \dots & \dots & \dots & \dots & \dots & 0 & -3 & 0 & 0 \end{bmatrix},$$

$$B_2 := \frac{1}{d}\begin{bmatrix} -{}^{17}\!/_6 & 0 & {}^3\!/_2 & 0 & {}^3\!/_2 & 0 & -{}^1\!/_6 & 0 & \dots & 0 \\ 0 & -{}^{17}\!/_6 & 0 & {}^3\!/_2 & 0 & {}^3\!/_2 & 0 & -{}^1\!/_6 & \dots & 0 \\ -3 & 0 & 0 & 0 & 3 & 0 & 0 & 0 & \dots & 0 \\ 0 & -3 & 0 & 0 & 0 & 3 & 0 & \ddots & \ddots & 0 \\ 0 & 0 & -3 & 0 & 0 & 0 & 3 & 0 & \ddots & \vdots \\ \vdots & \ddots & \ddots & \ddots & \ddots & \ddots & \ddots & \ddots & \ddots & \vdots \\ \vdots & \ddots & \ddots & \ddots & \ddots & 0 & -3 & 0 & 0 & 0 \\ 0 & \dots & \dots & \dots & \dots & \dots & 0 & -3 & 0 & 0 \end{bmatrix},$$

.

$$K_1 := \begin{bmatrix} -\frac{2c}{3\gamma} f^{(1)}(\boldsymbol{q}_0(t), \boldsymbol{y}_0(t), t) \\ -\frac{2c}{3\gamma} f^{(2)}(\boldsymbol{q}_0(t), \boldsymbol{y}_0(t), t) \\ 0 \\ 0 \\ \vdots \\ 0 \end{bmatrix} \quad \text{and} \quad V_1 := \frac{2c}{3\gamma}\begin{bmatrix} \left.\frac{\partial q^{(1)}(\xi(x),t)}{\partial t}\right|_0 \\ \left.\frac{\partial q^{(2)}(\xi(x),t)}{\partial t}\right|_0 \\ 0 \\ 0 \\ \vdots \\ 0 \end{bmatrix}.$$

Acknowledgements

Words cannot express my gratitude to my supervisor,..

Bibliography

[1] Mark J Ablowitz and Athanassios S Fokas. *Complex variables: Introduction and applications.* Cambridge University Press, 1997.

[2] Grégoire Allaire, Sidi Mahmoud Kaber, Karim Trabelsi, and Grégoire Allaire. *Numerical linear algebra.* Vol. 55. 2008. Springer, 2008.

[3] Elena Alexandronva Alshina, Nikolai Nikolaevich Kalitkin, and Sergey Leonidovich Panchenko. "Numerical solution of boundary value problems in unlimited area". In: *Matematicheskoe modelirovanie* 14.11 (2002), pp. 10–22.

[4] Uri M Ascher, Steven J Ruuth, and Raymond J Spiteri. "Implicit-explicit Runge-Kutta methods for time-dependent partial differential equations". In: *Applied Numerical Mathematics* 25.2-3 (1997), pp. 151–167.

[5] Tim R Auton, JCR Hunt, and M Prud'Homme. "The force exerted on a body in inviscid unsteady non-uniform rotational flow". In: *Journal of Fluid Mechanics* 197 (1988), pp. 241–257.

[6] Sanjeeva Balasuriya, Nicholas T Ouellette, and Irina I Rypina. "Generalized Lagrangian coherent structures". In: *Physica D: Nonlinear Phenomena* 372 (2018), pp. 31–51.

[7] Nishanta Baral. "Dynamics of Inertial and Non-Inertial Particles in Geophysical Flows". MA thesis. Montclair State University, 2023.

[8] Alfred Barnard Basset. *A treatise on hydrodynamics: with numerous examples.* Vol. 2. Deighton, Bell and Company, 1888.

[9] Francisco J Beron-Vera, Maria J Olascoaga, and GJ Goni. "Oceanic mesoscale eddies as revealed by Lagrangian Coherent Structures". In: *Geophysical Research Letters* 35.12 (2008).

[10] Francisco J Beron-Vera, Maria J Olascoaga, and P Miron. "Building a Maxey–Riley framework for surface ocean inertial particle dynamics". In: *Physics of Fluids* 31.9 (2019).

[11] Joseph Boussinesq. “Sur la resistance qu’oppose un fluide indefini en repos, sans pesanteur, au mouvement varie d’une sphere solide qu’il mouille sur toute sa surface, quand les vitesses restent bien continues et assez faibles pour que leurs carres et produits soient negligiables”. In: *CR Acad. Sc. Paris* 100 (1885), pp. 935–937.

[12] F Candelier, JR Angilella, and M Souhar. “On the effect of the Boussinesq–Basset force on the radial migration of a Stokes particle in a vortex”. In: *Physics of Fluids* 16.5 (2004), pp. 1765–1776.

[13] Shing Bor Chen and Xiangnan Ye. “Faxen’s laws of a composite sphere under creeping flow conditions”. In: *Journal of colloid and interface science* 221.1 (2000), pp. 50–57.

[14] Raffaele Colombi, Michael Schlüter, and Alexandra von Kameke. “Three dimensional flows beneath a thin layer of 2D turbulence induced by Faraday waves”. In: *Experiments in fluids* 62 (2021), pp. 1–13.

[15] Raffaele Colombi, Niclas Rohde, Michael Schlüter, and Alexandra von Kameke. “Coexistence of inverse and direct energy cascades in faraday waves”. In: *Fluids* 7.5 (2022), p. 148.

[16] Wikipedia contributors. *LU decomposition - Wikipedia — en.wikipedia.org*. `https://en.wikipedia.org/wiki/LU_decomposition`. [Accessed 13-06-2024].

[17] SE Corrsin and J Lumley. “On the equation of motion for a particle in turbulent fluid”. In: *Applied Scientific Research, Section A* 6.2 (1956), pp. 114–116.

[18] John Crank and Phyllis Nicolson. “A practical method for numerical evaluation of solutions of partial differential equations of the heat-conduction type”. In: *Mathematical proceedings of the Cambridge philosophical society*. Vol. 43. 1. Cambridge University Press. 1947, pp. 50–67.

[19] Cathal P Cummins, Olayinka J Ajayi, Felicity V Mehendale, Roman Gabl, and Ignazio Maria Viola. “The dispersion of spherical droplets in source–sink flows and their relevance to the COVID-19 pandemic”. In: *Physics of Fluids* 32.8 (2020).

[20] Anton Daitche. “Advection of inertial particles in the presence of the history force: Higher order numerical schemes”. In: *Journal of Computational Physics* 254 (2013), pp. 93–106.

[21] Mazyar Dawoodian and Amalendu Sau. “Kinetics and prey capture by a paddling jellyfish: Three-dimensional simulation and Lagrangian Coherent Structure analysis”. In: *Journal of Fluid Mechanics* 912 (2021), A41.

[22] Bernard Deconinck, Qi Guo, Eli Shlizerman, and Vishal Vasan. “Fokas’s unified transform method for linear systems”. In: *Quarterly of Applied Mathematics* 76.3 (2018), pp. 463–488.

[23] Emmanuele DiBenedetto. *Real analysis*. Springer, 2002.

[24] JR Dormand and PJ Prince. “A reconsideration of some embedded Runge—Kutta formulae”. In: *Journal of computational and applied mathematics* 15.2 (1986), pp. 203–211.

[25] Husam A Elghannay and Danesh K Tafti. “Development and validation of a reduced order history force model”. In: *International Journal of Multiphase Flow* 85 (2016), pp. 284–297.

[26] Mohammad Farazmand and George Haller. “The Maxey–Riley equation: Existence, uniqueness and regularity of solutions”. In: *Nonlinear Analysis: Real World Applications* 22 (2015), pp. 98–106.

[27] Riccardo Fazio and Alessandra Jannelli. “Finite difference schemes on quasi-uniform grids for BVPs on infinite intervals”. In: *Journal of Computational and Applied Mathematics* 269 (2014), pp. 14–23.

[28] N Flyer and AS Fokas. “A hybrid analytical–numerical method for solving evolution partial differential equations. I. The half-line”. In: *Proceedings of the Royal Society A: Mathematical, Physical and Engineering Sciences* 464.2095 (2008), pp. 1823–1849.

[29] Athanassios S Fokas. *A unified approach to boundary value problems.* SIAM, 2008.

[30] D Garaboa-Paz and Vicente Pérez-Muñuzuri. “A method to calculate finite-time Lyapunov exponents for inertial particles in incompressible flows”. In: *Nonlinear Processes in Geophysics* 22.5 (2015), pp. 571–577.

[31] Rene Gatignol. “The Faxen formulae for a rigid particle in an unsteady non-uniform Stokes flow”. In: (1983).

[32] Alireza Hadjighasem, Daniel Karrasch, Hiroshi Teramoto, and George Haller. “Spectral-clustering approach to Lagrangian vortex detection”. In: *Physical Review E* 93.6 (2016), p. 063107.

[33] Charles R. Harris, K. Jarrod Millman, Stéfan J. van der Walt, Ralf Gommers, Pauli Virtanen, David Cournapeau, Eric Wieser, Julian Taylor, Sebastian Berg, Nathaniel J. Smith, Robert Kern, Matti Picus, Stephan Hoyer, Marten H. van Kerkwijk, Matthew Brett, Allan Haldane, Jaime Fernández del Río, Mark Wiebe, Pearu Peterson, Pierre Gérard-Marchant, Kevin Sheppard, Tyler Reddy, Warren Weckesser, Hameer Abbasi, Christoph Gohlke, and Travis E. Oliphant. “Array programming with NumPy”. In: *Nature* 585.7825 (Sept. 2020), pp. 357–362. DOI: `10.1038/s41586-020-2649-2`. URL: `https://doi.org/10.1038/s41586-020-2649-2`.

[34] Christopher A Kennedy and Mark H Carpenter. *Diagonally implicit Runge-Kutta methods for ordinary differential equations. A review.* Tech. rep. 2016.

[35] Joy Klinkenberg, HC De Lange, and Luca Brandt. “Linear stability of particle laden flows: the influence of added mass, fluid acceleration and Basset history force”. In: *Meccanica* 49 (2014), pp. 811–827.

[36] Kunihiko Kodaira. *Introduction to complex analysis.* Cambridge ; New York : Cambridge University Press, 1984.

[37] Miglena N Koleva. “Numerical solution of the heat equation in unbounded domains using quasi-uniform grids”. In: *International Conference on Large-Scale Scientific Computing.* Springer. 2005, pp. 509–517.

[38] Wilhelm Kutta. *Beitrag zur näherungsweisen Integration totaler Differentialgleichungen.* Teubner, 1901.

[39] Gabriel Provencher Langlois, Mohammad Farazmand, and George Haller. “Asymptotic dynamics of inertial particles with memory”. In: *Journal of nonlinear science* 25 (2015), pp. 1225–1255.

[40] Sanjiva K Lele. “Compact finite difference schemes with spectral-like resolution”. In: *Journal of computational physics* 103.1 (1992), pp. 16–42.

[41] James Malele, Phumlani Dlamini, and Simphiwe Simelane. “Highly accurate compact finite difference schemes for two-point boundary value problems with Robin boundary conditions”. In: *Symmetry* 14.8 (2022), p. 1720.

[42] Martin R Maxey and James J Riley. “Equation of motion for a small rigid sphere in a nonuniform flow”. In: *The Physics of Fluids* 26.4 (1983), pp. 883–889.

[43] Martin R Maxey et al. “The equation of motion for a small rigid sphere in a nonuniform or unsteady flow”. In: *ASME-PUBLICATIONS-FED* 166 (1993), pp. 57–57.

[44] Renwei Mei and Ronald J Adrian. “Flow past a sphere with an oscillation in the free-stream velocity and unsteady drag at finite Reynolds number”. In: *Journal of Fluid Mechanics* 237 (1992), pp. 323–341.

[45] Igor Mezić, Sophie Loire, Vladimir A Fonoberov, and P Hogan. “A new mixing diagnostic and Gulf oil spill movement”. In: *Science* 330.6003 (2010), pp. 486–489.

[46] E Mograbi and E Bar-Ziv. “On the asymptotic solution of the Maxey-Riley equation”. In: *Physics of Fluids* 18.5 (2006).

[47] Patricio A Moreno-Casas and Fabian A Bombardelli. “Computation of the Basset force: recent advances and environmental flow applications”. In: *Environmental Fluid Mechanics* 16 (2016), pp. 193–208.

[48] Francesco Nencioli, Francesco d’Ovidio, AM Doglioli, and AA Petrenko. “Surface coastal circulation patterns by in-situ detection of Lagrangian Coherent Structures”. In: *Geophysical Research Letters* 38.17 (2011).

[49] María J Olascoaga and George Haller. “Forecasting sudden changes in environmental pollution patterns”. In: *Proceedings of the National Academy of Sciences* 109.13 (2012), pp. 4738–4743.

[50] CW Oseen. “Hydrodynamik (Leipzig 1927)”. In: *Akademische Verlagsgesellschaft* (1927).

[51] Kathrin Padberg-Gehle and Christiane Schneide. “Network-based study of Lagrangian transport and mixing”. In: *Nonlinear Processes in Geophysics* 24.4 (2017), pp. 661–671.

[52] M Parmar, S Annamalai, S Balachandar, and A Prosperetti. “Differential formulation of the viscous history force on a particle for efficient and accurate computation”. In: *Journal of Fluid Mechanics* 844 (2018), pp. 970–993.

[53] S Ganga Prasath, Vishal Vasan, and Rama Govindarajan. “Accurate solution method for the Maxey–Riley equation, and the effects of Basset history”. In: *Journal of Fluid Mechanics* 868 (2019), pp. 428–460.

[54] Kenneth Franklin Riley, Michael Paul Hobson, and Stephen John Bence. “Mathematical methods for physics and engineering”. In: *(No Title)* (1998).

[55] Carl Runge. “Ueber die numerische Auflösung totaler Differentialgleichungen”. In: *Nachrichten von der Gesellschaft der Wissenschaften zu Göttingen, Mathematisch-Physikalische Klasse* 1905 (1905), pp. 252–257.

[56] Daniel Ruprecht, Achim Schädle, Frank Schmidt, and Lin Zschiedrich. “Transparent boundary conditions for time-dependent problems”. In: *SIAM journal on scientific computing* 30.5 (2008), pp. 2358–2385.

[57] II Rypina, Michael G Brown, Francisco J Beron-Vera, Huseyin Koçak, Maria J Olascoaga, and IA Udovydchenkov. “On the Lagrangian dynamics of atmospheric zonal jets and the permeability of the stratospheric polar vortex”. In: *Journal of the Atmospheric Sciences* 64.10 (2007), pp. 3595–3610.

[58] L Schlegel. “Implicit-explicit Time-Stepping for the Maxey-Riley Equations”. Bachelor’s Thesis. Technische Universität Hamburg, 2023.

[59] Mark W Schmeeckle. “Numerical simulation of turbulence and sediment transport of medium sand”. In: *Journal of Geophysical Research: Earth Surface* 119.6 (2014), pp. 1240–1262.

[60] Christian Seifert. *Lecture notes in Numerical methods for ODEs.* 2021.

[61] Shawn C Shadden. *Tutorial in Lagrangian Coherent Structures.* 2005. URL: `https://shaddenlab.berkeley.edu/uploads/LCS-tutorial/examples.html` (visited on 04/15/2005).

[62] Shawn C Shadden, Francois Lekien, and Jerrold E Marsden. “Definition and properties of Lagrangian Coherent Ctructures from finite-time Lyapunov exponents in two-dimensional aperiodic flows”. In: *Physica D: Nonlinear Phenomena* 212.3-4 (2005), pp. 271–304.

[63] Shadden Lab, University of California Berkeley. *LCS Tutorial: Brief Overview — shaddenlab.berkeley.edu.* `https://shaddenlab.berkeley.edu/uploads/LCS-tutorial/FTLE-derivation.html`. [Accessed 18-06-2024]. 2005.

[64] Murray R Spiegel and Seymour Lipschutz. *Schaum’s outline of vector analysis.* McGraw Hill Professional, 2009.

[65] George Gabriel Stokes et al. “On the effect of the internal friction of fluids on the motion of pendulums”. In: (1851).

[66] M Sudharsan, Steven L Brunton, and James J Riley. “Lagrangian Coherent Structures and inertial particle dynamics”. In: *Physical Review E* 93.3 (2016), p. 033108.

[67] Alexander Y Suhov and Adi Ditkowski. “Artificial boundary conditions for the simulation of the heat equation in an infinite domain”. In: *SIAM Journal on Scientific Computing* 33.4 (2011), pp. 1765–1784.

[68] Wenbo Tang, Brent Knutson, Alex Mahalov, and Reneta Dimitrova. “The geometry of inertial particle mixing in urban flows, from deterministic and random displacement models”. In: *Physics of Fluids* 24.6 (2012).

[69] FB Tatom. “The Basset term as a semiderivative”. In: *Applied Scientific Research* 45.3 (1988), pp. 283–285.

[70] CM Tchen. “Mean Value and Correlation Problems Connected with the Motion of Small Particles Suspended in a Turbulent Fluid”. In: (1947).

[71] Lloyd N Trefethen and David Bau. *Numerical linear algebra.* SIAM, 2022.

[72] Julio Urizarna-Carasa and Leon Schlegel. *JulioUri/Thesis_Efficient-Numerics-on-MRGE: v1.1 - Thesis release*. Version v1.0. Feb. 2025. DOI: `10.5281/zenodo.14837893`. URL: `https://doi.org/10.5281/zenodo.14837893`.

[73] Julio Urizarna-Carasa, Leon Schlegel, and Daniel Ruprecht. "Efficient numerical methods for the Maxey-Riley-Gatignol equations with Basset history term". In: *Computer Physics Communications* (2025), p. 109502.

[74] Julio Urizarna-Carasa, Daniel Ruprecht, Alexandra von Kameke, and Kathrin Padberg-Gehle. "A Python toolbox for the numerical solution of the Maxey-Riley equation". In: *PAMM* 22.1 (2023), e202200242.

[75] Julio Urizarna-Carasa, Daniel Ruprecht, Alexandra von Kameke, and Kathrin Padberg-Gehle. "Relevance of the Basset history term for Lagrangian particle dynamics". In: *arXiv preprint arXiv:2407.01041* (2024).

[76] MAT Van Hinsberg, JHM ten Thije Boonkkamp, and Hans JH Clercx. "An efficient, second order method for the approximation of the Basset history force". In: *Journal of Computational Physics* 230.4 (2011), pp. 1465–1478.

[77] Pauli Virtanen, Ralf Gommers, Travis E. Oliphant, Matt Haberland, Tyler Reddy, David Cournapeau, Evgeni Burovski, Pearu Peterson, Warren Weckesser, Jonathan Bright, Stéfan J. van der Walt, Matthew Brett, Joshua Wilson, K. Jarrod Millman, Nikolay Mayorov, Andrew R. J. Nelson, Eric Jones, Robert Kern, Eric Larson, C J Carey, İlhan Polat, Yu Feng, Eric W. Moore, Jake VanderPlas, Denis Laxalde, Josef Perktold, Robert Cimrman, Ian Henriksen, E. A. Quintero, Charles R. Harris, Anne M. Archibald, Antônio H. Ribeiro, Fabian Pedregosa, Paul van Mulbregt, and SciPy 1.0 Contributors. "SciPy 1.0: Fundamental Algorithms for Scientific Computing in Python". In: *Nature Methods* 17 (2020), pp. 261–272. DOI: `10.1038/s41592-019-0686-2`.

[78] Wikipedia contributors. *Finite difference coefficient — Wikipedia, The Free Encyclopedia.* [Online; accessed 24-July-2024]. 2024. URL: `https://en.wikipedia.org/w/index.php?title=Finite_difference_coefficient&oldid=1230644148`.

[79] Wikipedia contributors. *Finite difference method — Wikipedia, The Free Encyclopedia.* [Online; accessed 8-February-2024]. 2024. URL: `https://en.wikipedia.org/w/index.php?title=Finite_difference_method&oldid=1199043638`.

[80] Wikipedia contributors. *Fourier transform — Wikipedia, The Free Encyclopedia.* [Online; accessed 12-July-2024]. 2024. URL: `https://en.wikipedia.org/w/index.php?title=Fourier_transform&oldid=1233567982`.

[81] Wikipedia contributors. *Green's theorem — Wikipedia, The Free Encyclopedia.* [Online; accessed 9-July-2024]. 2023. URL: `https://en.wikipedia.org/w/index.php?title=Green%27s_theorem&oldid=1188897720`.

[82] Wikipedia contributors. *Hamiltonian system — Wikipedia, The Free Encyclopedia.* `https://en.wikipedia.org/w/index.php?title=Hamiltonian_system&oldid=1216705422`. [Online; accessed 14-August-2024]. 2024.

[83] Wikipedia contributors. *Trapezoidal rule — Wikipedia, The Free Encyclopedia.* `https://en.wikipedia.org/w/index.php?title=Trapezoidal_rule&oldid=1181282452`. [Online; accessed 24-January-2024]. 2023.